Stéphane Longeville
Laboratoire Léon Brillouin
CEA-Saclay

Influence de l'environnement cytoplasmique sur la diffusion et la stabilité des protéines

Habilitation à Diriger les Recherches.

Soutenue le 1^{er} Décembre 2009, devant le jury composé de :

S. Cribier, Professeur, *Université de Paris VI*
M. Daoud, Physicien, *Commissariat à l'Energie Atomique*
W. Doster, Professeur, *TU München*
D. Durand, Directeur de Recherche CNRS, *Université de Paris Sud*
J.-P. Hansen, Professeur, *Université de Cambridge*
F. Mezei, Professeur *Los Alamos National Laboratory*

Université Paris VI, Pierre & Marie Curie

Sommaire

Préambule **3**

1 Présentation générale **5**
1.1 Généralités . . . 5
1.2 Notion de volume accessible et volume exclu . . . 7
1.3 La non-idéalité d'une solution . . . 8
1.4 Influence de l'encombrement cytoplasmique sur l'équilibre et la cinétique des réactions . . . 9
1.5 Influence de l'encombrement cytoplasmique sur la diffusion des protéines et les mécanismes de transport . . . 10
1.6 Présentation du manuscrit . . . 10

2 Influence de l'encombrement cellulaire sur la diffusion de protéines **13**
2.1 Introduction . . . 13
2.1.1 Les systèmes biologiques . . . 16
2.1.2 Motivations . . . 18
2.2 Un modèle pour les interactions protéine-protéine . . . 19
2.3 Diffusion de la myoglobine et de l'hémoglobine *in-vitro* . . . 20
2.3.1 Recherche du coefficient de diffusion à temps court . . . 24
2.3.2 Dépendance en vecteur d'onde de D(q) . . . 26
2.4 Diffusion de l'hémoglobine *in-vivo* . . . 26
2.5 Implications physiologiques de la diffusion de l'hémoglobine et de la myoglobine dans le transport d'oxygène . . . 29
2.5.1 Généralités . . . 29
2.5.2 Transport de l'oxygène par la myoglobine dans les muscles . . . 30
2.5.3 Influence de la diffusion de l'hémoglobine sur la capture et la libération de l'oxygène par les globules rouges . . . 31
2.6 Perspectives . . . 34

3 Influence de l'environnement cytoplasmique sur la stabilité des protéines **37**
3.1 Introduction . . . 37
3.2 Un système modèle pour l'état dénaturé . . . 40
3.2.1 Introduction : approche expérimentale . . . 40
3.2.2 L'encombrement cytoplasmique : le Ficoll 70 . . . 41
3.2.3 Etude de la compression d'une chaîne Gaussienne . . . 42
3.2.4 Dépendance en fonction R_g^{PEG}/R_g^{F70} . . . 44
3.2.5 Conformation de la chaîne compressée . . . 48
3.3 Conclusion . . . 49

3.4 Perspectives 50

4 Conclusion générale **53**

Liste de publications **61**
Articles publiés dans des revues à parution régulière et comité de lecture . . 63

Encadrement **67**
Etudiants doctorants 67
Etudiants stagiaires 67

Publications **69**
C. Le Coeur, J. Teixeira, P. Busch and S. Longeville, Phys. Rev. E **81** (2010) 0.61914 71
C. Le Coeur, B. Demée and S. Longeville, Phys. Rev. E **79** (2009) 0.31910 75
C. Le Coeur and S. Longeville, Chem. Phys. **345** (2008) 298-304 . . . 79
W. Doster and S. Longeville, Biophys. J **93** (2007) 1360-1368 87
R. E. Lechner and S. Longeville, Neutrons in Biology 97
S. Longeville, W. Doster and G. Kali, Chem. Phys. **292** (2003) 413-424 145

Préambule

Ce manuscrit fait le bilan de mes activités de recherche, qui se sont étalées sur environ 16 ans depuis le début de mon travail de thèse. Le fil conducteur aura certainement été les mesures de dynamiques de la matière condensée par diffusion de neutrons. Depuis la physique du solide (ma thèse de doctorat) en allant vers les systèmes désordonnés et les liquides, et finalement les systèmes biologiques, la complexité ne cesse de croître. En perdant les symétries de translation, les puissants objets que sont les fonctions de Bloch et les zones de Brillouin deviennent obsolètes et les études dynamiques qui ont fait (et font toujours) la gloire des spectromètres 3 axes deviennent inapplicables. Des liquides aux systèmes hors d'équilibre, la perte d'ergodicité du système entraîne une forte complexité de la dynamique et son étalement sur plusieurs décades en temps. Un autre degré de complexité apparaît dans les systèmes biologiques avec la notion fondamentale de fonction biologique : "comment les atomes et les molécules s'organisent-ils et bougent-ils pour réaliser cette fonction ?". D'un point de vue personnel, ces études m'ont permis de couvrir tous les types de spectrométries de neutrons à moyenne et haute résolutions ; des 3-axes, en passant par les temps de vol et retrodiffusion, jusqu'aux spin-échos. J'ai décidé dans ce manuscrit de ne pas suivre un ordre chronologique qui pourrait apparaître comme décousu et totalement indigeste. Je préfère présenter les activités de mes 5 à 7 dernières années sur les systèmes biologiques qui, à mon avis, posent des questions tout à fait fondamentales. Le choix de cette thématique est bien sûr risqué, car l'impact des études par diffusion de neutrons en "biologie" ou plus précisément en biophysique reste confidentiel, malgré l'intérêt général pour le développement des sciences de la vie et de son interface avec les autres disciplines scientifiques. Il y a plusieurs facteurs qui peuvent contribuer à expliquer ce constat. On pourrait citer en premier lieu la difficulté d'accès aux faisceaux de neutrons puisque ces études nécessitent une source de neutrons qui ne peut être qu'un réacteur ou une source à spallation. Je ne pense pas que cet argument soit recevable car les demandes de temps de faisceau dans ce domaine restent relativement faibles, bien que le rapport entre temps demandé et attribué puisse atteindre un facteur 4 sur certains spectromètres. La compétition devrait induire une augmentation de la qualité. La raison fondamentale est sans doute plus large et provient de la relation complexe entre les physiciens et les biologistes. Objectivement, il ne devrait pas y avoir de problème puisque même les systèmes biologiques doivent obéir aux lois de la physique, et la fonction biologique trouve son origine dans l'assemblage et le mouvement des biomolécules. Le problème est plus celui de la complexité, de sorte que la biologie ne peut-être comprise simplement par quelques lois physiques fondamentales. A ce stade, le facteur humain entre en compte dans les difficultés relationnelles de ces deux communautés. Pour être schématique, à la limite de la caricature, les physiciens cherchent autant que possible à simplifier les problèmes afin d'obtenir une description de leurs propriétés avec quelques lois fondamentales, au risque d'en oublier la fonction. Les biologistes,

quant à eux, travaillent sur des objets biologiques mais avec des expériences souvent empiriques et essayent de déduire des lois générales à partir d'une statistique parfois douteuse. Toute la difficulté est d'éviter les écueils que sont ces deux comportements extrêmes, et pour notre cas particulier d'éviter de rester trop loin de la fonction biologique. Il existe une vieille histoire chez les biologistes à propos des physiciens. Un jour, on demanda à l'un d'entre eux s'il pouvait aider à augmenter la production de lait chez les vaches, bien que de nombreux éleveurs, vétérinaires, biologistes et physiologistes aient essayé de résoudre ce problème sans grand succès auparavant. Quelques semaines plus tard, le physicien réunit tout ce monde afin de présenter ses résultats en affirmant avoir trouvé la solution. Il se présenta devant le tableau noir et commença, "Bon, imaginons une vache sphérique au milieu d'un champ infini ...".

Chapitre 1

Présentation générale

1.1 Généralités

L'environnement cellulaire est un milieu complexe composé de nombreux objets, de tailles et de formes très différentes. Hormis quelques cas très particuliers [1], on y trouve une multitude de protéines, des filaments, des ribosomes, de l'ARN, et cette liste est loin d'être exhaustive. Chaque espèce est en général présente à relativement faible concentration, mais la fraction volumique totale occupée par toutes les macromolécules atteint des valeurs proches de $\Phi \simeq 0,3$ [1, 2, 3, 4]. En anglais, on utilise pour décrire ce milieu le terme de "macromolecular crowding", de "crowd" la foule. La langue française n'offre pas de mot équivalent, une traduction pourrait-être un milieu "encombré", nous utiliserons ce terme dans la suite du manuscrit. La chimie de la vie, par opposition à la biochimie du laboratoire, va donc se tenir dans un milieu très dense. Par exemple, la figure 1.1 est une représentation schématique du cytoplasme d'un eucaryote (d'après Goodsell [5]). Les études *in-vitro* sont généralement réalisées à des concentrations de l'ordre du $g.l^{-1}$, par opposition aux quelques 100 $g.l^{-1}$ *in-vivo* [6]. Le volume exclu, dû à la présence des nombreuses macromolécules présentes en solution, va affecter un certain nombre de phénomènes d'importance biologique [7]. Le terme de volume exclu sous entend que les interactions entre la molécule étudiée et celles du milieu sont non-spécifiques, c'est-à-dire qu'elles ne dépendent que très peu des détails des structures primaires, secondaires, voire tertiaires des macromolécules. Elles résultent plutôt des propriétés globales telles que la charge nette ou la forme des macromolécules. Les interactions non-spécifiques peuvent être répulsives (répulsions stériques, ainsi que des faibles interactions électrostatiques très écrantées par la forte salinité du milieu) ou attractives (électrostatiques, hydrophobes). Elles sont en général bien plus faibles que les interactions spécifiques.

[1] Le globule rouge en est un exemple, puisqu'il ne contient quasi-exclusivement que de l'hémoglobine

[1] Zimmerman, S. B. ; Minton, A. P. *Ann. Rev. Biophys. Biomol. Struct.* **1993,** *22,* 27-65.
[2] Ellis, R. J. *Curr. Opin. in Struc. Biol.* **2001,** *11,* 114-119.
[3] Ellis, R. J. ; Minton, A. P. *Nature* **2003,** *425,* 27-28.
[4] Minton, A. P. *Curr. Biol.* **2001,** *16,* R269-271.
[5] Goodsell, D. S. *The machinery of life ;* Springer-Verlag New York Inc., New York : 1993.
[6] Fulton, A. B. *Cell* **1982,** *30,* 345-347.
[7] Minton, A. P. *Biopolymers* **1981,** *20,* 2093-2120.

Les phénomènes de transport par simple diffusion vont être ralentis par l'encombrement cytoplasmique. Les équilibres chimiques devraient également être influencés par le volume exclu, si les réactifs et les produits réagissent à celui-ci à des degrés différents. Un type de réaction, qui est commun dans les systèmes biologiques, est le changement de conformation d'une macromolécule. Si ce changement s'accompagne d'une augmentation ou d'une diminution de son volume effectif alors, dans la cellule, l'équilibre sera déplacé dans un sens ou un autre par rapport à une solution diluée. En d'autres termes, les équilibres chimiques devraient être influencés par le volume exclu si les réactifs et les produits d'une réaction réagissent à des degrés différents à l'exclusion. La cinétique des réactions peut être également modifiée ; par la simple diffusion des molécules qui aura tendance à la ralentir, mais également par le changement de concentration effective des molécules qui aura tendance à augmenter à cause de l'encombrement, entraînant une augmentation de l'activité chimique. La cinétique des réactions pourra également être affectée par l'encombrement macromoléculaire si le volume exclu influence les états intermédiaires des réactions.

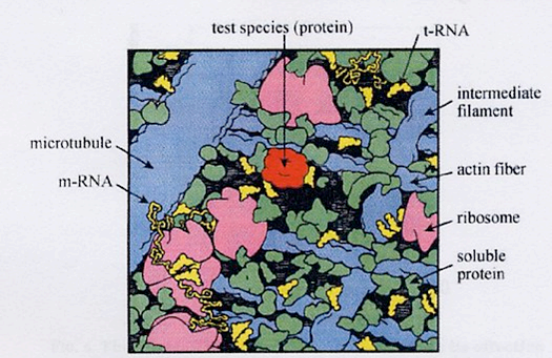

FIG. 1. **Cartoon of eukaryotic cytoplasm at a magnification of 1,000,000 ×.** The test protein molecule (*red*) is in a fluid medium that is crowded by soluble proteins (*green*), RNA species (*yellow*), and ribosomes (*pink*) and confined by cytoskeletal fibers (*blue*). Modified from Ref. 47 and reproduced with permission of the copyright holder.

FIG. 1.1 – Représentation schématique de l'encombrement cellulaire d'un eucaryote (d'après Goodsell [5]).

Les premières études visant à évaluer l'effet de l'encombrement cellulaire sur les propriétés biologiques remontent à la fin des années 40. Les pionniers dans ce domaine étaient T. C. Laurent [8] et A. G. Ogston [9] qui étudiaient l'acide hyaluronique (AH), un polysaccharide présent à forte concentration dans les tissus conjonctifs extracellulaires et le fluide synovial. Les questions physiologiques étaient d'essayer de comprendre la stabilisation du tissu conjonctif et la lubrification des joints. Les auteurs ont pu observer l'exclusion d'une protéine d'un réseau d'AH et l'expliquer par l'introduction de la notion de volume exclu [10]. Avec une version légèrement modifiée de la

[8] Laurent, T. C. *Biophysical Biochemistry.* **1995,** *57*, 7-14.
[9] Ogston, A. G. *Biophysical Biochemistry.* **1995,** *57*, 3-5.
[10] Ogston, A. G. *Trans. Faraday Soc.* **1958,** *54*, 1754-1757.

théorie de Flory pour les solutions diluées de polymères, ils ont pu expliquer qualitativement et quantitativement quelques propriétés physico-chimiques de ces systèmes mixtes polymère-protéine AH/BSA (BSA : Bovine Serum Albumine).

Bien que la première théorie semi-quantitative date du début des années 80, un réel effort pour quantifier expérimentalement les effets de l'encombrement cytoplasmique sur différentes réactions biologiques n'a été développé que durant ces dix dernières années.

1.2 Notion de volume accessible et volume exclu

Le volume exclu représente le volume simplement inaccessible à une particule par la simple présence d'autres macromolécules dans une solution. La figure 1.2 est une représentation schématique des notions de volume accessible et de volume exclu (adapté d'après [11]). La figure 1.2-a représente une solution de macromolécules identiques de rayon r_s occupant un volume d'environ 30%. Le volume libre v_l correspond au volume laissé vacant par les molécules (bleu) soit dans ce cas 70%. Si l'on cherche maintenant à insérer dans la solution une particule test de rayon r_t, le volume accessible correspond à la région de l'espace dans laquelle on peut mettre le centre de la particule. Dans le cas $r_t \ll r_s$, comme représenté en figure 1.2-b, le volume accessible correspond quasi-totalement au volume libre, qui est représenté en bleu. Par contre, si l'on est dans le cas ou $r_t \simeq r_s$, le volume accessible au centre de la particule est très fortement réduit par rapport au volume libre de la solution 1.2-c.

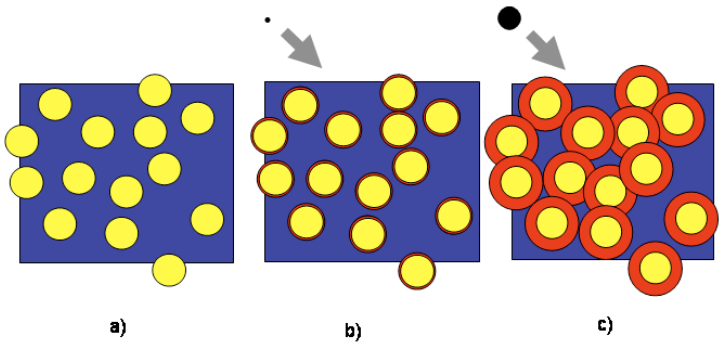

FIG. 1.2 – Représentation bi-dimensionnelle des notions de volume libre et de volume accessible. a : solution de macromolécules occupant une fraction "volumique" d'environ 30%, le volume libre v_l est représenté en bleu ($\simeq 70\%$). b : le volume accessible à une particule test de rayon $r_t \ll r_s$ est proche du volume libre. c : le volume accessible à une particule test de rayon $r_t \simeq r_s$ est fortement réduit par rapport au volume libre (adapté d'après [11]).

[11] Minton, A. P. *The Journal of Biological Chemistry* **2001,** *276,* 10577-10580.

1.3 La non-idéalité d'une solution

Une solution idéale de macromolécules A peut être considérée comme un gaz parfait de soluté dans un solvant. Si le solvant est en très large excès et les interactions soluté-soluté peuvent être négligées, la pression osmotique (Π) de la solution obéit à la loi de Van't Hoff :

$$\Pi = \frac{N}{V}kT = \rho kT \tag{1.1}$$

ρ correspond à la densité de molécules. L'augmentation de la concentration en macromolécules dans la solution va entraîner une augmentation de la pression osmotique, et par intégration de la loi de l'équation de Van't Hoff (1.1) on obtient la variation du potentiel chimique des macromolécules (l'énergie libre par particule) en fonction de la concentration pour une solution idéale.

$$\mu_A^I = \mu_A^0 + RTlnc_A \tag{1.2}$$

μ_A^0 est le potentiel chimique d'une molécule A en solution et c_A la concentration molaire en A.

A l'instar des gaz réels, quand la concentration de macromolécules en solution augmente, les interactions soluté-soluté ne peuvent plus être négligées : la solution est dite non-idéale. La pression osmotique est alors développée en fonction des puissances de la concentration, et l'équation de Van't Hoff n'est que le premier terme d'un développement du viriel de Π :

$$\Pi = \rho kT(1 + a_2\rho + a_3\rho^2 + ...) \tag{1.3}$$

Les termes a_2, a_3 (...) sont respectivement les second, troisième (...) coefficients du viriel. Le second viriel a une signification physique relativement claire puisqu'il s'agit du volume exclu entre deux molécules :

$$a_2 = 2\pi \int_0^\infty [1 - e^{-U(r)/kT}]r^2 dr \tag{1.4}$$

Pour des sphères dures de rayon R on obtient $a_2 = 4V$ ou V est le volume des sphères.

Le potentiel chimique est quant à lui défini à partir d'une concentration effective, l'activité chimique a_i, qui contient le terme de non-idéalité de la solution $a_i = \gamma_i c_i$.

$$\mu_A^{NI} = \mu_A^0 + RTlna_i = \mu_A^0 + RTlnc_i + RTln\gamma_i = \mu_A^I + RTln\gamma_i \tag{1.5}$$

γ_i est le coefficient de non-idéalité et pour une solution de macromolécules interagissant par leur seule répulsion stérique, il peut être exprimé comme le rapport du volume total sur le volume disponible [12] :

$$\gamma_i = \frac{a_i}{c_i} = \frac{v_t}{v_{a,i}} \tag{1.6}$$

Nous utilisons le terme d'encombrement cytoplasmique pour décrire l'effet du volume exclu à une molécule par la présence d'autres molécules, mais il faut également

[12] Lebowitz, J. L. ; Helfand, E. ; Praestgaard, E. *The Journal of Chemical Physics* **1965,** *43*, 774-779.

noter que le cytoplasme contient de nombreux obstacles fixes, tels que des fibres ou des membranes qui constituent la matrice cytoplasmique. Des effets similaires au confinement vont donc intervenir dans le cytoplasme qui peuvent également modifier l'équilibre des réactions [13]. La réalité biologique relève donc d'une bien plus grande complexité que le cadre dans lequel nous nous plaçons, mais ce type d'étude a le mérite de chercher à prendre en compte un effet qui, jusqu'à relativement récemment, était totalement négligé.

1.4 Influence de l'encombrement cytoplasmique sur l'équilibre et la cinétique des réactions

On détermine l'équilibre d'une réaction chimique à partir de l'équation de Nernst, qui relie la variation d'énergie libre des constituants d'une réaction. Prenons l'exemple d'une réaction chimique simple

$$\alpha A + \beta B \rightleftarrows \gamma C + \zeta D \tag{1.7}$$

la constante d'équilibre de cette solution est

$$\Gamma = e^{-\frac{\Delta G_0}{RT}} = \frac{[C]^\gamma [D]^\zeta}{[A]^\alpha [B]^\beta} \tag{1.8}$$

avec

$$\Delta G_0 = \gamma \Delta G_0^C + \zeta \Delta G_0^D - (\alpha \Delta G_0^A + \beta \Delta G_0^B) \tag{1.9}$$

Cette relation, faisant intervenir les concentrations des différents constituants, n'est valable que dans des solutions idéales, c'est-à-dire lorsque les potentiels chimiques dépendent du logarithme de la concentration. Dans le cytoplasme, comme nous l'avons déjà mentionné, les interactions entre les différents constituants ne peuvent être négligées et les concentrations sont remplacées par les activités chimiques qui dépendent de tous les constituants de la cellule, même ceux qui ne sont pas impliqués dans la réaction. A partir des dépendances relatives des différents potentiels chimiques au volume exclu, il va donc pouvoir être possible, dans des cas simples, de prédire l'influence de l'encombrement macromoléculaire sur l'équilibre et la cinétique des réactions biologiques. En règle générale, les composants ayant les conformations les plus étendues vont être plus affectés par le volume exclu et celui-ci aura pour effet de favoriser les conformations les plus compactes [7], obéissant ainsi au principe empirique de *Le Chatelier*.

La cinétique des réactions va, quant à elle, être influencée à plusieurs niveaux par l'encombrement cytoplasmique et donc le volume exclu :

1. La concentration effective en solution des constituants augmente ce qui va favoriser la cinétique des réactions.
2. La diffusion des constituants va très fortement diminuer, ce qui peut devenir un facteur limitant dans la cinétique des réactions.
3. Lorsque la réaction va présenter des états intermédiaires qui vont être affectés par l'encombrement.

[13] Minton, A. P. *Biophys. J.* **1992,** *63*, 1090-1100.
[7] Minton, A. P. *Biopolymers* **1981,** *20*, 2093-2120.

1.5 Influence de l'encombrement cytoplasmique sur la diffusion des protéines et les mécanismes de transport

La diffusion des protéines dans la cellule, ou d'autres objets biologiques, est un aspect fondamental du fonctionnement cellulaire. Elle est l'étape préliminaire à toute réaction biochimique qui permet aux divers réactants d'entrer en contact. La diffusion intervient également dans les phénomènes de transport, la signalisation, la mobilité cellulaire, elle agit donc à de nombreux niveaux du métabolisme de la cellule.

Les protéines vont se trouver dans deux environnements fondamentalement différents : soit elles sont confinées (dans des membranes, le squelette cytoplasmique ...) ou associées avec des membranes, soit elles sont en phase aqueuse, dans un milieu très encombré (cytoplasme, nucléoplasme ...). Elles pourront diffuser, être immobilisées ou même être transportées de manière active. On va donc pouvoir distinguer dans la cellule trois grands modes de diffusion : la diffusion normale des protéines, la diffusion anormale et le transport actif, c'est-à-dire assisté, ayant un coût énergétique. La diffusion des protéines va dépendre de leurs tailles et de la viscosité du milieu mais également des interactions physico-chimiques dans la cellules, telles que les interactions protéine-protéine, ou la formation de complexes transitoires. Les liaisons avec la matrice cellulaire et les collisions avec les autres éléments de la cellule vont également ralentir leur diffusion.

1.6 Présentation du manuscrit

La diffusion de neutrons est une technique particulièrement adaptée à l'étude des systèmes concentrés, pour diverses raisons. Elle permet tout d'abord l'étude des mouvements moléculaires de protéines sur des distances qui correspondent aux distances intermoléculaires dans la cellule. Ceci notamment grâce aux spectromètres à écho de spin. Dans les globules rouges la distance surface-surface entre deux molécules d'hémoglobine adjacentes est de l'ordre de 10 à 20 Å. Assez récemment, grâce à la découverte de la GFP[2] (Green Fluorescente protein) et les développements de l'imagerie par fluorescence, l'étude de la mobilité des protéines dans les cellules est devenue possible. Les techniques de fluorescence [14] telles que le FRAP [15] (fluorescence recovery after photobleaching), le FRET (fluorescence resonance by energy transfer) et la FCS (fluorescence correlation spectroscopy) sont venues compléter *in-vivo* [16] les techniques habituellement utilisées pour les mesures de diffusion moléculaire (DLS, RMN, ...). Toutes ces techniques sondent la diffusion des protéines sur des échelles de l'ordre de celle de la cellule. Seuls les neutrons vont nous permettre d'étudier ces mouvements sur des distances inter-moléculaires et donc de pouvoir remonter au(x)

[2] Scientific Background on the Nobel Prize in Chemistry 2008 : O. Shimomura, M. Chalfie and R. Y. Tsien

[14] Lippincott-Schwartz, J. ; Snapp, E. ; Kenworthy, A. *Nature* **2001,** *2*, 444-456.
[15] Phair, R. D. ; Misteli, T. *Nature* **2000,** *404*, 604-609.
[16] Tsien, R. Y. *Annu. Rev. Biochem.* **1998,** *6*7, 509-544.

mécanisme(s) physique(s) à l'origine de la diminution de leur mobilité.

En utilisant la différence de longueurs de diffusions entre les deux principaux isotopes de l'hydrogène on peut éteindre le signal d'une molécule, même si celle-ci est présente en très grande quantité. Dans l'étude des milieux encombrés, on voit immédiatement le parti à tirer d'une telle propriété : on va pouvoir observer une molécule sonde, marquée et présente à très faible concentration, en présence d'un agent d'encombrement qui sera présent en très forte concentration mais éteint par le solvant constitué d'un mélange d'eau lourde et d'eau légère. Cet agent, même présent à des concentrations de 50 à 100 fois plus fortes que la molécule sonde, ne contribuera pas au spectre de diffusion aux petits angles.

Une autre propriété particulière des neutrons, leur neutralité, ainsi que leurs faibles énergies les rendent très pénétrants dans la matière et peu destructeurs. Il sera donc possible d'étudier les mouvements et les conformations de molécules à l'intérieure des cellules.

Le manuscrit comporte deux parties distinctes. L'une concerne l'étude de la diffusion de solutions concentrées de protéines ainsi que l'étude de la diffusion de l'hémoglobine dans les globules rouges. La deuxième concerne l'étude de l'influence de l'environnement cytoplasmique sur la conformation de protéines dénaturées.

Chapitre 2

Influence de l'encombrement cellulaire sur la diffusion de protéines

2.1 Introduction

La diffusion des macromolécules est directement affectée par l'encombrement cytoplasmique. Au-delà des simples mécanismes de transport, c'est la cinétique de nombreuses réactions biochimiques qui va être influencée par l'étape préliminaire de rencontre des réactants. La topologie complexe du cytoplasme modifie la cinétique de ces réactions, dans la mesure où elles sont parfois limitées par l'étape de diffusion.

On peut séparer les mécanismes de transport dans la cellule en trois grandes familles :

1. Le *transport actif* qui se fait avec consommation d'énergie (hydrolyse de l'ATP).
2. La diffusion normale, dite brownienne, où le déplacement carré moyen des molécules est une fonction linéaire du temps, $\langle r^2 \rangle \sim D_s t$. Elle obéit à la loi d'Einstein.
3. La diffusion anormale, par opposition à la précédente, lorsque l'on s'écarte de la dépendance linéaire en temps du déplacement carré moyen, $\langle r^2 \rangle \sim D_s t^\alpha$. On distingue le cas ou $\alpha > 1$ qui est le régime sur-diffusif et $\alpha < 1$ qui est le régime sous-diffusif. Dans la cellule on s'attend principalement à observer le cas sous-diffusif.

Les études semblent maintenant converger vers le fait que dans la cellule le processus dominant est celui qui se fait par simple diffusion [17] (transport non actif) encore que l'hypothèse d'une diffusion combinée soit avancée par certains auteurs [18] notamment dans le noyau cellulaire, sans réellement trancher entre normale et anormale. Nous nous restreindrons par la suite à l'étude de ce type de mécanisme et ne traiterons

[17] Dix, J. A. ; Verkman, A. S. *Annu. Rev. Biophys.* **2008,** *37*, 247-263.
[18] Carmo-Fonseca, M. ; Platani, M. ; Sweldow, J. R. *TRENDS in Cell Biology* **2002,** *12*, 491-495.

pas le transport actif.

Pour une solution infiniment diluée, et en l'absence de tout champ, le mouvement de diffusion d'une particule peut être décrit par une marche aléatoire :

$$< r^2 >= 6D_s t \tag{2.1}$$

$< r^2 >$ est le carré moyen de la distance parcourue par la particule en un temps t, D_s est le coefficient de diffusion de la particule (s pour "self-diffusion") donné par la relation d'Einstein [19] : $D_s = k_B T/f$. T est la température en Kelvin, k_B la constante de Boltzmann, et f est un terme de friction que Stokes a montré être égal à $6\pi\eta R$ pour une particule sphérique de rayon R dans un solvant continu de viscosité η. La présence de nombreuses autres molécules dans l'environnement cytoplasmique va très fortement diminuer la valeur de D_s qui va devenir dépendante de la fraction volumique occupée : $D_s(\Phi)$ de sorte que, pour des fractions volumiques de l'ordre de $\Phi \simeq 0.3 - 0.4$, celui-ci peut être réduit d'un facteur 20 à 50. De nombreuses études expérimentales et théoriques visent à essayer de mesurer et comprendre l'origine physique de l'evolution des mécanismes de diffusion. C'est un problème très compliqué, car à un seul coefficient pour une solution infiniment diluée, vont se substituer de nombreux coefficients de diffusion : coefficients à temps courts et à temps longs, d'auto-diffusion et corrélation de paires, tous dépendants du vecteur d'onde. Le traitement théorique de la réduction de la diffusion d'une particule en présence d'autres molécules en solution devient donc un problème extrêmement complexe. En plus des interactions directes entre les molécules viennent s'ajouter les interactions portées par le solvant ; les interactions hydrodynamiques. Des modèles ont été développés pour décrire la statique et la dynamique de solutions micellaires et colloïdales. Ce sont, en général, des objets beaucoup plus gros que les protéines, puisque le régime en vecteur d'onde autour du premier pic d'interaction peut être sondé par diffusion de lumière. Le solvant y est traité comme un continuum qui est défini par ses propriétés macroscopiques telles que la viscosité ou sa constante diélectrique.

La structure de ce type de solution a été décrite par Hayter et Penfold [20] qui ont dérivé une forme analytique du facteur de structure de particules chargées interagissant par un potentiel de Coulomb écranté. Cette théorie, du type MSA (Mean Spherical Approximation), n'est valable que dans le cas ou la contribution à l'intensité diffusée des contre-ions peut être négligée ; ils n'interviennent donc que par l'intermédiaire de l'écrantage du potentiel Coulombien. Celui-ci décroît alors avec une forme de type Yukawa plutôt qu'en 1/r. Hansen et Hayter [21] on introduit ensuite une renormalisation du rayon effectif de la particule afin d'étendre le domaine de validité de la théorie vers les faibles concentrations en colloïdes fortement chargés. Pour des objets fortement chargés, le potentiel de contact est très nettement supérieur à $k_B T$, et donc la probabilité de contact entre les particules est quasi nulle $g(r \gtrsim 2a) \simeq 0$. Le potentiel de sphère dure ne joue pas de rôle physique. Leur méthode consiste donc à redimentionner la valeur du rayon a de la particule. En 1986, Belloni [22] apporte une nouvelle amé-

[19] Einstein, A. *Ann.der Physik* **1905,** *17*, 549-560.
[20] Hayter, J. B. ; Penfold, J. *Mol. Physics* **1981,** *42*, 109-118.
[21] Hansen, J. P. ; Hayter, J. B. *Molecular Physics* **1982,** *46*, 651-656.
[22] Belloni, L. *J. Chem. Phys.* **1986,** *85*, 519-526.

lioration qui vise à donner une valeur plus physique au potentiel de contact, il prend notamment en compte la concentration en colloïdes dans le calcul de la longueur de Debye de la solution et donc de l'écrantage des charges électrostatiques.

La description théorique de la diffusion de particules browniennes chargées a subit un net regain d'intérêt avec l'avènement du laser et les études de diffusion quasi-élastique de la lumière (DLS). Dès 1908 et 1910, avec les travaux de Smoluchovsky et d'Einstein, on savait que les fluctuations de densité de la matière condensée entraînaient des inhomogénéïtés locales qui pouvaient donner lieu à une diffusion de la lumière. En 1914, Brillouin a mis en évidence une intensité inélastique associée aux modes acoustiques et, quelques années plus tard, Gros observait un pic central en plus des lignes de Brillouin. L'interprétation de cette raie Rayleigh a été donnée par Landau et Placzek en 1934 qui ont montré que le ratio des intensité des pics de Rayleigh sur ceux de Brillouin pouvaient être reliés aux capacités calorifiques à volume et à pression constantes $I_R/2I_B = \frac{C_p - C_v}{C_v}$. Les études en sont restées à ce point par manque d'intensité des sources lumineuses, jusqu'au début des années 60, où tout a radicalement changé avec l'arrivé du laser. Le premier à avoir pu analyser la dépendance en vecteur d'onde de la raie Rayleigh a été R. Pecora qui en 1962, durant sa thèse, a observé que la largeur a mi-hauteur de la raie variait avec le carré du vecteur d'onde la reliant ainsi avec la diffusion de macromolécules en solutions : $\Delta\omega_{1/2} \simeq Dq^2$. Cette propriété avait déjà été observée par diffusion de neutrons dans les liquides, par exemple pour l'eau par B. N. Brockhouse dès 1959 [23]. Les études expérimentales sur des systèmes colloïdaux par DLS se sont alors multipliées avec en parallèle les papiers théoriques visant à essayer de comprendre les grandeurs mesurées. Phillies [24][25] a introduit la relation de Stokes-Einstein généralisée qui détermine le coefficient de diffusion mutuel mesuré par DLS :

$$D_m = \frac{(1-\Phi)}{f}\left(\frac{\partial \pi}{\partial c}\right)_{P,T} \tag{2.2}$$

$\frac{-1}{c}(\partial\pi/\partial c)^{-1}$ est la compressibilité osmotique de la solution et Φ la fraction volumique hydrodynamique occupée par les macromolécules en solution. Pour de très faibles concentrations, où les interactions entre macromolécules sont négligeables D_0 et D_m sont égaux. Mais, lorsque la concentration augmente, les interactions ne peuvent plus être négligées et les deux coefficients deviennent très significativement différents [26]. En plus de coefficients par nature différents, on doit séparer différents régimes temporels. On en distingue en général trois ; $t << \tau_B$, avec τ_B qui correspond au temps que met la vitesse des particules à relaxer, c'est donc la période nécessaire afin d'atteindre un régime brownien. $\tau_B \simeq M/f$ est de l'ordre de 10 ps pour les protéines de rayon de quelques dizaines d'angströms. Pour $\tau_B << t << \tau_i$ (τ_i est le temps que met la particule avant d'interagir avec ses voisines) on définit un coefficient de diffusion à temps court ; les particules ne sont soumises qu'aux interactions hydrodynamiques. Dans le régime $t >> \tau_i$, on observe la diffusion de la particule dans la solution, les interactions hydrodynamiques et directes sont établies et on parle de coefficient de diffusion à temps long.

[23] Brockhouse, B. N. *Phys. Rev. Letters* **1959,** *2*, 287-289.
[24] Phillies, G. D. J. *J. Chem. Phys.* **1974,** *60*, 976-982.
[25] Phillies, G. D. J. *J. Chem. Phys.* **1975,** *62*, 3925-3932.
[26] Hall, R. S. ; Johnson, C. S. *J. Chem. Phys.* **1980,** *72*, 4251-4253.

Dans le domaine temporel des temps courts, la relaxation où les effets mémoire peuvent être négligés et les fonctions dynamiques peuvent s'exprimer en fonction des distributions d'équilibre ; la théorie est maintenant relativement aboutie [27, 28, 29]. Ackerson a notamment dérivé une expression du coefficient de diffusion apparent qui sépare les contributions des interactions directes et hydrodynamiques :

$$D = D_0 \frac{H(q)}{S(q)} \tag{2.3}$$

Beenakker et Mazur [30, 31] ont calculé le facteur hydrodynamique (H(q)) pour des solutions de sphères dures concentrées. Ils ont notamment montré la dépendance caractéristique de H(q) en fonction du vecteur d'onde, pour différentes fractions volumiques Φ. Les prédictions théoriques pour $H(q, \Phi)$ peuvent être comparées aux résultats expérimentaux.

La dépendance des coefficients d'auto-diffusion à temps courts et à temps longs, D_s^s et D_s^L, en fonction de la fraction volumique en particules ne peut être calculée exactement, mais plusieurs approximations théoriques ont été développées. Plusieurs auteurs ont ainsi découplé les contributions hydrodynamiques des interactions directes, notamment Beenakker et Mazur. Médina-Noyola [32] a introduit une méthode de calcul de D_s^L à partir de D_s^s et du facteur de structure de la solution. Tokuyama et Oppenheim [33] ont, quant à eux, développé une théorie plus systématique pour le calcul de D_s^s et D_s^L qui inclut interactions directes et hydrodynamiques pour des solutions de sphères dures.

Dans ce chapitre, je vais résumer les études que nous avons menées sur des solutions concentrées de myoglobine et d'hémoglobine. Nous avons appliqué les traitements théoriques développés pour les solutions colloïdales, et mis en évidence les régimes ou ceux-ci devenaient inapplicables. Enfin, je discuterai l'intérêt de la diffusion des protéines d'un point de vue biologique, d'abord en rappelant l'intérêt pour la myoglobine. Et de manière plus spéculative, je discuterai l'apport de ce type d'études à la compréhension de la capture de l'oxygène par le globule rouge, au niveau des alvéoles pulmonaires.

2.1.1 Les systèmes biologiques

L'hémoglobine et la myoglobine sont deux protéines globulaires transporteuses d'oxygène.

[27] Pusey, P. N. *J. Phys. A : Math. Nucl. Gen.* **1975,** *8,* 1433-1440.
[28] Ackerson, B. J. *J. Chem. Phys.* **1976,** *64,* 242-246.
[29] Ackerson, B. J. *J. Chem. Phys.* **1978,** *69,* 684-690.
[30] Beenakker, C. W. J. ; Mazur, P. *Physica* **1983,** *120A,* 388-410.
[31] Beenakker, C. W. J. ; Mazur, P. *Physica* **1984,** *126,* 349-370.
[32] Médina-Noyola, M. *Phys. Rev. Lett* **1988,** *60,* 2705-2708.
[33] Tokuyama, M. ; Oppenheim, I. *Phys. Rev. E* **1994,** *50,* R16-R19.

L'hémoglobine est une protéine de 64kDa présente à très forte concentration dans les globules rouges. Si l'on excepte l'eau c'est même son composant principal, puisqu'elle représente $\sim 93\%$ de la masse sèche du globule. La figure 2.1 est une représentation schématique de l'intérieur du globule rouge (GR) donnée par D. Goodsell [34]. L'hémoglobine native est composée de quatre chaînes polypeptidiques qui peuvent chacune fixer une molécule de gaz di-ou tri-atomique. Sa forme est très proche d'une sphère de rayon d'environ R=28Å. Son rôle physiologique consiste donc à capturer les gaz, les fixer pendant le transport sanguin, puis à les relâcher en fonction de la demande. Le transport d'oxygène est exemplaire du rôle de cette protéine. Lorsqu'un globule rouge transite dans des capillaires proches des alvéoles pulmonaires, l'hémoglobine qu'il contient va se charger en oxygène. Pendant tout le transport des poumons vers, par exemple les muscles en activité, l'hémoglobine gardera fixé l'oxygène, puis lorsque la demande sera forte elle le relâchera. Cette effet est dû à une propriété singulière de fixation de l'oxygène par l'hémoglobine en fonction de la pression partielle d'oxygène (cf figure 2.2). Le caractère sigmoïdal de la courbe traduit l'effet coopératif de fixation de l'oxygène par l'hémoglobine : lorsqu'une molécule d'O_2 est fixée par un hème la probabilité de fixation par les 3 autres de la protéine augmente. Dans les capillaires pulmonaires, où la pression partielle d'oxygène est de l'ordre de 13 kPa (100 mmHg), toutes les molécules d'hémoglobine sont saturées en oxygène, puis au fur et à mesure que le sang circule dans les artères, et enfin les muscles ou les organes où la demande va être forte, cette pression partielle va diminuer entraînant la libération des molécules d'O_2. La pression partielle correspondant à la demi-saturation est d'environ 25 mmHg, valeur qui peut bouger en fonction de différents facteurs comme le pH (effet Bohr), la température, ou la concentration en 2,3-DPG (2,3-diphosphoglycerate, qui est un organophosphate).

La myoglobine est, quant à elle, présente dans les muscles, c'est une protéine de 17kD composée d'une seule chaîne polypeptidique. Son rôle physiologique est de stocker l'oxygène dans les muscles et des études tendent à montrer qu'elle assiste le transport d'oxygène par diffusion jusqu'aux mitochondries. La courbe de dissociation de la myoglobine ne présente pas d'effet coopératif et est décalée par rapport à celle de l'hémoglobine vers les plus basses pressions partielles en O_2 (cf figure 2.2). Lorsque l'hémoglobine relâche les molécules d'oxygène celles-ci vont donc pouvoir être captées par la myoglobine. La myoglobine s'écarte plus d'une forme sphérique que l'hémoglobine, elle s'apparente plus à un ellipsoïde d'axes principaux 44*44*25 $Å^3$.

Sur le principe, les mécanismes physiques qui vont conduire à la réduction de la mobilité de la myoglobine et de l'hémoglobine sont naturellement très différents. La myoglobine est présente dans un milieu cellulaire en même temps que toute la machinerie habituelle. Elle va être ralentie par des interactions avec des objets fixes et mobiles de natures et de tailles très différentes. Les interactions vont donc être extrêmement complexes. L'hémoglobine est elle située dans les globules rouges, des cellules qui pour des raisons de fluidité sanguine sont très souples et déformables. Comme elle est le quasi unique constituant du globule rouge elle est un excellent modèle de solution de sphères dures nanométriques faiblement chargées à très forte concentration.

[34] Goodsell, D. S. *Structure* **2005,** *13*, 347-354.

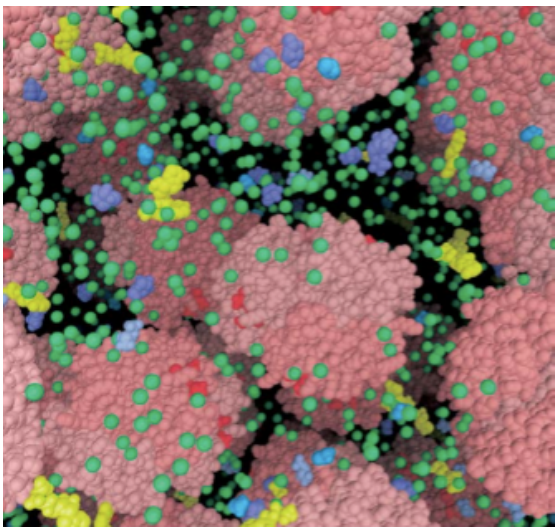

FIG. 2.1 – Représentation schématique de l'intérieur du globule rouge. L'hémoglobine est représentée en rouge, les petites molécules en bleu et jaune, et les ions en vert (d'après [34]).

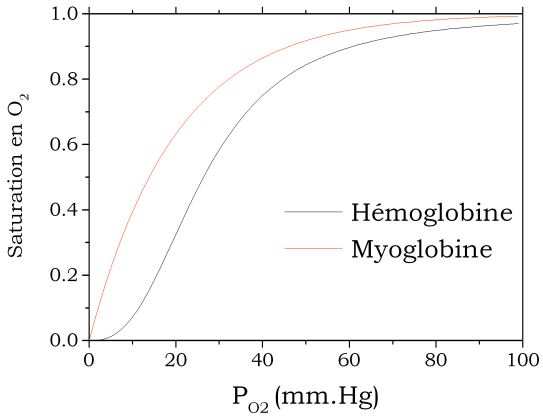

FIG. 2.2 – Courbes de saturation/dissociation de l'hémoglobine et de la myoglobine. A faible pression partielle d'oxygène, l'hémoglobine relâche l'O_2 qui est capturé par la myoglobine.

2.1.2 Motivations

Nous avons entrepris, en collaboration avec Wolfgang Doster de la Technische Universität München, une étude par diffusion aux petits angles et spectroscopie à écho de spin de neutrons de solutions de protéines. Nous avons pu ainsi étudier les interactions et les mécanismes de diffusion de solutions de myoglobine et d'hémoglobine concentrées, puis de l'hémoglobine dans les globules rouges. Comme nous l'avons déjà men-

tionné en introduction, la diffusion de neutrons est la technique de choix pour ce genre d'étude pour plusieurs raisons ;

1. Les courtes longueurs d'ondes des neutrons froids ($\lambda \simeq 3 - 20$Å) ainsi que leurs faibles énergies (quelques meV) permettent de mesurer les structures moléculaires et les temps caractéristiques des mouvements de translation à des concentrations correspondant à celles des milieux biologiques. En utilisant les modèles développés pour les colloïdes nous avons pu extraire les potentiels intermoléculaires par DNPA, et mesurer la diffusion sur ces échelles par spectroscopie à écho de spin. On peut donc remonter au mécanisme physique qui conduit au ralentissement de la diffusion.

2. On peut mesurer les fonctions d'auto-corrélations et de corrélations de paires.

3. Le problème de l'absorption et de la diffusion multiple sont négligeables sous certaines conditions expérimentales ce qui est particulièrement intéressant pour le cas de solutions opaques comme celles de myoglobine et d'hémoglobine concentrées.

4. La forte pénétration des neutrons dans la matière ainsi que l'utilisation du contraste H/D permet d'étudier la structure et les mécanismes de diffusion à l'intérieur des cellules.

2.2 Un modèle pour les interactions protéine-protéine

La première étape de l'étude consiste à essayer de modéliser les interactions protéine-protéine. Hayter et Penfold [20] ont calculé le facteur de structure d'une solution de colloïdes dont le potentiel d'interaction est de type sphère dure (de rayon r_0) plus électrostatique (MSA : Mean Spherical Approximation). Mathématiquement ce potentiel est décrit par une fonction de type Yukawa $\beta V(r) = V_{ij}(2r_0)2r_0\frac{e^{-\kappa(r-2r_0)}}{r}$ pour $r > 2r_0$ et $V(r) = \infty$ pour $r < 2r_0$. $V_{ij}(2r_0)$ est le potentiel de contact qui dépend de la charge de surface Z_p. κ est l'inverse de la longueur de Debye L_D, qui traduit l'écrantage du potentiel électrostatique. Nous avons donc étudié la structure des solutions de myoglobine en fonction de la concentration jusqu'à des fractions volumiques de l'ordre de $\Phi \simeq 0.4$ [35]. Pour des raisons de contraste, les solutions sont dialisées contre de l'eau lourde. Des études similaires ont été menées sur des solution d'hémoglobine [36]. L'intensité diffusée par une solution de particules monodisperses et de symétrie sphérique peut être décrite par :

$$I(Q) = \Phi v_0(\Delta\rho)^2 F^2(Q).S(Q) \tag{2.4}$$

Φ est la fraction volumique occupée par les particules, v_0 leur volume, $\Delta\rho$ est la différence de densité de longueur de diffusion entre le soluté et le solvant (en cm^{-2}), F(Q)

[20] Hayter, J. B. ; Penfold, J. *Mol. Physics* **1981,** *42*, 109-118.
[35] Longeville, S. ; Doster, W. ; Kali, G. *Chem. Phys.* **2003,** *292*, 413-424.
[36] Krueger, S. ; Chen, S.-H. ; Hofrichter, J. ; Nossal, R. *Biophys. J* **1990,** *58*, 745-757.

le facteur de forme de la particule et S(Q) le facteur de structure particule-particule. Le facteur de forme de la protéine peut être mesuré à très faible concentration (quelques $mg.ml^{-1}$), ce qui permet d'accéder au facteur de structure des solutions par simple division des spectres mesurés par F(Q). Les spectres sont ensuite affinés en utilisant le facteur de structure calculé par Hayter et Penfold [20] avec la correction introduite par Belloni [22] pour les fortes concentrations en protéines. Les spectres bruts et facteur de forme sont donnés respectivement en figure 2 et 3 de la référence [35] (cf. Annexe). Les facteurs de structure qui en sont extraits ainsi que les affinements sont présentés en figure 4 pour 3 concentrations différentes en myoglobine. Les deux paramètres pertinents du modèle sont le rayon des sphères dures et la charge effective de la protéine Z_p. Le rayon obtenu grâce à l'analyse MSA est légèrement plus faible que celui qui peut être calculé à partir de la structure de la myoglobine $r_0 \simeq 16$ Å (contre 17.1 Å). On obtient également $Z_p \simeq 2$e, cette faible valeur est tout à fait compatible avec le fait que la protéine est en solution concentrée et va donc imposer une valeur de pH proche de son point isoélectrique. De plus celle-ci ne dépend pas de la concentration en protéine, ce qui tend à rendre le modèle relativement robuste.

2.3 Diffusion de la myoglobine et de l'hémoglobine *in-vitro*

Les études ont été réalisées par spectroscopie à écho de spin de neutrons [37] ; le principe détaillé de la méthode est présenté dans l'article *Quasielastic Neutron Scattering in Biology Part I : methods* co-écrit avec R. E. Lechner du Hahn-Meitner-Institut (Berlin) [38] (cf. annexe).

La grandeur mesurable par spectrométrie à écho de spin (nous utiliserons le sigle anglais NSE) est la fonction intermédiaire de diffusion : $I(q,t)$. Il s'agit d'une mesure de la fonction de diffusion de l'échantillon dans le domaine des temps et des vecteurs d'onde. Les relations entre fonctions de diffusion et fonctions de corrélation sont détaillées dans de nombreux articles et ouvrages, dont deux sont particulièrement remarquables, le livre de G. L. Squires [39] et un article assez peu connu de F. Mezei [40]. Elles sont également détaillées dans l'article en annexe. $I(q,t)$ s'écrit de manière générale :

$$I(\mathbf{q},t) = \frac{1}{N}\langle \sum_i b_i^* e^{-i\mathbf{q}.\mathbf{r}_i(0)} . \sum_j b_j e^{i\mathbf{q}.\mathbf{r}_j(t)} \rangle \tag{2.5}$$

N est le nombre de centres diffusants, $\mathbf{r}_i$ la position du noyau i de longueur de diffusion b_i. Comme je l'ai rappelé plus haut, l'étude de la dynamique de solutions concentrées de myoglobine ne présente qu'un intérêt biologique limité, car ces pro-

[20] Hayter, J. B. ; Penfold, J. *Mol. Physics* **1981,** *42*, 109-118.
[22] Belloni, L. *J. Chem. Phys.* **1986,** *85*, 519-526.
[35] Longeville, S. ; Doster, W. ; Kali, G. *Chem. Phys.* **2003,** *292*, 413-424.
[37] Mezei, F. *Z. Physik B* **1972,** *255*, 146-160.
[38] Lechner, R. E. ; Longeville, S. *Springer, Ed. J. Fitter, T. Gutberlet and J. Katsaras.* **2006,** 309-354.
[39] Squires, G. L. *Introduction to the theory of thermal neutron scattering ;* Dover publication, Inc. : 1978.
[40] Mezei, F. *Neutron scattering and collective dynamics in liquids and glasses, in Liquids, Freezing and Glass transition ;* J.P. Hansen, D. Levesque and J. Zinn-Justin, eds, North Holland Pub. : 1991.

téines évoluent dans les cellules musculaires, dans un milieu très complexe. Nous avons néanmoins commencé ces études pour des raisons pratiques : il est plus facile d'obtenir des solutions concentrées de myoglobine que d'hémoglobine sans agrégation à partir des produits en vente commerciale. De plus la myoglobine étant plus petite que l'hémoglobine elle rentre plus facilement dans la fenêtre temporelle du spectromètre à écho de spin de Saclay.

Nous avons donc entrepris une étude relativement systématique de solutions de myoglobine en fonction de la concentration et du vecteur d'onde afin d'obtenir la gamme la plus large possible de coefficients de diffusion apparents. Afin de maximiser la contribution cohérente de la diffusion de neutrons (favorable en spin-écho), les mesures sont réalisées dans le domaine des petits angles et, toujours pour des raisons de contraste, les solutions de myoglobine étaient dialysées dans de l'eau lourde. Les mesures sont réalisées à la température physiologique de 37˚C. Les spectres ont été mesurés en grande partie sur le spectromètre G_1Bis du LLB, mais également sur IN15 à l'Institut Laue-Langevin, qui possède une fenêtre temporelle décalée vers les grands temps (~ 350 ns par rapport à 20 ns pour G_1Bis) afin de compléter les résultats à forte concentration en myoglobine et aux petits angles.

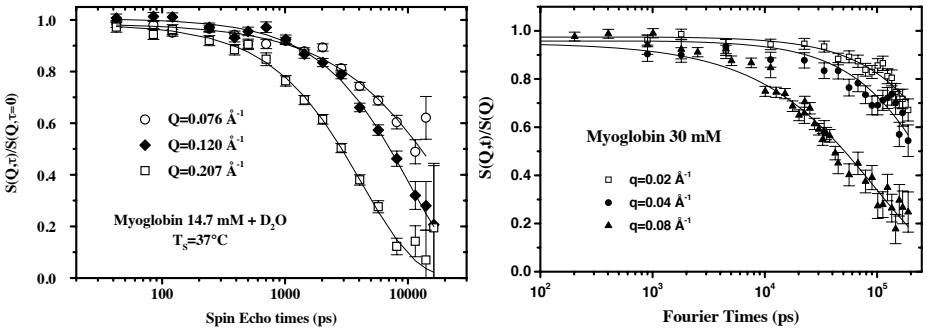

FIG. 2.3 – Fonctions intermédiaires de diffusion I(q,t), mesurées sur le spectromètre G_1bis du LLB (gauche), pour une solution de myoglobine concentrée à 14.7 mM ($\Phi \simeq 0.2$), et sur le spectromètre IN15 de l'ILL (droite) pour une solution de myoglobine concentrée à 30mM ($\Phi \simeq 0.4$) .

Le figure 2.3 présente des fonctions intermédiaires $I(q,t)$ mesurées sur G_1bis et $IN15$ pour différents vecteurs d'ondes et différentes concentrations en myoglobine. Si les deux spectromètres ont un domaine spectral qui couvre le même nombre de décades, ils ne couvrent pas la même gamme temporelle. Un affinement des spectres par une exponentielle étirée $e^{-(t/\tau)^\beta}$ donne un exposant β qui est très proche de 1, les courbes ne s'écartent que très peu d'un comportement relaxationel simple (avec un seul temps de corrélation). L'affinement a donc été réalisé par une fonction exponentielle permettant d'obtenir un coefficient de diffusion apparent $D(q)$ qui ne depend plus du temps[1]. Dans le domaine de vecteur d'onde mesuré on reste dans une approximation petits angles ; $1/\lambda >> d$ ou d est la distance entre deux centres diffusants. La diffusion cohérente de neutrons, qui est sensible aux fluctuations de densité de longueurs de diffusion, est donc établie par le contraste entre le solvant et les protéines. Pour une

[1]La fonction réellement utilisée est un peu plus complexe car nous avons pris en compte le couplage entre la dépendance en q^2 de la diffusion et celle en λ^3 des lignes de spin-écho.

molécule sphérique et de densité de longueur de diffusion homogène, la diffusion cohérente de neutrons n'est sensible qu'aux mouvements translationnels des centres de masse, et non aux autres mouvements de type rotationel. $I(q,t)$ prend donc la forme

$$\frac{I(q,t)}{\Phi v_p(\Delta\rho)^2 F(q)} \simeq \frac{1}{\varrho}\langle\sum_{i,j}^{\varrho} e^{-i\mathbf{q}.[\mathbf{r}_i(0)-\mathbf{r}_j(t)]}\rangle \tag{2.6}$$

$\mathbf{r}_i(0)$ est la position du centre de masse de la protéine i au temps t=0 et $\mathbf{r}_j(t)$ celle de la protéine j au temps t. $\varrho = \frac{N}{V}$ est la densité de protéines, les autres grandeurs ont été définies dans la partie concernant l'étude de la structure. Nous traiterons les solutions de myoglobine dans le cadre de cette approximation.

La figure 2.4 présente l'évolution des coefficients de diffusion apparents en fonction du vecteur d'onde pour des solutions à différentes concentrations en myoglobine. Quelle que soit la concentration la dépendance en fonction du vecteur d'onde de $D(q)$ est identique, une remontée aux petits angles (qui est due à la nature de la fonction de corrélation mesurée : corrélation de paires) et un plateau aux grands vecteurs d'onde.

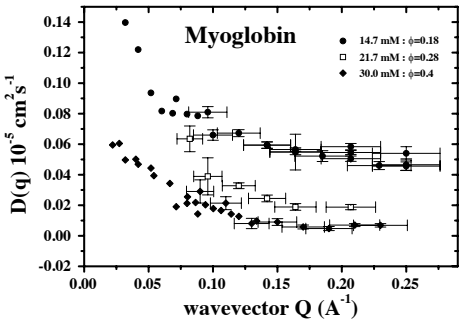

FIG. 2.4 – Dépendance en vecteur d'onde du coefficient de diffusion apparent mesuré pour des solutions de myoglobine à 3 concentrations différentes correspondant à des fractions volumiques $\Phi \approx 0.18$, $\Phi \approx 0.28$ et $\Phi \approx 0.4$.

On observe le plateau dans le domaine de vecteur d'onde qui correspond à $S(q) \approx 1$, ce que l'on appelle généralement l'approximation incohérente de la diffusion cohérente. On mesure donc un coefficient d'auto-diffusion : D^s. D'un point de vue plus mathématique, dans le domaine $qr_0 \gg 1$ (r_0= rayon de la protéine), une faible variation des positions relatives des protéines $\mathbf{r}_i(0) - \mathbf{r}_j(t)$ va entraîner une forte variation des termes de phase $\mathbf{q}.(\mathbf{r}_i(0) - \mathbf{r}_j(t))$. Les termes croisés $i \neq j$ de l'équation 2.6 vont donc s'annuler et seuls restent les termes d'auto-corrélation.

Du fait des flux de photons très élevés par rapport à ceux de neutrons, les mesures réalisées par spectroscopie de corrélation de photons sur les systèmes colloïdaux [41] ont une bien meilleure statistique. Il est alors possible de séparer les coefficients d'auto-diffusion à temps court D_s^S(q) et à temps longs $D_s^L(q)$, le premier étant obtenu

[41] Pusey, P. N. *Colloidal suspensions, in Liquids, Freezing and Glass transition ;* J.P. Hansen, D. Levesque and J. Zinn-Justin, eds, North Holland Pub. : 1991.

à partir du premier cumulant tandis que le second est extrapolé à temps longs. Il existe théoriquement un vecteur d'onde limite au-delà duquel on ne doit mesurer que D_s^S, où le mouvement est sondé sur de si faibles distances, qu'il n'est affecté que par les seules intéractions hydrodynamiques. On doit mesurer $D_s^S(q)$ dans une gamme temporelle située entre le temps de relaxation Brownien τ_B, quand les fluctuations des vitesses de la particule ont relaxé, c'est-à-dire que l'on a atteint le regime hydrodynamique, et avant que les particules n'interagissent entre elles via les interactions directes. $\tau_B \approx M/f \approx 10ps$, tandis qu'un calcul rapide de τ_i en utilisant une approximation gaussienne et le coefficient de diffusion mesuré en solution infiniment diluée (c'est-à-dire que l'on néglige les interactions hydrodynamiques) nous donne $\tau_i \approx 5 - 10ns$. Si l'on ne se réfère qu'aux temps caractéristiques de la mesure, la quantité mesurée semble être D_s^S. On peut obtenir un ordre de grandeur très approximatif du vecteur d'onde en deçà duquel on ne peut certainement pas négliger les interactions directes, c'est-à-dire que les surfaces protéine-protéine entrent en contact. En faisant une approximation d'un réseau cubique et en négligeant les interactions électrostatiques on obtient $\Phi = \varrho\frac{4\pi}{3}R^3 = \frac{1}{d^3}\frac{4\pi}{3}R^3$. Ce qui conduit finalement à $q \approx \frac{2\pi}{d-2R} \sim 0.5\text{Å}^{-1}$. Dans le domaine de vecteur d'onde que l'on sonde, on ne peut pas négliger les interactions directes et l'on semble plutôt mesurer une coefficient à temps long D_s^L.

La dépendance de $D_s(\Phi) = lim_{qR\gg 1}D^{\Phi}(q)$ en fonction de la fraction volumique est représentée sur la figure 2.5. La ligne continue représente le résultat d'un ajustement des données obtenues par des méthodes de traceurs [42], par nature macroscopiques, qui donnent donc accès aux coefficients de diffusion à temps long. Les courbes en tirets et en pointillés correspondent respectivement aux coefficients d'auto-diffusion à temps court D_s^S et à temps long D_s^L calculés pour des suspensions de sphères dures par Tokuyama et Oppenheim [33]. Ces prédictions théoriques correspondent bien aux mesures expérimentales réalisées sur des systèmes de colloïdes de tailles caractéristiques de plusieurs milliers d'angströms. La comparaison entre les données de Muramatsu et Minton [42] semble indiquer clairement que la nature de notre mesure est un coefficient de diffusion à temps long. Mais la comparaison avec les prédictions théoriques reste mauvaise puisque les résultats expérimentaux restent très en deçà des prédictions théoriques. Le volume utilisé pour calculer les fractions volumiques est le volume spécifique de la protéine, qui est un volume "sec" : $v_d = 0.75\ cm^3/g$. Le rapport de la surface sur le volume varie en 1/R, il est donc probable que la couche d'hydratation qui peut-être négligée dans le cas des colloïdes de plusieurs centaines de nanomètres de rayon ne puisse pas l'être pour une protéine de quelques nanomètres. Nous avons donc recalculé une fraction volumique hydrodynamique $\Phi_h = c_p v_h$ à partir de $v_h = v_d + \delta v_s$. v_s est le volume spécifique du solvant et δ ($0 \leq \delta \leq 1$) la fraction volumique de solvant lié à la protéine. En prenant la valeur de $\delta = 0.35$ que l'on trouve communément dans la littérature, on peut redéfinir une fraction volumique Φ_h. Les carrés représentent les résultats de spin écho en fonction du volume hydrodynamique de la protéine. On observe une relativement bonne concordance entre les prédictions théoriques pour D_s^L et les résultats de nos mesures. Le solvant, qui est traité comme un continuum dans le cas de solutions de colloïdes ne semble pas pouvoir l'être pour des solutions de protéines de beaucoup plus faible taille.

[42] Muramatsu, N. ; Minton, A. P. *Proc. Natl. Acad. Sci. USA* **1988,** *85,* 2984-2988.
[33] Tokuyama, M. ; Oppenheim, I. *Phys. Rev. E* **1994,** *50,* R16-R19.

La prise en compte du volume hydrodynamique de protéines avait déjà été suggérée pour décrire la viscosité de solutions d'hémoglobine [43].

Afin de pouvoir étayer notre raisonnement nous avons cherché à mettre en évidence une transition entre une mesure d'un coefficient à temps longs vers celui à temps courts à plus grands vecteurs d'onde.

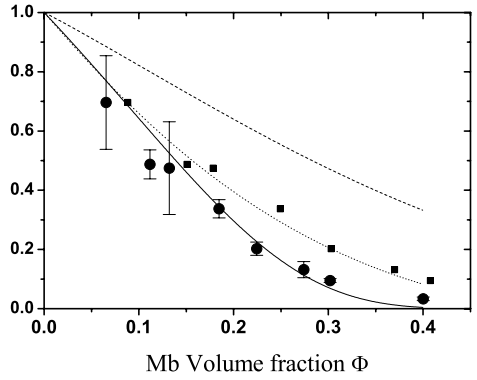

FIG. 2.5 – Variation de $D_s(\Phi)/D_0 = lim_{qR\gg 1} D^{\Phi}(q)/D_0$ en fonction de la fraction volumique de protéine mesurée par écho de spin (•). La ligne continue correspond à un affinement des données obtenues par des méthodes de traceurs [42]. Les courbes en tirets et en pointillés correspondent respectivement aux coefficients d'autodiffusion à temps court D_s^s et à temps long D_s^L calculés pour des suspensions de sphères dures [33]. Les carrés pleins (■) correspondent aux données d'écho de spin après renormalisation par le volume hydrodynamique de la myoglobine.

2.3.1 Recherche du coefficient de diffusion à temps court

A grand vecteur d'onde, pour des questions de polarisation du faisceau diffusé les mesures doivent être réalisées avec des solutions totalement hydrogénées. Nous avons donc entrepris ces mesures dans le cadre de la thèse de Clémence Le Coeur. En collaboration avec Sophie Combet et avec l'aide précieuse de Serge Pin, Clémence a pu préparer des solutions d'hémoglobine à partir de la purification de poches de sang. On peut ainsi atteindre des concentrations de près de 400 mg.ml^{-1} sans aucune trace d'agrégation et en grande quantité. Nous avons donc décidé de chercher la transition d'un régime de coefficient à temps long, D_s^L, vers un régime à temps court D_s^S, dans des solutions d'hémoglobine correspondant aux concentrations physiologiques (~ 350 $mg.ml^{-1}$). La figure 2.6 présente la fonction intermédiaire de diffusion obtenue à q=1Å^{-1}, à 310K, pour une solution d'hémoglobine concentrée ainsi que celle obtenue pour l'eau.

[43] Ross, P. D. ; Minton, A. P. *Biochemical and biophysical reasearch communications* **1977,** *76,* 971-976.

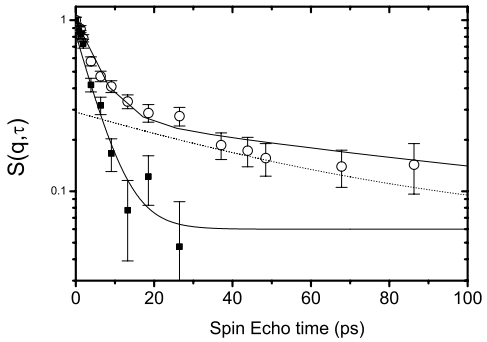

FIG. 2.6 – Fonction intermédiaire de diffusion mesurée pour une solution d'hémoglobine concentrée de $\sim 350mg.ml^{-1}$ à T=310 K ($\circ$) ainsi que pour l'eau (**.**) dans les mêmes conditions expérimentales. On distingue très nettement la contribution de la protéine (en tirets) qui a un temps de relaxation $\tau \simeq 67ps$.

Dans une solution de protéine hydrogénée dans de l'eau légère, la diffusion incohérente domine largement aux grands angles et la contribution de chaque composant est proportionnelle à sa quantité de protons. La contribution de la protéine représente donc environ 25% du signal total. On peut très nettement séparer la relaxation du solvant (quelques ps) et celle de la protéine dont le temps de relaxation est de l'ordre de $67 \pm 15ps$. Pour l'eau pure, on extrait un coefficient de diffusion de $D_s = 2.28(\pm 0.06) * 10^{-5}cm^2s^{-1}$ très proche de $D_s = 2.37 * 10^{-5}cm^2s^{-1}$ que l'on peut trouver dans la littérature [44, 45]. La diffusion de l'eau dans la solution est légèrement ralentie, avec un temps caractéristique de relaxation d'environ 50% supérieur à celui de l'eau pure. Le coefficient de diffusion apparent de la protéine est $D^{app}_{mes} = 14.9(\pm 3) * 10^{-7}cm^2s^{-1}$ ce qui plus de 2 fois celui mesuré en solution infiniment diluée : $D^0_s = 6.8 * 10^{-7}cm^2s^{-1}$, qui doit normalement être la valeur limite supérieure pour D^L_s et D^s_s. L'introduction d'un phénomène de relaxation supplémentaire est donc nécessaire à l'interprétation des résultats. Les protéines subissent des mouvements rotationels aléatoires de nature similaire à la translation que l'on appelle des mouvements rotationels browniens. Leur origine physique est un moment aléatoire créé par une balance non équilibrée des collisions des molécules du solvant avec la protéine. A grands vecteurs d'onde, ces mouvements vont contribuer à la diffusion translationelle, sous la forme d'une composante additionnelle $\tilde{D}^r \simeq R^2_g Dr$. En prenant les valeurs de la littérature [46] et en supposant que dans une solution de $\sim 350mg.ml^{-1}$ $D^s_s \simeq D^0_s/2$ (ce qui correspond aux prédictions théoriques) on obtient un ordre de grandeur de $D^{app} = \tilde{D}^r_{rbc} + D_s \simeq 6.2 * 10^{-7}cm^2.s^{-1}$ ce qui reste très inférieur à la valeur mesurée. Une contribution supplémentaire [47], autre que brownienne, (probablement un mouvement interne) doit donc contribuer à la relaxation mesurée, des

[44] Mills, R. *J Phys. Chem.* **1973,** *77*, 685-688.
[45] Dipple, T. *Ph. D. Thesis*, Thesis, Max Planck Institüt für Metallforschung, Institut Physik Stuttgart., 1991.
[46] Lavalette, D. ; Tetreau, C. ; Tourbez, M. ; Blouquit, Y. *Biophys. J.* **1999,** *76*, 2744-2751.

mesures sont en cours visant à étudier sa dispersion ainsi que sa dépendance en fonction de la concentration en hémoglobine. Il est intéressant de noter qu'une contribution similaire a été mise en évidence par spectrométrie par retro-diffusion dans des solutions de myoglobine [48].

2.3.2 Dépendance en vecteur d'onde de D(q)

Comme le montre la figure 2.4, la dépendance en vecteur d'onde du coefficient de diffusion est similaire quelle que soit la concentration en protéine de la solution. Comme nous l'avons déjà mentionné, ce comportement est caractéristique de la nature collective du coefficient de diffusion apparent mesuré, $D(q)$. Dans les liquides moléculaires les interactions résultent des forces directes. P.-G. de Gennes a calculé en 1959 la relation entres les seconds moments des raies de diffusion cohérente et incohérente [49] : $\omega_{coh}^2 = \omega_{inc}^2/S(q)$. Dans des solutions colloïdales ou de protéines, des interactions supplémentaires portées par le solvant apparaissent : les interactions hydrodynamiques, qui sont données par la formule 2.1, dérivée par Ackerson [28]. Dans la limite des petits vecteurs d'onde, D(q) doit tendre vers la grandeur mesurée par diffusion de la lumière, cette valeur ne dépend que faiblement de la concentration car l'augmentation de la friction est partiellement compensée par la forte variation de la compressibilité osmotique. Lorsque le module du vecteur d'onde augmente, le facteur de structure augmente également ce qui explique la décroissance de $D(q)$. Formellement la relation 2.1 n'est valable que dans la limite des temps courts, domaine où l'on peut négliger la variation position des protéines environnantes et les considérer comme fixes. C'est-à-dire que le coefficient de diffusion apparent doit être celui mesuré à temps court. Nous avons montré que notre mesure nous donnait accès à D_s^L, et non à D_s^S, ce qui devrait exclure toute possibilité de calcul du facteur hydrodynamique H(q). Le haut de la figure 2.7 représente le produit $D(q) * S(q)/D_0$, le résultat présente plusieurs aspects intéressants. Conformément aux prédictions théoriques pour H(q) [31], ce produit oscille en phase avec le facteur de structure et, après renormalisation par une constante visant à prendre en compte la différence entre les coefficients de diffusions à temps court et à temps long, l'accord entre les prédictions théoriques et les résultats expérimentaux est tout à fait correct. P. Segrè et P. Pusey ont mis en évidence une dépendance similaire en vecteur d'onde des coefficients à temps court et à temps long, $D^S(q)$ et $D^L(q)$, dans des solutions de colloïdes [50] jusqu'à des fractions volumiques de l'ordre de 30%. Cette observation ne possède pas d'explication théorique claire. Malgré ces réserves, la figure 2.7 semble indiquer une forte contribution des interactions hydrodynamiques à la réduction de la mobilité des protéines.

2.4 Diffusion de l'hémoglobine *in-vivo*

La mesure expérimentale de la mobilité de l'hémoglobine dans les globules rouges n'est pas facile. La diffusion dynamique de la lumière est dominée par les fluctua-

[47] Busch, S. ; Doster, W. ; Longeville, S. ; Garcai-Sakai, V. ; Unruh, T. *Proc. of QENS 2006 Mat. Res. Soc.* **2006,** *1*, 107-114.
[48] de Gennes, P.-G. *Physica* **1959,** *25*, 825.
[28] Ackerson, B. J. *J. Chem. Phys.* **1976,** *64*, 242-246.
[31] Beenakker, C. W. J. ; Mazur, P. *Physica* **1984,** *126*, 349-370.
[49] Segrè, P. N. ; Pusey, P. N. *Phys. Rev. Lett.* **1996,** *77*, 771-774.

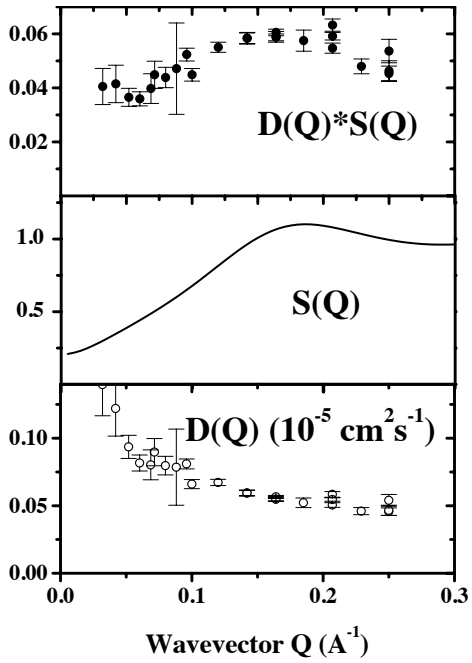

FIG. 2.7 – Dépendance en vecteur d'onde du coefficient de diffusion apparent (bas), du facteur de structure (milieu) et du produit $D(q) * S(q)/D_0$ mesurés pour une solution de myoglobine de 14.7mM ($\Phi \approx 0.18$).

tions de la membrane [51], tandis que la RMN et les techniques optiques enregistrent les déplacements sur des distances de plusieurs centaines de nanomètres où l'effet de confinement cellulaire devient important. Le neutrons étant neutres peuvent pénétrer très fortement dans la matière. Cette propriété à été utilisée par Krueger et Nossal [52] pour étudier la structure de l'hémoglobine dans les globules rouges. Notre contribution a été de mesurer la diffusion de l'hémoglobine par spectroscopie à écho de spin dans les globules rouges [53].

Krueger et Nossal [52] ont cherché à séparer les contributions de la membrane et de l'hémoglobine par variation de contraste. Le signal émanant de la membrane ne peut pas être éliminé stricto-sensus, car celle-ci n'est pas simplement composée d'une bicouche lipidique, mais est très hétérogène, puisqu'elle comporte de nombreuses protéines membranaires. En éteignant le signal de l'hémoglobine, les auteurs ont pu mettre en évidence que la contribution membranaire se situait dans un domaine de vecteur d'onde très différent de celui de la protéine. Nous avons donc mesuré les fonctions intermédiaires de diffusion autour du pic de structure de l'hémoglobine. Les résultats sont qualitativement très proches de ceux mesurés dans des solutions de protéines *in-vitro*. La figure 2.8 résume les résultats obtenus sous la même forme que nous avons précédemment discuté pour des solutions de myoglobine.

[50] Jones, C. R. ; Johnson, C. S. ; T., P. J. *Biopolymers* **1978,** *17*, 1581-1593.
[51] Krueger, S. ; Nossal, R. *Biophys. J* **1988,** *53*, 97-105.
[52] Doster, W. ; Longeville, S. *Biophys. J* **2007,** *93*, 1360-1368.

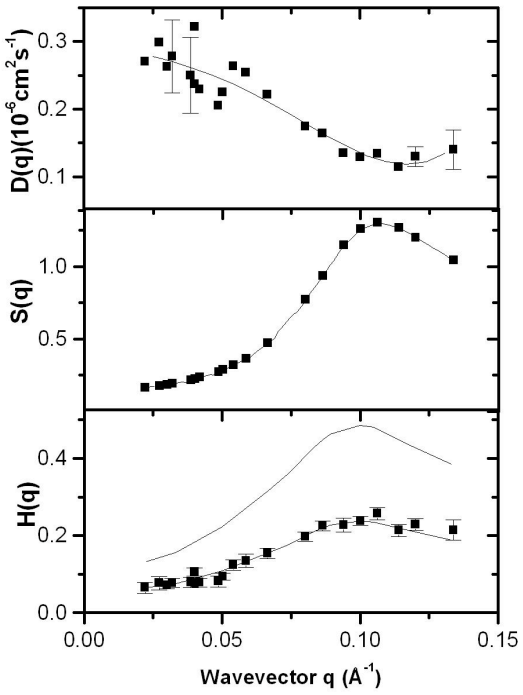

FIG. 2.8 – Dépendance en vecteur d'onde du coefficient de diffusion apparent (haut), du facteur de structure (milieu) et du produit $D(q) * S(q)/D_0$ (bas) mesurés pour l'hémoglobine dans le globule rouge.

On peut ainsi résumer les résultats :

1. Le coefficient d'auto-diffusion de l'hémoglobine dans le globule est égal à $D_s = 1.75(\pm 0.2).10^{-7} cm^2.s^{-1}$, dans l'eau lourde et à 37˚C. Corrigé de la température et des rapports des viscosités de l'eau lourde et de l'eau légère, on obtient un équivalent de $D_s = 1.1(\pm 0.2).10^{-7} cm^2.s^{-1}$ dans l'eau à 20˚C.

2. La diffusion des protéines à forte concentration peut être comprise sur la base des concepts théoriques développés pour les suspensions colloïdales. La principale différence est que la fraction volumique effective de la protéine doit inclure la couche d'hydratation à cause du fort rapport surface sur volume des protéines.

3. La friction protéine-protéine dans les globules est en grande partie contrôlée par les interactions hydrodynamiques. Cette conclusion est basée sur la dépendance en vecteur d'onde du coefficient de diffusion apparent, et ne peut être simplement déduite de la dépendance de D_s en fonction de la fraction volumique, puisque celle-ci peut être reproduite par simulation de dynamique brownienne de pro-

téines sans interactions hydrodynamiques [54].

2.5 Implications physiologiques de la diffusion de l'hémoglobine et de la myoglobine dans le transport d'oxygène

2.5.1 Généralités

Nous avons mesuré la dépendance en concentration de la diffusion de la myoglobine et de l'hémoglobine afin d'appréhender les mécanismes physiques qui sont responsables de la diminution de la mobilité des protéines en solutions concentrées. Mais quelle genre d'intérêt ce type d'étude peut-il avoir pour la compréhension d'un phénomène biologique ?

Le premier à avoir émis l'hypothèse que l'hémoglobine pouvait jouer un rôle dans le transport d'oxygène à l'intérieur du globule rouge est Rougthon qui, dès 1932, dans un papier intitulé "Diffusion and chemical reaction velocity as joint factors in determining the rate of uptake of oxygen and carbon monoxide by red blood cells corpuscules" [55]. L'idée sous-jacente est simple. Dans le transport de molécules deux facteurs entrent en jeu : leur nombre et leur coefficient de diffusion (dans le cas où leur déplacement obéit à un mouvement de diffusion brownien). Pour le cas de l'oxygène, le transport peut se faire sous deux états différents, sous forme libre ou sous forme liguandée à une protéine transporteuse ; les deux flux vont s'additionner. Il est évident que les molécules d'O_2 diffusent de manière beaucoup plus rapide que l'hémoglobine ou la myoglobine, mais la très faible solubilité du di-oxygène dans l'eau ou le plasma, contrebalance cet effet. Dans le globule rouge par exemple, à saturation de l'hémoglobine, le rapport entre la quantité d'oxygène fixée par l'hémoglobine (en mM) et libre en solution est de près de $20.3/0.177 \simeq 115$ (environ 30 pour la myoglobine dans les muscles). Le rapport des coefficients de diffusion est $D^{0_2}/D^{Hb} \simeq 130$. Bien plus tard, au début des années 1960, Schölander [56] et Wittenberg [57] ont, de manière concomitante, pu mettre en évidence expérimentalement cet effet pour des solutions de myoglobine et d'hémoglobine. L'expérience, simple, elle consiste à mesurer le flux d'oxygène diffusé à travers une solution contenant de l'hémoglobine en fonction de la pression partielle d'oxygène. Dans un cas, l'état d'oxydation du fer de l'hème permet la fixation de l'hémoglobine (oxy-Hb). Dans une autre expérience test, celui-ci est dans l'état ferri qui ne permet pas la fixation d'O_2 (met-Hb). Les résultats montrent sans ambiguïté une augmentation du flux diffusé en présence d'oxy-hémoglobine, qui est en relatif d'autant plus important que la pression partielle d'oxygène est faible. Dans un papier ultérieur, Wittenberg [58] a également montré que cet effet était très fortement dépendant de la concentration en hémoglobine, d'abord ascendant puis après avoir atteint un maximum vers une concentration de 9 mM en hème, il décroît plus lentement à forte concentra-

[53] Dwyer, J. D. ; Bloomfield, V. A. *Biophys. J* **1993,** *65*, 1810-1916.
[54] Roughton, F. J. W. *Proc. Roy. Soc. (London), Ser. B.* **1932,** *111*, 1-36.
[55] Scholander, P. F. *Science* **1960,** *131*, 585-590.
[56] Wittenberg, J. B. *The Biological Bulletin* **1959,** *117*, 402-403.
[57] Wittenberg, J. B. *The J. of Biological Chemistry* **1966,** *241*, 104-114.

tion, formant ainsi une courbe en cloche. Collins [59] et Wyman [60] ont montré que cette diffusion facilitée pouvait s'expliquer par la diffusion brownienne translationnelle de l'hémoglobine, plutôt que par une diffusion par saut de l'oxygène d'une molécule à l'autre, la contribution de la diffusion rotationnelle pouvant être négligée. L'implication de cette observation au milieu vivant a depuis fait l'objet de nombreux travaux. D'une part, afin de déterminer le rôle de la diffusion de l'hémoglobine dans le globule pour la capture de l'oxygène au niveau des alvéoles pulmonaires, ou sa libération au niveau des tissus. Et d'autre part, afin de préciser l'éventuel rôle joué par la myoglobine comme transporteur d'O_2 dans le sarcoplasme des cellules musculaires, de la membrane aux mitochondries où l'oxygène va être utilisé pour la production d'énergie.

2.5.2 Transport de l'oxygène par la myoglobine dans les muscles

Pour que le transport d'oxygène facilité par la myoglobine dans les cellules soit efficace trois conditions sont requises :

1. On doit être en condition de faible pression partielle d'oxygène.
2. Un gradient de MbO_2 (myoglobine oxygénée) doit exister entre la surface de la cellule et les mitochondries. Celui-ci servira de moteur à la diffusion facilitée (par l'intermédiaire de la loi de Fick).
3. La concentration en MbO_2 doit être suffisante et sa diffusion suffisamment rapide.

Les conditions 1 et 2 sont généralement considérées comme acquises, bien que faisant encore l'objet d'études. La concentration en myoglobine est, comme nous l'avons mentionné plus haut, environ 30 fois supérieure à celle de l'oxygène dissout. Le problème reste donc la mesure du coefficient de diffusion de la myoglobine dans la cellule. Cette grandeur peut alors être utilisée pour calculer la fraction d'oxygène transportée par la myoglobine (le transport facilité). Les premières estimations du coefficient de diffusion ont été faites à partir de mesures de solutions concentrées de myoglobine [61], à des concentrations sensées être similaires à celles que l'on trouve dans la cellule. Le coefficient de diffusion de la myoglobine à 180 $mg.ml^{-1}$ est $D_{Mb} \sim 8\ 10^{-7}\ cm^2.s^{-1}$ (la réalité doit être en fait plus proche de 300 $mg.ml^{-1}$). Avec cette valeur, le transport facilité d'oxygène par la myoglobine est significatif [62]. L'effort expérimental s'est ensuite porté sur la mesure de la diffusion de la myoglobine *in-vivo* afin de pouvoir affiner les modèles. D. T. Levingstone et coll. [63] furent les premiers à avoir reporté une mesure de diffusion dans des cellules musculaires, par Résonance Magnétique Nucléaire (RMN). Ils montrent que le temps de relaxation rotationel de la myoglobine dans la cellule n'est multiplié que par un facteur 2.3 par rapport à celui dans une solution diluée et en déduisent que celle-ci contribue fortement au transport d'oxygène. En utilisant des méthodes optiques, une équipe allemande [64] a montré que la diffusion de la myoglobine était en fait beaucoup plus faible dans la cellule que celle déterminée par les auteurs précédents, en obtenant $D_{Mb} \sim 1.2\ 10^{-7}\ cm^2.s^{-1}$. En utilisant cette valeur, ils estiment que la contribution de la diffusion facilitée ne dépasse

[58] Collins, R. E. *Science* **1961,** *133*, 1593-1594.
[59] Wyman, J. *The J. of Biological Chemistry* **1966,** *241*, 115-121.
[60] Riveros-Moreno, V. ; Wittenberg, J. B. *The J. of Biological Chemistry* **1972,** *247*, 895-901.
[61] Wittenberg, ; Wittenberg, J. B. ; Caldwell, P. R. B. *The J. of Biological Chemistry* **1975,** *250*, 9038-9043.
[62] Livingstone, D. J. ; Mar, G. N. L. ; Brown, W. D. *Science* **1983,** *220*, 71-73.
[63] Jürgens, K. D. ; Peters, T. ; Gros, G. *Proc. Natl. Acad. Sci. USA* **1994,** *91*, 3829-3833.

pas les 4% de la diffusion totale d'O_2 [65]. Ces auteurs ont également pu mesurer le coefficient de diffusion radial dans les cellules des muscles squelettiques, et montrer qu'il était similaire au longitudinal [66]. Récemment des mesures par RMN du coefficient de diffusion tranlationnel dans des cellules cardiaques de rat [67] rapportent une valeur notablement plus élevée que celle obtenue par FRAP $D_{Mb} \sim 4.2410^{-7}$ $cm^2.s^{-1}$, et concluent que la diffusion facilitée contribue de manière significative au transport d'oxygène. La question semble donc rester ouverte. Une autre approche, purement biologique, pour comprendre le rôle de la myoglobine a été développée [68]. Il s'agit simplement de bloquer les gènes qui codent la myoglobine (gene knock-out) et donc de produire des souris sans myoglobine. Un aspect particulièrement spectaculaire est que le muscle cardiaque perd sa couleur rouge et devient blanc. Les auteurs ont constaté que non seulement les sujets étaient viables, mais qu'ils pouvaient se reproduire et ne présentaient pas de capacités physiques altérées par rapport aux souris avec myoglobine. Leurs observations les ont conduits à mettre en doute l'utilité de cette protéine. Une autre équipe [69], qui a développé cette technique quasi simultanément, à pu démontrer que des souris sans myoglobine développaient de multiples mécanismes de compensation visant à se substituer au rôle habituellement joué par la myoglobine (augmentation de la densité capillaire, du flux coronarien ..).

2.5.3 Influence de la diffusion de l'hémoglobine sur la capture et la libération de l'oxygène par les globules rouges

La capture de l'oxygène par les globules rouges (GR) au niveau des poumons est un phénomène complexe qui s'étale sur différentes échelles de temps et d'espace. Le flux sanguin transporte les GR au niveau des capillaires des alvéoles pulmonaires, où les échanges gazeux vont avoir lieu. Si l'on adopte une vision statique du transport gazeux, alors, dans les capillaires pulmonaires où la pression partielle en oxygène P_{0_2} est élevée (typiquement $\simeq 100$ Torr), les molécules d'hémoglobine vont libérer les gaz qu'elles doivent évacuer (ex : CO_2 ...) et vont se charger en O_2. Puis, à travers le transport dans le corps, tandis que la pression partielle en oxygène va diminuer (typiquement vers les muscles lorsque la demande est forte), l'hémoglobine relâche les molécules d'O_2 et va se charger en CO_2.

Le transfert de l'O_2 des alvéoles pulmonaires vers l'hémoglobine fait l'objet de nombreuses études théoriques, expérimentales et par simulations numériques. C'est un phénomène très complexe durant lequel l'oxygène doit diffuser à travers des membranes, le plasma et doit se lier à l'hémoglobine. Il s'agit donc d'un phénomène fortement dynamique dans lequel de nombreuses constantes de temps vont intervenir. Pour un rendement maximum du transport gazeux, le temps de capture de l'oxygène au niveau des alvéoles pulmonaires doit être inférieur au temps de transit des globules rouges dans ces alvéoles.

Un modèle cinétique pour la libération de l'oxygène par les globules rouges a été

[64] Jürgens, K. D. ; Papadopoulos, S. ; Peters, T. ; Gros, G. *News Physiol. Sci.* **2000,** *15*, 269-274.
[65] Papadopoulos, S. ; Endeward, V. ; Revesz-Walker, B. ; Jürgens, K. D. ; Gros, G. *Proc. Natl. Acad. Sci. USA* **2001,** *98*, 5904-5909.
[66] Lin, P.-C. ; Kreutzer, U. ; Jue, T. *J. Physiol.* **2007,** *578.2*, 595-603.
[67] Garry, D. J. ; Ordway, G. A. ; Lorenz, J. N. ; Radford, N. B. ; Chin, E. R. ; Grange, R. W. ; Bassel-Duby, R. ; Williams, R. S. *Nature* **1998,** *395*, 905-908.
[68] Gödecke, A. ; Flögel, U. ; Zanger, K. ; Ding, Z. ; Hirchenhain, J. ; Decking, U. K. ; Schrader, J. *Proc. Natl. Acad. Sci. USA* **1999,** *96*, 10495-10500.

introduit en 1985 [70]. D'après ce modèle le temps τ_1 de libération de l'oxygène par un globule dépend de 4 temps caractéristiques et est estimé à :

$$\tau_1 = \frac{\tau_{KC} + \tau_{KS}}{\tau_{KS}/\tau_{DS} + \tau_{KC}/\tau_{DC}}$$

$\tau_{KS} = k^{-1}$, k est la constante de dissociation de la réaction chimique $Hb + O_2 \rightleftarrows HbO_2$ avec k=44 s^{-1}.

$\tau_{KC} = (kN_T/N_{50})^{-1}$ correspond au temps nécessaire pour que la moitié de l'hémoglobine d'un globule rouge capture/libère de l'O_2 à une pression partielle donnée d'oxygène dans le plasma. N_T est le nombre de molécules par unité de volume et N_{50} la densité d'O_2 nécessaire pour avoir 50% des hèmes ayant fixé une molécule d'oxygène.

$\tau_{DS} = \frac{a^2}{D_{Hb}}$ est le temps caractéristique que met l'hémoglobine pour diffuser du centre à la surface du globule. Dans le modèle, la forme de la cellule est cylindrique de rayon R et d'épaisseur 2a (avec 2a<<R). D_{Hb} est le coefficient de diffusion de l'hémoglobine. Les coefficients de transport peuvent être soit individuels soit collectifs, principalement en fonction des gradients de concentration. Quand un fort gradient de concentration est présent, et que les interactions entre les molécules ne peuvent être négligées, le coefficient de transport est un coefficient de diffusion collectif. Dans le cas des globules rouges la concentration en hémoglobine est relativement homogène, hormis quelques fluctuations. On doit donc utiliser le coefficient d'auto-diffusion de l'hémoglobine. Il est néanmoins intéressant de noter que dans cette approximation on néglige l'effet du changement de charge des molécules lorsque celles-ci fixent une molécule d'oxygène ce qui devrait créer un léger gradient de champ électrique qui pourrait conduire à des mouvements de convection. Etant données les faibles charges mises en jeu, ainsi que la forte salinité du milieu et donc l'écrantage des interactions électrostatiques, cette approximation semble raisonnable.

$\tau_{DC} = \frac{a^2}{D_{O_2}}$ est le temps caractéristique que met l'oxygène pour diffuser du centre du GR à la surface ou vice-versa (dépendant du fait que l'on observe la capture ou la libération d'oxygène). D_{O_2} est le coefficient de diffusion de l'oxygène moléculaire.

A partir d'un modèle simple qui avait été développé pour essayer d'estimer les temps caractéristiques τ_1 dans différentes conditions de concentration et de pression partielle en O_2, nous avons cherché à essayer de répondre à la question simple : quelle est la concentration optimum en hémoglobine qui permet de maximiser le transport d'oxygène ? Comme je l'ai mentionné précédemment, deux phénomènes se contrebalancent : plus la concentration en hémoglobine augmente plus la capacité de transport des globules rouges augmente, mais parallèlement la mobilité des molécules diminue. De plus, l'augmentation de la concentration en macromolécules diminue de fait la quantité de solvant et donc d'oxygène dissout dans le plasma. On a donc deux phénomènes opposés : un effet de masse contrebalancé par un effet cinétique.
La fraction d'hémoglobine chargée en oxygène en fonction de la pression partielle en oxygène est donnée par la courbe de Hill :

[69] Jr., A. C. ; W. J. Federspiel, a. P. A. A. C. ; Cokelet, G. R. *Biophys. J.* **1985,** *47*, 171-181.

$$S = \frac{(P/P_{50})^n}{1+(P/P_{50})^n} = \frac{(N_o/N_{50})^n}{1+(N_o/N_{50})^n}$$

P est la pression partielle en O_2 dans la solution (en mmHg) et N_o la densité d'oxygène en $g\ cm^{-3}$. Ils sont liés par le coefficient de Bunsen : $N_{O_2} = P_{O_2} B_u$. $P_{50} = 26.4$ mmHg, n=2.65. La dépendance de N_{50} en fonction de la concentration est donnée par [70] $N_{50}(\Phi) = 3.728 * 10^{-8}(1 + 0.042\Phi)$.

A partir de nos données expérimentales, nous avons obtenu une loi empirique déterminant la variation du coefficient de diffusion de l'hémoglobine en fonction de la concentration $D_{Hb}(\Phi) = D_{Hb}(0)e^{-\alpha\Phi^\beta}$ avec $D_{Hb}(0) = 0.156 * 10^{-5} cm^2 s^{-1}$, $\alpha = 12.8$, $\beta = 1.5$. En fait, la dépendance en concentration des coefficients de diffusion de l'hémoglobine et de la myoglobine obtenus par diffusion de neutrons sont très proches de ceux obtenus par des techniques de traceur [61] mais sur une plus large gamme de concentration.

Dans une moindre mesure, la diffusion de l'oxygène dépend également de la concentration en hémoglobine : à 37^oC dans le globules rouges les auteurs estiment que $D_s^{O_2} = 9.5 * 10^{-6} cm^2.s^{-1}$ tandis qu'il est $D_s^{O_2} = 1.96 * 10^{-5} cm^2.s^{-1}$ dans l'eau pure H_2O [71]. Nous avons donc pris une dépendance en fonction de la concentration en hémoglobine $D_s^{O_2}(\Phi) = 1.96 * 10^{-5} e^{-4.84\Phi}$.

On peut donc calculer le temps $\tau_1(\Phi)$ de capture de l'oxygène en fonction de la concentration en hémoglobine. Il est ensuite possible, connaissant le temps de transit dans les capillaires près de alvéoles pulmonaires, d'estimer la quantité d'oxygène qui va être transportée en fonction de Φ :

$$\tilde{N}(\Phi) = N(\Phi) * exp(-\tau_1(\Phi)/\tau_R)$$

Le temps de transit, τ_R, est le temps durant lequel les GR vont se trouver dans les capillaires pulmonaires où la pression partielle en oxygène va être élevée.

$\tilde{N}(\Phi)$ est représenté sur la figure 2.9 pour différents temps de transit en supposant d'abord que l'hémoglobine est immobile ($D_s^{Hb} = 0$) (gauche), puis en utilisant la dépendance de $D_s^{Hb}(\Phi)$ (droite) en fonction de la concentration. Les échelles des deux représentations sont identiques.

1. On observe très clairement que la diffusion de l'hémoglobine dans le globule rouge permet d'augmenter significativement la quantité d'oxygène transportée. Le mouvement de diffusion de l'hémoglobine vers la surface de la cellule afin d'aller capturer l'O_2 semble donc augmenter la capacité de transport des globules rouges. D'après ce modèle ultra-simplifié on observe un facteur 2 à 3 entre les maxima avec et sans diffusion quel que soit le temps de transit.
2. La deuxième observation notable que l'on peut déduire de la courbe concerne l'optimum de transport d'oxygène en fonction de la fraction volumique d'hémoglobine. Lorsque l'on prend en compte la diffusion de l'hémoglobine, ce maximum correspond à des fractions volumiques en hémoglobine s'étalant de $\Phi = 0.27$ à $\Phi = 0.42$, pour des temps de transit de 0.1 a 0.8 secondes. Il est intéressant de noter que, pour les faibles temps de transit qui correspondent à ceux observés lorsque le sujet est en activité physique intense, la concentration en

[60] Riveros-Moreno, V. ; Wittenberg, J. B. *The J. of Biological Chemistry* **1972,** *247,* 895-901.
[70] McCarthy, M. R. ; Vandegriff, K. D. ; Winslow, R. M. *Biophys. Chem.* **2001,** *92,* 103-117.

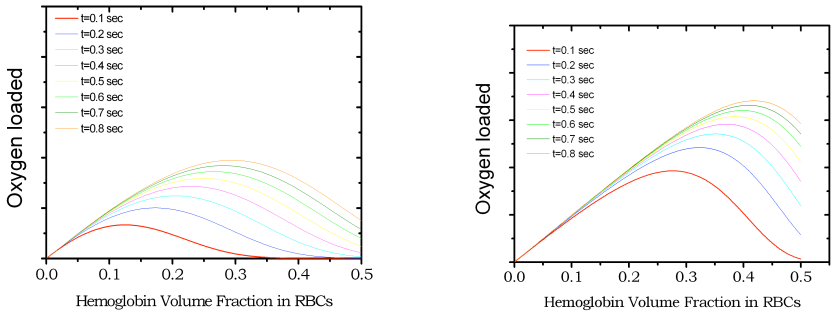

FIG. 2.9 – Nombre de moles de HbO_2 par cm^3 dans les globules rouges en fonction de la fraction volumique d'Hb. On suppose qu'au temps t=0 aucune molécule d'O_2 n'est liée à l'hémoglobine et que le temps de transit est de τ_R sec. A gauche le calcul est réalisé sans prendre en compte la diffusion de l'Hb , à droite avec diffusion de l'hémoglobine.

hémoglobine physiologique correspond à un optimum du transport d'oxygène. On peut supposer que la sélection naturelle s'est faite plutôt avec des sujets en activité qu'au repos.

3. La forme biconcave des GR humains est généralement expliquée par deux approches. En premier l'approche moléculaire, qui suppose que cette géométrie dépend directement de la structure moléculaire de la membrane. La deuxième est une vision mécanique. Pour cette seconde approche, la torsion moléculaire de la structure biconcave se fait à faible coût énergétique. Les GR, très souples, peuvent ainsi s'adapter et être transportés dans des capillaires de très faibles diamètre (inférieurs à celui des cellules) réduisant ainsi la viscosité sanguine. L'analyse de ce modèle simple pour la capture de l'oxygène nous fait émettre une troisième hypothèse. Cette forme réduit fortement la distance entre le centre du globule et la surface où l'hémoglobine doit diffuser afin de se charger en oxygène. Cette distance se traduit dans la valeur de a qui tend à faire diminuer τ_{DS}. Dans cette hypothèse, la forme biconcave permet donc de minimiser le temps de capture (et de rejet) des gaz par le globule rouge.

2.6 Perspectives

Nous avons réalisé une étude du système biologique le plus simple que l'on puisse concevoir : des cellules contenant un seul type de protéine quasi-sphérique. En réalité les GR incluent de nombreux autres types de molécules mais comme leurs tailles sont bien plus petites, elles ne contribuent pas au signal mesuré par diffusion de neutrons. Le signal de la membrane apparaît de plus dans un domaine de vecteur d'onde différent et en dehors de notre fenêtre expérimentale [36]. La modélisation était donc relativement simple. La diffusion des macromolécules dans les cellules cytoplasmiques est en réalité bien plus compliquée, car le cytoplasme est organisé sur différentes échelles s'étalant de quelques μm à quelques nm. Des éléments sont soit mobiles, soit fixes, comme par exemple les éléments du cytosquelette. Tous ces éléments confèrent donc au cytoplasme un bien plus haut degré de structuration et de complexité que les globules

rouges. La diffusion des protéines est subdiffusive. La diffusion de neutrons dans un système très complexe comme celui-ci ne donnerait certainement que peu de résultats interprétables, et la description des spectres serait purement qualitative. Tout ceci sans compter que si les molécules ne sont plus identiques, il faudra envisager d'éteindre le signal du cytoplasme pour mesurer la diffusion de particules sondes, ce qui est difficilement envisageable dans un système très hétérogène. De plus, le signal en écho de spin dépend de $\Delta\rho^2 P$ et non plus $\Delta\rho^2$ comme aux petits angles (P est la polarisation du faisceau diffusé), l'ajout d'hydrogène dans la solution altérant drastiquement la polarisation. Il faut avoir réalisé des mesures par écho de spin sur des systèmes mélangeant signaux cohérent et incohérent de spin pour mesurer la force de cet interdit.

Il existe une variante bien connue de l'hémoglobine qui est l'hémoglobine S (HbS). Elle ne diffère de l'hémoglobine normale (HbA) que par la substitution d'un acide aminé (AA) : l'acide glutamique (hydrophile) en position 6 de la structure primaire est remplacé par une valine (hydrophobe). Cette simple substitution (1 AA sur presque 600) entraîne la polymérisation de l'HbS lorsque la pression partielle d'oxygène diminue, qui aboutit à une pathologie des GR qui se déforment et finissent par adopter la forme d'une serpe, tout en devenant rigides. La maladie, nommée drépanocytose, peut devenir extrêmement grave chez les sujets homozygotes puisqu'elle entraîne une anémie qui peut être mortelle. Les globules polymérisés devenant rigides, ils n'ont plus la capacité de se déformer pour passer dans les capillaires très fins et finissent par les obstruer. Cette polymérisation est réversible en présence d'une quantité suffisante d'oxygène. S'ils sont normalement oxygénés au niveau du passage dans les poumons, les GR retrouvent leur forme normale. Dans de nombreux cas l'oxygènation n'est pas suffisante et les globules restent partiellement polymérisés. L'oxygénation pourrait être incomplète à cause d'un problème de diffusion de l'hémoglobine, qui ne lui permettrait pas de migrer vers la membrane du globule, et donc de se charger en oxygène durant le temps de transit pulmonaire. Nous pourrions essayer de corréler la présence d'oligomères ou de fibres de protéines avec la réduction de la diffusion au niveau du globule.

Chapitre 3

Influence de l'environnement cytoplasmique sur la stabilité des protéines

3.1 Introduction

Une protéine, dans sa forme biologiquement active, possède en général une structure compacte et parfaitement définie (hors fluctuations thermiques), dite native. Les protéines natives correspondent aux structures qui sont thermodynamiquement stables sous des conditions physiologiques. Le repliement des protéines est le processus physique qui permet à une chaîne polypeptidique complètement dépliée d'acquérir sa forme native. Ce mécanisme fait l'objet de très intenses recherches alliant études théoriques et expérimentales [72]. Le mauvais repliement est un processus pathologique qui se trouve à l'origine nombreuses maladies et dégénérescences du type des maladies d'Alzheimer ou de Creutzfeldt-Jakob, l'encéphalopathie spongiforme bovine ou même certains types de diabètes. La compréhension du mécanisme de repliement revêt donc un caractère fondamental.

Il est généralement admis que toute l'information nécessaire au bon repliement d'une chaîne polypeptidique en protéine native est contenue dans sa séquence d'acides aminés [73] (dite structure primaire). Les premières études sur le repliement des protéines remontent aux années 1930. Mirsky et Pauling [74] ont proposé en 1936 que le mécanisme principal qui servait de force au repliement était la création de liaisons hydrogènes. Le groupe de Pauling a ensuite prédit que les protéines natives devaient avoir des hélices-α et des feuillets-β. La première détermination d'une structure tridimensionnelle par Kendrew [75] en 1958, celle de la myoglobine (figure 3.1-a), est venue confirmer ces prédictions pour les hélices-α, et peu après, les feuillets-β ont été mis en évidence. Les prédictions théoriques de la structure et du repliement des protéines étaient basées sur des notions de cinétique des réactions chimiques. Cyrius

[71] Dobson, C. M. ; Sali, A. ; Karplus, M. *Angewandte Chemie-international edition* **1998,** *37*, 868-893.
[72] Anfinsen, C. B. *Biochem J.* **1972,** *128*, 737-749.
[73] Mirsky, A. E. ; Pauling, L. *Proc. Nat. Acad. Sci. USA* **1936,** *22*, 439-447.
[74] Kendrew, J. C. ; Bodo, G. ; Dintzis, H. M. ; Parrish, R. G. ; Wyckoff, H. ; Phillips, D. C. *Nature* **1958,** *181*, 662-666.

Levinthal [76], en 1968, a pointé le fait que l'exploration systématique et aléatoire de toutes les conformations d'une chaîne polypeptidique de quelques centaines d'acides aminés prendrait des temps géologiques. Le repliement des protéines devait donc suivre différents chemins bien spécifiques. Il émettait ainsi une conjecture qui reste sous le nom de paradoxe de Levinthal. Prenons l'exemple d'une petite chaîne comprenant 100 acides animés et dont la configuration entre 2 proches voisins soit déterminée par deux angles ψ, Φ pouvant prendre chacun 2 valeurs, le nombre de configurations différentes pour cette petite chaîne s'élève à $4^{100} \simeq 10^{60}$. L'image était alors une sorte de repliement séquentiel, d'abord formation des structures secondaires (hélices-α et feuillets-β) puis l'assemblage de celles-ci en structures tertiaires grâce aux interactions hydrophiles/hydrophobes. Les chemins étaient multiples et branchés, c'est-à-dire qu'ils pouvaient facilement se croiser, mais limitaient très fortement les conformations accessibles. Il est intéressant de noter, comme l'a lui même fait C. Levinthal, que l'état natif ne devait pas nécessairement être à l'équilibre thermodynamique mais pouvait très bien correspondre à un état métastable.

Vers les années 1990, de nouveaux concepts théoriques ont été introduit. Cette *nouvelle vague* a développé une approche basée plus sur la mécanique statistique et la physique des polymères, pour essayer de comprendre le repliement. Dans cette approche, c'est la courbure de la surface de potentiel qui va limiter les configurations accessibles, mais il n'existe plus de chemins de repliement spécifiques. Le moteur n'est plus la création de liaisons hydrogènes mais plutôt un problème de solvatation. La première étape est un collapse rapide de la chaîne, induit par la volonté des groupements hydrophobes d'échapper au contact de l'eau. La formation rapide d'un objet compact va limiter les conformations à quelques 10^{10}, suit ensuite une phase d'exploration stochastique de l'espace des phases afin d'atteindre l'état natif, qui devient la conformation thermodynamiquement la plus stable. Le moteur initial du repliement n'est donc plus porté par le squelette mais par les groupements latéraux (hydrophile ou hydrophobe). La surface, ou le paysage énergétique, prend la forme d'un entonnoir, le "funnel" (figure 3.1-b).

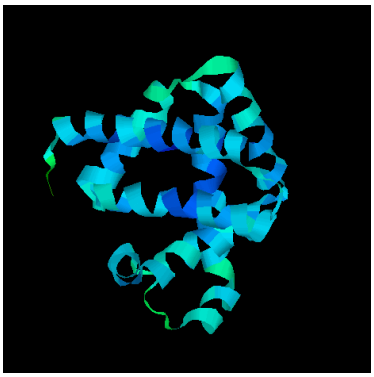

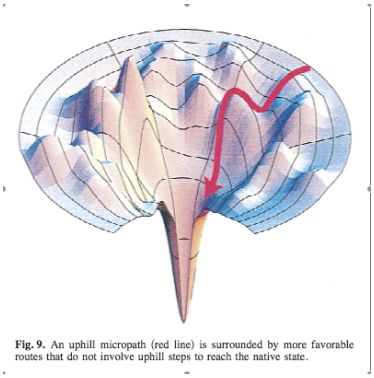

Fig. 9. An uphill micropath (red line) is surrounded by more favorable routes that do not involve uphill steps to reach the native state.

FIG. 3.1 – a) Structure tri-dimensionnelle de la myoglobine. b) Paysage énergétique du repliement d'une protéine (d'après K. Dill).

Récemment, l'attention c'est portée sur les différences possibles entre le processus repliement tel qu'il est observé *in-vitro* et tel qu'il doit être dans un environnement

[75] Levinthal, C. *J. Chim. Phys. et de Physico-Chimie Biologique* **1968,** *65*, 44-45.

cellulaire (*in-vivo*). La forte concentration de protéines dans la cellule peut altérer le processus de repliement en provoquant par exemple l'agrégation des chaînes polypeptidiques dépliées ou partiellement repliées. La majorité des recherches s'est focalisée sur les chaperons moléculaires, ces protéines qui vont assister le repliement d'autres protéines [77]. Bien que le mécanisme d'action de ces chaperons reste encore largement incompris, il semble que leur rôle n'est pas de modifier le processus de repliement, qui est principalement dicté par des considérations thermodynamiques, mais d'éviter de possibles réactions parasites, tels que l'agrégation [78].

L'équilibre entre l'état natif et un ensemble d'états dénaturés est typique du genre de réaction qui doit être affectée par le volume exclu. Dans des travaux théoriques récents, Allen Minton [79, 80] prédit que la stabilité des protéines pourrait être significativement affectée par l'environnement cytoplasmique. Il suggère que l'équilibre ($N \rightleftharpoons D_i$) entre l'état natif (N) et l'ensemble des états dénaturés (D_i) des protéines serait déplacé vers l'état natif à cause du volume exclu dans le cytoplasme. Le volume exclu à forte concentration en macromolecules rigides exercerait une force de compression qui réduirait le "volume" d'une chaîne polypeptidique. Les conformations les plus étendues des chaînes dépliées étant préférentiellement déstabilisées par rapport aux conformations plus compactes, qui incluent l'état natif. Les calculs réalisés sur des systèmes modèles, où l'état dénaturé est modélisé par une chaîne Gaussiènne [81] et les macromolécules par des sphères dures, prédisent que le rayon de giration des chaînes serait fortement réduit à des fractions volumiques équivalentes à celles physiologiques.

Expérimentalement l'environnement cytoplasmique est modèlisé soit par des polysaccharides ramifiés comme le Ficoll 70 ou le Dextran, soit par des polymères. Les premières études remontent à 1999, l'activité des protéines [82], ou le dichroïsme circulaire [83][84][1] ont été mesurés dans des conditions de solvant dénaturant, en fonction de la fraction volumique de cosoluté. Les auteurs ont observé un déplacement de l'équilibre $N \rightleftharpoons D_i$ qui tend à confirmer, au moins de manière qualitative les prédictions d'A. Minton. Il a également été montré que la température n'avait qu'un impact limité sur l'effet de stabilisation dû à l'environnement cytoplasmique, les dénaturations chaudes et froides étant supprimées dans un environnement encombré [85]. Des simulations numériques confirment également les prédictions théoriques [86]. Plus récemment, un groupe a mis en évidence que le volume exclu augmentait les structures à l'intérieur des protéines natives [87]. Toutes ces études observent une stabilisation de l'état natif, mais aucune n'a pu mettre en évidence de manière direct le mécanisme physique à l'origine de cette stabilisation. C'est l'objet de notre étude.

[1] Les structures secondaires du type hélices α ou feuillets β sont optiquement actives, l'absorption différentielle des composantes droite et gauche de la lumière polarisée dans le plan induit une ellipticité caractéristique à chaque structure.

[76] Gething, M.-J. ; Sambrook, J. *Nature* **1992,** *355*, 33-45.
[77] Ellis, R. J. *Curr. Biol.* **1997,** *7*, R531-R533.
[78] Minton, A. *Biophys. J.* **2000,** *78*, 101-109.
[79] Minton, A. *Biophys. J.* **2005,** *88*, 971-985.
[80] Shortle, D. *FASEB J* **1996,** *10*, 27.
[81] van der Berg, B. ; Ellis, R. J. ; Dobson, C. M. *The EMBO J.* **1999,** *18*, 6927-6933.
[82] Tokuriki, N. ; Kinjo, M. ; Negi, S. ; Hoshino, M. ; Goto, Y. ; Urabe, I. ; Yomo, T. *Protein science* **2004,** *13*, 125-133.
[83] Zhou, B.-R. ; Lang, Y. ; Du, F. ; Zhou, Z. ; Chen, J. *The J. of Biol. Chem.* **2004,** *279*, 55109-55116.
[84] McPhie, P. ; Ni, Y.-S. ; Minton, A. P. *J. Mol. Biol.* **2006,** *361*, 7-10.
[85] Cheung, M. S. ; Klimov, D. ; Thirumalai, D. *Proc. Nat. Acad. Science* **2005,** *102*, 4753-4758.
[86] Perham, M. ; Stagg, L. ; Wittung-Stafshede, P. *FEBS* **2007,** *581*, 5065-5069.

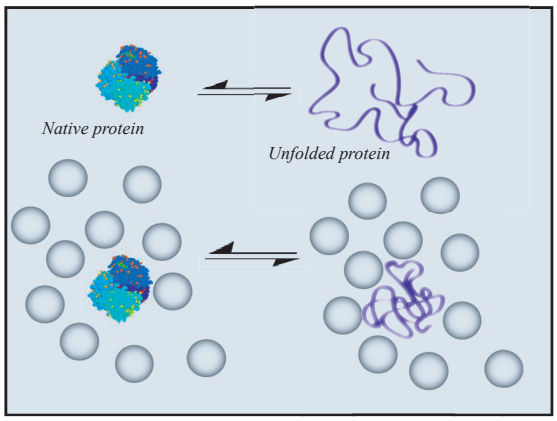

FIG. 3.2 – Principe physique de la stabilisation des protéines natives par un encombrement cytoplasmique. L'effet de volume exclu tend a préferentiellement déstabiliser les états dénaturés spatialement plus étendus que les états plus compacts, parmi lesquels se trouve l'état natif. Cet effet tend à déplacer l'équilibre $N \rightleftharpoons D_i$ vers l'état natif et donc à stabiliser les protéines.

3.2 Un système modèle pour l'état dénaturé

3.2.1 Introduction : approche expérimentale

Les conformations de polymères en solutions, en fondu ou dans des mélanges, sont étudiées par les techniques de diffusion de rayonement. Dans les solutions relativement concentrées, ou dans les fondus, c'est principalement par diffusion de neutrons que ces études ont été menées, grâce à leur forte propension à distinguer les isotopes d'hydrogène (H^1) et de deutérium (D=H^2) [88]. Avec la technique de diffusion de neutrons aux petits angles (on restera sur l'acronyme anglais : SANS) il est possible de regarder la conformation d'une seule chaîne marquée dans un fondu de polymère.

Les techniques de diffusion des rayonnements nous renseignent sur la taille des polymères, et bien que les informations conformationnelles restent relativement limitées, l'affinement des spectres par la simple loi de Debye [89] pour une chaîne Gaussiènne a permis des avancées fondamentales dans le domaine. Emmenés par les développements théoriques introduit par P.-G. de Gennes, les chercheurs du laboratoire[2] ont largement contribué à la validation des théories sur les lois d'échelles dans les domaine des polymères.

[2]Citons les pionniers J.-P. Cotton, G. Jannink, B. Farnoux et M. Daoud, mais de nombreux autres ont participé à ces études.

[87] Cotton, J.-P. ; Farnoux, B. ; Jannink, G. *J. Chem. Phys.* **1972,** *57*, 290-294.
[88] Debye, P. *J. of Physical and colloid chemistry* **1947,** *51*, 18-32.

Notre but est d'étudier les changements de conformation de protéines dénaturées en fonction de l'encombrement, et d'essayer de les corréler à la stabilisation des protéines. On cherche donc à étudier quelques molécules sondes (typiquement quelques $mg.ml^{-1}$) dans un environnement très encombré ($300 - 400\ mg.ml^{-1}$). Afin d'observer que le signal qui nous interesse, nous devons utiliser un solvant qui sera un mélange d'eau lourde et d'eau légère ($xD_2O + (1-x)H_2O$) dont la densité de longueur de diffusion sera égale à celle des co-solutés qui modèlisent l'effet de l'environnement cytoplasmique. Cette condition est obtenue pour $x \simeq 0.41$ pour le Ficoll 70. Le signal d'une protéine hydrogénée s'éteint autour de $x \simeq 0.4$; pour des raisons de contraste nous devons donc disposer soit de protéines deutériés, soit d'un agent de confinement deutérié. Comme les protéines dénaturées possèdent une structure Gaussiènne, nous avons donc commencé notre étude en utilisant un système modèle, que l'on peut se procurer facilement dans le commerce, à des coûts relativement raisonnables. La protéine dénaturée est modèlisée par du PolyEthylèneGlycol, un polymère simple pour lequel l'eau est un bon solvant. Le Ficoll 70 (F70) est utilisé comme agent d'encombrement visant à modéliser l'effet de l'environnement cytoplasmique. Dans les théories de volume exclu, le rapport entre la taille de l'agent d'encombrement et l'objet dont on étudie les propriétés est un paramètre fondamental [90]. Nous avons donc étudié différentes masses de PEG, de 17 kD à 130kD, la première ayant une rayon de giration identique à celui du F70.

3.2.2 L'encombrement cytoplasmique : le Ficoll 70

Le Ficoll 70 est un polysaccharide très fortement ramifié de masse moléculaire de 70 kDa acheté chez Sigma. Il est très soluble dans l'eau dans laquelle il peut être dissout jusqu'à des concentrations de 450 $mg.ml^{-1}$. Nos études ont été menées sur des fractions massiques de F70 s'étalant de $\Phi_f = 0$ jusqu'à $\Phi_f \simeq 0.4$, afin d'atteindre les fractions observées dans le cytoplasme.

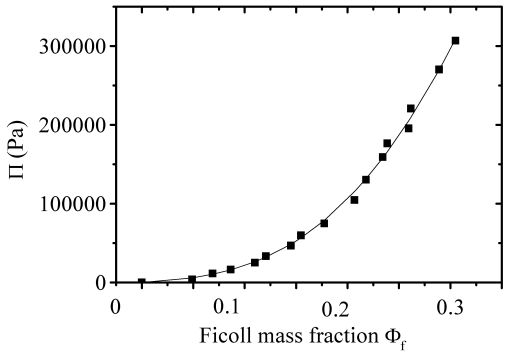

FIG. 3.3 – Pression osmotique d'une solution de F70 en fonction de la fraction massique Φ_f (■). La courbe correspond à la pression calculée pour des sphères dures de rayon $R = 34$ et un volume spécifique de $v_s = 0.4\ cm^3.g^{-1}$.

[89] Minton, A. *J. of Pharmaceutical sciences* **2005,** *94,* 1668-1675.

Nous avons mesuré la pression osmotique de solutions de F70 à différentes concentrations par compression osmotique (figure 3.3). Elle atteint près de 3.10^5 Pascals pour une solution de F70 de $\Phi \simeq 0.4$.

3.2.3 Etude de la compression d'une chaîne Gaussienne

Nous avons commencé notre étude [91] par la mesure de solutions de PEG à des concentrations de 5 et 10 $mg.ml^{-1}$ avec différentes fractions massiques en F70 qui s'étalent de $\Phi_f = 0$ à $\Phi_f \simeq 0.4$. Les spectres obtenus sur D22, après traitements standards, sont présentés en figure 3.4 gauche. Ils ont été affinés par une intensité théorique du type :

$$I(q) = \frac{c_p(\Delta\rho)^2 v_s^2}{N_A} M_a(\Phi_f) P(q)(1 + 2M_a(\Phi_f)c_p a_2(\Phi_f)) \tag{3.1}$$

$\Delta\rho$ est la différence de densité de longueurs de diffusion entre le PEG et le solvant, N_A le nombre d'Avogadro, $P(q) = \frac{2}{x^2}(x - 1 + e^{-x})$ est le facteur de forme d'une chaîne Gaussienne avec $x = (qR_g)^2$. $a_2(\Phi_f)$ est le second coefficient du viriel et $M_a(\Phi_f)$ est la masse apparente du polymère, qui dépend de Φ_f. Elle est obtenue par extrapolation de I(q) à concentration en PEG nulle. v_s est le volume spécifique du polymère. La figure 3.4 montre les spectres obtenus pour deux fractions massiques en F70 ($\Phi_f = 0$ et $\Phi_f = 0.3$) pour des concentrations identiques en PEG. On observe une différence significative entre les deux spectres.

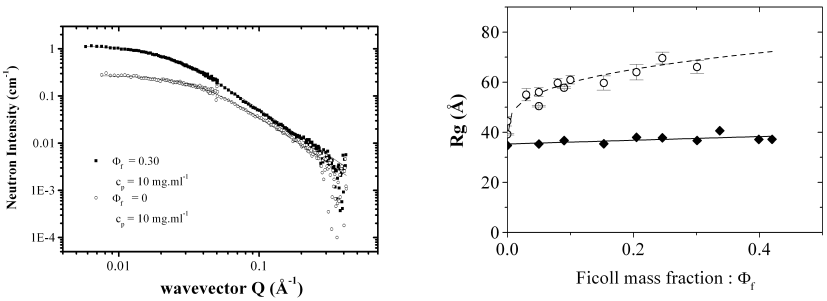

FIG. 3.4 – Gauche : Spectres du PEG deutérié mesurés sur D22 à des concentrations $c_p = 10\ mg.ml^{-1}$ pour deux fractions massiques en F70 différentes (0 et 0.3). La densité de longueur de diffusion du solvant est identique à celle du F70. Droite : Evolution du rayon de giration d'une solution D-PEG à une concentration de $c_p = 10\ mg.ml^{-1}$ en fonction de la fraction massique en agent d'encombrement Φ : Sucrose $\Phi = \Phi_s$; $\circ$ F70 : $\Phi = \Phi_f$.

L'évolution du rayon de giration du PEG mesuré pour une concentration de $c_p \simeq 10mg.ml^{-1}$ en fonction de la fraction massique en Ficoll Φ_f est tracée sur la figure 3.4 (droite) ($\circ$). On observe une nette augmentation du rayon de giration lorsque l'on augmente Φ_f. La masse apparente des objets diffusants augmente également avec la fraction de F70. L'ajout de F70 à une solution de PEG à faible concentration va donc pro-

[90] Coeur, C. L. ; Demé, B. ; Longeville, S. *Phys. Rev. E* **2009,** *79*, 031910.

voquer une séparation de phase entre le PEG et le F70 : l'augmentation de la taille apparente des polymères est due à leur agrégation. Au-delà d'une certaine concentration les solutions deviennent turbides. Comme le F70 est une polysaccharide, nous avons réalisé le même type de mesure dans des solutions en fractions massiques équivalentes en sucrose, son monomère, afin de vérifier si il n'existe pas d'interactions spécifiques entre le PEG et le Ficoll. Le R_g du PEG mesuré ne dépend pas de la fraction massique en sucrose ($\diamond$ sur la figure 3.4). La qualité du solvant n'est donc pas modifiée par la présence du sucre ; il n'existe pas d'interactions spécifiques entre le F70 et le PEG. Les interactions sont donc de type volume exclu, et le mécanisme physique à l'origine de l'agrégation est probablement similaire à la déplétion observée dans les mélanges de polymères et de colloïdes. Ce mécanisme d'agrégation, ou de séparation de phase dans des mélanges protéine-polymère, est un phénomène bien connu à l'échelle macroscopique puisqu il est largement utilisé pour la purification et la cristallisation des protéines. Depuis 1982, Hermans [92] a montré que l'origine physique était probablement le volume exclu.

Afin de déterminer l'effet de l'addition de F70 sur la conformation de notre polymère, nous devons donc nous affranchir de ce problème d'agrégation. Les spectres doivent donc être mesurés en fonction de la concentration en PEG et les résultats obtenus extrapolés à concentration nulle en chaîne Gaussiènne : $c_p = 0$, ceci pour chaque fraction massique en F70. La figure 3.5 (gauche) représente la dépendance en concentration de la masse apparente du PEG pour différentes fractions en F70 s'étalant de $\Phi_f = 0$ à $\Phi_f \simeq 0.27$. Cette masse est déduite à partir de :

$$M_a(\Phi_f) = \lim_{c_p \to 0} \frac{N_a}{c_p (\Delta\rho)^2 v_s^2} I(0) \tag{3.2}$$

On peut tirer deux informations principales de cette analyse :

1. Toutes les concentrations convergent vers la même intersection dans la limite $c_p \to 0$. La masse ainsi obtenue (18 kD) correspond à celle fournie par le fabricant du PEG. Cette observation est particulièrement importante dans le cadre de notre étude, puisque l'on peut donc affirmer que dans la limite de concentration en PEG nulle, on mesure le signal correspondant à une seule chaîne de polymère.
2. Toutes les courbes sont linéaires en fonction de la concentration en PEG, mais leurs pentes varient très fortement avec la fraction massique en F70. Cette pente est proportionnelle au second coefficient du viriel qui traduit les interactions PEG-PEG. A_2 est positif pour $\Phi_f = 0$ (pente négative) : les interactions PEG-PEG sont répulsives dans l'eau. Lorsque Φ_f augmente il devient nul et même négatif au delà de $\Phi_f = 0.1$: les interactions effectives deviennent attractives, ce qui induit l'agrégation des chaînes à fort Φ_f.

La figure 3.5 (droite) montre la dépendance du rayon de giration du PEG en fonction de la concentration c_p pour différentes fractions massiques de Ficoll de F70 Φ_f. Comme pour la figure 3.5 (gauche), on observe une claire augmentation de la taille des objets diffusants lorsque la fraction de F70 augmente. La pente des droites B_2, une quantité de nature similaire à celle du second viriel a_2, observe le même comportement passant de positif pour $\Phi \lesssim 0.1$ à négatif à plus fortes fractions en agent d'encombrement. Comme il n'existe pas d'interactions spécifiques entre le F70 et le

[91] Hermans, J. *J. Chem. Phys.* **1982,** *77*, 2193-2203.

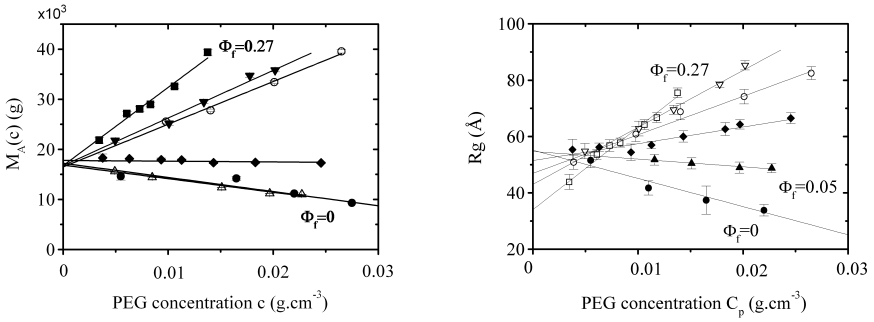

FIG. 3.5 – $M_a(c_p, \Phi_f)$ (gauche) et $R_g(c_p, \Phi_f)$ (droit) pour différentes fractions massiques en F70 s'étalant $\Phi_f = 0$ à $\Phi_f = 0.27$.

PEG, l'augmentation de la taille des objets diffusants peut probablement être reliée aux observations expérimentales [82] et prédictions théoriques [93] qui indiquent que l'encombrement cytoplasmique favoriserait l'agrégation des protéines dénaturées.

Le point particulièrement intéressant de la figure 3.5 (droite) concerne l'extrapolation à $c_p = 0$ du rayon de giration du PEG pour différents Φ_f. On observe sa très nette diminution lorsque l'on augmente la fraction massique en F70. Pour $\Phi_f = 0$ (solution PEG+eau), $R_g \simeq 57$ Å tandis qu'il est d'environ $R_g \simeq 35$ Å pour $\Phi_f \simeq 0.27$. Hors, de la figure 3.5 (gauche), nous avons conclu que l'on observe le signal d'une seule chaîne de PEG dans la limite de $c_p = 0$. Ce résultat est donc est une très claire signature expérimentale de la compression des chaînes de PEG due à l'encombrement créé par la présence de F70. La réduction du rayon de giration de la chaîne, d'un solvant sans encombrement macromoléculaire à une solution encombrée de 270 $mg.ml^{-1}$, est d'environ 30% et bien que les incertitudes expérimentales soient grandes, il semble atteindre 50% pour 330 $mg.ml^{-1}$ de F70 (cf. figure 3.6).

3.2.4 Dépendance en fonction R_g^{PEG}/R_g^{F70}

Nous avons vu dans l'introduction que le volume accessible (et par conséquent le potentiel chimique) d'une particule dans un milieu encombré, dépend très fortement des rapports entre les rayons de la molécule sonde et de l'agent d'encombrement. Ces notions sont bien définies dans la théorie de volume exclu, ainsi que leur effet sur l'équilibre des réactions chimiques ou biochimiques. Nous avons donc étendu notre étude à des PEG de masses différentes afin de comparer nos résultats expérimentaux aux prédictions théoriques. Il est également intéressant de noter qu'une étude en fonction de la masse molaire du rayon de giration d'une molécule va nous permettre d'obtenir des informations sur la conformation qu'elle va adopter ($R_g \sim M^\nu$, ν est une caractéristique d'un type de conformation).

Nous avons donc réalisé le même type de mesures sur des PEGs de masses molaires $M_w = 42.8$ kDa et $M_w = 132$ kDa [94]. A concentration en Ficoll nulle ($\Phi_f = 0$) on

[81] van der Berg, B. ; Ellis, R. J. ; Dobson, C. M. *The EMBO J.* **1999,** *18*, 6927-6933.
[92] Minton, A. *Curr. Op. in Struc. Biol.* **2000,** *10*, 34-39.
[93] Coeur, C. L. ; Teixeira, J. ; Busch, P. ; Longeville, S. *submitted* **2009,** **, **.

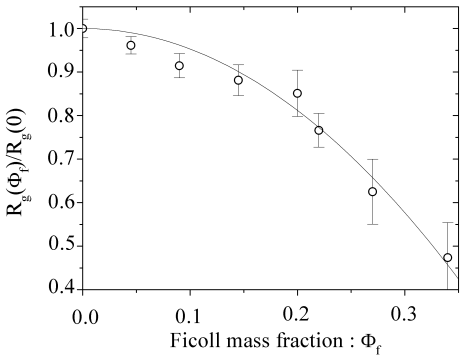

FIG. 3.6 – Evolution de $R_g(\Phi_f)/R_g(0)$ du D-PEG en fonction de la fraction massique Φ_f d'agent d'encombrement macromoléculaire (F70).

observe deux résultats caractéristiques d'une conformation de type chaîne Gaussiènne en bon solvant.

1. La figure 3.7 présente l'évolution du rayon de giration du PEG en fonction de sa masse molaire, extrapolé à concentration nulle, et en absence d'agent d'encombrement. La droite rouge, qui représente une évolution de $R_g \sim M^\nu$, avec $\nu = 0.5$, est en relativement bon accord les résultats expérimentaux.
2. La figure 3.8 de gauche présente, quant à elle, l'évolution du second coefficient du viriel pour les trois masses mesurées. A $\Phi_f = 0$, a_2 est positif et augmente en fonction du poid moléculaire ; les interactions polymère-polymère sont donc répulsives : le polymère est en bon solvant.

Dans la théorie de Flory, l'exposant critique d'une chaîne en bon solvant est $\nu = 3/5$, la répulsion monomère-monomère entraînant un léger gonflement de celle-ci. La droite en bleu sur la figure 3.7 montre l'évolution du rayon de giration du polymère avec un exposant $\nu = 3/5$. On observe une nette différence avec les résultats expérimentaux. Deux explications sont possibles, soit on se trouve en bon solvant mais comme nos mesures sont faites sur des chaînes relativement courtes, la probabilité qu'il y ait recouvrement entre les unités monomères est très faible et la chaîne adopte une conformation Gaussiènne. L'autre hypothèse est qu'à la température ambiante le PEG se trouve dans le régime θ, c'est-à-dire dans le domaine de température entre le point θ et le régime de bon solvant. Pour ce qui est l'objet de nos études, ces aspects relèvent de la sémantique et n'ont que peu d'importance, car nous cherchons avant tout à observer l'évolution d'une chaîne Gaussiènne en présence d'encombrement macromoléculaire.

Le point fondamental qui nous permet d'affirmer que l'on observe la compression d'une chaîne est que la masse apparente extrapolée à concentration nulle en polymère ($c_p \rightarrow 0$) corresponde à celle donnée par le fabricant, quelque soit la fraction massique de F70 (cf. figure 3.5 gauche pour $M_w = 18$ kDa). Pour les masses supérieures, $M_w = 42.8$ kDa et $M_w = 132$ kDa on observe également cette propriété. Dans la mesure où la variation de la masse apparente $M_a(c_p, \Phi_f)$ en fonction de la concentration en PEG, c_p, reste dans un régime linéaire, la pente de celle-ci est directement proportionnelle au second coefficient du viriel. La figure 3.8 de gauche montre l'évolution de $a_2(M_a, \Phi_f) = A_2(M_a, \Phi_f) * M_a^2$ pour les trois masses mesurées. $a_2(M_a, \Phi_f)$ a

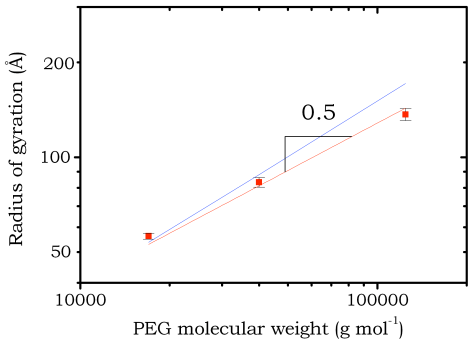

FIG. 3.7 – Evolution du rayon de giration d'une chaîne de PEG en solution diluée en l'absence d'agent d'encombrement.

la dimension d'un volume. Comme nous l'avons observé précédemment il augmente très vite à $\Phi_f = 0$, avec la masse moléculaire de la chaîne. Lorsque l'on augmente la fraction massique en agent d'encombrement $a_2(M_a, \Phi_f)$ tend vers zéro puis devient négatif, traduisant le changement de nature des interactions effectives entre chaînes qui passent de répulsives à attractives. On observe ce genre de comportement dans les polymères lorsque la qualité du solvant est modifiée, de bon à mauvais, en passant par le solvant θ : les chaînes se condensent sur elles-même ou s'agrègent en fonction de leur concentration [95, 96]. Un aspect qui semble intéressant, bien que la quantité et la qualité des données ne permettent pas de conclure sur ce point, est que pour les trois masses mesurées les interactions chaîne-chaîne semblent s'annuler pour la même concentration en F70. La dépendance du second viriel $a_2(M_a, \Phi_f)$ est d'autant plus forte que la masse moléculaire augmente, les interactions effectives deviennent beaucoup plus fortes à grandes masses M_a et le domaine de stabilité en Φ_f se réduit.

L'évolution du rayon de giration normalisé ($R_g(\Phi_f)/R_g(0)$) pour les trois masses est représentée sur la figure 3.8 de droite ($R_g(\Phi_f) = \lim_{c_p \to 0} R_g(\Phi_f, c_p)$). On observe très clairement la compression de la chaîne quelque soit la masse moléculaire, malgré le fait que les domaines de miscibilité soient réduits pour les grandes masses. Pour $\Phi_f = 0.1$, la diminution du rayon de giration est de l'ordre de 20% pour une masse de $M_w = 132$ kDa tandis qu'elle n'est que d'environ 10% et 5% respectivement pour $M_w = 18$kDa et $M_w = 42.8$ kDa. La compression s'opère donc à plus faible fraction en agent d'encombrement lorsque l'on augmente la taille de la chaîne par rapport à celle du F70.

Allen Minton [79, 80] a calculé, à partir de différents modèles, l'effet de la présence de sphères dures sur la conformation de chaînes Gaussiènnes (ou à volume exclu) et par conséquence, sur l'équilibre entre état natif et dénaturé. Dans le second pa-

[94] Daoud, M. ; Cotton, J. ; Farnoux, B. ; Jannink, G. ; Sarma, G. ; Benoit, H. ; Duplessix, R. ; Picot, C. ; de Gennes, P. G. *Macromolecules* **1975,** *8*, 804-818.
[95] Daoud, M. ; Jannink, G. *J. de Physique (Paris)* **1976,** *37*, 973-979.
[78] Minton, A. *Biophys. J.* **2000,** *78*, 101-109.
[79] Minton, A. *Biophys. J.* **2005,** *88*, 971-985.

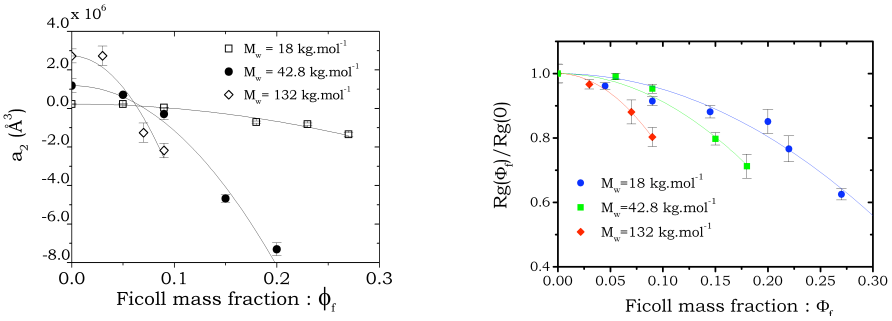

FIG. 3.8 – $a_2(c_p, \Phi_f)$ (gauche) et $R_g(c_p, \Phi_f)$ (droit) pour différentes fractions massiques en F70 s'étalant $\Phi_f = 0$ à $\Phi_f = 0.27$ pour 3 masses molaires en PEG $M_w = 18kDa$, $M_w = 42.8kDa$ et $M_w = 132kDa$.

pier [80], l'ensemble des états dénaturés est modélisé par la distribution semiempirique de Lhuillier [97]. Cette distribution, qui a été proposée à l'origine pour décrire la distribution des rayons de giration des homopolymères en bon solvant, est celle qui décrit le mieux l'ensemble des états dénaturés simulés par Goldenberg [98] . L'influence de la présence de sphères dures sur le potentiel chimique d'une chaîne est ensuite calculé en utilisant un modèle de nuage Gaussien de monomères. Les résultats de ces calculs sont présentés sur la figure 3.9, pour des chaînes de longueurs identiques à celles que nous avons mesurées. Afin de pouvoir comparer avec nos résultats, les sphères dures sont prises de sortes qu'elles aient le même rayon de giration que celui du Ficoll 70.

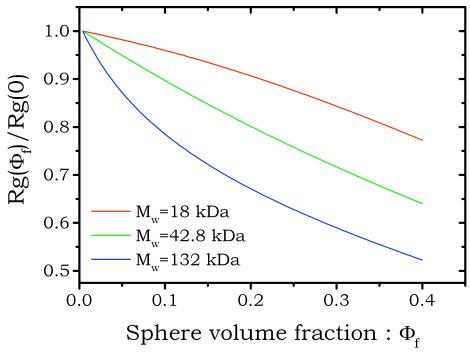

FIG. 3.9 – Calcul de l'évolution de $R_g(\Phi_f)/R_g(0)$ de chaînes à volume exclu en fonction de la fraction volumique de sphères dures, les trois différentes masses correspondent à celles mesurées expérimentalement. Les sphères ont un rayon de giration identique à celui du Ficoll.

Les courbes présentent deux propriétés similaires aux mesures expérimentales, l'ajout d'un agent d'encombrement entraîne bien la compression des chaînes et cette

[96] Lhuillier, D. *J. Phys.* **1988,** *49*, 705-710.
[97] Goldenberg, D. P. *J. Mol Biol.* **2003,** *326*, 1615-1633.

compression s'opère à plus faible fraction volumique lorsque leur taille augmente. Qualitativement l'évolution de $R_g(\Phi_f)/R_g(0)$ diffère néanmoins des résultats expérimentaux ce qui découle probablement de la relative simplicité du modèle.

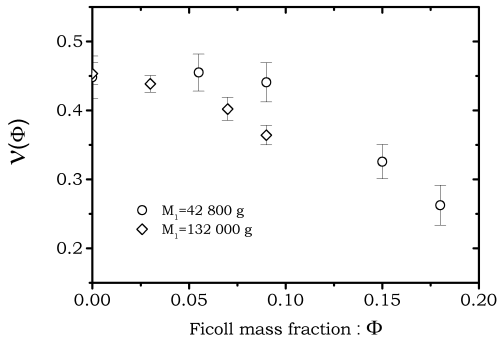

FIG. 3.10 – Rayon de Flory apparent du D-PEG pour deux masses moléculaires ($M_w = 42.8kDa$ et $M_w = 132kDa$) en fonction de la fraction massique de F70.

3.2.5 Conformation de la chaîne compressée

Nous avons vu sur la figure 3.7, que le rayon de giration de la chaîne variait en $R_g \sim M^{1/2}$. L'exposant $\nu = 0.5$ est caractéristique d'une chaîne Gaussiènne. Il serait intéressant de déterminer l'évolution de l'exposant ν en fonction de la fraction massique en agent d'encombrement, afin d'en déduire les changements éventuels de la conformation de la chaîne. Malheureusement, comme le domaine de miscibilité de la solution se restreint au fur et à mesure de l'augmentation de la taille du polymère, cette détermination ne pourrait se faire que pour les faibles concentrations en F70, Φ_f. Nous avons donc calculé l'exposant de Flory apparent pour les deux masses moléculaires les plus élevées avec, comme référence la masse $M_w = 18$ kDa, en utilisant :

$$\nu(M_1, M_2, \Phi) = ln(Rg(M_1\Phi)/Rg(M_2, \Phi))/ln(M_1/M_2) \tag{3.3}$$

La figure 3.10 présente le résultat obtenu. On distingue très nettement le passage d'un exposant proche de $\nu = 0.5$ obtenu avec $\Phi_f = 0$ vers une valeur proche de $\nu = 0.3$ à fort Φ. Cette diminution de $\nu(\Phi_f)$ s'effectue à d'autant plus faible Φ_f que la masse molaire de la chaîne augmente. $\nu = 1/3$ est caractéristique de l'augmentation de la taille d'un objet dense, ce qui semble en contradiction avec un facteur de forme de type Debye, comme nous l'observons même aux plus fortes concentrations en agent d'encombrement. Un objet présentant une interface nette avec le solvant présente une dépendance en q^{-4} du facteur de forme dans le régime des "grands angles" (tout relatif car on doit rester dans le domaine ou $1/q \gg d$, la distance entre centres diffusants). Si dans ce domaine une contribution en q^{-2} de la molécule existe elle va rapidement devenir dominante. C'est par exemple le cas pour une nanoparticule couverte de polymère. Dans notre système qui est homogène, cela signifie que la structure locale des objets va rester Gaussiènne jusqu'à une certaine taille ζ, mais que ces objets vont s'empiler

de manière compacte. La condensation ne s'observe donc pas localement, mais plutôt à relativement grande échelle.

3.3 Conclusion

Un nombre grandissant d'expériences indiquent la stabilisation des protéines dans un milieu encombré, par rapport à une solution extrêmement diluée. Des travaux théoriques récents prédisent que le mécanisme qui induit cette stabilisation est l'influence du volume exclu sur les conformations les plus étendues de l'équilibre entre état natif et dénaturé ($N \rightleftharpoons D_i$). L'effet du volume exclu est d'entraîner la compression des états dénaturés et donc de déplacer l'équilibre vers l'état natif. Dans un premier temps, notre contribution était donc d'essayer de mettre en évidence la compression d'une chaîne dans un milieu encombré, en utilisant la diffusion de neutrons aux petits angles et son puissant outils de variation de contraste. Pour des raisons de contraste entre la chaîne Gaussiènne et l'agent d'encombrement nous avons commencé l'étude sur un polymère en relativement bon solvant dans l'eau, le PEG. Comme ces mélanges ont des domaines de miscibilité très restreints, et que les chaînes s'associent très rapidement lorsque leur concentration augmente, l'étude de la conformation d'une chaîne seule doit être réalisée par extrapolation à concentration nulle en polymère. Si nous étions partis directement sur l'étude de la conformation d'une protéine deutérié, nos tâtonnements de départ auraient rendu ces mesures impossibles par manque de matériel (il est difficile de disposer de plus de 100 mg de protéine deutériée). La compression de la chaîne apparaît comme un résultat expérimental difficilement contestable puisque le rayon de giration diminue de près de 50% aux plus hautes fractions massiques en agent d'encombrement. Un aspect particulièrement intéressant, est que cette compression dépend fortement des tailles relatives entre l'agent d'encombrement et la chaîne Gaussiènne étudiée. Lorsque la taille de la chaîne augmente, la compression, ainsi que l'association chaîne-chaîne, s'opèrent à plus faible fraction Φ_f. Ce comportement est prédit par les théories de volume exclu bien que, qualitativement, théories et expériences aient des comportements légèrement différents. La condensation d'une chaîne d'homopolymère, qui résulte d'un équilibre subtil entre effets enthalpique et entropique a fait l'objet de nombreuses recherches, tant d'un point de vue théorique [99, 100] qu'expérimental [95, 101, 102, 103, 104]. Les premières observations de la condensation d'un polymère étaient obtenues en changeant la qualité du solvant, par la température ou le mélange de solvants de différentes qualités, à relativement faibles concentrations en polymère. "The better the solvent the greater the "swelling" of the molecule, conversely the poorer the solvent the smaller the molecule" [99]. Dans nos échantillons, la situation est différente, c'est le volume exclu qui entraîne la diminution du rayon de giration de la chaîne et non plus le changement de qualité du solvant. C'est pourquoi nous parlons de compression plutôt que de condensation (collapse en anglais), car le

[98] Flory, P. *Principles of polymer chemistry ;* Ithaca : Cornell Univ. Press : 1953.
[99] de Gennes, P.-G. *J. Phys. Lettre (Paris)* **1975,** *36*, L-55. L-57.
[94] Daoud, M. ; Cotton, J. ; Farnoux, B. ; Jannink, G. ; Sarma, G. ; Benoit, H. ; Duplessix, R. ; Picot, C. ; de Gennes, P. G. *Macromolecules* **1975,** *8*, 804-818.
[100] Nierlich, M. ; Cotton, J.-P. ; Farnoux, B. *J. Chem. Phys.* **1978,** *69*, 1379-1383.
[101] Cunibertie, C. ; Bianchi, U. *Polymer* **1974,** *15*, 346.
[102] Williams, C. ; Brochard, F. ; Frisch, H. L. *Ann. Rev. Phys. Chem.* **1981,** *32*, 433-451.
[103] Briber, R. M. ; Liu, X. ; Bauer, B. J. *Science* **1995,** *268*, 395-397.

mécanisme est intrinsèquement différent. La compression de la chaîne qui a été observée dans une matrice de polymères réticulés [104] est certainement plus proche de notre cas. A cause du coût entropique très élevé associé à un effondrement complet d'une chaîne d'homopolymère on ne s'attend pas à l'observer pour le cas d'un système comme le PEG. Par contre, dans des systèmes plus complexes tels que des chaînes polypeptidiques possédant des liaisons à courtes portées, telles que des liaisons hydrogènes entre les différents segments, ou des interactions hydrophobes entre les groupements non-polaires, un effondrement total pourrait être envisagé. Les gains enthalpiques pouvant compenser la perte d'entropie et stabiliser un état de globule fondu. Si nous pouvions mettre en évidence un tel effet, nous pourrions améliorer de manière significative notre compréhension de la stabilité des protéines en milieu cellulaire.

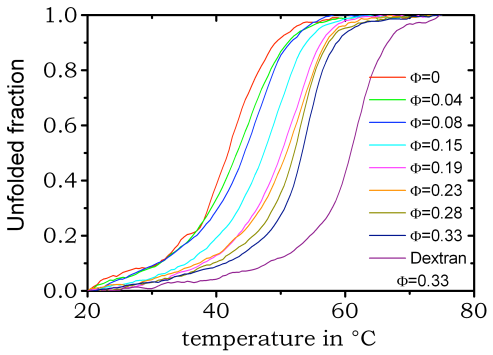

FIG. 3.11 – Courbes de dénaturation de la myoglobine en fonction de la température, obtenues en milieu dénaturant (6M d'urée) et en fonction de la fraction massique en agent d'encombrement, pour le F70, de $\Phi_f = 0$ à $\Phi_f = 0.33$, et une courbe pour le dextran à $\Phi_f = 0.33$. On observe la très nette stabilisation de la protéine lorsque Φ_f augmente.

3.4 Perspectives

L'étape suivante est naturellement l'étude de la conformation d'une chaîne polypeptidique en milieu encombré, et sa corrélation à la stabilisation de la protéine. On reste sur un modèle de cytoplasme et l'on va chercher à étudier la dénaturation d'une protéine en fonction de la fraction massique en agent d'encombrement. La figure 3.11 présente l'étude de la dénaturation de la myoglobine en fonction de la température, mesurée par dichroïsme circulaire pour différentes fractions massiques en Ficoll 70. Cette technique permet de suivre les structures secondaires de la protéine, pour la myoglobine les hélices-α. L'étude est réalisée dans un milieu fortement dénaturant, une solution de 6M d'urée. On observe une très nette stabilisation de la myoglobine lorsque l'on augmente la fraction massique d'agent d'encombrement, l'évolution de la température de dénaturation (T_u) avec Φ_f est présentée sur la figure 3.12. D'une solution de myoglobine extrêmement diluée à une fraction massique en agent d'encombrement équivalente à celle observée en milieu cellulaire, la température de dénaturation augmente de près de 12˚C.

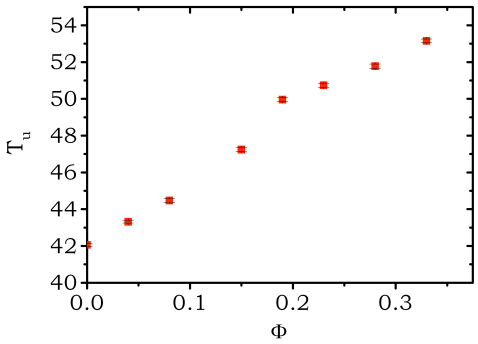

FIG. 3.12 – Evolution de la température de dénaturation de la myoglobine en fonction de la fraction massique en Ficoll70. Les études ont été réalisées en solution d'urée de 6M.

D'un point de vue expérimental, en diffusion de neutrons, l'idéal serait de disposer d'un agent d'encombrement qui soit deutérié en grande quantité. Les agents couramment utilisés sont des polysaccharides qui sont très difficiles à deutérier. Nous partons donc plutôt sur la solution d'une protéine deutériée, dont il faut disposer d'environ 150 mg. Ces études seront menées avec en parallèle une technique biologique permettant de suivre in-situ l'état de la protéine, très probablement du dichroïsme circulaire.

Au-delà des études de stabilité des protéines, la variation de contraste et donc la possibilité d'observer le signal de molécules sondes en faible quantité dans un milieu présentant un grande fraction de molécules qui ne contribuent pas au signal ouvre de nombreuses perspectives. Un aspect particulièrement intéressant, que nous avons partiellement effleuré dans ce travail, est l'agrégation des protéines. On sait que c'est un mécanisme qui est accéléré par l'encombrement cytoplasmique et qui se retrouve dans de nombreuse pathologies, notamment dans les maladies neurodégénératives du type type Creutzfeld-Jacob ou Encéphalopathies Spongiforme Bovine. L'étude de la formation des petits agrégats de protéines dénaturés par DNPA pourrait être particulièrement intéressante.

Chapitre 4

Conclusion générale

L'application de la diffusion de neutrons à l'étude des systèmes biologiques reste un art difficile et un long chemin pavé de nombreux écueils. Il s'agit d'une technique de diffusion qui permet donc d'obtenir des moyennes d'ensembles sur l'échantillon. L'analyse en énergie de la diffusion incohérente de neutrons permet d'obtenir une information sur la fonction d'autocorrélation des centres diffusants, signal largement dominé par les protons. Les premières études dans ce domaine on été réalisées par W. Doster [105, 106] qui a pu mettre en évidence que l'ensemble des protons d'une protéine opérait une transition dynamique vers 200K. Cette transition avait été mise en évidence quelques années auparavant sur le déplacement carré moyen des atomes par analyse de la diffraction des rayons-X dans un monocristal de myoglobine [107] ainsi que sur le Fer de l'hème de la myoglobine par spectroscopie Mössbauer [108, 109] . Près de 20 ans après, de nombreuses études ont montré que ce phénomène était omniprésent dans les systèmes biologiques, l'origine de cette transition reste toujours un sujet de discussions. Malheureusement de nombreuses études de la "dynamique" de ces systèmes, mesurée par diffusion incohérente de neutrons, sont réalisées par la simple séparation des contributions élastiques et inélastiques, ce qui conduit souvent à des interprétations hasardeuses et largement sujettes à caution. La diffusion cohérente doit être séparée entre statique et dynamique. En dynamique le nombre d'études est très limitée, puisque hormis nos études de la diffusion globale des protéines une méthode a été récemment développée, également par spectrométrie à écho de spin, permettant à partir de l'écart à la loi en q^2, de remonter aux mouvements des domaines de la protéine [110]. La diffusion de neutrons est également utilisée avec succès en géométrie de réflectivité pour l'étude de la dynamique de membranes biologique [111]. L'analyse de la structure de monocristaux de protéines par diffraction de neutrons est utilisée dans les cas où les rayons-X se révèlent peu efficaces, comme par exemple pour la localisation des protons dans la structure [112]. La diffusion de neutrons aux petits angles, sans

[104] Doster, W. ; Cusack, S. ; Petry, W. *Nature* **1989,** *337*, 754-756.
[105] Doster, W. ; Cusack, S. ; Petry, W. *Phys. Rev. Lett.* **1990,** *65*, 1080-1083.
[106] Frauenfelder, H. ; Petsko, G. A. ; Tsernoglou, D. *Nature* **1979,** *280*, 558-563.
[107] Keller, H. ; Debrunner, P. G. *Phys. Rev. Lett.* **1980,** *45*, 68-71.
[108] Parak, F. ; Knapp, E. W. ; Kucheida, D. *J. Mol. Biol.* **1982,** *161*, 177-194.
[109] Bu, Z. ; Biehl, R. ; Monkenbusch, M. ; Richter, D. ; Callaway, D. J. E. *Proc. Nat. Acad. Sci.* **2005,** *102*, 17646-17651.
[110] Rheinstaedter, M. C. ; Haeussler, W. ; Salditt, T. *Physical Review Letters* **2006,** *97*, 048103.
[111] Norvell, J. C. ; Nunes, A. C. ; Schoenborn, B. P. *Science* **1975,** *190*, 568-570.

être une technique prépondérante en biologie (loin s'en faut) est relativement utilisée, soit pour l'étude de molécules à faibles concentrations en utilisant le contraste avec un solvant deutérié, soit pour l'étude de complexes de protéines qui peuvent être résolus en deutérant certains éléments [113].

L'étude de l'effet de l'encombrement cytoplasmique constitue certainement un domaine où la diffusion de neutrons pourrait trouver une place non négligeable, avec sa capacité à éteindre le signal de molécules en grandes quantités. Nous restons néanmoins sur des encombrements modèles relativement éloignés de la réalité cytoplasmique avec son organisation multi-échelle. Notre champ reste donc sinon infini, de bien grande taille. Mais en se rapprochant des systèmes réels et, en ayant bien ancré à l'esprit la notion de fonction biologique, nous espérons que notre vache est un peu moins sphérique, et qu'après l'étape de modélisation indispensable à toute démarche physique nous nous rapprochons des problèmes biologiques réels.

[112] Capel, M. S. ; Engelman, D. M. ; Freeborn, B. R. ; Kjeldgaard, M. ; Langer, J. A. ; Ramakrishan, V. ; Schindler, D. G. ; Schneider, D. K. ; Schoenborn, B. P. ; Sillers, I.-Y. ; Yabuiu, S. ; Moore, P. B. *Science* **1987,** *238,* 1403-1406.

Bibliographie

[1] S. B. Zimmerman and A. P. Minton. Macromolecular crowding : Biochemical, biophysical and physiological consequences. *Ann. Rev. Biophys. Biomol. Struct.*, 22 :27–65, 1993.

[2] R. J. Ellis. Macromolecular crowding : an important but neglected aspect of the intracellular environment. *Curr. Opin. in Struc. Biol.*, 11 :114–119, 2001.

[3] R. J. Ellis and A. P. Minton. Join the crowd. *Nature*, 425 :27–28, 2003.

[4] A. P. Minton. Macromolecular crowding. *Curr. Biol.*, 16 :R269–271, 2001.

[5] D. S. Goodsell. *The machinery of life*. Springer-Verlag New York Inc., New York, 1993.

[6] A. B. Fulton. How crowded is the cytoplasm ? *Cell*, 30 :345–347, 1982.

[7] A. P. Minton. Excluded volume as a determinant of macromolecular structure and reactivity. *Biopolymers*, 20 :2093–2120, 1981.

[8] T. C. Laurent. Personal recollections. *Biophysical Biochemistry.*, 57 :7–14, 1995.

[9] A. G. Ogston. Personal recollections. *Biophysical Biochemistry.*, 57 :3–5, 1995.

[10] A. G. Ogston. The space in a uniform random suspension of fibres. *Trans. Faraday Soc.*, 54 :1754–1757, 1958.

[11] A. P. Minton. The influence of macromolecular crowding and macromolecular confinement on biochemical reactions in physiological media. *The Journal of Biological Chemistry*, 276 :10577–10580, 2001.

[12] J. L. Lebowitz, E. Helfand, and E. Praestgaard. Scaled particle theory of fluid mixtures. *The Journal of Chemical Physics*, 43 :774–779, 1965.

[13] A. P. Minton. Confinement as a determinant of macromolecular structure and reactivity. *Biophys. J.*, 63 :1090–1100, 1992.

[14] J. Lippincott-Schwartz, E. Snapp, and A. Kenworthy. Studying protein dynamics in living cells. *Nature*, 2 :444–456, 2001.

[15] R. D. Phair and T. Misteli. High mobility of proteins in the mamalian cell nucleus. *Nature*, 404 :604–609, 2000.

[16] R. Y. Tsien. The green fluorescence protein. *Annu. Rev. Biochem.*, 67 :509–544, 1998.

[17] J. A. Dix and A. S. Verkman. Crowding effects on diffusion in solutions and cells. *Annu. Rev. Biophys.*, 37 :247–263, 2008.

[18] M. Carmo-Fonseca, M. Platani, and J. R. Sweldow. Macromolecular mobility inside cell nucleus. *TRENDS in Cell Biology*, 12 :491–495, 2002.

[19] A. Einstein. Über die von der molekularkinetischen theorie der wärme geforderte bewegung von in ruhenden flüssigkeiten suspendierten teilchen. *Ann.der Physik*, 17 :549–560, 1905.

[20] J. B. Hayter and J. Penfold. An analytical struture factor for macroion solutions. *Mol. Physics*, 42 :109–118, 1981.

[21] J. P. Hansen and J. B. Hayter. A rescaled msa structure factor for dilute charged colloïdal dispersions. *Molecular Physics*, 46 :651–656, 1982.

[22] L. Belloni. Electrostatic interactions in colloïdal solutions - comparaison between primitive and one-component model. *J. Chem. Phys.*, 85 :519–526, 1986.

[23] B. N. Brockhouse. Diffusive motions in liquids and neutron scattering. *Phys. Rev. Letters*, 2 :287–289, 1959.

[24] G. D. J. Phillies. Effects of intermolecular interactions on diffusion .1. 2-component solutions. *J. Chem. Phys.*, 60 :976–982, 1974.

[25] G. D. J. Phillies. Continuum hydrodynamic interactions and diffusion. *J. Chem. Phys.*, 62 :3925–3932, 1975.

[26] R. S. Hall and C. S. Johnson. Experimental-evidence that mutual and tracer diffusion-coefficients for hemoglobin are not equal. *J. Chem. Phys.*, 72 :4251–4253, 1980.

[27] P. N. Pusey. Scaled particle theory of fluid mixtures. *J. Phys. A : Math. Nucl. Gen.*, 8 :1433–1440, 1975.

[28] B. J. Ackerson. Correlations for interacting brownian particles. *J. Chem. Phys.*, 64 :242–246, 1976.

[29] B. J. Ackerson. Correlations for interacting brownian particles .2. *J. Chem. Phys.*, 69 :684–690, 1978.

[30] C. W. J. Beenakker and P. Mazur. Self-diffusion of spheres in a concentrated suspension. *Physica*, 120A :388–410, 1983.

[31] C. W. J. Beenakker and P. Mazur. Diffusion of spheres in a concentrated suspension 2. *Physica*, 126 :349–370, 1984.

[32] M. Médina-Noyola. Long-time self-diffusion in concentrated colloidal dispersions. *Phys. Rev. Lett*, 60 :2705–2708, 1988.

[33] M. Tokuyama and I. Oppenheim. Dynamics of hard sphere suspension. *Phys. Rev. E*, 50 :R16–R19, 1994.

[34] D. S. Goodsell. Visual methods from atoms to cells. *Structure*, 13 :347–354, 2005.

[35] S. Longeville, W. Doster, and G. Kali. Myoglobin in crowded solutions : structure and diffusion. *Chem. Phys.*, 292 :413–424, 2003.

[36] S. Krueger, S.-H. Chen, J. Hofrichter, and R. Nossal. Small-angle neutron-scattering studies of hba in concentrated solutions. *Biophys. J*, 58 :745–757, 1990.

[37] F. Mezei. Neutron spin-echo - new concept in polarized thermal-neutron techniques. *Z. Physik B*, 255 :146–160, 1972.

[38] R. E. Lechner and S. Longeville. Quasielastic neutron scattering in biology part i : Methods in 'neutron scattering in biology, techniques and applications'. *Springer, Ed. J. Fitter, T. Gutberlet and J. Katsaras.*, pages 309–354, 2006.

[39] G. L. Squires. *Introduction to the theory of thermal neutron scattering*. Dover publication, Inc., 1978.

[40] F. Mezei. *Neutron scattering and collective dynamics in liquids and glasses, in Liquids, Freezing and Glass transition*. J.P. Hansen, D. Levesque and J. Zinn-Justin, eds, North Holland Pub., 1991.

[41] P. N. Pusey. *Colloidal suspensions, in Liquids, Freezing and Glass transition*. J.P. Hansen, D. Levesque and J. Zinn-Justin, eds, North Holland Pub., 1991.

[42] N. Muramatsu and A. P. Minton. Tracer diffusion of globular-proteins in concentrated protein solutions. *Proc. Natl. Acad. Sci. USA*, 85 :2984–2988, 1988.

[43] P. D. Ross and A. P. Minton. Hard quasispherical model for the viscosity of hemoglobin solutions. *Biochemical and biophysical reasearch communications*, 76 :971–976, 1977.

[44] R. Mills. Self-diffusion in normal and heavy-water in range 1-45 degrees. *J Phys. Chem.*, 77 :685–688, 1973.

[45] T. Dipple. *Ph. D. Thesis*. PhD thesis, Max Planck Institüt für Metallforschung, Institut Physik Stuttgart., 1991.

[46] D. Lavalette, C. Tetreau, M. Tourbez, and Y. Blouquit. Microscopic viscosity and rotational diffusion of proteins in a macromolecular environment. *Biophys. J.*, 76 :2744–2751, 1999.

[47] C. Le Coeur and S. Longeville. Microscopic protein diffusion at high concentration by neutron spi-echo spectroscopy. *Chem. Physics*, 345 :298–304, 2008.

[48] S. Busch, W. Doster, S. Longeville, V. Garcai-Sakai, and T. Unruh. Microscopic protein diffusion at high concentration. *Proc. of QENS 2006 Mat. Res. Soc.*, 1 :107–114, 2006.

[49] P.-G. de Gennes. Liquid dynamics and inelastic scattering of neutrons. *Physica*, 25 :825, 1959.

[50] P. N. Segrè and P. N. Pusey. Scaling of the dynamic scattering function of concentrated colloidal suspensions. *Phys. Rev. Lett.*, 77 :771–774, 1996.

[51] C. R. Jones, C. S. Johnson, and Penniston J. T. Photon correlation spectroscopy of hemoglobin - diffusion of oxy-hba and oxy-hbs. *Biopolymers*, 17 :1581–1593, 1978.

[52] S. Krueger and R. Nossal. Sans studies of interacting hemoglobin in intact erythrocytes. *Biophys. J*, 53 :97–105, 1988.

[53] W. Doster and S. Longeville. Microscopic diffusion and hydrodynamic interactions of hemoglobin in red blood cells. *Biophys. J*, 93 :1360–1368, 2007.

[54] J. D. Dwyer and V. A. Bloomfield. Brownian dynamics simulations of probe and self-diffusion in concentrated protein and dna solution. *Biophys. J*, 65 :1810–1916, 1993.

[55] F. J. W. Roughton. Diffusion and chemical reaction velocity as joint factors in determining the rate of uptake of oxygen and carbon monoxide by the red blood corpuscle. *Proc. Roy. Soc. (London), Ser. B.*, 111 :1–36, 1932.

[56] P. F. Scholander. Oxygen transport through hemoglobin solutions. *Science*, 131 :585–590, 1960.

[57] J. B. Wittenberg. Oxygen transport - a new function proposed for myoglobin. *The Biological Bulletin*, 117 :402–403, 1959.

[58] J. B. Wittenberg. Molecular mechanism of hemoglobin facilitated oxygen diffusion. *The J. of Biological Chemistry*, 241 :104–114, 1966.

[59] R. E. Collins. Transport of gases through hemoglobin solution. *Science*, 133 :1593–1594, 1961.

[60] J. Wyman. Facilitated diffusion and possible role of myoglobin as a transport mechanism. *The J. of Biological Chemistry*, 241 :115–121, 1966.

[61] V. Riveros-Moreno and J. B. Wittenberg. Self-diffsuion coefficients of myoglobin and hemoglobin in concentrated solutions. *The J. of Biological Chemistry*, 247 :895–901, 1972.

[62] Wittenberg, J. B. Wittenberg, and P. R. B. Caldwell. Role of myoglobin in oxygen supply ro red skeletal-muscle. *The J. of Biological Chemistry*, 250 :9038–9043, 1975.

[63] D. J. Livingstone, G. N. La Mar, and W. D. Brown. Myoglobin diffusion in bovine heart muscle. *Science*, 220 :71–73, 1983.

[64] K. D. Jürgens, T. Peters, and G. Gros. Disffusivity of myoglobin in intact skeletal-muscle cells. *Proc. Natl. Acad. Sci. USA*, 91 :3829–3833, 1994.

[65] K. D. Jürgens, S. Papadopoulos, T. Peters, and G. Gros. Myoglobin : Just an oxygen store or also an oxygen transporter ? *News Physiol. Sci.*, 15 :269–274, 2000.

[66] S. Papadopoulos, V. Endeward, B. Revesz-Walker, K. D. Jürgens, and G. Gros. Radial and longitudinal diffusion of myoglobin in single living heart and skeletal muscle cells. *Proc. Natl. Acad. Sci. USA*, 98 :5904–5909, 2001.

[67] P.-C. Lin, U. Kreutzer, and T. Jue. Myoglobin translational diffusion in rat myocardium and its implication on intracellular oxygen transport. *J. Physiol.*, 578.2 :414–422, 2007.

[68] D. J. Garry, G. A. Ordway, J. N. Lorenz, N. B. Radford, E. R. Chin, R. W. Grange, R. Bassel-Duby, and R. S. Williams. Mice without myoglobin. *Nature*, 395 :905–908, 1998.

[69] A Gödecke, U. Flögel, K. Zanger, Z. Ding, J. Hirchenhain, U. K. Decking, and J. Schrader. Scaled particle theory of fluid mixtures. *Proc. Natl. Acad. Sci. USA*, 96 :10495–10500, 1999.

[70] A. Clark Jr., and P. A. A. Clark W. J. Federspiel, and G. R. Cokelet. Oxygen delivery from red-cells. *Biophys. J.*, 47 :171–181, 1985.

[71] M. R. McCarthy, K. D. Vandegriff, and R. M. Winslow. The role of facilitated diffusion in oxygen transport by cell-free hemoglobins : implications for the design of hemoglobin-based oxygen carriers. *Biophys. Chem.*, 92 :103–117, 2001.

[72] C. M. Dobson, A. Sali, and M. Karplus. Protein folding : A perspective from theory and experiment. *Angewandte Chemie-international edition*, 37 :868–893, 1998.

[73] C. B. Anfinsen. Formation and stabilization of proteins structures. *Biochem J.*, 128 :737–749, 1972.

[74] A. E. Mirsky and L. Pauling. On the structure of native, denatured, and coagulated proteins. *Proc. Nat. Acad. Sci. USA*, 22 :439–447, 1936.

[75] J. C. Kendrew, G. Bodo, H. M. Dintzis, R. G. Parrish, H. Wyckoff, and D. C. Phillips. 3-dimensional model of the myoglobin molecule obtained by x-rays analysis. *Nature*, 181 :662–666, 1958.

[76] C. Levinthal. Are there pathways for protein folding ? *J. Chim. Phys. et de Physico-Chimie Biologique*, 65 :44–45, 1968.

[77] M.-J. Gething and J. Sambrook. Protein folding in the cell. *Nature*, 355 :33–45, 1992.

[78] R. J. Ellis. Molecular chaperones : Avoiding the crowd. *Curr. Biol.*, 7 :R531–R533, 1997.

[79] A. Minton. Effect of a concentrated 'inert' macromolecular cosolute on the stability of a globular protein with respect to denaturation by heat and by chaotropes : A statistical-thermodynamical model. *Biophys. J.*, 78 :101–109, 2000.

[80] A. Minton. Models for excluded volume interaction between an unfolded protein and rigid macromolecular cosolutes : Macromolecular crowding and protein stability revisited. *Biophys. J.*, 88 :971–985, 2005.

[81] D. Shortle. The denatured state (the other half of the folding equation) and its role in protein stability. *FASEB J*, 10 :27, 1996.

[82] B. van der Berg, R. J. Ellis, and C. M. Dobson. Effects of macromolecular crowding on protein folding and aggregation. *The EMBO J.*, 18 :6927–6933, 1999.

[83] N. Tokuriki, M. Kinjo, S. Negi, M. Hoshino, Y. Goto, I. Urabe, and T. Yomo. Protein folding by the effects of macromolecular crowding. *Protein science*, 13 :125–133, 2004.

[84] B.-R. Zhou, Y. Lang, F. Du, Z. Zhou, and J. Chen. Mixed macromolecular crowding accelerates the oxidative refolding of reduced, denatured lysozyme : implications for protein folding in intracellular environments. *The J. of Biol. Chem.*, 279 :55109–55116, 2004.

[85] P. McPhie, Y.-S. Ni, and A. P. Minton. Macromolecular crowding stabilizes the molten globule form of apomyoglobin with respect to bath cold and heat unfolding. *J. Mol. Biol.*, 361 :7–10, 2006.

[86] M. S. Cheung, D. Klimov, and D. Thirumalai. Molecular crowding enhances native state stability and refolding rates of globular proteins. *Proc. Nat. Acad. Science*, 102 :4753–4758, 2005.

[87] M. Perham, L. Stagg, and P. Wittung-Stafshede. Macromolecular crowding increases structural content of folded proteins. *FEBS*, 581 :5065–5069, 2007.

[88] J.-P. Cotton, B. Farnoux, and G. Jannink. Neutron diffraction in dilute and semidilute polymer solutions. *J. Chem. Phys.*, 57 :290–294, 1972.

[89] P. Debye. Molecular-weight determination by light scattering. *J. of Physical and colloid chemistry*, 51 :18–32, 1947.

[90] A. Minton. Influence of macromolecular crowding upon the stability and state of association of proteins : Predictions and observations. *J. of Pharmaceutical sciences*, 94 :1668–1675, 2005.

[91] C. Le Coeur, B. Demé, and S. Longeville. The compression of random coils due to macromolecular crowding. *Phys. Rev. E*, 79 :031910, 2009.

[92] J. Hermans. Excluded-volume theory of polymer protein interactions based on polymer-chain statistics. *J. Chem. Phys.*, 77 :2193–2203, 1982.

[93] A. Minton. Implications of macromolecular crowding for protein assembly. *Curr. Op. in Struc. Biol.*, 10 :34–39, 2000.

[94] C. Le Coeur, J. Teixeira, P. Busch, and S. Longeville. The compression of random coils due to macromolecular crowding : Scaling effects. *submitted*, ** :**, 2009.

[95] M. Daoud, J.P. Cotton, B. Farnoux, G. Jannink, G. Sarma, H. Benoit, R. Duplessix, C. Picot, and P. G. de Gennes. Solution of flexible polymers -neutron experiments and interpretation. *Macromolecules*, 8 :804–818, 1975.

[96] M. Daoud and G. Jannink. Temperature-concentration diagram of polymer-solutions. *J. de Physique (Paris)*, 37 :973–979, 1976.

[97] D. Lhuillier. A simple model for polymeric fractals in a good solvent and an improved version of the flory approximation. *J. Phys.*, 49 :705–710, 1988.

[98] D. P. Goldenberg. Computer simulation of the statistical properties of unfolded proteins. *J. Mol Biol.*, 326 :1615–1633, 2003.

[99] P. Flory. *Principles of polymer chemistry*. Ithaca : Cornell Univ. Press, 1953.

[100] P.-G. de Gennes. Collapse of a polymer chain in poor solvents. *J. Phys. Lettre (Paris)*, 36 :L–55. L–57, 1975.

[101] M. Nierlich, J.-P. Cotton, and B. Farnoux. Observation of collapse of a polymer-chain in poor solvent by small-angle neutron-scattering. *J. Chem. Phys.*, 69 :1379–1383, 1978.

[102] C. Cunibertie and U. Bianchi. Dilute-solution behavior of polymers near phase separation temperature. *Polymer*, 15 :346, 1974.

[103] C. Williams, F. Brochard, and H. L. Frisch. Polymer collapse. *Ann. Rev. Phys. Chem.*, 32 :433–451, 1981.

[104] R. M. Briber, X. Liu, and B. J. Bauer. The collapse of free polymer-chains in a network. *Science*, 268 :395–397, 1995.

[105] W. Doster, S. Cusack, and W. Petry. Dynamical transition of myoglobin revealed by inelastic scattering. *Nature*, 337 :754–756, 1989.

[106] W. Doster, S. Cusack, and W. Petry. Dynamic instability of liquidlike motions in a globular protein observed by inelastic neutron scattering. *Phys. Rev. Lett.*, 65 :1080–1083, 1990.

[107] H. Frauenfelder, G. A. Petsko, and D. Tsernoglou. Temperature-dependent x-ray diffraction as a probe of protein structural dynamics. *Nature*, 280 :558–563, 1979.

[108] H. Keller and P. G. Debrunner. Evidence for conformational and diffusional mean square displacements in frozen aquous solution of oxymyoglobin. *Phys. Rev. Lett.*, 45 :68–71, 1980.

[109] F. Parak, E. W. Knapp, and D. Kucheida. Mossbauer spectroscopy on deoxy-myoglobin. *J. Mol. Biol.*, 161 :177–194, 1982.

[110] Z. Bu, R. Biehl, M. Monkenbusch, D. Richter, and D. J. E. Callaway. Coupled protein domain motion in taq polymerase revealed by neutron spin-echo spectroscopy. *Proc. Nat. Acad. Sci.*, 102 :17646–17651, 2005.

[111] M. C. Rheinstaedter, W. Haeussler, and T. Salditt. Dispersion relation of lipid membrane shape fluctuations by neutron spin-echo spectrometry. *Physical Review Letters*, 97 :048103, 2006.

[112] J. C. Norvell, A. C. Nunes, and B. P. Schoenborn. Neutron-diffraction analysis of myoglobin -structure of cardon monoxyde derivative. *Science*, 190 :568–570, 1975.

[113] M. S. Capel, D. M. Engelman, B. R. Freeborn, M. Kjeldgaard, J. A. Langer, V. Ramakrishan, D. G. Schindler, D. K. Schneider, B. P. Schoenborn, I.-Y. Sillers, S. Yabuiu, and P. B. Moore. A complete mapping of the proteins in the small ribosomal subunit of escherichia coli. *Science*, 238 :1403–1406, 1987.

Liste de publications

Articles dans des revues à parution régulière et comité de lecture

[1] C. Le Coeur, J. Teixeira, P. Busch and S. Longeville, The Compression of Random coils due to Macromolecular Crowding : Scaling effects, *Phys. Rev. E*, **81** (2010) 061914.

[2] C. Le Coeur, B. Demé and S. Longeville, The Compression of Random coils due to Macromolecular Crowding, *Phys. Rev. E*, **79** (2009) 031910.

[3] N. Malikova, S. Longeville, J.-M. Zanotti, E. Dubois, V. Marry, P. Turq and J. Ollivier, Signature of low dimensional diffusion in complex systems, *Phys. Rev. Letters*, **101** (2008) 265901.

[4] C. Le Coeur and S. Longeville, Microscopic protein diffusion at high concentration by neutron spin-echo spectroscopy, *Chem. Phys.*, **345** (2008) 298-304.

[5] V. Marry, N. Malikova, A. Cadene, E. Dubois, S. Durand-Vidal, P. Turq, J. Breu, J.-M. Zanotti and S. Longeville, Water diffusion in a synthetic hectorite by neutron scattering - beyond the isotropic translational model, *J. of Phys :Cond. Matt.* **20** (2008) 104205.

[6] N. Malikova, A. Cadene, E. Dubois, S. Durand-Vidal, V. Marry, P. Turq, J. Breu, S. Longeville and J.-M. Zanotti, Water diffusion in a synthetic hectorite clay studied by quasi-elastic neutron scattering, *J. Phys. Chem. C*, **111** (2007) 17603-17611.

[7] W. Doster and S. Longeville, Microscopic diffusion and hydrodynamic interactions of hemoglobin in red blood cells, *Biophys. J.*, **93** (2007) 1360-1368.

[8] K. Yoshida, T. Yamaguchi, M.-C. Bellissent-Funel and S. Longeville, Hydration water in dynamics of a hydrated beta-lactoglobulin, *Eur. Phys. J :Special topics* , **141** (2007) 223-226.

[9] J. Teixeira, A. Luzar and S. Longeville, Dynamics of hydrogen bonds : how to probe their role in the unusual properties of liquid water, *J. of Phys :Cond. Matt.* **18** (2007) S2353-S2362.

[10] J. Swenson, H. Jansson, W. E. Howells, and S. Longeville, Reply to "Comment on 'Dynamics of water in a molecular sieve by quasielastic neutron scattering'" [J. Chem. Phys. 125, 077101 (2006)], *J. Chem. Phys.* **125** (2006) 077102.

[11] N. Malikova, A. Cadene, V. Marry, E. Dubois, P. Turq, J.-M. Zanotti and S. Longeville, Diffusion of water in clays - microscopic simulation and neutron scattering, *Chem. Phys.*, **317** (2005) 226-235.

[12] J. Swenson, H. Jansson, W. E. Howells, and S. Longeville, Dynamics of water in a molecular sieve by quasielastic neutron scattering, *J. Chem. Phys.* **122** (2005) 084505.

[13] J. Swenson, R. Bergman, W. E. Howells, and S. Longeville, Response to Comment on "Quasielastic neutron scattering of two-dimensional water in a vermiculite clay" [J. Chem. Phys. 113, 2873 (2000)] and "A neutron spin-echo study of confined water" [J. Chem. Phys. 115, 11299 (2001)], *J. Chem. Phys.* **121** (2004) 9195-9195.

[14] J. Ollivier, B. Rufflé, S. Longeville, P. Bourges, R. E. Lechner and B. Toudic, Central peak near the incommensurate displacive phase transition of BCPS, *Chem. Phys.*, **292** (2003) 171-183.

[15] S. Longeville, W. Doster and G. Kali., Myoglobin in crowded solutions : structure and diffusion, *Chem. Phys.*, **292** (2003) 413-424.

[16] J. Swenson, R. Bergman and S. Longeville., Experimental support for a dynamic transition of confined water, *J. non cryst solids.*, **307** (2002) 573-578.

[17] A. Faivre, C. Levelut, D. Durand, S. Longeville and G. Ehlers, Influence of the microstructure of PPO-based glass-formers on their dynamics as investigated by neutron spin echo, *J. non cryst solids.*, **307** (2002) 712-718.

[18] M. Kaisermayr, M. Rennhofer, G. Vogl, C. Pappas and S. Longeville, Neutron spin-echo spectroscopy for diffusion in crystalline solids *Phys. Rev. B*, **66** (2002) 024302.

[19] J. Swenson, R. Bergman, D. T. Bowron and S. Longeville, Water structure and dynamics in a fully hydrated sodium vermiculite clay, *Philo. Mag. B*, **82** (2002) 497-506.

[20] J. Swenson,R. Bergman, S. Longeville, A neutron spin-echo study of confined water, *J. Chem. Phys.*, **115** (2001) 11299-11305.

[21] A. Faraone, S. Magaza, R. E. Lechner, S. Longeville, G. Maisano, D. Majolino, P. Migliardo, and U. Wanderlingh, Quasielastic neutron scattering from trehalose aqueous solutions, *J. Chem. Phys.*, **115** (2001) 3281-3286.

[22] J. Swenson, R. Bergman, S. Longeville and W. S. Howels, Dynamics of 2D-water as studied by quasi-elastic neutron scattering and neutron resonance spin-echo, *Physica B*, **301** (2001) 28-34.

[23] M. Russina, F. Mezei, R. E. Lechner, S. Longeville and B. Urban, Comment on "Experimental evidence for fast heterogeneous collective stuctural relaxation in a supercooled liquid near the glass transition" - Russina et al. reply, *Phys. Rev. Lett.*, **26** (2000) 5670-5670.

[24] M-C. Bellissent-Funel, S. Longeville, J. M. Zanotti and S. H. Chen, Experimental observation of the $\alpha-$relaxation in supercooled water. *Phys. Rev. Lett.*, **85**, 2000, 3644,

[25] B. Rufflé, J. Ollivier, S. Longeville and R. E. Lechner, Neutron time-of-flight measurement techniques : new possibilities of TOF spectroscopy with NEAT at BENSC, *Nuclear Instrument and methods, Phys. Res. A*, **449**, (2000), 322.

[26] M. Russina, F. Mezei, R. Lechner, S. Longeville and B. Urban, Experimental evidence for fast heterogeneous collective structural relaxation in a supercooled liquid near the glass transition. *Phys. Rev. Lett.* , **84**, 2000, 3630.

[27] B. Rufflé, J. Ollivier, S. Longeville and R. E. Lechner, TOF diffraction experiments with NEAT at BENSC, *Physica B*, **276-278**, (2000), 170-171.

[28] S. Longeville and R. E. Lechner, Light and heavy water dynamics, *Physica B*, **276-278**, (2000), 534-535.

[29] S. Magazu, R. E. Lechner, S. Longeville, G. Maisano, D. Majolino, P. migliardo and U. Wanderlingh, Diffusive dynamics in trehalose aqueous solution by QENS, *Physica B*, **276-278**, (2000), 475-476.

[30] S. Dellerue, A. Petrescue, J. C. Smith, S. Longeville and M.-C. Bellisent-Funel, Collective dynamics of a photosynthetic protein probed by neutron spin echo spectroscopy and molecular dynamics simulation, *Physica B*, **276-278**, (2000), 514-515.

[31] J. A. Stride, U. A. Jayasooriya, N. Mbogo, R. P. White, G. J. Kearley and S. Longeville, Restricted proton mobility in the self-organizing system 3,5-dimethylpyrazole, *Physica B*, **276-278**, (2000), 308-309.

[32] M. Roepke, E. Holland-Morritz, B. Büchner, H. Berg, R.E. Lechner, S. Longeville, J. Fitter, R. Kahn, G. Coddens, and M. Ferrand, 4f-spin dynamics in $La_{2-x-y}Sr_xNd_yCuO_4$, *Phys. Rev. B* **60** (1999), 9793-9800.

[33] M. Koeppe, M. Bleuel, R. Gähler, R. Golub, P. Hank, T. Keller, S. Longeville, U. Rauch and J. Wuttke, Prospects on resonance spin-echo, *Physica B*, **266**, (1999), 75-86.

[34] A. Matic, J. Swenson, L. Börjesson, S. Longeville, R.E. Lechner, W. S. Howells, T. Akai and S. W. Martin, Ionic motion of silver in super-ionic glasses, *Physica B*, **266**, (1999), 69-74.

[35] M. Roepke, E. Holland-Morritz, R. Müller, G. Coddens, R.E. Lechner, S. Longeville and J. Fitter, Spin dynamics in the high Tc superconductor $La_{2-x-y}Sr_xNd_yCuO_4$, *J. Phys. Chem. Solids* **59**, (1998), 2233.

[36] S. Longeville, M. Bertault, J. Even and F. Moussa, Experimental evidence of strongly anisotropically correlated field induced by polymer chains in a monomer matrix *J. Phys. I France*, **7**, (1997), 1245-1258. .

[37] J. Even, M. Bertault and S. Longeville, A calorimetric Comparative study of the hydrogenated and deuterated diacetylene 2,4-hexadynylene bis (p-toluene sulfonate) : Phase transition and polymerization, *J. Polym Sci B : Polym Phys*, **35**, (1997), 789-798.

[38] S. Longeville, M. Bertault, J. Even, J. Étrillard and B. Toudic, Local properties in disordered mixed $M_{1-x}P_x$ monomer-polymer crystals : a D-NMR study, *Mol. Cryst. Liq. crystals*, **277**, (1996), 315-322.

[39] J. Even, M. Bertault, S. Longeville, A. Girard and Y. Delugeard, Ferroelectric and Antiferroelectric Phase transition in symmetrical Polymerizable diacetylene crystal, *Ferroelectrics*, **186**, (1996), 251-254.

[40] S. Longeville, M. Bertault, J. Even, J.L. Fave, A. Girard and Y. Delugeard, A Raman scattering study of the disorder induced by Polymer chains in Mixed Monomer-Polymer Crystals of diacetylene pTS-D, *Chemical Physics*,**195**, (1995) 371.

[41] J. Étrillard, J. Even, M. Sougoti, P. Launois, S. Longeville and B. Toudic, Elastic neutron scattering study of high order satellites in the incommensurate phase of the bis (4-chlorophenyl) sulphone, *Solid State Com.*,**87**, (1993), 47-51.

Articles de revue et participation à des ouvrages collectifs

[42] Quasielastic Neutron scattering in Biology Part I : Methods in "Neutron scattering in Biology, Techniques and Applications", R. E. Lechner and S. Longeville Springer, Ed. J. Fitter, T. Gutberlet and J. Katsaras. 309-354. (review article)

[43] Quasielastic Neutron scattering in Biology Part II : Applications in "Neutron scattering in Biology, Techniques and Applications", R. E. Lechner and S. Longeville Springer, Ed. J. Fitter, T. Gutberlet and J. Katsaras. 355-397. (review article)

[44] Neutron Resonance Spin Echo : Oxygen Transport in Crowded Protein Solutions, S. Longeville, W. Doster, M. Diehl, R. Gähler and W. Petry, in Neutron Spin Echo Spectroscopy, Basic trends and Applications, Lecture Notes in Physics, 325-335, vol 601, Eds F. Mezei, C. Pappas and T. Gutberlet, Springer, Berlin, 2003.

[45] Future Developments in Resonance Spin-Echo, M. Bleuel, F. Demmel, R. Gähler, K. Habicht, T. Keller, S. Klimko, I. Köper, S. Longeville and S. Prokudayo, in Neutron Spin Echo Spectroscopy, Basic trends and Applications, Lecture Notes in Physics, 176-200, vol 601, Eds F. Mezei, C. Pappas and T. Gutberlet, Springer, Berlin, 2003.

[46] La spectroscopie à écho de spin par résonance, S. Longeville, *J. Phys. IV France* **10**, (2000) 59-75, Ed. M. Bée, éditions de physique.

Encadrement

Etudiants doctorants

1. Ingo Koepper (1999-2002)
2. Clémence Le Coeur (2006-2009)

Etudiants

1. Daria Makarenko (DEA)
2. Alexandre Lourosa (DEA)
3. Alexandre Mallet (2^{nd} Année Supelec)
4. Clémentine Foulon (Master II)
5. Clémence Le Coeur (Master II KTH, 3^{me} Année Centrale Lyon)

Annexe I

PHYSICAL REVIEW E **81**, 061914 (2010)

Compression of random coils due to macromolecular crowding: Scaling effects

C. Le Coeur,[1] J. Teixeira,[1] P. Busch,[2] and S. Longeville[1]
[1]*Laboratoire Léon Brillouin, CEA-CNRS, CEA Saclay, 91191 Gif-sur-Yvette, France*
[2]*Forschungszentrum Jülich GmbH, Jülich Centre for Neutron Science (JCNS), FRM II, Lichtenbergstr. 1, 85747 Garching, Germany*
(Received 27 August 2009; revised manuscript received 5 May 2010; published 11 June 2010)

The addition of a macromolecular crowding agent to a dilute solution of polymer exerts a compressive force that tends to reduce the size of the chain. We study here the effect of changing the size ratio between the random coil and the crowding agent. The compression occurs at lower crowding agent concentration, Φ when polymer molecular weight increases. The Flory exponent $\nu(\Phi)$ decreases from $\nu(0) \simeq 0.48$ in water down to 0.3 with macromolecular crowding. The effective polymer-polymer interactions change from repulsive to strongly attractive inducing aggregation of the chains. This effect changes drastically for larger polymer sizes, being much more pronounced at high molecular weights.

DOI: 10.1103/PhysRevE.81.061914 PACS number(s): 87.15.Cc, 61.25.he, 61.05.fg

The early stages of protein folding include a rapid collapse of an unfolded coil-like polypeptide chain to a more compact molten globule state. It is commonly admitted that this collapse is driven by hydrophobic interactions between side groups of the chain and is believed to restrict the number of accessible configurations of the molecule. Even for a chain with a rather short number of residues, the number of conformations of a polypeptide chain cannot be sampled exhaustively in times of the order of seconds or less as is observed for the folding of proteins (the Levinthal paradox [1]). For a compact state a systematic exploration of the phase space can be achieved in a reasonable time to find the minimum energy configuration of the folded biologically active protein. In this view the collapse is a stage participating to solve the Levinthal paradox.

The interior of cells is a very crowded media [2,3], where although each protein is present at a rather low concentration the over all occupied volume fraction can range up to values as high as $\Phi \simeq 0.3$. The excluded volume [4] (i.e., the space physically not accessible to a molecule due to the presence of the other ones) affects a number of phenomena when compared to highly dilute concentrations. Recent theoretical works [5,6] suggested that the presence of a crowded media would modify the equilibrium between the unfolded and the folded state of the proteins. The proteins in the unfolded state (U_i) occupy an apparent volume which is larger than the compact folded state (F). Thus the more extended conformation of the unfolded state ensemble is preferentially destabilized with respect to the folded state by the excluded volume. It is predicted that these extended conformations are compressed due to macromolecular crowding. This effect induces a shift of the $U_i \rightleftharpoons F$ equilibrium to the folded state and hence a stabilization of the native protein: in this view the proteins are more stable in cells than in dilute solution. Different groups have now reported experimental evidence of protein stabilization by the presence of an inert macromolecular crowder at high concentration by using different experimental methods [7–10]. But a direct experimental evidence of the physical mechanism responsible for the stabilization remains to be shown. Neutron scattering is a unique tool for such study because it allows to measure the form factor of a small quantity of a molecule in presence of a large amount of background molecules. Using the coherent scattering length differences between hydrogen and deuterium it was originally possible to measure the form factor of a polymer chain deuterated solvent [11]. Using the same property, in a ternary mixture (solvent, test molecule and macromolecular crowder) one can match the signal of one molecule using an appropriate mixture of H_2O and D_2O (for example the crowder) and observe the signal of a test molecule, although at low concentration. With this method we were able to measure the compression of random coils due to macromolecular crowding [12]. The signal of deuterated polyethylene glycol (PEG) at low concentration was measured as a function of the mass fraction of a background macromolecule, the Ficoll 70 (F70 [13]), a heavily branched polymer of sucrose. The F70 is a molecule that is commonly used to mimic the interior of the cytoplasm because it is inert and can be diluted in water up to very high concentrations (up to a mass fraction of $\Phi \simeq 0.4$). Due to the tendency of the PEG to aggregate at high concentration of F70 the results were obtained by extrapolation to zero PEG concentration where only the signal of one chain was observed [12]. The compression of a chain of radius similar to the F70 was observed to be as high as 50% at Ficoll mass fraction of $\simeq 0.35$. In this paper, we report the compression of the chain as a function of its mass in order to compare with the prediction of crowding theories and to try to get further information on the conformation of the compressed chain.

In our previous study [12], F70 was used as crowding agent: it is highly ramified nonionic synthetic polymer of sucrose, with an almost spherical shape and a radius of gyration $R_g^{F70} \simeq 50$ Å. Poly(ethylene glycol) (PEG) was used as a model of random coil. The first measurements were performed on a deuterated PEG of weight-average molecular weight $M_w = 18$ kDa, purchased from *polymer source*, having a radius of gyration in dilute solution of $R_g \simeq 52$ Å. To study the effect of the ratio between the radii of gyration of the crowder and of the polymer we extended the measurements to PEGs of molecular weights $M_w = 42.8$ kDa and $M_w = 132$ kDa, keeping F70 as a macromolecular crowder. In order to mimic the volume fraction occupied *in vivo* we added F70 to the highest possible volume fractions before phase separation was observed.

The neutron scattering experiments were performed on

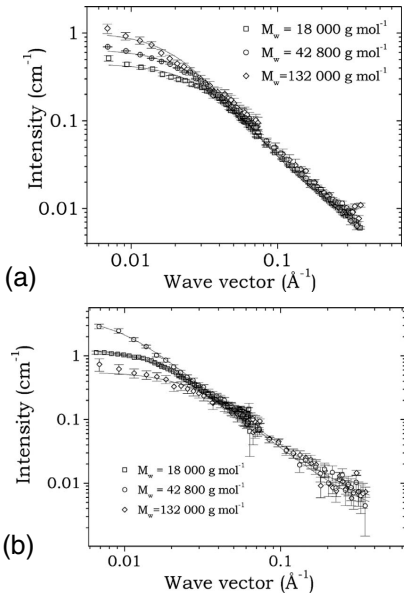

FIG. 1. Spectra measured on KWS-2 for three different polymer molecular weights: 18, 42.8, and 132 kD without Ficoll (upper graph) and with a mass fraction of Ficoll of $\Phi \simeq 0.15$ (lower graph). The solvent scattering length density is matched to the F70 signal (see text).

the small-angle neutron scattering (SANS) spectrometer KWS-2 of the Jülich Centre for Neutron Science at FRM II (Germany), and on the SANS spectrometer PACE of the Laboratoire Léon Brillouin (France).

The matching point of F70 corresponds to a mixture of D_2O and H_2O solution with a D_2O mole fraction $x \sim 0.41$. Mixtures of PEG and F70 have a tendency to segregate at rather low PEG concentration especially for high mass fractions of F70. Thus, as we reported in [12], we measured different concentrations c_p of PEG per F70 mass fraction and extrapolated the data to zero PEG concentration.

Typical spectra obtained on KWS-2 are presented on Fig. 1 for the 3 PEG with different molecular weights without crowding agent and at F70 mass fractions of $\Phi \simeq 0.15$. The spectra were fitted using

$$I(q) = \frac{c_p(\Delta\rho)^2 v_s^2}{N_A} M_a(\Phi) P(q)[1 - 2M_a(\Phi)c_p A_2(M_a,\Phi)] \tag{1}$$

$\Delta\rho$ is the neutron scattering length density contrast between the deuterated PEG and the solvent, N_A is the Avogadro number, $P(q) = \frac{2}{x^2}(x - 1 + e^{-x})$ is the molecular form factor of a Gaussian chain [14] with $x = (qR_g)^2$. A_2 is the second virial coefficient and $M_a(\Phi)$ is the concentration dependent molar mass. We obtain the mass of the polymer

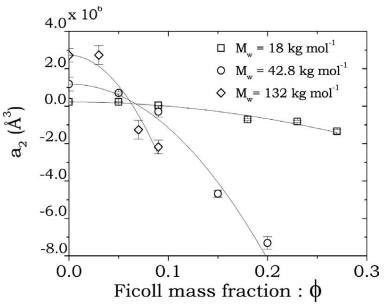

FIG. 2. Apparent second virial coefficient $a_2(M_a,\Phi)$ obtained from the slope of the forward intensity as a function of the Ficoll mass fraction Φ. The dependence is presented for the three different molecular weights of PEG.

$M_a(\Phi=0)$ by extrapolation to zero PEG concentration. v_s is the specific volume of the monomer. The molecular weight dependence of the radius of gyration extrapolated to zero PEG concentration in water ($\Phi=0$) follows a scaling law $R_g[M_a(\Phi=0)] \sim M_a^{\nu}(\Phi=0)$ with $\nu=0.48$, which is close to the theoretical value for a Gaussian chain. This result supports the random coil structure of the PEG in water for this range of molecular weights.

As reported in [12] for the 18 kDa PEG, the extrapolations of apparent masses $M_a(\Phi)$ to zero PEG concentration ($c_p=0$) converge, for all F70 mass fractions, to the values which are given by the D-PEG supplier. This behavior was also observed for the different polymer weights of $M_w = 42.8$ and $M_w = 132$ kDa, and is a sound signature that by extrapolation to zero PEG concentration ($c_p \to 0$) we do capture the conformation of a single chain.

The evolution of the apparent molecular mass as a function of the polymer concentration c_p can be described by a virial expansion. As far as it remains in the linear regime, the slope of $M_a(c_p,\Phi)$ as a function of c_p is proportional to the second virial coefficient which is a direct measure of the excluded volume between pairs of chains. The F70 mass fraction dependence of the virial coefficients $a_2(M_a,\Phi) = A_2(M_a,\Phi) * M_a^2$ is presented on Fig. 2 for the three polymer molecular weights studied (we preferred the representation of a_2 rather than A_2 because a_2 has the dimension of a volume). In the absence of F70, $a_2(M_a,0)$ is positive, the PEG-PEG interactions are repulsive, the chains strongly repeal and do not interpenetrate each other. This is characteristic of a polymer in a good solvent. $a_2(M_a,0)$ strongly depends on M_a and is of the order of the volume occupied by the chain, but due to the limited number of molecular weights we did not investigate further this point. When increasing the F70 mass fraction, the second virial coefficients tend to zero and become negative for the three molecular weights. Such a behavior is usually observed in polymers when the quality of the solvent is changed, and the chains either collapse or aggregate, mainly depending on their concentration [15,16]. Our system is a ternary system, and the interactions measured by pairs of polymer are modified by the presence of the

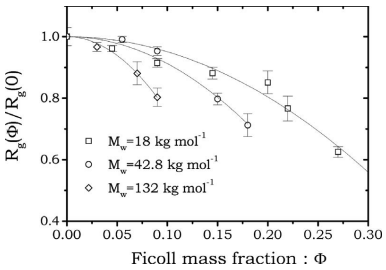

FIG. 3. Ficoll fraction dependence of the radius of gyration of the D-PEG normalized to its value at $\Phi=0$ for the three different molecular weights.

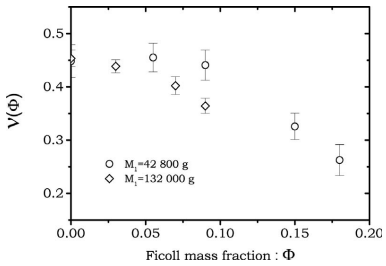

FIG. 4. Apparent Flory exponent $\nu(\Phi)$ of the D-PEG as a function of the mass fraction Φ of the macromolecular crowding agent (F70) (see text).

F70. $a_2(M_a,\Phi)$ tends to zero at rather low F70 mass fraction, around 5–6 % and interestingly this fraction seems to be independent of the polymer molecular weight, although we must remain cautious on this point due to experimental uncertainties and the limited number of molecular weights studied. The F70 mass fraction dependence of the second virial coefficient depends very strongly on the polymer molecular weights, meaning that the aggregation of the polymer strongly increases with increasing the chain length. This is the reason why from $M_w=18$ to $M_w=132$ kDa the stability of the solution strongly decreases, and beyond these values the solution is turbid.

As reported in [12], the Φ dependence of the radius of gyration of the chains was obtained by extrapolation to zero PEG concentration $[R_g(\Phi)=\lim_{c_p\to 0} R_g(\Phi,c_p)]$. The evolution of the normalized radii of gyration $R_g(\Phi)/R_g(0)$ as a function of the F70 mass fraction for the three molecular weights of PEG is shown on Fig. 3. The compression of the chain is clearly observed whatever the polymer weights, but again due to aggregation of the PEGs, $R_g(\Phi)/R_g(0)$ was measured in a limited F70 range for the higher masses. Nevertheless a diminution of the radius of gyration R_g of 20% and 30% were, respectively, observed for the 42.8 and 132 kDa, respectively, at $\Phi\sim 0.1$ and $\Phi\sim 0.18$. The compression occurs thus at smaller crowder fraction when increasing the molecular weights of PEG, which is the relative size of the coil as compared to that of F70.

Whatever the molecular mass up to 132 kDa the PEG adopt a random coil conformation in water as it can be seen by both the form factor and the molecular weight dependence of the radius of gyration. From the repulsion of the chain we can deduce that water is a good solvent for PEG at room temperature. In this case the exponent ν should be closer to $\nu=0.588$ rather than $\nu=0.5$, the difference probably arises from both the rather limited range of chain lengths and the uncertainty of the data. When we add in the solution a cosolute like the F70, we observe a clear compression of the chains, with a very significant decrease of the radius of gyration. The evolution of $R_g(\Phi)/R_g(0)$ depends on the ratio between the molecular weights (i.e., the respective size) of the F70, used as a simple model for a sphere, and the PEG that takes a random coil conformation. What is the change of conformation due to the presence of the macromolecular crowder and what can we learn from the molecular weight dependence? Figure 4 depicts the apparent Flory exponent $\nu(\Phi)$ between two molecular weights which is obtained by $\nu(M_1,M_2,\Phi)=ln[R_g(M_1\Phi)/R_g(M_2,\Phi)]/ln(M_1/M_2)$ as a function of Φ. From an experimental point of view it is rather difficult to measure different molecular weights at the same Ficoll fraction, therefore we used the refined values for the first weight (18 kDa) to compute the exponent for the other masses. The value of 0.3 is close to the one observed when increasing the size of a compact object. This behavior seems to be contradicted by the form factors because the intensity still decays as q^{-2} at high wave vectors and thus is not compatible to either a sphere of at least a compact shape. If the chains were totally collapsed, the respective radius of gyration for the PEGs with $M_w=18$, 42.8 and 132 kDa would be 14.1, 18.8, and 27.5 Å which is far from the values measured at the highest F70 mass fractions respectively 26.6, 60.7 and 109 Å. The shape of the objects still remains quite open. The picture that emerges is that, up to a certain size ζ, the polymer adopts a random coil structure and, at high F70 fraction, the compressed polymer is formed by a compact addition of these objects. The compression of the chain occurs over long distances. This picture is similar to a compact addition of thermal blobs although the nature of our objects probably differs because of the size of the blobs. Notice that a value of ν smaller than 0.3 can be obtained when increasing the size and changing the conformation simultaneously.

The decrease of the radius of gyration of a polymer in a good solvent when increasing concentration is fairly well understood; theoretical approaches have led to the prediction that it scales with $c^{-1/8}$ in the semidilute regime and this dependence was experimentally supported by small-angle neutron scattering measurements [15,17]. The same behavior was observed in a polymer mixture; the radius of a host polymer decreases when increasing the concentration of guest one [18]. In both cases the changes in the radius of gyration are due to unfavorable interaction between unlike monomers either from the same [15,17] or from a different polymer [18]. The compression we observe here, due to macromolecular crowding, is fundamentally different from the polymer collapse because, in our case, the quality of the solvent is not changed. This was verified by the absence of conformational change of the PEGs in the presence of simi-

lar fractions of the F70 monomer, the sucrose. No significant change neither in the form factor nor in the radius of gyration is observed up to mass fraction of $\Phi \sim 0.4$ [12]. The F70-PEG interactions are neither favorable nor unfavorable.

The theories developed to study the influence of macromolecular crowding on protein stability, calculate the change in the chemical potential due to macromolecular crowding using the scaled particle theory. From the respective changes between the chemical potential of the native state and the unfolded state ensemble it is possible to calculate the change in equilibrium of the $U_i \rightleftharpoons F$ reaction, and consequently get information on protein stability in cells [5,6]. The signature of the stabilization is the compression of the unfolded state ensemble which is modeled by random coil-like structure with a distribution of the radius of gyration. We calculated the effect of a given volume fraction of added hard spheres on the mean radius of gyration of the distribution [6] and found that the radius of gyration strongly decreases as a function of the volume fraction of added hard spheres, with an order of magnitude similar to that we measured. Moreover this effect strongly depends on the size of the chain that is compressed as we observed experimentally.

Early stages of protein folding [19,20] include the collapse of an unfolded polypeptide coil into a more compact molten globule state. The introduction of excluded volume effects to the equilibrium ($U_i \rightleftharpoons F$) between the native state and the unfolded state ensemble leads theoretically to the stabilization of proteins, which was observed experimentally by [21] and others [7–10]. In this paper we reported observation of Gaussian chain compression and scaling effects that support the theoretical prediction of excluded volume effect [5,6].

[1] C. Levinthal, J. Chim. Phys. **65**, 44 (1968).
[2] S. B. Zimmerman and A. P. Minton, Annu. Rev. Biophys. Biomol. Struct. **22**, 27 (1993).
[3] R. John Ellis, Curr. Opin. Struct. Biol. **11**, 114 (2001).
[4] A. P. Minton, Biopolymers **20**, 2093 (1981).
[5] A. P. Minton, Biophys. J. **78**, 101 (2000).
[6] A. P. Minton, Biophys. J. **88**, 971 (2005).
[7] B. van den Berg, R. J. Ellis, and C. M. Dobson, EMBO J. **18**, 6927 (1999).
[8] N. Tokuriki, M. Kinjo, S. Negi, M. Hoshino, Y. Goto, I. Urabe, and T. Yomo, Protein Sci. **13**, 125 (2004).
[9] B.-R. Zhou, Y. Lang, F. Du, Z. Zhou, and J. Chen, J. Biol. Chem. **279**, 55109 (2004).
[10] P. McPhie, Y.-S. Ni, and A. P. Minton, J. Mol. Biol. **361**, 7 (2006).
[11] J.-P. Cotton, B. Farnoux, and G. Jannink, J. Chem. Phys. **57**, 290 (1972).
[12] C. Le Coeur, B. Demé, and S. Longeville, Phys. Rev. E **79**, 031910 (2009).
[13] F70 is a trademark of Pharmacia Inc.
[14] P. Debye, J. Appl. Phys. **15**, 338 (1944).
[15] M. Daoud, J.-P. Cotton, B. Farnoux, G. Jannink, G. Sarma, H. Benoit, R. Duplessix, C. Picot, and P. G. de Gennes, Macromolecules **8**, 804 (1975).
[16] M. Daoud and G. Jannick, J. Phys. (Paris) **37**, 973–979 (1976).
[17] J. S. King, W. Boyer, G. D. Wignall, and R. Ullman, Macromolecules **18**, 709 (1985).
[18] M. S. Kent, M. Tirrel, and T. P. Lodge, Polymer **32**, 314 (1991).
[19] C. M. Dobson, Nature (London) **426**, 884 (2003).
[20] H. S. Chan and K. A. Dill, Phys. Today **46**, 24 (1993).
[21] B. L. Steadman, P. A. Trautman, E. Q. Lawson, M. J. Raymond, D. A. Mood, J. A. Thomson, and C. R. Middaugh, Biochemistry **28**, 9653 (1989).

PHYSICAL REVIEW E **79**, 031910 (2009)

Compression of random coils due to macromolecular crowding

C. Le Coeur,[1] B. Demé,[2] and S. Longeville[1]
[1]*Laboratoire Léon Brillouin, CEA-CNRS, CEA Saclay, 91191 Gif-sur-Yvette, France*
[2]*Institut Laue–Langevin, 6 rue Jules Horowitz, BP 156-38042, Grenoble Cedex 9, France*
(Received 29 April 2008; published 20 March 2009)

The conformation of a linear polymer chain is studied as a function of the concentration of a macromolecular crowding agent by neutron scattering. Excluded volume to random coil due to macromolecular crowding in cells is predicted to exert a compressive force that will tend to reduce its size. It is shown that when reducing free volume due to macromolecular crowding, we observe a compression of the polymer chain with a reduction in its radius of gyration of up to $\simeq$30% and that the effective chain-chain interactions are strongly modified.

DOI: 10.1103/PhysRevE.79.031910 PACS number(s): 87.15.Cc, 61.25.he, 61.05.fg

I. INTRODUCTION

The interior of the cells is filled with a very high quantity of space-filling macromolecules with very different sizes and shapes. Generally the concentration of each species is rather low, but the overall occupied volume fraction can range up to 0.3; the cellular environment is highly packed. The excluded volume due to this macromolecular crowding affects a number of phenomena of biological importance. Although the first quantitative theory was developed in the early 1980s [1], real effort to quantify the effect of macromolecular crowding of the cytoplasm on various processes was developed only during the last 10 years [2–4].

Theoretical works [5,6] predicted that excluded-volume interactions in cells [4,7] could significantly influence protein stability. Model calculations suggest that macromolecular crowding stabilizes the native state of proteins relative to unfolded states. The excluded volume to a polypeptide chain by high concentrations of rigid macromolecule would be expected to exert a compressive force reducing its average dimension. The more extended conformations of the unfolded chain ensemble are predicted to be preferentially destabilized relative to more compact conformations, including the native state. The equilibrium ($N \rightleftharpoons S_i$) between the native (N) and the unfolded states ensemble (S_i) of proteins is thus shifted toward the native state. The calculations were performed on a model system of hard spheres (to account for crowding effects of the cytoplasm) and the unfolded states of the protein were assumed to adopt random coil conformations [8]. The validity of this assumption is supported by diffraction studies on unfolded protein conformation. At sufficiently high chemical denaturant concentration, it was shown that the unfolded state of a protein adopts a Gaussian-type conformation [9].

Experimental studies to verify whether proteins are stabilized by excluded-volume effects were performed on test macromolecules in presence of polysaccharides such as Ficoll 70 of Dextran to mimic the crowding of the cytoplasm. Protein activities [10] or circular dichroism [11,12] was measured in denaturing solvent conditions as a function of the volume fraction of cosolute molecules to check change in the $N \rightleftharpoons S_i$ equilibrium. These results tend to confirm, at least qualitatively, the prediction of Minton [5,6]. It was also demonstrated that temperature has a little impact on the stabilization effect due to crowding; heat and cold denaturation are suppressed in the presence of crowded environment [13]. Numerical simulations also confirm the theoretical predictions [14]. A recent experimental study on the effect of macromolecular crowding on native protein seems to show that excluded volume increases the structural content of folded proteins [15]. To our knowledge there was no direct evidence of the changes in Gaussian chain conformation due to the presence of macromolecular crowder, by scattering techniques, which could help to understand the physical mechanism inducing stabilization.

The conformations of polymer chains are studied by scattering methods. Small-angle neutron scattering (SANS) is especially suited to study polymer conformations in polymer blends or mixtures because of the strong ability of neutron to discriminate between hydrogenated and deuterated isotopes [16]. Using isotope contrast one can look at the conformation of a single marked chain in a polymer bulk or mixture. Scattering methods tell us the size of polymer coils. Polymer conformation is refined by simple Gaussian chain models whose approximate form factor was computed by Debye [17] in the absence of any excluded-volume effects. The experimental studies range from chemically identical polymers to multicomponent polymer mixtures. Generally, chemically different polymers are not miscible, although some homogeneous mixtures were reported. To overcome this problem and more generally the effects of interactions, measurements of marked chains at very low concentrations are performed and the single-chain parameters are determined by extrapolation to zero concentration. Using Debye-type form factors one can obtain the radius of gyration R_g of the polymer, its average mass weight M, and the second virial coefficient which provides information on intermolecular interactions.

In this paper, we report a study by SANS of the conformation of a Gaussian chain as a function of the weight fraction of a macromolecular crowding agent, with the attempt to figure out the conformational changes induced by increasing concentration of the latter. In particular, we want to verify whether significant diminution of the radius of gyration of the Gaussian chain is observed as was theoretically predicted [6]. As a first step, we choose polymer and crowding agent with similar radii of gyration.

II. MATERIAL AND METHODS

A. Sample preparation

Our model system is constituted of deuterated poly(ethylene glycol) [D-PEG (for deuterated), the Gaussian chain which will be referred to as polymer in the text] and an almost spherical molecule: Ficoll 70® (F70), which will be referred to as the crowding agent. The osmotic pressure of a Ficoll solution with $\Phi_f \simeq 0.3$ is around 3×10^5 Pa. The weight-averaged molecular weight of the PEG was $M_w = 18\,000$ Da with $M_w/M_n = 1.05$ provided by Polymer Source Inc. The F70 is a highly ramified polysaccharide with molecular weight of 70 kDa and was purchased from Sigma [18]. F70 is highly soluble in water, where it can be dissolved up to concentrations of more than 450 mg ml^{-1}. In our measurements, the F70 fraction weights range from $\Phi_f = 0$ up to more than $\Phi_f \simeq 0.4$ to simulate the macromolecular crowding of the cytoplasm.

B. Neutron-scattering experiments

The neutron-scattering experiments were carried out on the SANS instrument PACE at the Laboratoire Léon Brillouin (France) and D22 at the Institut Laue-Langevin (France) at room temperature. Both instruments were used to cover the full wave-vector range necessary for the experiments. The very high neutron flux available on D22 is a strong advantage for getting high statistical accuracy due to the reduced contrast between the solvent and the PEG (due to F70 matching) and the necessity to extrapolate to zero PEG concentration.

Due to the coherent-scattering length differences between hydrogen and deuterium, the neutron-scattering length density differences between fully hydrogenated F70 and the deuterated polymers are very significant. It is thus possible to match the solvent $[xD_2O + (1-x)H_2O]$ and F70 scattering length densities (for $x \simeq 0.41$) and keep a significant contrast between the solvent and the D-PEG. Under such conditions only the PEG contribution appears as a wave-vector-dependent intensity in the spectra whatever the F70 concentration is. For each F70 weight fraction different D-PEG concentrations were studied in order to trace Zimm-type plots (from a few mg ml^{-1} to few tens of mg ml^{-1} of D-PEG). It is then possible to follow the conformational changes in the D-PEG induced by changes in F70 concentration. The polymer concentrations are chosen to remain far from the overlap concentration.

III. EXPERIMENTAL RESULTS

The spectra were refined using

$$I(q) = \frac{c_p(\Delta\rho)^2}{N_A v_s^2} M_a(c_p, \Phi_f) P(q)(1 + 2M_a c_p A_2). \qquad (1)$$

$\Delta\rho$ is the neutron-scattering length density contrast between the deuterated PEG and the solvent, N_A is the Avogadro number, and $P(q) = \frac{2}{x^2}(x - 1 + e^{-x})$ is the molecular form factor of a Gaussian chain, with $x = (qR_g)^2$. A_2 is the second virial coefficient and $M_a(c_p, \Phi_f)$ is the concentration-dependent molar mass. We obtain the mass of the polymer, M_a, by extrapolation to zero concentration $M_a(c_p \to 0, \Phi)$. v_s is the specific volume of the macromolecule. Figure 1 shows the measured spectra for the two different F70 mass fractions $\Phi_f = 0$ and $\Phi_f = 0.3$ on D22 after standard corrections and background subtraction. The lines are the results of refinement of the spectra by a Gaussian chain form factor.

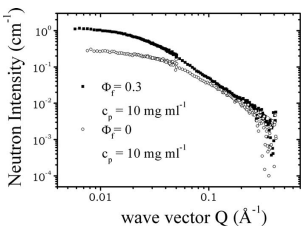

FIG. 1. D-PEG spectra measured on D22 at concentration $c_p = 10$ mg ml^{-1} for two different F70 mass fractions (0 and 0.3). The solvent scattering length density is matched to the F70: only the PEG appears as a wave-vector-dependent intensity.

Figure 2 is a plot of the PEG radius of gyration measured for a concentration of $c_p \simeq 10$ mg ml^{-1} as a function of the Ficoll mass fraction Φ_f (open circle). One can clearly observe an increase in the radius of gyration of the scattering objects with increasing Φ_f, which reflects the tendency to aggregation. Above a given F70 fraction, which depends on the PEG concentration, the solution even becomes turbid. The F70 is a polysaccharide of sucrose. In order to verify if specific interaction occurs between the PEG and the monomer, we measured spectra with equivalent mass fraction of sucrose (open diamond). The radius of gyration of the polymer in the presence of sucrose at almost the same mass fraction is also shown in Fig. 2. The conformation of the polymer is not modified by the presence of the sucrose, and R_g is almost equal to the one measured at $\Phi_f = 0$ whatever Φ_f is. This observation supports the fact that the quality of the solvent is not significantly modified by the presence of the F70 monomer. Thus no preferential interactions occur between the monomer of the PEG and the sucrose. We interpret this feature as an indication that the PEG-F70 interactions are mainly steric (crowding effects).

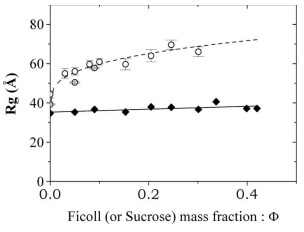

FIG. 2. R_g of the D-PEG at concentration $c_p = 10$ mg ml^{-1} as a function of Φ, the mass fraction of macromolecular crowding agent added. ◇: sucrose, $\Phi = \Phi_s$; ○: F70, $\Phi = \Phi_f$.

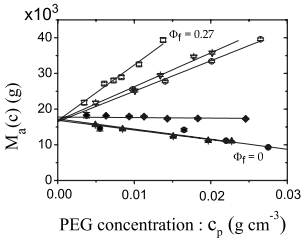

FIG. 3. $M_a(c_p)$ for different Φ_f ranging from Φ_f=0 to Φ_f =0.27.

To determine the effect of the presence of F70 at high mass fraction, we have to overcome the tendency to clustering or aggregation. This implies the necessity to extrapolate the effect of increasing Φ_f to zero PEG concentration. Figure 3 presents the PEG concentration-dependent apparent molecular mass deduced from zero wave-vector intensity:

$$M_a(c_p) = \frac{N_A v_s^2}{c_p(\Delta\rho)^2} I(q \to 0, c_p). \quad (2)$$

These results are presented as a function of the PEG concentration c_p for different mass fractions Φ_f of F70, ranging from Φ_f=0 (full circle) to Φ_f=0.27. The six concentrations converge to the same intercept at zero PEG concentration which corresponds to the mass of the polymer given by the provider. This feature is particularly interesting for our purpose because it means that by extrapolation to zero PEG concentration, the molecular form factor of a single chain can be obtained whatever the F70 concentration is. The PEG mass concentration dependence $[M(c_p)]$ exhibits a linear behavior as a function of c_p whatever the F70 concentration is, and the slopes are very strongly dependent on Φ_f. These slopes are proportional to the second virial coefficient A_2. When $\Phi_f \to 0$, A_2 is positive, which states the small repulsive interaction between PEG chains. The transition, when Φ_f increases, to a negative value of the pseudo-second-virial term A_2 reflects the tendency of PEG chains to associate, which is fully consistent with the plot in Fig. 2. When increasing Φ_f, the PEG concentration at which the spectra significantly differ from Gaussian-chain-like form factors diminishes. This reflects the fact that when increasing Φ_f the aggregation occurs at smaller c_p.

Figure 4 shows the dependence of the R_g deduced from the Debye formula as a function of the PEG concentration c_p for different F70 mass fractions Φ_f. As with Fig. 3, the clear tendency to clustering is observed when increasing F70 concentration, but this time with the strong increase in the radius of gyration of the scattering objects. The slope changes from negative value for $\Phi_f < 0.1$ up to strongly positive ones for $\Phi_f \simeq 0.3$. This slope is proportional to B_2, a quantity which is similar in nature to the second virial coefficient of the osmotic pressure and reflects molecular interactions. This observation can be related to the previous experimental observation [10] and theoretical predictions [19] that macromolecular crowding increases the unfolded protein aggregation. No specific interactions occur between the F70 and the PEG chains. Thus the changes in the second virial coefficient from small positive to large negative value reflect this tendency of clustering simply due to macromolecular crowding.

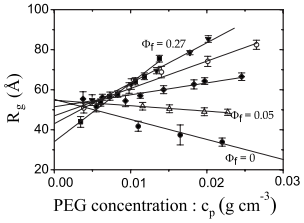

FIG. 4. Concentration dependence of the radius of gyration of the D-PEG for different F70 mass fractions.

The particularly interesting point here concerns the extrapolation of the radius of gyration to c_p=0 for different Φ_f (Fig. 5). It clearly diminishes when F70 concentration Φ_f increases. For Φ_f=0 (only the PEG is in solution) R_g $\simeq$57 Å, whereas it reduces to $R_g \simeq 35$ Å for $\Phi_f \simeq 0.27$. This result, together with the conclusion for Fig. 3 that only one polymer chain contributes to the signal at zero PEG concentration, is a clear experimental observation of the compression of the chain due to the presence of macromolecular crowding. The R_g reduction of the polymer chain from a solvent without any macromolecular crowding to a solution of 270 mg ml^{-1} is nearly 30%, although experimental uncertainties become significant when the reduction reaches 50% for 330 mg ml^{-1} of F70.

IV. DISCUSSION

Direct comparison to the theoretical predictions [5,6] is not straightforward for various reasons. First the F70 does certainly not behave as a hard sphere. Although it is much more compact than a Gaussian chain, its radius of gyration is the same as the one of the PEG with an average weight of 70 kDa, whereas the latter is only 18 kDa. The molecular form factor of F70 $[F(q)]$ measured in D_2O at almost the same

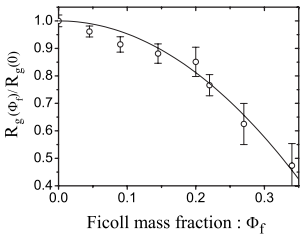

FIG. 5. $R_g(\Phi)/R_g(0)$ of the D-PEG as a function of the mass fraction Φ_f of the macromolecular crowding agent (F70).

concentration as the PEG does not fit to the hard-sphere one. At high q the slope of $F(q)$ is closer to q^{-2} (Gaussian chain) than q^{-4} predicted for hard sphere. However such decay at high q of the form factor can be quite easily reproduced with a hard-sphere core decorated with some polymers on its surface or with random-walk polymer confined in a sphere [20]. Thus the true F70 potential is certainly not a hard-sphere one but softer than that. Nevertheless the results of the computation of Minton [5,6] for different unfolded proteins predict a reduction in the R_g of nearly 30% due to macromolecular crowding, which is comparable to our results obtained for homopolymers.

Homopolymer collapse, as a result of a delicate balance between enthalpic and entropic effects, was a subject of intense research activity over the past, both theoretically [21,22] and experimentally [23–26]. The first observations of the collapse were driven by the solvent quality, by change in temperature, or by mixture of solvent of different qualities at rather low polymer concentration. "The better the solvent the greater the 'swelling' of the molecule; conversely the poorer the solvent the smaller the molecule" [21]. Later the compression of a polymer chain was observed in a matrix of cross-linked polymers [26] by neutron scattering. In our experiments the situation is different because the solvent quality is not modified; therefore we speak of compression of the chain rather than collapse, the mechanism of which is basically different [27]. Because of the large loss of configurational entropy associated with total collapse and monomer-excluded interactions, volume exclusion is not predicted to induce collapse of simple polymers such as PEG. However it may induce collapse in more complex polymers such as polypeptides, where short-ranged intramolecular hydrogen bonding between segments of the backbone and hydrophobic interactions between nonpolar side chains can stabilize a collapsed (or molten globulelike) state and compensate for the loss of configurational entropy.

V. CONCLUSION

We have measured the compression of a polymer chain due to macromolecular crowding by neutron scattering using contrast method. When increasing cosolute mass fraction (Ficoll 70) up to $\Phi \simeq 0.3$, the radius of gyration of the chain is decreased by a factor of 2. Models for excluded-volume interactions [6] due to hard spheres are consistent with our experimental results. If such a compression behavior could be observed for polypeptide chains, it could have significant influence on our understanding of protein stability in cytoplasmic environment.

ACKNOWLEDGMENT

We would like to thank A. Minton for critical reading of the paper.

[1] A. P. Minton, Biopolymers **20**, 2093 (1981).
[2] S. B. Zimmerman and A. P. Minton, Annu. Rev. Biophys. Biomol. Struct. **22**, 27 (1993).
[3] R. John Ellis, Curr. Opin. Struct. Biol. **11**, 114 (2001).
[4] R. John Ellis, Trends Biochem. Sci. **26**, 597 (2001).
[5] A. P. Minton, Biophys. J. **78**, 101 (2000).
[6] A. P. Minton, Biophys. J. **88**, 971 (2005).
[7] A. P. Minton, J. Biol. Chem. **276**, 10577 (2001).
[8] D. Shortle, FASEB J. **10**, 27 (1996).
[9] P. Calmettes, D. Durand, M. Desmadril, P. Minard, V. Receveur, and J. C. Smith, Biophys. Chem. **53**, 105 (1994).
[10] B. van den Berg, R. J. Ellis, and C. M. Dobson, EMBO J. **18**, 6927 (1999).
[11] N. Tokuriki, M. Kinjo, S. Negi, M. Hoshino, Y. Goto, I. Urabe, and T. Yomo, Protein Sci. **13**, 125 (2004).
[12] B.-R. Zhou, Y. Lang, F. Du, Z. Zhou, and J. Chen, J. Biol. Chem. **279**, 55109 (2004).
[13] P. McPhie, Y.-S. Ni, and A. P. Minton, J. Mol. Biol. **361**, 7 (2006).
[14] M. S. Cheung, D. Klimov, and D. Thirumalai, Proc. Natl. Acad. Sci. U.S.A. **102**, 4753 (2005).
[15] M. Perham, L. Stagg, and P. Wittung-Stafshede, FEBS Lett. **581**, 5065 (2007).
[16] J.-P. Cotton, B. Farnoux, and G. Jannink, J. Chem. Phys. **57**, 290 (1972).
[17] P. Debye, J. Appl. Phys. **15**, 338 (1944).
[18] F70® is a trademark of Pharmacia Inc.
[19] A. P. Minton, Curr. Opin. Struct. Biol. **10**, 34 (2000).
[20] D. Lairez and J. Pelta, Biophys. J. **84**, 3904 (2003).
[21] P. Flory, *Principles of Polymer Chemistry* (Cornell University Press, Ithaca, 1953).
[22] P.-G. de Gennes, J. Phys. (Paris), Lett. **36**, L55 (1975).
[23] M. Nierlich, J.-P. Cotton, and B. Farnoux, J. Chem. Phys. **69**, 1379 (1978).
[24] C. Cuniberti and U. Bianchi, Polymer **15**, 346 (1974).
[25] C. Williams, F. Brochard, and H. L. Frisch, Annu. Rev. Phys. Chem. **32**, 433 (1981).
[26] R. M. Briber, X. Liu, and B. J. Bauer, Science **268**, 395 (1995).
[27] M. Rubinstein and R. H. Colby, *Polymer Physics* (Oxford University Press, New York, 2003).

Available online at www.sciencedirect.com
ScienceDirect
Chemical Physics 345 (2008) 298–304
Chemical Physics
www.elsevier.com/locate/chemphys

Microscopic protein diffusion at high concentration by neutron spin-echo spectroscopy

C. Le Coeur, S. Longeville *

Laboratoire Léon Brillouin, CEA-CNRS, CEA Saclay, 91191 Gif-sur-Yvette, France

Received 16 May 2007; accepted 27 September 2007
Available online 1 October 2007

Abstract

Molecular transport and reactions in biological cells are strongly affected by the presence of macromolecules at high concentration. We studied the intermolecular structure and diffusion of oxygen carriers myoglobin and hemoglobin in concentrated solutions using neutron diffraction and spin-echo spectroscopy. The self-diffusion coefficient measured by NSE spectroscopy is compatible with theoretical prediction for long-time self-diffusion coefficient for colloids. We measured $I(q,t)$ for $q \simeq 1$ Å^{-1} trying to observe the short-time diffusion coefficient. A signal which can be attributed to the protein is observed but which origin can neither be attributed to translational nor rotational diffusion.

Keywords: Macromolecular crowding; Protein interactions and diffusion; Neutron spin-echo

The first step of a biochemical reaction implying two molecules is the diffusion of at least one species to recognize each other. In the complex interior of biological cells the free volume and molecular mobility are strongly reduced. The reactions can become diffusion-limited. The volume fraction of macromolecules in such crowded environments ranges up to $\Phi \sim 0.3$, and this affects various physical, chemical or biological properties of proteins [1]. The question of the diffusion mechanism of proteins at high volume fraction and in crowded media is a subject of intense research activity [2,3]. We present in this paper a study of two oxygen transport proteins: hemoglobin and myoglobin.

Hemoglobin is the main and almost unique constituent of the red blood cells (RBCs) (≃93% of the dry weight). It binds 4 molecules of oxygen when circulating in the capillaries close to the alveolar lungs, and after transport by heart driven flux of blood is able to release it where oxygen is demanded. The solubility of oxygen in plasma is very low, and the time spent by RBCs in the capillary lungs to uptake oxygen is limited (from 0.1 to 0.7 s depending on the authors). Diffusion of hemoglobin to the cell surface reduces the time of oxygen capture by RBC. Optimum O_2 transport would correspond to a maximum of hemoglobin packing inside the RBC but this effect is counterbalanced by the very nonlinear protein mobility reductions which severely increases the time of oxygen uptake.

Myoglobin is an heme protein present in muscle fibers, which binds one oxygen molecule reversibly and facilitates oxygen transport by macromolecular diffusion from the sarcoplasm to the mitochondria [4,5]. The affinity of myoglobin for molecular oxygen is higher than the one of hemoglobin so that O_2 transfer from hemoglobin to myoglobin can operate at intermediate oxygen partial pressure.

In this context it becomes biologically relevant to understand the influence of protein interactions on microscopic transport. The mechanism of physical hindrance may be different for hemoglobin (high volume fraction almost unique constituent) and myoglobin (rather small concentration in a crowded medium with fixed and mobile obstacles of very different sizes). Nevertheless, as a first step we have studied volume fraction dependence of both proteins

* Corresponding author.
E-mail address: slongeville@cea.fr (S. Longeville).

0301-0104/$ - see front matter © 2007 Elsevier B.V. All rights reserved.
doi:10.1016/j.chemphys.2007.09.042

up to a volume fraction corresponding to physiological concentration of hemoglobin in the RBCs. Our aim is to try to unravel the mechanism responsible for protein mobility reduction.

Understanding diffusion in concentrated solutions and complex media requires studies on various time- and length-scales and addressing the problem of self- and collective-diffusion. The techniques of dynamic light scattering (DLS), pulsed field gradient NMR (PFG NMR), or fluorescence recovery after photo bleaching (FRAP) operate on length scales, which exceed those of the intermolecular distance between proteins at relevant concentrations (≈200 nm versus few nm) which yields a long-time diffusion coefficient D^{I} [6]. Neutron scattering provides insight on a more microscopic scale: (i) Due to the small wavelength ($\lambda \simeq 1$–20 Å) and energies of cold neutrons (few meV) one can measure the intermolecular structures at high concentration and the time scales associated with the translational motions over intermolecular distances, (ii) both, the pair- and self-correlation functions can be studied, (iii) the problem of absorption and multiple scattering is negligible for some particular experimental conditions, an essential advantage in the case of opaque protein solutions, (iv) the high penetrating power of neutrons in matter and the H/D contrast variation method provide the capability to study structure and diffusion mechanism directly inside cells [7,8].

The paper is divided as follows: In a first section we will introduce the theoretical background necessary for the interpretation of the neutron scattering measurements. After a short description of materials and methods in a second section we present the experimental results and discussion and finally the conclusions of the paper.

1. Theoretical background

The small-angle neutron scattering intensity of a solution of almost spherical macromolecules can be written as [9]

$$I(q) = v_{\mathrm{p}}\Phi(\Delta\rho)^2F^2(q)\cdot S(q) \tag{1}$$

v_{p} is the volume of the macromolecule, Φ is the volume fraction of the molecule in the solution, $\Delta\rho$ is the scattering length density contrast between the molecule and the solvent in cm^{-2}. $F(q)$ is the form factor of the macromolecule and $S(q)$ the structure factor of the solution.

In the wave vector range $2\pi/q \gg d$, (where d is the average distance between two scattering centers) the intermediate scattering function reads:

$$\frac{I(q,t)}{\Phi v_{\mathrm{p}}(\Delta\rho)^2F^2(q)} \simeq \frac{1}{N}\left\langle \sum_{i,j}^{N} \mathrm{e}^{-i\mathbf{q}.[\mathbf{r}_i(0)-\mathbf{r}_j(t)]} \right\rangle \tag{2}$$

In this case, i and j run over all N proteins. The intermediate scattering function $I(q,t)$ is the pair correlation function which measures the relative motions of the macromolecules. For contrast reason, measurements are performed on solutions of protonated-protein diluted in a deuterated buffer, coherent scattering strongly dominates the signal in the small angle regime.

Spin incoherent scattering induces a 2/3 fraction of the neutrons to flip their spin, whereas both coherent and isotope incoherent scattering do not operate with spin-flip. The scattered beam polarization $P(q)$ (i.e. the measured quantity by NSE) of a fully incoherent sample should then theoretically be reduced to $P = -1/3$. In practice, coherent and incoherent scattering coexist in organic samples. The scattered beam is therefore composed with a mixture of neutrons with and without spin-flip: $P(q) \simeq -1/3\sigma^{\mathrm{inc}} + \sigma^{\mathrm{coh}}(q)$. This can be problematic for NSE because $P(q)$ is effectively the measured quantity, to be related to the intermediate scattering function [10]. As mentioned before, in the SANS regime the coherent scattering strongly dominates therefore one tries to minimize incoherent scattering by the use of a deuterated buffer. At higher wave vectors ($q \gtrsim 1$ Å^{-1}) a concentrated solution of protein in deuterated buffer, coherent and incoherent scattering ratio are so that the scattered beam polarization tends to 0. It is therefore necessary to measure intermediate scattering function in hydrogenated buffer; the signal is almost fully incoherent because strongly dominated by incoherent scattering of the protons. This induce two consequences: (1) the scattered beam polarization is no more 1 but rather 1/3 which has a strong cost in measuring time and (2) the protein contribution is proportional to the ratio α of its protons with respect to all those of the solution (typically 25–30% for concentrated solutions). The protons can be divided into two populations (belonging to the protein (p) and the solvent (s)) then one gets for the intermediate scattering function:

$$I(q,t) \sim \alpha\left\langle \mathrm{e}^{-i\mathbf{q}.\left[\mathbf{r}_i^{\mathrm{p}}(0)-\mathbf{r}_i^{\mathrm{p}}(t)\right]} \right\rangle + (1-\alpha)\left\langle \mathrm{e}^{-i\mathbf{q}.\left[\mathbf{r}_i^{\mathrm{s}}(0)-\mathbf{r}_i^{\mathrm{s}}(t)\right]} \right\rangle \tag{3}$$

From the intermediate scattering functions one can extract a generalized time- and wavevector-dependent diffusion coefficient which can denote either collective of self-diffusion for pair- and self-correlation functions respectively:

$$D(q,t) = -\frac{1}{q^2}\frac{\partial}{\partial t}\ln(I(q,t)) \tag{4}$$

If no significant departure from a single relaxation decay is observed the wavevector dependent diffusion coefficient can be extracted directly by

$$I(q,t) \sim \mathrm{e}^{-D(q)q^2t} \tag{5}$$

2. Materials and methods

2.1. Neutron scattering experiments

The neutron scattering experiments were performed at the Orphée reactor of the Laboratoire Léon Brillouin (LLB) at Saclay, France, and the European High Flux

reactor of the Institut Laue-Langevin (ILL) at Grenoble. We used the small-angle neutron scattering (SANS) spectrometer PACE of the LLB for static measurements and the neutron spin-echo (NSE) spectrometers G1bis (LLB) and IN15 (ILL) for measurements of the intermediate scattering function ($I(q,t)$) [10–12]. On PACE, the spectra were recorded at fixed concentration steps ($\delta\Phi \simeq 0.05$) up to volume fraction $\Phi \sim 0.4$. The incident wavelength was set to $\lambda = 6.07$ Å with a wavelength spread of $\Delta\lambda/\lambda = 0.1$. Two configurations of the spectrometer (distance sample to detector $L_{SD} = 0.9$ m and $L_{SD} = 5$ m) were used in order to cover the wave vector range of interest $q = 0.01$–0.4 Å^{-1}. The spectra were measured using the medium wave vector spin-echo spectrometer G1bis (LLB) in the range of $q = 0.05$–0.3 Å^{-1} and on IN15 (ILL) for smaller q values down to $q = 0.022$ Å^{-1}.

The experiments were performed both on myoglobin and hemoglobin. For NSE time window reasons, the concentration dependence of the evolution of wavevector dependent diffusion coefficients was studied on myoglobin; It is indeed a smaller protein than hemoglobin and enter the time window of the spin-echo spectrometer at Saclay. Hemoglobin was studied at different concentrations and in red blood cells on IN15 [8]. The study of the high q regime and high concentrations was performed on hemoglobin, because preparation of high quality samples is easier than for myoglobin. The spectra were measured on G1bis at Saclay.

2.2. Sample preparation

2.2.1. Myoglobin

Details on myoglobin sample preparations can be found elsewhere [15]. For small angle measurements (SANS and NSE) the samples were dialyzed against D_2O (for contrast reason see for example [13]). No salt was added. Several solutions were studied with protein concentrations ranging from 5.2 mM to 31.2 mM in heme at physiological temperature ($T = 37$ °C). This corresponds to a range of volume fraction between $\Phi \sim 0.07$ up to $\Phi \sim 0.4$.

2.2.2. Hemoglobin

High wave vector experiments were performed with human oxy-hemoglobin at 350 mg ml^{-1}. Hemoglobin has been extracted from human blood. Blood is first centrifuged at 3000g during 5 min and the supernatant solution is eliminated. A NaCl solution at 0.9% is added (1 volume of NaCl solution for 2 of red blood cells). The solution is centrifuged and separated again. This procedure is performed three times. A water lyses enable to liberate hemoglobin by agitating. Membranes are then precipitated by adding a phosphate solution (2.8 M, pH = 6.8, 1 volume of phosphate solution for 10 volumes of initial solution). The solution is then agitated and centrifuged at 4500g during 30 min. The supernatant hemoglobin is dialyzed against water, and then passed on a ion-exchange column in order to liberate hemoglobin from 2,3-diphosphoglycerate. The obtained oxy-hemoglobin solution is then concentrated by centrifugation. The concentration of hemoglobin has been determined by the absorbance of heme at 576 nm [14].

3. Results and discussion

3.1. A model for protein–protein interactions

In this paragraph we summarize the results presented in Ref. [15]. The myoglobin molecular form factor was measured on two dilute solutions of 0.25 and 0.5 mM. Both spectra were corrected for background and normalized to $F^2(0)$, the wave vector dependent discrepancies of $F^2(q)$ were within the uncertainties of the measurements. This means that interactions between proteins were negligible at such concentrations. At higher volume fractions, after some preliminary data treatment and background correction, the measured intensity was described by the formula (1). As was mentioned in the previous paragraph this formula describes accurately the intensity scattered by a solution of spherical molecules. To account for the small departure of the molecules from a spherical symmetry we refined the spectra using a theoretical model for interacting spheres to calculate $S(q)$ and the measured form factor $F(q)$ of the myoglobin. $S(q)$ was calculated using the analytical mean spherical approximation (MSA) [16] with correction for protein volume fraction dependence of the contact potential [17]. In this theory, the protein–protein potential is described by a hard sphere part and a Yukawa tail to account for the screened electrostatic potential ($U(r) = U_0 e^{-\kappa r}$). Three parameters are relevant for this description: the Debye length $L_D = 1/\kappa$, the protein radius and the absolute protein charge $|Z_p|$. The Debye length was set to the computed value for monovalent salt solution of 0.01 M. As shown in Fig. 1 a reasonable description of the structure factor was obtained over all refined concentrations with a protein diameter $\sigma_p \simeq 32 \pm 2$ Å and a charge $|Z_p| \simeq 1.7 \pm 0.4e$ [15]. The "hard sphere" diameter of the myoglobin, which can be approximately calculated

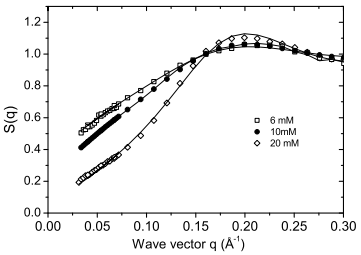

Fig. 1. Structure factor $S(q)$ of myoglobin solutions at three different concentrations (6 mM, 10 mM and 20 mM) deduced from the SANS spectra. The continuous line are best refinements using MSA analysis (see text).

from the specific volume, is 34 Å, thus the MSA refinements give a slightly lower value. It should be emphasized that this small reduction of the diameter value is different from the one generally observed in the form factor either due to the protein solvent contrast, or the partial exchange of labile protons of the protein [18]. In our analysis this uncertainty was removed by refining with the measured form factor. Myoglobin was dissolved in heavy water at a pD corresponding approximately to its isoelectric point. The exact number of charges (≈2) is somewhat uncertain, but its value is almost independent of the volume fraction although the contact potential varies strongly with Φ [17,15]. From the SANS analysis we can conclude that the protein–protein direct interactions are reasonably modeled by a hard sphere (HS) potential with a small residual electrostatic interaction below $V_{ij}(r)/k_BT \sim 0.1$ for $\Phi = 0.25$ at the mean intermolecular distance $r \simeq \tilde{d}$.

3.2. Microscopic protein diffusion in the small q regime

The coherent scattering length density differences between protein and solvent are strong enough to neglect any other contribution than those coming from the protein molecules: this assumption is confirmed by polarization analysis that shows that for $q \lesssim 0.3$ Å^{-1} spin incoherent scattering can be neglected. Within the entire range of wave vectors and concentrations, $I(q,t)$ was well approximated by a single exponential decay in time (Fig. 2): The generalized time-dependent diffusion coefficient (4) becomes time-independent. It follows that $I(q,t) \sim \exp(-\Gamma(q)t)$ with $D(q) = \Gamma(q)/q^2$. In the investigated wave vector range, we observe mainly coherent scattering events which is a measure of the pair correlation function. The interpretation of diffusion coefficients measured by coherent neutron scattering is not straightforward: All protein–protein pair contributions should be included in the computation of $I(q,t)$. The resulting diffusion coefficient $D(q)$ of relative motions is thus collective in nature similar to what is measured with dynamic light scattering however in a higher range of wave vectors: $2\pi/q \sim \tilde{d}$ for physiological concentrations. The collective-diffusion coefficient reflects the relaxation of concentration fluctuations. The wave vector dependence of the apparent diffusion coefficient $D(q)$ does not change qualitatively with concentration, $D(q)$ tends to a constant for wave vectors $q \gg q^*$, while it increases for small q values [15]. In the SANS analysis of the structure factor we have shown that in the q range $q \gg q^*$, $S(q) \simeq 1$, and $I(q,t)$ probes protein concentration fluctuations over rather short distances ($\simeq 20$ Å for $q = 0.3$ Å^{-1}). It was stressed in a previous paper [15] that similarly to colloids $D(q)$ turns out to be a self-diffusion coefficient [22].

Typical relaxation times of the protein's velocity can be estimated by $\tau_v \sim \frac{m}{f_{ps}}$. m is the protein mass and f_{ps} the protein–solvent friction coefficient of the Stokes–Einstein relation which yields $\tau_v \approx 10$ ps. Since typical times which are measured by NSE are of the order of or longer than 1 ns one can assume that the particles are in a Brownian regime. At infinite dilution the self-diffusion coefficient of a single protein is defined by Stokes–Einstein relation:

$$D_0 = \frac{k_B T}{f_{ps}} \tag{6}$$

k_B is the Boltzmann constant and T the temperature. When the protein volume fraction Φ increases protein–protein interactions create an additional friction term $f_{pp}(\Phi)$. One can write:

$$D_s^{\Phi} = \frac{k_B T}{f_{ps} + f_{pp}(\Phi)} \tag{7}$$

At this stage we do not speculate on the physical origin of $f_{pp}(\Phi)$ and only consider it as a phenomenological parameter to describe the concentration dependence of a "local viscosity". $f_{pp}(\Phi)$ computed from our results is plotted in Fig. 3. In the scale which is used f_{ps} corresponds to 1 therefore f_{pp} at high concentration is almost 30 times in excess of the solvent protein friction at $\Phi \simeq 0.4$.

The time dependent self-diffusion coefficient is usually divided into short- and long-time diffusion. The former is defined as the short-time expansion (first cumulant) of the intermediate scattering function at high wave vectors

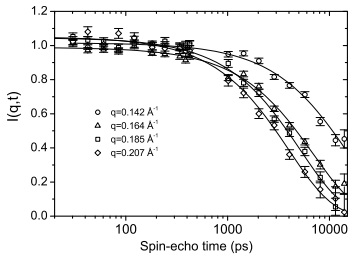

Fig. 2. Intermediate scattering function measured in the small q regime, measured on G1bis (Saclay), on myoglobin solution (18 mM) for four different wave vectors ranging from $q = 0.142$ Å^{-1} to $q = 0.207$ Å^{-1}.

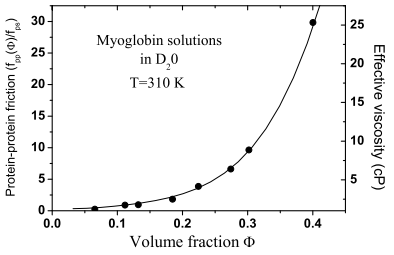

Fig. 3. Volume fraction dependence of the protein–protein friction in myoglobin solutions: $f_{pp}(\Phi)$. The protein–solvent friction f_{ps} corresponds to 1 in the scale used on the left hand. The right hand scale corresponds to the effective viscosity in centi-Poise.

with respect to the maximum of the structure factor (when $S(q) \simeq 1$). The latter is the long-time decay of $I(q,t)$. Physically the short-time diffusion coefficient $D_s^s(\Phi)$ reflects the particle mobility reduction due to hydrodynamic interactions only. It should be observed in a time range between the Brownian time and the interaction time τ_i. Protein motions can only respond to direct interactions after a time τ_i on a scale of the intermolecular distance where potential cannot be neglected with respect to $k_B T$. Then the protein diffusion is slowed down by memory effects and the long-time diffusion coefficient is measured. At infinite dilution one has $D_s^l(\Phi \to 0) = D_s^s(\Phi \to 0) = D_0$. Theoretical calculations of the hydrodynamic interaction were performed by Beenakker and Mazur [19] whereas Tokuyama and Oppenheim [20] computed both the effect of hydrodynamic and direct interaction for hard-sphere solutions. They were consequently able to derive both $D_s^s(\Phi)$ and $D_s^l(\Phi)$. Another interesting approach was developed by Medina-Noyola [21] for the particular case were $\tau_B \ll \tau \ll \tau_i$. The author computed $D_s^l(\Phi)$ starting from $D_s^s(\Phi)$ and the structure factor of the solution $S(q)$. His approach is thus to use the $D_s^s(\Phi)$ and consequently the protein mobility reduction due to hydrodynamic interactions as an input. Using the structure factor, he computes the additional reduction due to direct interactions.

From the structure factor analysis we can reasonably assume that the interaction time τ_i corresponds to the diffusion time for the surfaces to get in contact. For a myoglobin volume fraction of $\Phi \simeq 0.2$ one can roughly estimate $\tau_i \approx 5$–10 ns. For the same volume fraction and $q = 0.3$ Å^{-1} (where the plateau in $D(q)$ is reached) the typical relaxation time of $I(q,t)$ is however in the range of nanoseconds so that $\tau_v < \tau < \tau_i$. The protein displacements are thus recorded at sufficiently long times to be in the hydrodynamic regime: the velocity correlations are relaxed in contrast to those of short-range direct interactions.

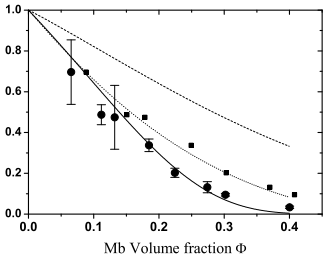

Fig. 4. Concentration dependence of the myoglobin diffusion coefficient $D_s^s(\Phi)/D_0$ measured by NSE (full circles). The continuous line is the results of the refinements of measurements of $D_s^l(\Phi)/D_0$ by tracer methods [24] (continuous). The dash and dot lines are the results of $D_s^l(\Phi)/D_0$ and $D_s^s(\Phi)/D_0$ calculated for hard-spheres suspensions [20]. The squares are the results of computation of $D_s^l(\Phi)/D_0$ from $D_s^s(\Phi)/D_0$ using the model of Ref. [21]. The full square correspond to the result for myoglobin after "hydrodynamic volume fraction" renormalization (see text).

The data displayed in Fig. 4 show the ratio of the self-diffusion coefficient measured by NSE spectroscopy versus D_o as a function of myoglobin volume fraction (full circles). For comparison the results of Tokuyama and Oppenheim [20] are shown for $D_s^s(\Phi)$ and $D_s^l(\Phi)$. The volume fraction dependence obtained by Beenakker and Mazur [19] for $D_s^s(\Phi)$ is very close to the one of Tokuyama and Oppenheim, and impossible to discriminate within our experimental uncertainties. While the theoretical predictions and experimental results agree reasonably for non-charged colloidal particles [22], it is shown in Fig. 4 that for protein solutions theoretical predictions significantly underestimate the measured decrease of $D_s(\Phi)/D_0$ at almost all concentrations even for long-time predictions. Moreover when looking at the typical time scales measured by NSE one could speculate that the measured diffusion coefficient is closer to the short than to the long-time values. This, when compared to theoretical calculation can be totaly excluded even for the lower concentrations. Two hypothesis arise to explain this discrepancy (1) theoretical calculations which are quite accurate for colloids of typical radius of several 100 nm are not appropriate for the description of protein diffusion of a few nanometers, (2) the experimental quantity is not a short-time diffusion coefficient. A definitive answer can not be given from such measurements but a striking feature tends to support the second one. As it was mentioned previously for hemoglobin inside RBCs [8], the volume used to compute the protein volume fraction corresponds to the "dry" specific volume $v_d = 0.75$ cc/g. The surface to volume ratio is almost inversely proportional to the radius of the particle. As a matter of a fact nanometer radius proteins diffusion should be more sensitive to surface effects than colloids with 100 time larger radius. For proteins, the hydration shell should significantly contribute to hydrodynamic properties whereas it does not for thermodynamic quantities such as specific volume. Including the hydration shell can lead to define an "hydrodynamic volume" v_h which should be the relevant quantity for hydrodynamic properties and can be defined as

$$v_h = v_d + \delta v_s \tag{8}$$

v_s is the specific volume of the solvent and δ ($0 \leqslant \delta \leqslant 1$) the fraction of solvent contributing to the hydrodynamic volume. From this formula the dry effective volume $\Phi_d = c_p v_d$ which serves as abscissa in Fig. 4 can be renormalized into the "hydrodynamic volume fraction" (c_p is the protein concentration in g/cc). The full square symbol in Fig. 4 corresponds to the diffusion coefficients measured by spin-echo spectroscopy as a function of their hydrodynamic volume $\Phi_h = c_p v_h$ with $\delta = 0.35$ as is commonly referred in the literature. It is a striking feature that the experimental values match reasonably to the calculation of Tokuyama and Oppenheim for hard sphere long-time self-diffusion coefficient volume fraction dependence.

Inclusion of the hydration shell was shown to explain the 30% discrepancies between the calculated (from

Stokes–Einstein relation or computer hydrodynamic calculations) and the measured rotational diffusion coefficient at low concentration [23]. The translational diffusion coefficient is usually less sensitive than rotational diffusion because the latter $\sim a^3$ whereas the former $\sim a$, a being the protein radius. Because of excluded volume effects it appears that the translational diffusion coefficient at high protein concentration becomes very sensitive to a small volume increase due to hydration shell.

If the characteristic time scales seem to be compatible with the measurements of the short-time self-diffusion coefficient, looking at the spacial scales seems to be less favorable. For $\Phi \simeq 0.2$ and $q = 0.3\ \text{Å}^{-1}$ one probes diffusion over typical distances of $d = 2\pi/0.3 \simeq 20$ Å, whereas the surface–surface distance can roughly be estimated as 13 Å. Direct interactions should be seen in the measurements.

In order to check whether it is possible to measure the true short-time self-diffusion coefficient we undertook measurements at high wave vectors; the measurements were performed with two type of spectrometer, backscattering [25] and NSE spectrometer. We report here measurements performed on neutron spin-echo spectrometer.

3.3. Microscopic protein diffusion at intermediate wave vectors

Fig. 5 shows the self-intermediate scattering function measured on hemoglobin solutions of 350 mg ml^{-1} at $q = 1.0\ \text{Å}^{-1}$ and $T = 300$ K (open circles). The full squares correspond to the self-intermediate scattering function of water measured exactly under the same conditions. For hemoglobin solutions both water and hemoglobin contribute to the signal and, as incoherent scattering is measured, the contributions are proportional to their respective number of protons. The two contributions are clearly time separated. The refinements of the spectra have been performed assuming a contribution of hemoglobin of 22% of the signal. The diffusion coefficient extracted from the wave vector dependence of the time decay of $I(q,t)$ for pure water

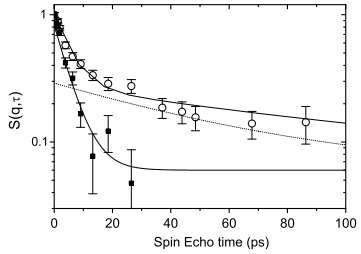

Fig. 5. Self-intermediate scattering function $I(q,t)$ measured on hemoglobin solution of 350 mg ml^{-1} at $T = 300$ K and $q = 1.0\ \text{Å}^{-1}$ (open circles) and water (full squares) in the same conditions. In hemoglobin solution two contributions are clearly separated arising from water and hemoglobin. The characteristic time measured for hemoglobin is $\tau \simeq 67 \pm 15$ ps (see text).

was found to be $D_s = 2.28\ (\pm 0.06) \times 10^{-5}$ cm^2 s^{-1} whereas it can be found in the literature $D_s = 2.37 \times 10^{-5}$ cm^2 s^{-1} [26,27]. In the protein solution water dynamics measured in this wave vector range seems to be slightly affected by the presence of the protein: In the refinements the diffusion time for water was found 50% higher than to the one measured in pure water. It was not possible to extract the relaxation time of the protein contribution with a high accuracy: $\tau \simeq 67 \pm 15$ ps for $q = 1.0\ \text{Å}^{-1}$. The rather large uncertainty of the results does not allow to extract a clear wave vector dependence of τ to verify any q^2 dependence of a diffusive process. If the process was purely self-diffusion of hemoglobin the measured diffusion coefficient associated with this time τ would be $D^{\text{app}}_{\text{mes}} = \frac{1}{\tau q^2}$. We found a value of $D^{\text{app}}_{\text{mes}} = 14.9\ (\pm 3) \times 10^{-7}$ cm^2 s^{-1}. This value must be compared on one hand to the long-time self-diffusion coefficient measured at the same temperature by NSE spectroscopy directly in red blood cells where the hemoglobin concentration is the same as in our solution: $D^{\text{l}}_s = 1.1 \times 10^{-7}$ cm^2 s^{-1} [8]. On the other hand the self-diffusion coefficient measured at infinite dilution $D^0_s = 6.8 \times 10^{-7}$ cm^2 s^{-1} [28]. In the time separation hypothesis D^0_s is the highest limit for the short-time self-diffusion coefficient, and it is further reduced by hydrodynamic interactions when the concentration increases. It appears on formula (7) since at infinite dilution protein–protein friction $f_{\text{pp}}(\Phi)$ can be neglected. D^{l}_s is affected by both hydrodynamic and direct interactions. From the measurements we get $D^{\text{app}}_s > D^0_s$ that rules out any interpretation of the measured relaxation time in terms of short-time translational diffusion coefficient. To which motion is associated that time?

The protein undergoes random rotational motions similar in origin to the translational one usually called rotational Brownian motion. The physical origin is due to the random torque created by the unbalanced colliding solvent molecules. For homogeneous spherical particles rotational motions do not contribute to coherent scattering but do have a significative influence to incoherent signal. For macromolecules at high wave vectors rotational diffusion can be transformed into apparent diffusion coefficients, as the signal follows a characteristic q^2 dependence $\tilde{D}^{\text{r}} \simeq R^2_g D_r$. The rotational diffusion D_r is little affected by macromolecular crowding. The rotational diffusion time $\tau_r = 1/2D_r$ was measured for hemoglobin in dilute solution (sol) and in red blood cells (rbc) [29]: the authors found respectively $\tau_{\text{sol}} = 37.7 \pm 2.1 \times 10^{-9}$ s and $\tau_{\text{rbc}} = 84.0 \pm 4.3 \times 10^{-9}$ s. This leads to apparent translational diffusion coefficients of $\tilde{D}^{\text{r}}_{\text{sol}} = 6.4 \times 10^{-7}$ cm^2 s^{-1} and $\tilde{D}^{\text{r}}_{\text{rbc}} = 2.8 \times 10^{-7}$ cm^2 s^{-1}. From this one can estimate the apparent diffusion coefficient for both rotational and translational Brownian motion, $D^{\text{app}} = \tilde{D}^{\text{r}}_{\text{rbc}} + D_s$. One finally gets around $\tilde{D}^{\text{app}}_{\text{sol}} = 6.2 \times 10^{-7}$ cm^2 s^{-1} for 350 mg ml^{-1} when hydrodynamic interactions at this concentration are supposed to reduce the short-time self-diffusion coefficient by a factor of 2 with respect to the infinite dilution (see Fig. 4). Although the uncertainties of our measurements are quite large it appears that the motions which leads to the decay of the

intermediate scattering function has a characteristic time which hardly seems to be compatible with rotational motions of the protein: $D_{\mathrm{mes}}^{\mathrm{app}} = 14.9(\pm 3) \times 10^{-7}\ \mathrm{cm^2\ s^{-1}}$ is 2.5 time larger than $\tilde{D}_{\mathrm{sol}}^{\mathrm{app}} = 6.2 \times 10^{-7}\ \mathrm{cm^2\ s^{-1}}$.

4. Conclusion

The protein volume fraction dependence of the self-diffusion coefficient D^{s} measured by NSE spectroscopy in the small angle regime (plateau in $D(q)$ around $q = 0.2$–$0.3\ \mathrm{\AA}^{-1}$) does not match with theoretical prediction for colloids. When comparing the characteristic time of protein diffusion D_{s} should be compatible with short-time coefficient. However the volume fraction reduction of $D_{\mathrm{s}}(\Phi)$ is much higher than theoretical prediction for the short and even long-time self-diffusion coefficient. After volume renormalization of the protein solutions due to the incorporation of the hydration shell, experimental results match the theoretical long-time self-diffusion volume fraction dependence. We undertook a measurement at higher wave vectors to evidence a cross-over from long- to short-time diffusion regime by neutron spin-echo spectroscopy. Due to unfavorable balance between coherent and incoherent scattering in D_2O solution we studied fully hydrogenated samples. A signal which can be attributed to protein motion is clearly observed in the spectra but cannot be explained in terms of short-time diffusion. We show that the characteristic time of the motion is also not compatible with rotational diffusion. NSE spectroscopy measure quasi-elastic processes in the time domain. When different processes are present and one strongly dominates in intensity the technique is less suited than techniques measuring in the energy domain. We hope that backscattering results will be able to evidence the short-time diffusion. We would like to thank W. Doster for very fruitful discussions.

References

[1] A.P. Minton, J. Biol. Chem. 276 (2001) 10577.
[2] R. John Ellis, Trends Biochem. Sci. 26 (2001) 597.
[3] S.H. Northup, Curr. Opin. Struct. Biol. 4 (1994) 269.
[4] J. Wyman, J. Biol. Chem. 241 (1966) 115.
[5] J.B. Wittenberg, B.A. Wittenberg, J. Exp. Biol. 206 (2003) 2011.
[6] D^0: infinite dilution limite of the self-diffusion coefficient, equal to $D^0 = k_{\mathrm{B}}T/f$. $D^{\mathrm{I}}: t \to \infty$ limit of a diffusion coefficient. $D_{\mathrm{s}}^{\mathrm{I}}(\Phi)$: volume fraction dependent $t \to \infty$ limit of the self-diffusion coefficient. $D_{\mathrm{s}}^{\mathrm{s}}(\Phi)$: volume fraction dependent $t \to 0$ limit of the self-diffusion coefficient. $D(q,t)$: generalized time- and wavevector dependent coefficient. $D(q,t)$: wavevector dependent coefficient. $D_{\mathrm{s}}^{\mathrm{app}}$: apparent self-diffusion coefficient computed from the relaxation time measured by NSE at a given wave vector by $D_{\mathrm{s}}^{\mathrm{app}} = \frac{1}{q^2\tau}$. D_{t}: rotational diffusion coefficient $\mathrm{s^{-1}}$. $\tilde{D}^{\mathrm{r}}$: contribution of rotational motions to diffusion calculated with $\tilde{D}^{\mathrm{r}} \simeq R_{\mathrm{g}}^2 D_{\mathrm{r}}$ in $\mathrm{cm^2\ s^{-1}}$.
[7] S. Krueger, R. Nossal, Biophys. J. 53 (1988) 97.
[8] W. Doster, S. Longeville, Biophys. J. 93 (2007) 1360.
[9] S.H. Chen, Annu. Rev. Phys. Chem. 37 (1986) 351.
[10] F. Mezei, Z. Phys. B 255 (1972) 146.
[11] F. Mezei (Ed.), Neutron Spin-Echo, Lecture Notes in Physics, Springer Verlag, 1980.
[12] F. Mezei, C. Pappas, T. Gutberlet (Eds.), Neutron Spin Echo Spectroscopy, Basic trends and Applications, Lecture Notes in Physics, vol. 601, Springer, Berlin, 2002.
[13] B. Jacrot, Rep. Prog. Phys. 39 (1976) 911.
[14] E. Antonini, M. Brunori, Hemoglobin and Myoglobin in their Reactions with Ligands, The North-Holland Publishing Company, 1971.
[15] S. Longeville, W. Doster, G. Kali, Chem. Phys. 292 (2003) 413.
[16] J.B. Hayter, J. Penfold, Mol. Phys. 42 (1981) 109.
[17] L. Belloni, J. Chem. Phys. 85 (1986) 519.
[18] K. Ibel, H.B. Stuhrmann, J. Mol. Biol. 93 (1975) 255.
[19] C.W.J. Beenakker, P. Mazur, Physica 120A (1983) 388.
[20] M. Tokuyama, I. Oppenheim, Phys. Rev. E 50 (1994) R16.
[21] M. Medina-Noyola, Phys. Rev. Lett. 60 (1988) 2705.
[22] P.N. Pusey, in: J.P. Hansen, D. Levesque, J. Zinn-Justin (Eds.), Liquids, Freezing and Glass Transition, Elsevier, Amsterdam, 1991.
[23] B. Halle, M. Davidovic, Proc. Natl. Acad. Sci. USA 100 (2003) 12135.
[24] N. Muramatsu, A.P. Minton, Proc. Nat. Acad. Sci. 85 (1988) 2984.
[25] S. Busch, W. Doster, private communication.
[26] R. Mills, J. Phys. Chem. 77 (1973) 685.
[27] T. Dipple, Doktorarbeit, Max Planck Institüt für Metallforschung, Institut Physik Stuttgart, 1991.
[28] R.S. Hall, C.S. Jonhson, J Chem. Phys. 72 (1980) 4251.
[29] D. Wang, U. Kreutzer, Y. Chung, T. Jue, Biophys. J. 73 (1997) 2764.

1360 Biophysical Journal Volume 93 August 2007 1360–1368

Microscopic Diffusion and Hydrodynamic Interactions of Hemoglobin in Red Blood Cells

Wolfgang Doster* and Stéphane Longeville†
*Physics Department, Technical University Munich, Garching, Germany; and †Laboratoire Léon Brillouin, CEA-CNRS, CEA Saclay, Gif-sur-Yvette, France

ABSTRACT The cytoplasm of red blood cells is congested with the oxygen storage protein hemoglobin occupying a quarter of the cell volume. The high protein concentration leads to a reduced mobility; the self-diffusion coefficient of hemoglobin in blood cells is six times lower than in dilute solution. This effect is generally assigned to excluded volume effects in crowded media. However, the collective or gradient diffusion coefficient of hemoglobin is only weakly dependent on concentration, suggesting the compensation of osmotic and friction forces. This would exclude hydrodynamic interactions, which are of dynamic origin and do not contribute to the osmotic pressure. Hydrodynamic coupling between protein molecules is dominant at short time- and length scales before direct interactions are fully established. Employing neutron spin-echo-spectroscopy, we study hemoglobin diffusion on a nanosecond timescale and protein displacements on the scale of a few nanometers. A time- and wave-vector dependent diffusion coefficient is found, suggesting the crossover of self- and collective diffusion. Moreover, a wave-vector dependent friction function is derived, which is a characteristic feature of hydrodynamic interactions. The wave-vector and concentration dependence of the long-time self-diffusion coefficient of hemoglobin agree qualitatively with theoretical results on hydrodynamics in hard spheres suspensions. Quantitative agreement requires us to adjust the volume fraction by including part of the hydration shell: Proteins exhibit a larger surface/volume ratio compared to standard colloids of much larger size. It is concluded that hydrodynamic and not direct interactions dominate long-range molecular transport at high concentration.

INTRODUCTION

Biological processes often depend on diffusive transport of macromolecules within cells and tissue. In the heterogeneous environment of the cytoplasm, one has to discriminate between fixed obstacles and protein interactions affecting passive transport. The latter has been termed crowding, since excluded volume effects play a dominant role (1–4). In the following we investigate, on a mesoscopic scale, how diffusion of a single protein in a biological cell is modified by interactions at high concentration: Hemoglobin, the main component of red blood cells (92%), assumes a concentration of 330 mg/ml under physiological conditions, corresponding to a volume fraction of $\Phi = 0.25$ (5). With an average center-to-center distance of 7 nm and a protein diameter of 6 nm, the molecules interact within their sphere of rotation, as was already noted by Perutz (6). The rotational diffusion coefficient of hemoglobin in red blood cells (RBCs) is a factor-of-two lower than in dilute solution (7). However, the translational diffusion coefficient is diminished by a factor of five according to field gradient NMR- and fluorescence recovery experiments (8,9). An even larger reduction (1/10) is found in the diffusivity of myoglobin, which is the oxygen carrier in striated muscle cells (10). Tracer diffusion experiments with hemoglobin and myoglobin by Wittenberg et al. (11) yield a roughly exponential decrease with concentration, which is attributed to obstruction effects by excluded volume interactions. Hemoglobin diffusion presumably facilitates the exchange of oxygen across the erythrocyte surface in the lung (11), but the magnitude of the effect is still debated (12).

The red blood cell is not an easy object for optical inspection, because of the high absorption coefficient of the heme group. Dynamic light scattering experiments in the visible range yield information about the RBC surface and the fluctuations of the cell membrane, but cannot penetrate into the cell interior (13). This may be possible in the near future with FCS versions of two-photon fluorescence excitation in the IR (14,15). NMR and optical techniques record displacements on a scale of several hundred nanometers. The molecular interactions in RBCs are established, however, on a length scale of a few nanometers—the mean distance between hemoglobin molecules. This range can be studied using energy-resolved neutron scattering methods, in particular spin-echo spectroscopy, which allows recording the time evolution of protein diffusion on the relevant spatial scale. With this technique we address the question whether hemoglobin diffusion can be understood based on concepts developed for nearly uncharged colloidal particles (16,17): Molecular liquids interact by direct forces, van der Waals and electrostatic; whereas, for a colloid, hydrodynamic interactions, which are mediated by the solvent, play an important role. Each molecule moves in the flow field induced by the motion of its neighbors. The different types of interactions can be sorted out by measurements of the short- and long-time diffusion coefficients at various length scales. The

Submitted October 17, 2006, and accepted for publication February 26, 2007.

Address reprint requests to W. Doster, Tel.: 49-89-2891-2456; E-mail: wdoster@ph.tum.de.

Editor: Ron Elber.

0006-3495/07/08/1360/09 $2.00

doi: 10.1529/biophysj.106.097956

latter is selected by varying the wave-vector of the scattering experiment: Hydrodynamic interactions dominate at short times, and their propagation occurs with the speed of sound, while direct forces are established during the structural relaxation time of the colloidal solution, τ_D. This requires diffusion across the center-to-center distance d: $\tau_D \approx d^2/6D$. One distinguishing property of proteins is their small size, with diameters of a few nanometers, in contrast to several hundred nanometers of a standard colloid. Whether the solvent can be treated equivalently as a continuum for large and small colloids and within what range of size remains to be established. The theoretical interpretation of diffusion in colloidal suspensions in the presence of direct and hydrodynamic interactions has reached a certain degree of refinement: For self-diffusion it has been shown that direct interactions are relatively unimportant compared to hydrodynamic interactions. Approximate short- and long-time diffusion coefficients as a function of volume fraction and wave-vector have been derived, which agree reasonably well with experimental data taken with standard colloids (16–19). In contrast, for collective diffusion, direct interactions play an important role (20). In the following we investigate whether these concepts can be applied on a mesoscopic scale to concentrated protein solutions and, in particular, to hemoglobin diffusion inside RBCs.

THEORETICAL CONCEPTS

We assume a binary solution of an aqueous solvent and a solute of protein molecules. Macromolecular diffusion thus results in concentration fluctuations, which modulates the local density. The basic experimental quantity to be determined with neutron spin-echo spectroscopy is the intermediate scattering function, $S(\mathbf{q},\tau)$, which records the correlations of intermolecular density fluctuations due to relative protein displacements $\mathbf{r}_i$-$\mathbf{r}_j$ (21),

$$S(q,\tau) \equiv \frac{1}{N}\sum_{i,j}\langle \exp[-i\mathbf{q}\cdot(\mathbf{r}_i(\tau=0)-\mathbf{r}_j(\tau))]\rangle, \quad (1)$$

where $\mathbf{q}$ is the scattering vector, $q = 4\pi/(\lambda)sin(\theta/2)$, λ is the wavelength of the incident neutrons, and Θ is the scattering angle. With q, one selects a particular length scale $d = 2\pi/q$, and τ denotes the time shift. N is the total number of particles. The brackets $\langle \ldots \rangle$ imply ensemble averaging over initial positions of the particles. Assuming spherical particles without internal degrees of freedom, the displacements in Eq. 1 exhibit a Gauss distribution at long times. The Gauss average of Eq. 1 yields

$$S(q,\tau) = S(q,0)\cdot\exp[-q^2\cdot D_c\cdot\tau]. \quad (2)$$

$S(q, 0)$ denotes the static structure factor. D_c is the collective or gradient diffusion coefficient defined by Fick's law. A phenomenological interpretation of D_c can be obtained from linear irreversible thermodynamics in combination with the Einstein equation. The latter relates a molar mobility (the Onsager coefficient) to a molecular friction coefficient f_c (22),

$$D_c = \frac{1}{N_A f_c}\left(\frac{\partial\Pi}{\partial c_p}\right)_T, \quad (3)$$

where N_A is the Avogadro number and c_p is the molar concentration of the macromolecule. The osmotic compressibility $\kappa_{os} = \partial c_p/\partial\Pi$ acts as a driving force: A low compressibility enhances the rate of restoring locally a uniform concentration. In dilute solutions the osmotic pressure varies linearly with concentration: $\Pi = RT\cdot c_p$, which, if inserted into Eq. 3, yields the familiar Einstein equation: $D_c = k_BT/f_c$.

The compressibility decreases with increasing concentration, implying faster collective diffusion. In parallel, enhanced particle interactions increase the collective friction coefficient, which compensates for the osmotic effect. In concentrated solutions exhibiting strong particle interactions, the molecular displacements can deviate from a Gauss distribution, involving a time- and q-dependent diffusion coefficient $D(q,\tau)$ in Eq. 2 (23–25). The short-time value reflects molecular motions of particles in a static environment, while long-time diffusion involves an adjustment due to structural relaxation on the scale of the interaction time τ_D. The correlation function $S(q,\tau)$ of strongly interacting systems is thus inherently heterogeneous in time.

Following Ackerson (24), we express $D(q,\tau)$ as the ratio of a so-called hydrodynamic function $H(q,\tau)$ and a static susceptibility, the interparticle structure factor $S(q)$,

$$D(q,\tau) = D_0\frac{H(q,\tau)}{S(q)}, \quad (4)$$

where D_0 denotes the free particle diffusion coefficient at infinite dilution, $D_0 = k_BT/f_0$, and f_0 is the coefficient of the protein-solvent friction.

The inverse of the hydrodynamic function is the friction factor, $f_c/f_0 = H(q,\tau)^{-1}$, resulting from direct and hydrodynamic interactions between protein molecules. At short times, $\tau \ll \tau_D$, only hydrodynamic interactions are involved. In the limiting case of low q-values and long times, Eq. 4 turns into the collective or gradient diffusion coefficient D_c of Eq. 3. The low-q structure factor is thus given by $S(q\rightarrow 0,\Phi) = RT\,\kappa_{os}$, which allows deriving the osmotic compressibility from scattering experiments at low scattering vectors. The self-diffusion coefficient D_s in contrast is independent of κ_{os} and involves only the self-friction coefficient f_s:

$$D_s(\tau) = \frac{k_BT}{f_s}. \quad (5)$$

The long-time self-diffusion coefficient is equivalent to the tracer diffusion coefficient $D_s^L \equiv D_t$. Its short-time value, D_s^S, can be measured with neutron spectroscopy, since the generalized collective diffusion coefficient $D(q,\tau)$ in Eq. 4 tends to D_s^S at $q \geq q_{max}$, above the structure factor maximum, where $S(q)$ approaches unity (23).

Experimental values of the collective and the tracer diffusion coefficients of hemoglobin and myoglobin versus the protein volume fraction Φ are displayed in Fig. 1. The self-diffusion coefficient of hemoglobin in red blood cells, as determined with NMR (8), fits well into the concentration series. It is striking that D_t and D_c diverge with increasing volume fraction (29): While D_c decreases only slightly in a linear fashion, a roughly exponential decrease with volume fraction is found for the tracer diffusion coefficient. The fit to $D_t \approx D_0 \cdot \exp(-\Phi/\Phi_0)$ yields $\Phi_0 = 0.15$. Experimental values of $\kappa_{os}(\Phi)$, represented by the solid line in Fig. 1, also decrease exponentially with the volume fraction yielding $\Phi_0 = 0.12$. According to Eq. 3, $D_c \propto \kappa_{os}^{-1}$ should thus increase exponentially with the volume fraction. Instead, a slight decrease is observed, which implies that osmotic and friction effects nearly compensate each other in Eq. 3, yielding $f_c(\Phi) \cdot \kappa_{os} \approx$ constant. Indeed, the osmotic compressibility declines in parallel with the tracer diffusion coefficient, which depends exclusively on f_s. The slight difference may reflect a nonequivalence of self- and collective friction. However, κ_{os} is a thermodynamic susceptibility that depends on excluded volume and other direct interactions, but not on hydrodynamic forces. The experimental values of κ_{os} for hemoglobin and myoglobin, displayed in Fig. 1 (*solid line*), are well represented by theoretical results of the virial expansion of $S(q)$ assuming a suspension of hard spheres (29,30). Although the compensation between friction and osmotic effects holds up to intermediate volume fractions ($\Phi < 0.3$), where both quantities vary by more than a factor of 10, there is no theoretical basis for such a relationship, which would exclude hydrodynamic interactions.

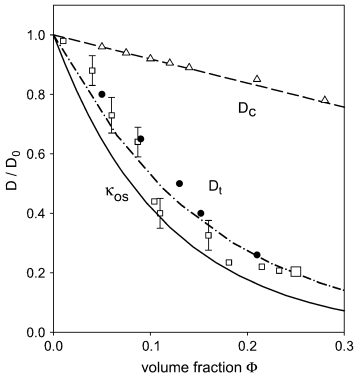

FIGURE 1 Normalized long-time diffusion coefficients $D(\Phi)/D_0$: (*triangles*) collective diffusion coefficient D_c of hemoglobin in solution (light scattering), (*dash-dotted line*) fit to $D_c/D_0 = 1 + B_1 \cdot \Phi$ with $B_1 = -0.76$. Tracer diffusions coefficients, D_t, of hemoglobin in solution (*small open squares*) (29,37) and in red blood cells (NMR): large open square (8), and of myoglobin in solution (*solid circles*) (11,37), (*dash-dotted line*) fit of D_t to an exponential function with $\Phi_0 = 0.15$, (*solid line*) exponential fit to the osmotic compressibility, κ_{os}, of hemoglobin and myoglobin yielding $\Phi_0 = 0.12$ (29,30).

MATERIALS AND METHODS

Sample preparation

Human blood samples, drawn by venipuncture from an adult male, were used immediately. Three types of D_2O-buffer solutions were prepared. Buffer A was a modified physiological sodium salt solution with the following ingredients (per liter): 9.0 g NaCl, 17.16 mg adenine, 26.22 mg inosine, 2.5 g albumin (fraction V), 10 ml vitamins (Nr. 273; Seromed Biochrom, Berlin, Germany) and 10 ml penicillin/streptomycin (Nr. A22129; Seromed Biochrom) adjusted to pD 7.4. Buffer B serves as the anti-coagulant and contains (per liter): 16 g Na-citrate, 25 g glucose, 17.1 mg adenine, 26.2 mg inosine, 2.5 g albumin, 10 ml vitamin E, and 10 ml Pen/Strep adjusted to pD 7.4 by citric acid. Buffer C, composed of 4 units of buffer A plus 1 unit of B, is the final buffer to dilute the RBCs at the standard osmolarity of 300 mOsm. The pD of 7.4 is close to the isoelectric point of hemoglobin. The preparation proceeds as follows: 4 units (by volume) of blood are mixed with one unit of buffer B. The resulting solution is then centrifuged for 5 min at 2000 g. After removal of the plasma and ''buffy coat'', the cells are washed five times with buffer C and centrifuged. The number of exchangeable hydrogens is then reduced by a factor of 100. The RBCs were inspected with a microscope to ensure the absence of significant deviations from their normal shape. For the neutron scattering experiments, the RBCs were centrifuged for 5 min at 2000 *g* and the concentrated solution was filled in a quartz-glass cell with 0.5 mm in thickness. The experiments were performed within 24 h after preparation. Human hemoglobin A samples were prepared by lysis of erythrocyte suspensions and purified by DEAE-cellulose chromatography. The concentrated samples were freeze-dried and resuspended in buffer C at the desired concentration (21 mM) before the experiment. The viscosity of buffer C was measured using a Schott capillary viscosimeter: $\eta(D_2O)/\eta(H_2O) = 1.243$ (± 0.05) at 20°C and $\eta(D_2O, 37°C)/\eta(D_2O, 20°C) = 0.6686$ (± 0.0004). The factor converting the diffusion coefficient from buffer C (D_2O) at 37°C to water at 20°C is then 0.79 (± 0.005).

Neutron scattering experiments

Protein-internal motions and diffusion have been studied by neutron time-of-flight and back-scattering spectroscopy (26,27). The neutron spin echo experiments with hemoglobin (28) were performed at the Orphée reactor of the Laboratoire Léon Brillouin (France) and the European high flux reactor of the Institut Laue Langevin. We employed the spin echo spectrometer *G1bis* at the LLB and *IN15* at the Institut Laue Langevin. On *G1bis* we measured the intermediate scattering function $S(q,\tau)$ using an incident wavelength $\lambda_0 = 10.3$ Å and a spread $\Delta\lambda/\lambda \sim 0.15$ within a wave-vector range $q \simeq 0.05$–0.3 Å^{-1}. Accessible spin echo times range from $\tau \simeq 27$ ps to 20 ns. On *IN15* two wavelengths were employed to cover the maximal wave vector range with appropriate spin echo times ($\lambda = 9$ Å and $\lambda = 15$ Å, $q \simeq 0.02$–0.13 Å^{-1}, $\tau \simeq 190$ ps to 190 ns).

In the relevant q-range ($0.01 \leq q \leq 0.25$ Å^{-1}) the distance between atomic scattering centers (≈ 1 Å) is much smaller than $2\pi/q \approx 25$ Å. By coherent neutron scattering, one thus probes the scattering length density contrast between solute and the solvent (here D_2O for optimal contrast). The signal, the scattered intensity, is thus proportional to $\Delta\rho^2$, the squared difference in scattering length density between solute and the solvent. As a result, one probes the density fluctuations induced by relative motions of protein molecules in the D_2O-solvent. The scattering function is dominated by hemoglobin but contains minor contributions (a few percent) from the cell membrane. Moreover, since the molecules are almost spherical and the molecular scattering density distribution is homogeneous at the low

q-values, translational and not rotational displacements dominate the scattering function.

RESULTS

Time- and wave-vector dependent diffusion

Fig. 2 displays the normalized intermediate scattering function $S(q,\tau)/S(q)$ of hemoglobin in RBCs at several wave-vectors. The fits to a single exponential decay on a logarithmic timescale are also shown. The decay rates increase with the wave-vector as expected for translational diffusion. The exponential fit emphasizes the overall or long-time decay of the correlation function. The resulting long-time diffusion coefficient $D^{\mathrm{L}}(q)$ is displayed in Fig. 4 (*top*). However, due to the large q-values or short length scales probed, as compared to light scattering, the short-time regime may still apply. To emphasize the short-time behavior, a plot of $\ln[S(q,\tau)]$ versus τ is shown in Fig. 3. A straight line (exponential decay) accounts for the data at the lower q-values; however, deviations become significant at high q, which is indicated by the dashed line. The initial slope yields the effective short-time diffusion coefficient $D^{\mathrm{S}}(q) = -1/(q^2 S(q))\,(dS/d\tau)_{\tau\to 0}$. For Gauss displacement distributions one expects the diffusion coefficient to be constant. In contrast, we observe a q- and time-dependent coefficient $D(q,\tau)$. Fig. 4 (*top*) shows the long-time value derived from an exponential fit to the data: $D(q)$ increases with decreasing wave-vector, while above $q = 0.1$ Å^{-1}, a plateau is reached. According to Eq. 4, $D(q)$ is composed of two q-dependent functions: the intermolecular structure factor $S(q)$ and the hydrodynamic function $H(q)$. We first investigate the effect of the structure factor on $D(q)$.

In previous work, we determined the structure factors of myoglobin and hemoglobin solutions from low-angle neutron scattering data (31). Applying the mean spherical approximation (MSA) with a hard sphere potential as input,

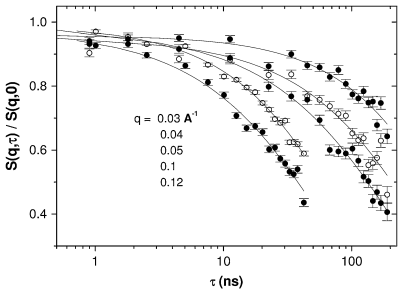

FIGURE 2 Normalized intermediate scattering functions $S(q,\tau)/S(q,0)$ of hemoglobin in RBCs on a log-timescale, measured with the neutron spin-echo-spectrometer IN 15 (Institut Laue-Langevin in Grenoble) at several wave-vectors q; (*lines*) fits of the data to a single exponential function as described in the text.

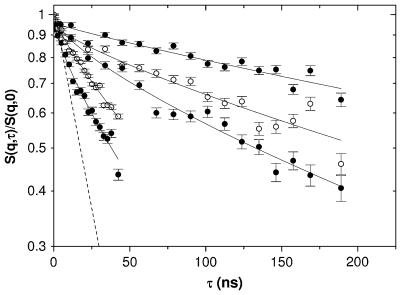

FIGURE 3 Semilogarithmic plot $\ln[S(q,\tau)/S(q,0)]$ of the intermediate scattering function shown in Fig. 2 at the same wave-vectors $q = 0.03$, 0.04, 0.05, 0.1, and 0.12 Å^{-1}. The lines are fits of the data to a single exponential function. The dashed line at $q = 0.12$ Å^{-1} refers to the fast component reflecting short-time diffusion.

reasonable fits to the data could be achieved. The contribution of electrostatic interactions was estimated to be small. This is reasonable, since the measurements were performed near the isoelectric point of the protein. The structure factor of red blood cells was analyzed earlier by Krueger et al. (5,32) using contrast variation methods. This allows our discriminating between membrane and protein scattering contributions to the structure factor. According to this work, it is not possible to eliminate the membrane scattering completely by contrast variation, because the respective scattering length density is inhomogeneous: The membrane is composed of lipid bilayers and a variety of membrane proteins. However, due to the small size of hemoglobin with respect to the cell dimension and its high relative bulk concentration, Krueger et al. were able to verify that the scattering contributions due to membrane and hemoglobin are mostly wave-vector separated. The data were refined in the relevant wave-vector range $q \geq 0.06$ Å^{-1} using the mean spherical approximation (MSA) method (33,34) and the result at $\Phi = 0.25$ is displayed in Fig. 4 (*middle*). The structure factor exhibits a broad maximum in the q-range of interest to our diffusion measurement (Fig. 4, *top*): The diffusion coefficient decreases where the structure factor shows a corresponding increase. This result is qualitatively in accordance with Eq. 4, since $D(q) \propto 1/S(q)$. Above $q_{\max}$, where the structure factor approaches unity, $D(q)$ tends to a constant value. This regime allows us to extract a self-diffusion coefficient $D_{\mathrm{s}}(q)$, since correlations diminish with $S(q) \to 1$. In contrast, at q-values below the structure factor maximum, coherent effects dominate, yielding $D_{\mathrm{c}}(q)$, the collective diffusion coefficient. The steplike increase in $D(q)$ in Fig. 4 (*top*) thus reflects the crossover from self- to collective diffusion. This mechanism closes the gap observed between D_{c} and D_{t} in Fig. 1. The gap exists not only on a macroscopic but also on a microscopic scale and is related to the

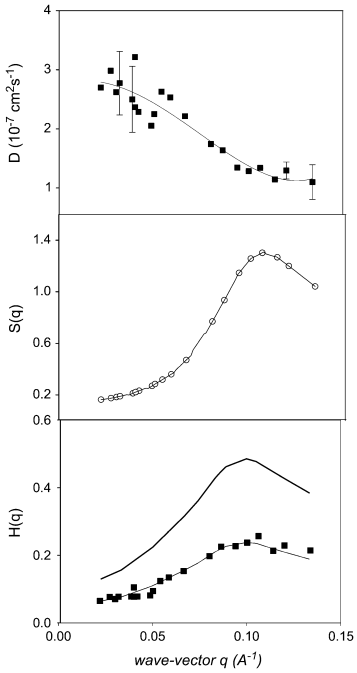

FIGURE 4 (*Top*) Generalized diffusion coefficient $D(q,\tau)$ (Eq. 4) of hemoglobin in RBCs at 37°C in D_2O-buffer C; the line is drawn to guide the eye. (*Middle*) Interparticle structure factor $S(q)$ of hemoglobin in RBCs, MSA calculations adjusted from Krueger et al. (5,32). (*Bottom*) Theoretical short-time hydrodynamic function of a hard-sphere colloid $H(q)$ at $\Phi = 0.25$ adjusted from Beenakker and Mazur (16), experimental $H(q) = D(q)/D_0 \cdot S(q)$; the solid line through data is the prediction $H(q)/2.1$ adjusted to fit the experimental data.

properties of the q-dependent osmotic compressibility. The limiting value of $D_c(q \rightarrow 0)$, observed with light scattering in Fig. 1, is not reached here because of a restricted experimental q-range. If the q-dependence of $D(q)$ could be attributed entirely to $S(q)$, there would be no room for hydrodynamic interactions. This is not the case, as will be demonstrated in the next section.

The hydrodynamic function $H(q)$

From Eq. 4 we derive the hydrodynamic function, since independent experimental information on $D(q)$ and $S(q)$ is available in Fig. 4 (*top* and *middle*). Interestingly, $H(q)$ is not constant, as shown in Fig. 4 (*bottom*, *data points*), but displays a broad maximum in phase with the structure factor $S(q)$. A wave-vector-dependent friction function was observed previously with concentrated myoglobin solutions (31). This indicates that the hydrodynamic function and the static structure factor are correlated as proposed by hydrodynamic theories: Beenakker and Mazur have calculated the short-time self-diffusion coefficient D_s^S of a concentrated suspension of hard spheres taking into account the hydrodynamic interactions between an arbitrary number of spheres (16). Direct interactions can be ignored at short times for $\tau \ll \tau_D$. They derive a wave-vector dependent function $H(q)$, oscillating in phase with the structure factor. Their result, adjusted for size and volume fraction of hemoglobin in RBCs, is displayed as the upper solid line in Fig. 4 (*bottom*). The theoretical result exhibits a similar q-dependence, but the absolute values are larger than the experimental data. This implies that the theory underestimates the magnitude of the hydrodynamic friction $\propto H(q)^{-1}$. Adjusting the theoretical result by a constant factor (2.1) fits the data in the respective q-range quite well.

Short- and long-time diffusion

The discrepancy in the magnitude of $H(q)$ is somewhat surprising, since the theory agrees quite well with experimental data on short-time self-diffusion coefficients of standard uncharged colloids at comparable concentrations (16,35). A likely origin of the discrepancy could be a difference in the relevant timescale: The diffusion coefficients in Fig. 4 (*top*) reflect the overall decay in $S(q,\tau)$ and therefore represent rather the long-time self-diffusion coefficient than D^S. Moreover, with neutron scattering we investigate much higher q-values than with light scattering.

Our experimental estimate of the self-diffusion coefficient of hemoglobin in RBCs is derived from the plateau in $D(q)$ at high q in Fig. 4 (*top*), where $S(q) \rightarrow 1$. Corrected to buffer C (H_2O) at 37°C, we obtain 1.75 ($\pm$0.2) $\cdot$ 10^{-7} cm^2/s for RBCs and 2.5 ($\pm$0.2) $\cdot$ 10^{-7} cm^2/s for hemoglobin at $\Phi = 0.25$. Corrected to 20°C and water, the coefficient in RBCs is 1.1 $\cdot$ 10^{-7} cm^2/s, a factor 6.2 lower than in dilute solution.

The normalized values D_s/D_0 of hemoglobin in RBCs and in solution assuming $D_0(37°C, D_2O) = 8.61 \cdot 10^{-7}$ cm^2/s are displayed in Fig. 5. Also shown is the self-diffusion coefficient of myoglobin (*solid circles*) measured in the same q-range with neutron spin-echo spectroscopy (31). The comparison with the data in Fig. 1 demonstrates that the self-diffusion coefficients measured at $q \geq q_{max}$ are nearly identical with the long-range tracer diffusion coefficient of hemoglobin and myoglobin. Both quantities exhibit essentially the same exponential decay with the volume fraction.

The D_s values of hemoglobin in RBCs and of hemoglobin in solution at the same volume fraction coincide within experimental error and fit quite well into the concentration series.

The dashed line in Fig. 5 represents the calculated short-time diffusion coefficient for a suspension of hard spheres, $D_s^S(\Phi)$ by Beenakker and Mazur (16,35). The experimental

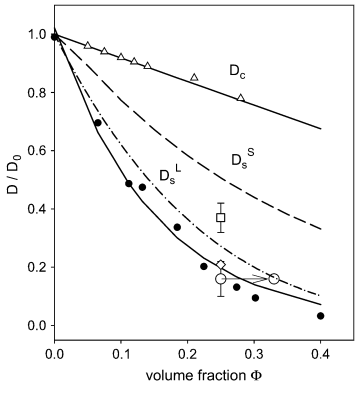

FIGURE 5 Normalized relative diffusion coefficients $D(\Phi)/D_0$: (*open triangles*) D_c, collective diffusion coefficient of hemoglobin in solution (dynamic light scattering) from Fig. 1, neutron scattering results at $q = 0.12$ Å^{-1}: (*open circles*) suggested long-time diffusion coefficient D_s^L of hemoglobin in blood cells and of hemoglobin in solution (*open diamonds*) at $\Phi = 0.25$. (*Open squares*) Short-time diffusion coefficient D_s^S of hemoglobin in RBCs from Fig. 3. (*Solid circles*) D_s^L of myoglobin in solution (31) and (*dash-dotted line*) exponential fit to D_s (Fig. 1) yielding $\Phi_0 = 0.15$, (*dashed line*) theoretical short-time self-diffusion coefficient, D_s^S, for hard sphere suspensions (16,17,35), and (*solid line*) theoretical long-time self-diffusion coefficient, D_s^L, for hard sphere suspensions (17).

data are significantly lower at all concentrations than the theoretical prediction. At $\Phi = 0.25$ the discrepancy amounts to a factor of two, which is the adjustment factor used in Fig. 4 (*bottom*). However, the data agree quite well with long-time tracer diffusion coefficients of hemoglobin and myoglobin at the same concentration. This suggests that the self-diffusion coefficient determined from the overall decay of the intermediate scattering function in Fig. 2 should be interpreted as a long-time value D_s^L. Due to memory effects by structural relaxation, the long-time diffusion coefficient is generally lower than the short-time value. The short-time self-diffusion coefficient can be estimated from the initial decay of the correlation function in Fig. 3. The corresponding short-time coefficient, indicated by an open square in Fig. 5, D_s^S at $q = 0.12$ Å^{-1}, is above D_s^L but still lower than the theoretical value. Possibly even higher q-values than those employed here need to be considered.

DISCUSSION

Comparison with hard sphere colloidal suspensions

The calculation of the short-time diffusion coefficient at high concentrations involves a consideration of many-body hydrodynamic interactions (16). At short times the configuration of particles remains essentially fixed. For the long-time diffusion coefficient memory, effects due to configurational relaxation have to be included. This leads to slowing down of particles motions: The long-time diffusion coefficient is thus generally lower than at short times. A complete solution to the latter problem, providing the full range nonexponential correlation functions versus volume fraction, is not available. Early calculations by Medina-Noyola were based on a decoupling approximation: The molecules perform short-time diffusion under the influence of hydrodynamic interactions, while the obstruction effect at later times is assumed to be independent of the short-time trajectories. Thus only D_0 is renormalized by hydrodynamic interactions (36), while the obstruction effect is derived from the static structure factor. The model predicts a significant difference between short- and long-time diffusion due to direct interactions. The model agrees with experimental data at high volume fractions ($\gtrsim$0.3) in the presence of strong direct forces. Later Tokuyama and Oppenheim developed a more systematic theory of concentrated hard-sphere suspensions, where both direct and hydrodynamic interactions are present (17,35). The volume fraction dependence of short- and long-time diffusion coefficients are calculated from a unifying point of view. Both the short- and long-range hydrodynamic interactions are shown to play an important role in both coefficients, while the direct interactions are drastically reduced by the hydrodynamic coupling. Their $D_s^S(\Phi)$ coincides essentially with the results of Beenakker-Mazur (16,35) shown in Fig. 5. The new feature is the calculation of a long-time diffusion coefficient $D_s^L(\Phi)$, which is represented by the full line in Fig. 5. The theory predicts experimental data of uncharged colloids at intermediate and high volume fraction quite well (17,18). Moreover, it is reasonably well approximated by an exponential function with $\Phi_0 = 0.19$ at low and intermediate volume fractions. Our experimental values of D_s^L, derived from the long-time decay of $S(q,\tau)$ of myoglobin and hemoglobin solutions, are conspicuously lower than those predicted for hard sphere colloidal suspensions. The difference may point to further attractive interactions, slowing down self-diffusion, since also the collective diffusion coefficient D_c (Fig. 5) decreases (instead of increasing) with concentration. Nevertheless, the calculated D_s^L accounts much better for the protein diffusion coefficients than the short-time values D_s^S. This comparison supports our previous conclusion that the long-time limit of the self-diffusion coefficient is achieved, at least above $\Phi = 0.2$, despite the mesoscopic q- and time-range covered by our experiment. How is this possible?

The largest q-value (0.125 Å^{-1} in Fig. 4, *top*) corresponds to a spatial scale of 50 Å, which is close to the center-to-center distance $d \approx 70$ Å between hemoglobin molecules at $\Phi = 0.25$. For the respective correlation time we find $\tau \approx$ 60 ns. Within this range, taking the value of the short-time diffusion coefficient, $D_s^S(\Phi = 0.25) \approx 0.5\, D_0$ (Fig. 5), as an upper limit, an average displacement of 40 Å is derived. In

addition, accounting for the diameter of hemoglobin, $\sigma = 56$ Å, a much smaller displacement of $d^* = d - \sigma = 14$ Å could lead to a collision. Thus deviations from the short-time behavior are expected for correlation times exceeding ~10 ns. It is thus plausible that the data in Fig. 4 (*top*) refer to the long-time regime of self-diffusion.

This interpretation of long-time diffusion is not easily reconciled with the q-dependence observed for $H(q)$ in Fig. 4 (*bottom*), which agrees with calculations in the short-time diffusion regime (16). However, Segre and Pusey found with hard sphere colloidal suspensions, that $D_s^L(q)$ and $D_s^S(q)$, while differing significantly in magnitude, exhibit nearly the same q-dependence (19). Thus the dynamical function $H(q)$, observed with hemoglobin in Fig. 4 (*bottom*), can be interpreted in terms of long-time self-diffusion, which is dominated by hydrodynamic interactions. Moreover, the factor that had to be chosen in Fig. 4 (*bottom*) to superimpose experimental $H(q)$ data and those calculated for short-time diffusion, ≈2.1, is close to the theoretical ratio of the short- and long-time diffusion coefficient at $\Phi = 0.25$ (17). Moreover, the fast initial decay of the correlation function observed at the highest q-value in Fig. 3 supports the existence of short-time diffusion.

Effect of the protein hydration shell

While the experimental values for the long-time self-diffusion coefficient of colloidal suspensions agree quite well with theoretical predictions at intermediate and high concentrations (17,18), consistently lower values are observed for hemoglobin and other proteins. As mentioned above, this discrepancy could indicate transient protein clusters due to attractive forces. For this reason we have performed extensive SANS studies of concentrated myoglobin solutions (31). The MSA analysis of the scattering curves was, however, consistent with hard-sphere monomers. For hemoglobin, a small fraction of oligomers had to be assumed to explain the scattering curves (5,32). Figs. 1 and 5 show that myoglobin and hemoglobin, as well as other proteins (37), exhibit nearly the same exponential decrease in the self-diffusion coefficient with volume fraction. Moreover, the diffusion coefficient is only weakly dependent on the molecular weight ($D \propto M^{-1/3}$), thus cluster formation as the major cause of the decline in $D_s(\Phi)$ can be excluded. Strong electrostatic interactions can also reduce the self-diffusion coefficient (38). However, close to the isoelectric point, the average charge of hemoglobin is small (5,31). Is there an alternative explanation?

According to Alpert and Phillies, the hydration shell of the macromolecule has to be included in the volume fraction to improve agreement with hydrodynamic calculations (39,40). Moreover, Phillies derives a stretched exponential decay of $D_s(\Phi)$ as the signature of hydrodynamic interactions between particles based on heuristic arguments (41). Up to this point it was assumed that the volume fraction can be calculated from the dry protein volume in a manner similar to a large colloid. With decreasing particle size, the surface gains relevance and may affect the dynamic properties. Proteins in general are surrounded by a thin layer of interfacial water. Due to the larger surface/volume ratio of protein molecules with respect to a conventional colloid, the weight fraction of the hydration shell, ~0.3 g/g protein, is significant. The interfacial water moves with the protein (stick condition) and thus contributes to the hydrodynamic volume v_h. The volume fraction discussed above refers to the bare protein and was calculated from the dry specific volume, $v_d = 0.75$ cc/g (42) using $\Phi = c_p \cdot v_d$, where c_p denotes the concentration in g/cc. Thus the 330 mg/ml of hemoglobin in RBCs yield a volume fraction of 0.247. The protein specific volume is a thermodynamic quantity, which does not include the hydration shell. Fitting the intermolecular structure factor $S(q)$ of protein solutions to a hard sphere model (MSA) yields the dry- and not the hydrodynamic volume as the relevant size parameter (5,32). The hydration shell, however, contributes to protein friction and the hydrodynamic function $H(q)$: The hard-sphere radius of hemoglobin determined from the static structure factor by scattering experiments is 28 (±1) Å (5), while the hydrodynamic radius determined from diffusion measurements amounts to 31 Å. The diffusion coefficient, which involves the ratio of $H(q)/S(q)$ thus depends on both the dry- and the hydrodynamic volume. Dry and hydrodynamic volume are related by Tanford (42): $v_h = v_d + \delta \cdot v_s$. Here v_s denotes the specific volume of the solvent and δ denotes the fraction of solvent contributing effectively to the protein volume. The volume fraction is now an adjustable parameter depending on $0 \leq \delta \leq 1$. For hemoglobin at $c_p = 330$ mg/ml, one has $\Phi_d = 0.25$, which we have used above, while the hydrated volume fraction is $\Phi_h = 0.36$, assuming $\delta = 0.35$. With the conventional definition of the volume fraction $\Phi = 4/3\pi\, n_p\, R^3$, one obtains, inserting the radius of the equivalent sphere ($R = 28$ Å), $\Phi_d = 0.27$, while with the hydrodynamic radius $R_H = 31$ (±0.05) Å one obtains $\Phi_h = 0.366$. Therefore the discrepancy observed between theoretical and experimental values of the long-time diffusion coefficient of colloidal protein solutions could be relieved by introducing a renormalized volume fraction, which takes the hydration shell into account. As mentioned above, the concentration dependence of theoretical and experimental values can be approximated by an exponential decay assuming a characteristic volume fraction Φ_0. For hemoglobin and myoglobin, one obtains $\Phi_0 = 0.15$ (±0.01), while the calculated long-time diffusion coefficient is approximated by $\Phi_0 = 0.189$. The renormalization factor would thus amount to 1.26. Attributing the discrepancy totally to this effect would yield an effective specific volume of 0.945 cc/g instead of 0.75 cc/g in the dry case. The dynamic effective volume fraction of hemoglobin in RBCs is then 0.32. This shift is indicated by an arrow in Fig. 4 and indeed improves the agreement with the calculated D_s^L.

CONCLUSIONS

We have shown that protein diffusion at high concentration and inside erythrocytes can be understood based on concepts developed for colloidal suspensions with particles of much larger size. The main difference is that the effective volume fraction of proteins includes the interfacial water due to the large surface/volume ratio. In crowded environments, excluded volume interactions determine the interprotein structure factor. However, the interprotein friction and the long-time self-diffusion coefficient are controlled mainly by hydrodynamic interactions. This conclusion is based essentially on the observed q-dependence of the self-diffusion coefficient, which is a characteristic feature of hydrodynamic interactions. The concentration dependence of D_s alone would not prove the point, since, for instance, the same trend could be reproduced by Brownian dynamics simulations of proteins assuming Lennard-Jones and screened electrostatic interactions without hydrodynamic coupling (43). A second argument concerns the compensation between osmotic and friction effects, discussed above in the context of Fig. 1. It gives rise to a nearly concentration-independent collective diffusion coefficient. This property, $D_c(\Phi) \approx$ constant, was derived for hard sphere colloids at short times, where hydrodynamic interactions prevail (16). Moreover, the friction factor $H(q)$ varies in phase with the structure factor $S(q)$ even at long times. This result establishes the missing link between osmotic and friction effects. It also provides a rational for the puzzling observation, derived from dynamic light scattering, that $H(q \rightarrow 0)$ of globular proteins decreases with the volume fraction at intermediate concentrations (20). According to calculations of Tokuyama and Oppenheim, long-range hydrodynamic forces play an important role at long times, while excluded volume interactions are drastically reduced (17). Thus a new mechanism of long-range communication in addition to electrostatic coupling between protein molecules in cells and tissue is proposed.

The deuterated erythrocytes were prepared by A. Chmel. Excellent technical assistance by members of the Institut Laue-Langevin in Grenoble (G. Kali) and the LLB in Paris are also very much acknowledged.

This work was supported partially by a grant of the Deutsche Forschungsgemeinschaft (No. SFB 533, TP B11), which is gratefully acknowledged.

REFERENCES

1. Ellis, R. J. 2001. Macromolecular crowding: obvious but underappreciated. *Trends Biochem. Sci.* 26:597–604.
2. Han, J., and J. Herzfeld. 1993. Macromolecular diffusion in crowded solutions. *Biophys. J.* 65:1155–1161.
3. Minton, A. P. 2001. The influence of macromolecular crowding and macromolecular confinement on biochemical reactions in physiological media. *J. Biol. Chem.* 276:10577–10580.
4. Zimmerman, S. B., and A. P. Minton. 1993. Macromolecular crowding: biochemical, biophysical, and physiological consequences. *Annu. Rev. Biophys. Biomol. Struct.* 22:27–65.
5. Krueger, S., and R. Nossal. 1988. SANS studies of interacting hemoglobin in intact erythrocytes. *Biophys. J.* 53:97–105.
6. Perutz, M. 1948. Submicroscopic structure of the red cell. *Nature.* 161:204.
7. Wang, D., U. Kreutzer, Y. Chung, and T. Jue. 1997. Myoglobin and hemoglobin rotational diffusion in the cell. *Biophys. J.* 73:2764–2770.
8. Everhart, C. H., and C. S. Johnson. 1982. The determination of tracer diffusion coefficients of proteins by means of pulsed field gradient NMR with applications to hemoglobin. *J. Mag. Res.* 48:466–474.
9. Kuchel, P. W., and B. E. Chapman. 1991. Translational diffusion of hemoglobin in human erythrocytes and hemolysates. *J. Mag. Res.* 94:574–580.
10. Papadopoulos, S., V. Endeward, B. Revesz-Walker, K. D. Jürgens, and G. Gros. 2001. Radial and longitudinal diffusion of myoglobin in single living heart and skeletal muscle cells. *Proc. Natl. Acad. Sci. USA.* 98:5904–5909.
11. Riveros-Moreno, V., and J. B. Wittenberg. 1972. The self-diffusion coefficients of myoglobin and hemoglobin in concentrated solutions. *J. Biol. Chem.* 247:895–901.
12. Clark, A., Jr., W. J. Federspiel, P. A. A. Clark, and G. R. Cokelet. 1985. Oxygen delivery from red cells. *Biophys. J.* 47:171–181.
13. Jones, C. R., and C. Johnson. 1978. Photon correlation spectroscopy of hemoglobin. *Biopolymers.* 17:1581–1593.
14. Berland, K. M., P. T. C. So, and E. Gratton. 1995. Two-photon fluorescence correlation spectroscopy: method and application to the intracellular environment. *Biophys. J.* 68:694–701.
15. Haustein, B., and P. Schwille. 2004. Single-molecule spectroscopic methods. *Curr. Opin. Struct. Biol.* 14:531–540.
16. Beenakker, C. W. J., and P. Mazur. 1984. Diffusion of spheres in a concentrated suspension II. *Phys.* 126A:349.
17. Tokuyama, M., and I. Oppenheim. 1994. Dynamics of hard-sphere suspensions. *Phys. Rev. E.* 50:R16–R19.
18. van Blaaderen, A., J. Peetermans, G. Maret, and J. K. Dhont. 1992. Tong-time self-diffusion of spherical colloidal particles measured with fluorescence recovery after photobleaching. *J. Chem. Phys.* 96:4591–4603.
19. Segre, P. N., and P. N. Pusey. 1997. Dynamics and scaling in hard-sphere colloidal suspensions. *Phys. A.* 245:9–18.
20. Fine, B. N., A. Lomakin, O. O. Ogun, and G. B. Benedek. 1996. Static structure factor and collective diffusion of globular proteins in concentrated aqueous solution. *J. Chem. Phys.* 104:326–335.
21. Dhont, J. K. 1996. An Introduction to Dynamics of Colloids. D. Möbius and R. Miller, editors. Elsevier, Dordrecht, The Netherlands.
22. Schmitz, K. S. 1990. An Introduction to Dynamic Light Scattering of Macromolecules. Academic Press, Boston.
23. Boon, J. P., and S. Yip. 1980. Molecular Hydrodynamics. Dover Publications, Mineola, NY.
24. Ackerson, B. J. 1976. Correlations for interacting Brownian particles. *J. Chem. Phys.* 64:242–246.
25. Pusey, P. N. 1989. Colloidal Suspensions in Liquids, Freezing and the Glass Transition. Elsevier Science Publishers, Les Houches.
26. Doster, W. 2005. Protein-water displacement distributions. *Biochim. Biophys. Acta.* 1749:173–186.
27. Perez, J., J. M. Zanotti, and D. Durand. 1999. Evolution of the internal dynamics of two globular proteins from dry powder to solution. *Biophys. J.* 77:454–469.
28. Lechner, R. E., and S. Longeville. 2005. Quasielastic Neutron Scattering in Biology, part 1: Methods. *In* Neutron Scattering in Biology: Techniques and Applications. J. Fitter, T. Gutberlet, and J. Katsaras, editors. Springer, Berlin.
29. Hall, R. S., and C. S. Johnson. 1980. *J. Chem. Phys.* 72:4251–4253.
30. Diehl, M. 1994. Diploma thesis. Munich, Germany.
31. Longeville, S., W. Doster, and G. Kali. 2003. Myoglobin in crowded solutions: structure and diffusion. *Chem. Phys.* 292:413–424.

32. Krueger, S., S. H. Chen, J. Hofrichter, and R. Nossal. 1990. Small angle neutron scattering studies of HbA in concentrated solutions. *Biophys. J.* 58:745–757.
33. Hayter, J. B., and J. Penfold. 1981. An analytic structure factor for macroion solutions. *Mol. Phys.* 42:109–118.
34. Belloni, L. 1986. Electrostatic interactions in colloidal solutions: comparison between primitive and one-component models. *J. Chem. Phys.* 85:519–526.
35. Tokuyama, M., and I. Oppenheim. 1995. On the theory of concentrated hard-sphere suspensions. *Phys. A.* 216:85–119.
36. Medina-Noyola, M. 1988. Long-time self-diffusion in concentrated colloidal dispersions. *Phys. Rev. Lett.* 60:2705–2708.
37. Le Bon, C., T. Nicolai, M. E. Kuil, and J. G. Hollander. 1999. Self-diffusion and cooperative diffusion of globular proteins in solution. *J. Phys. Chem.* 103:10294–10299.
38. Tokuyama, M. 2005. Statistical mechanical theory of short-time self-diffusion in dilute suspensions of highly charged colloids. *Phys. A.* 352:252–264.
39. Alpert, S. 1976. Hydration effects in the diffusion of spherical macromolecules. *J. Chem. Phys.* 65:4333–4334.
40. Phillies, G. D. 1976. Diffusion of spherical macromolecules at finite concentration. *J. Chem. Phys.* 65:4334–4335.
41. Phillies, G. D. J. 1988. The hydrodynamic scaling model for polymer self-diffusion. *J. Phys. Chem.* 93:5029–5039.
42. Tanford, C. 1961. Physical Chemistry of Macromolecules. John Wiley and Sons, New York, London, Sydney.
43. Dwyer, J. D., and V. A. Bloomfield. 1993. Brownian dynamics simulations of probe and self-diffusion in concentrated protein and DNA solutions. *Biophys. J.* 65:1810–1816.

Quasielastic Neutron Scattering in Biology Part I: Methods

Ruep E. Lechner[1] and Stéphane Longeville[2]

[1]Hahn-Meitner-Institut Berlin, Glienicker Strasse 100, D-14109 Berlin, Germany, and [2]Laboratoire Léon Brillouin, CEA Saclay, F-91191 Gif-sur-Yvette, France

1 Introduction

Biological macromolecules and biological systems, in general, are constructed according to well-defined building schemes exhibiting a certain degree of long-range order. But they are also characterized by an appreciable amount of disorder, for several reasons. One is that high structural symmetry is generally absent in native samples, except for the rare cases with integral single-crystalline regions. Another is that long-range order is limited to certain parts of the macromolecules and to part of the degrees of freedom. Furthermore, the ubiquitous presence of water which is generally a prerequisite for the unrestrained performance of biological function plays an important role. The interaction of water molecules with biological surfaces, their diffusion close to and within the hydration layers covering biological macromolecules, provides the latter with the indispensable additional space for the conformational degrees of freedom required for function. The presence of mobile water molecules not only allows or induces additional short-range translational and rotational diffusive motion of parts of biological macromolecules, but also causes damping of low-frequency vibrations in the macromolecules. All these motions which are believed to be essential for biological function, are an important part of the dynamical characteristics of biological matter. The ensemble of low-energy transfer inelastic (IENS) and quasielastic neutron scattering (QENS) techniques is particularly well-suited for their investigation. In the present article, the basic principles of these techniques are outlined from the viewpoints of theory, experiment and analysis, with an emphasis on application to biological problems. The method of QENS[1] focuses on scattering processes involving small amounts of energy exchange [2], with spectral distributions peaked at zero energy transfer. IENS spectra extend to somewhat higher energies, but are, by principle, also overlapping with the

[1] The acronym "QENS" is used for quasielastic neutron scattering in general, and "QINS", for quasielastic neutron scattering, when it is purely incoherent, in order to distinguish this case from the coherent one.

[2] in this context, "small " means: i) the concerned energy transfers are located in the low-energy region of inelastic neutron scattering spectra, and ii) they cover a region close to zero, but are still resolved by the elastic energy resolution

QENS energy region. Both together allow us to study dynamical phenomena in the *time* region of 10^{-13} to 10^{-7} s. Atomic and molecular motions are explored in *space*, on length scales comparable with the wavelengths of the neutrons used in the scattering experiments. Typical spatial parameters, such as vibrational displacements, jump distances, diffusion paths, and correlation lengths, are amenable to evaluation in the range from 10^{-9} cm to 10^{-6} cm. Quasielastic and inelastic neutron scattering experiments on such dynamic processes lead to spectra of energy transfers

$$\hbar\omega = E - E_0 \ , \tag{1}$$

in a range from 10 to 10^{-5} meV, where E_0 and E are the neutron energies before and after scattering, respectively. The corresponding momentum transfer $\hbar\mathbf{Q}$ in such a process is proportional to the scattering vector

$$\mathbf{Q} = \mathbf{k} - \mathbf{k}_0 \ , \tag{2}$$

where $\mathbf{k}_0$ and $\mathbf{k}$ are the neutron wave vectors before and after scattering, respectively. The wave-vector transfer values Q for elastic scattering, $Q = (4\pi/\lambda)\sin(\varphi/2)$, are typically in the region of 0.1 to 5 $\AA^{-1}$ (λ = neutron wavelength, φ = scattering angle, i.e. the angle between the vectors $\mathbf{k}_0$ and $\mathbf{k}$), such that $2\pi/Q$ ranges from the order of magnitude of interatomic distances to that of diameters of (e.g. biological) macromolecules. The neutron scattering intensity in such a process is proportional to the so-called *scattering function* or *dynamic structure factor* $S(\mathbf{Q},\omega)$, which can be calculated for typical dynamical processes; the calculation and determination of this function is the subject of the following paragraphs. The purpose of QENS experiments is mainly the study of the details of "quasielastic lines", i. e. of the low-energy spectra which are mostly due to some kind of diffusive or damped vibrational atomic and molecular motions. In the energy domain, this mainly refers to the part of the dynamical function which has a maximum centered around zero energy transfer. In the time domain, it corresponds to the relaxation of the dynamical functions. For instance, in the well-understood case of classical atomic (self-) diffusion, the relaxation function has a single exponential time decay for small Q values, $I_s(Q,t) \sim exp(-\Gamma t)$ with $\Gamma = 1/\tau = D_s Q^2$, where τ is the decay constant and D_s is the self-diffusion coefficient. This transforms in the energy domain to a Lorentzian function with the width Γ. For larger scattering vectors, Γ depends on the geometric and dynamic details of the diffusion process. Obviously, for a particle *at rest*, $\Gamma = 0$ and $S(\mathbf{Q},\omega)$ is a sharp (elastic) line $\delta(\omega)$ at $\hbar\omega = 0$. This is analogous to resonance absorption of gamma rays, where this corresponds to the well-known Mössbauer line.

The interpretation of the scattering function $S(\mathbf{Q},\omega)$ in terms of diffusive and/or vibrational processes is relatively simple, if

– such motions can be described by classical physics, i.e. when quantum effects can be completely neglected, and if - as in most practical cases -

– the scattering can be treated in first Born approximation. This allows an evaluation and interpretation of $S(\mathbf{Q},\omega)$ by pair correlation functions for the scattering nuclei in space and time, which includes the self-correlation function $S_{\rm s}(\mathbf{Q},\omega)$ as a special case.

This article (Part I) is organized in several sections dealing with the various topics relevant in our context in the following order :
Section 2: Basic theory of neutron scattering: Incoherent and coherent scattering functions and intermediate scattering functions; Van Hove correlation functions; coherent structure factor, elastic incoherent structure factor (EISF); experimental resolution and observation time.
Section 3: Instruments for QENS Spectroscopy in $(\mathbf{Q},\omega)$-space: direct and inverted geometry TOF, and BSC techniques.
Section 4: Instruments for QENS Spectroscopy in $(\mathbf{Q},t)$-space: NSE and NRSE techniques. For applications of these techniques in biological studies, the reader is referred to Part II in this Volume.

2 Basic Theory of Neutron Scattering

Information on the dynamic structure of condensed matter is obtained by analyzing the intensity of neutrons, for instance from a monochromatic beam scattered by a sample into a solid angle element $d\Omega$ and an energy interval $d(\hbar\omega)$. This is proportional to the double-differential scattering cross-section $\frac{\mathrm{d}^2\sigma}{\mathrm{d}\Omega\mathrm{d}\omega}$ which reads

$$\frac{\mathrm{d}^2\sigma}{\mathrm{d}\Omega\,\mathrm{d}\omega} = \frac{k}{k_0}\frac{\sigma}{4\pi}S(\mathbf{Q},\omega)\ . \tag{3}$$

It is factorized in three independent components: i) The ratio of the wavenumbers k and k_0 characterizing the scattering process, ii) the total scattering cross-section σ for a rigidly bound nucleus (where $\sigma = 4\pi b^2$ and b is the corresponding scattering length of the nucleus), and iii) the Van Hove scattering function $S(\mathbf{Q},\omega)$ [1]. The latter depends on the scattering vector $\mathbf{Q}$ and the energy transfer $\hbar\omega$ as defined by Eqs. (1) and (2). The structural and dynamical properties of the scattering sample are fully described by $S(\mathbf{Q},\omega)$ which, *for monatomic systems*, does not depend on neutron-nuclear interaction, i.e. on the nuclear cross-sections. The scattering function and its relation with several other functions important for the description of scattering experiments will be discussed below. The details of the derivation can be found in standard text books [2, 3, 4].

Before we can consider these relations and the properties of scattering functions, we have to note a complication due to the fact that a nuclear species consists of *isotopes* with different scattering lengths $b_1, b_2 \ldots$ and concentrations $c_1, c_2 \ldots$. Therefore the intensity of scattered neutrons will in general have to be summed over terms with different scattering lengths,

randomly distributed over the atomic sites $\mathbf{r}_i$. This randomness of the amplitudes destroys part of the interference one would observe due to neutron waves scattered by different nuclei, if they all had identical scattering lengths. A similar effect is caused by the *spin* of the nuclei and that of the neutron, because the scattering length depends on their relative orientations. This leads to scattering lengths b_+ and b_- corresponding to parallel and anti-parallel orientation, with fractions $c_+ = (I+1)/(2I+1)$ and $c_- = I/(2I+1)$, respectively, where I is the nuclear spin. If nuclei and/or neutron spins are unpolarized, this gives a random distribution of b_+ and b_-. Randomness *destroys part of the interference* and for ideal disorder the cross-section can be separated into a coherent part with interference terms due to pairs of atoms (including the self-terms) and an incoherent part, where interference between waves scattered by different nuclei has completely cancelled out, such that the double-differential cross-section reads

$$\frac{\mathrm{d}^2\sigma}{\mathrm{d}\Omega \mathrm{d}\omega} = \frac{k}{k_0}\left[\frac{\sigma_{\mathrm{coh}}}{4\pi} S_{\mathrm{coh}}(\mathbf{Q},\omega) + \frac{\sigma_{\mathrm{inc}}}{4\pi} S_{\mathrm{inc}}(\mathbf{Q},\omega)\right] . \tag{4}$$

The coherent scattering function, $S_{\mathrm{coh}}(\mathbf{Q},\omega)$ in the first term, is due to the atom-atom pair-correlations, whereas the incoherent scattering function, $S_{\mathrm{inc}}(\mathbf{Q},\omega)$ in the second term [3], merely conveys self-correlations of single atoms and, as a consequence, only intensities (and not amplitudes) from scattering by different nuclei have to be added.

One can easily show that the total scattering cross-sections σ_{coh} and σ_{inc} have the following meaning

$$\sigma_{\mathrm{coh}} = 4\pi \bar{b}^2 \quad with \quad \bar{b} = \sum c_i b_i \ , \tag{5}$$

$$\sigma_{\mathrm{inc}} = 4\pi \left(\bar{b^2} - \bar{b}^2\right) \quad with \quad \bar{b^2} = \sum c_i b_i^2 \ . \tag{6}$$

In subsequent sections we will mainly deal with the *incoherent*, and occasionally with the *coherent* scattering function. The reason is, that the neutron scattering from native biological material is in most cases largely dominated by that of hydrogen atoms which are usually present in large numbers in organic molecules. For the hydrogen nucleus (the proton), the incoherent scattering cross-section is between 10 and 20 times larger than other scattering cross-sections, such that the separation of the incoherent scattering function $S_{\mathrm{s}}(\mathbf{Q},\omega)$ is especially easy. In the case of scattering -density fluctuations with sizeable correlation lengths, the coherent scattering contribution becomes significantly higher than the incoherent one in the small angle scattering range where the contrast between *the coherent scattering length densities* of different molecules or molecular subunits contributes as the square of the number

[3] Note that the following notations for the scattering functions (dynamic structure factors) are customary in the literature : $S(\mathbf{Q},\omega)$ or $S_{\mathrm{coh}}(\mathbf{Q},\omega)$ for coherent, and $S_{\mathrm{s}}(\mathbf{Q},\omega)$ or $S_{\mathrm{inc}}(\mathbf{Q},\omega)$ for incoherent scattering.

of diffusing centers (see below). The total coherent and incoherent (bound) scattering cross-sections are empirically known and can be found in tables [5]. The fundamental aspects of neutron-nucleus scattering are treated in an excellent review, see [6].

2.1 Van Hove Scattering Functions and Correlation Functions

Let us now consider the connection between scattering functions and static structure factors. The momentum- and energy-dependent scattering function $S(\mathbf{Q},\omega)$ was derived by Van Hove starting from the well-known static structure factor $S(\mathbf{Q})$, which is the energy-integrated scattering intensity (traditionally called "diffraction pattern"). For the simplest case of N **identical** atoms at positions $\mathbf{r}_0, \mathbf{r}_1 \ldots \mathbf{r}_N$, this is proportional to the square of the sum of amplitudes, where the phase differences between the waves scattered by pairs of particles (i,j), located at instantaneous positions $(\mathbf{r}_i, \mathbf{r}_j)$ have been taken into account. The structure factor per atom is then given by

$$S(\mathbf{Q}) = N^{-1} \sum_{i=1}^{N} \sum_{j=1}^{N} \mathrm{e}^{-\mathrm{i}\mathbf{Q}(\mathbf{r}_i - \mathbf{r}_j)} = N^{-1} \left| \sum_{i=1}^{N} \mathrm{e}^{\mathrm{i}\mathbf{Q}\mathbf{r}_i} \right|^2 \tag{7}$$

If, however, with the aid of energy analysis in a scattering experiment, the motion of nuclei (connected e.g. with molecular vibrations and/or diffusion) is observed, the structure factor becomes time-dependent: one gets the so-called intermediate scattering function (or intermediate dynamic structure factor) with time-dependent space coordinates $\mathbf{r}(t)$

$$I(\mathbf{Q},t) = N^{-1} \sum_{i=1}^{N} \sum_{j=1}^{N} \left\langle \mathrm{e}^{-\mathrm{i}\mathbf{Q}\mathbf{r}_i(0)} \mathrm{e}^{\mathrm{i}\mathbf{Q}\mathbf{r}_j(t)} \right\rangle \ . \tag{8}$$

In the most general (i.e. the quantum-mechanical) case, $\mathbf{r}_i$ are operators, and $\langle \cdots \rangle$ is a thermal average of the expectation value for the product enclosed in the brackets. Under classical conditions, i.e. at sufficiently low energies and sufficiently high temperatures, which is usually fulfilled in the context of quasielastic neutron scattering on biological samples in a physiological environment, the quantities $\mathbf{r}$ are vectors in space and not operators, and $\langle \cdots \rangle$ is simply the thermal average. If the scattering is incoherent, we need only the self-terms in Eq. (8) which leads to

$$I_\mathrm{s}(\mathbf{Q},t) = N^{-1} \sum_{i=1}^{N} \left\langle \mathrm{e}^{-\mathrm{i}\mathbf{Q}\mathbf{r}_i(0)} \mathrm{e}^{\mathrm{i}\mathbf{Q}\mathbf{r}_i(t)} \right\rangle \ . \tag{9}$$

Here, since all the atoms are assumed to be identical, eq. (9) can be simplified: the index i may be omitted and the sum $\sum$ replaced by N. From

these relations Van Hove [1] derived the following expression for the coherent scattering function $S(\mathbf{Q},\omega)$:

$$S(\mathbf{Q},\omega) = (2\pi)^{-1} \int_{-\infty}^{+\infty} I(\mathbf{Q},t)\mathrm{e}^{-\mathrm{i}\omega t}\mathrm{d}t \ , \tag{10}$$

Similarly, for its self-part, namely the so-called "incoherent" contribution (see below), he obtained

$$S_\mathrm{s}(\mathbf{Q},\omega) = (2\pi)^{-1} \int_{-\infty}^{+\infty} I_\mathrm{s}(\mathbf{Q},t)\mathrm{e}^{-\mathrm{i}\omega t}\mathrm{d}t \ . \tag{11}$$

Furthermore, he defined the correlation functions [4], namely

$$G(\mathbf{r},t) = (2\pi)^{-3} \int_{-\infty}^{+\infty}\int_{-\infty}^{+\infty} \mathrm{e}^{-\mathrm{i}(\mathbf{Q}\mathbf{r}-\omega t)} S(\mathbf{Q},\omega)\mathrm{d}\mathbf{Q}\mathrm{d}\omega \ , \tag{12}$$

and for the self-part

$$G_\mathrm{s}(\mathbf{r},t) = (2\pi)^{-3} \int_{-\infty}^{+\infty}\int_{-\infty}^{+\infty} \mathrm{e}^{-\mathrm{i}(\mathbf{Q}\mathbf{r}-\omega t)} S_\mathrm{s}(\mathbf{Q},\omega)\mathrm{d}\mathbf{Q}\mathrm{d}\omega \ , \tag{13}$$

Finally, by inversion the scattering functions are expressed as time Fourier transforms of these correlation functions, i.e.,

$$S(\mathbf{Q},\omega) = (2\pi)^{-1} \int_{-\infty}^{+\infty}\int_{-\infty}^{+\infty} G(\mathbf{r},t)\mathrm{e}^{\mathrm{i}(\mathbf{Q}\mathbf{r}-\omega t)}\mathrm{d}\mathbf{r}\mathrm{d}t \ , \tag{14}$$

$$S_\mathrm{s}(\mathbf{Q},\omega) = (2\pi)^{-1} \int_{-\infty}^{+\infty}\int_{-\infty}^{+\infty} G_\mathrm{s}(\mathbf{r},t)\mathrm{e}^{\mathrm{i}(\mathbf{Q}\mathbf{r}-\omega t)}\mathrm{d}\mathbf{r}\mathrm{d}t \ . \tag{15}$$

The interpretation of eqs. (8) to (13) is straightforward in the *classical approximation*. The interference of neutron waves scattered by *pairs of different atoms* at positions $\mathbf{r}_i$ and $\mathbf{r}_j$ at different times 0 and t, respectively, is taken into account by the cross terms with $i \neq j$ in $I(\mathbf{Q},t)$. $I_\mathrm{s}(\mathbf{Q},t)$, however, does not contain such cross terms, because it is only due to the interference of waves scattered by the *same* nucleus which is in general located at different positions for different times. The classical meaning of the Van Hove correlation functions can therefore be described as follows: $G(\mathbf{r}_j - \mathbf{r}_i, t)$ is

[4] now called Van Hove correlation functions after this author

the conditional probability per unit volume to find an atom (nucleus) at a position $\mathbf{r}_j$ at time t, if this or another atom has been at a position $\mathbf{r}_i$, with a distance vector $\mathbf{r} = \mathbf{r}_j - \mathbf{r}_i$, at a previous time $t = 0$. Analogously, the self-correlation function, $G_s(\mathbf{r}, t)$, is the conditional probability per unit volume to find an atom at $\mathbf{r}(t)$ at time t, if the same atom has been at the origin $\mathbf{r} = 0$ at $t = 0$.
When using this classical interpretation, one should however not forget its limits. The conditions for the validity of the classical approximation are, that the amounts of energy and momentum exchanged in the scattering process remain sufficiently small to fulfill the following relations with the thermal energy:

$$|\hbar\omega| << \frac{1}{2}k_BT \tag{16}$$

$$(\hbar Q)^2/2M << \frac{1}{2}k_BT \tag{17}$$

where k_BT = Boltzmann's constant and M = atomic mass. Therefore quantum effects are expected for large $\mathbf{Q}$ and large ω (or for small $\mathbf{r}$ and small t). In the realm of quasielastic neutron scattering concerned with ranges of fairly small Q and ω, the scattering functions may nevertheless be calculated classically, if they are then corrected by the so-called detailed-balance factor, $exp(-\hbar\omega/2k_BT)$. Because of the energy dependence of level occupation according to the Boltzmann distribution, the exact (quantum-mechanical) scattering functions for energy gain and energy loss are always related in the following way:

$$S(-\mathbf{Q}, -\omega) = exp(+\hbar\omega/k_BT)S(\mathbf{Q}, \omega) \tag{18}$$

This asymmetry with respect to $\hbar\omega = 0$ distinguishes $S(\mathbf{Q}, \omega)$ from the classical function, $S^{cl}(\mathbf{Q}, \omega)$, which is symmetric in ω. The symmetric function obtained, if both sides of eq. (18) are multiplied by the detailed-balance factor, is a very good approximation of the true $S(\mathbf{Q}, \omega)$:

$$S(\mathbf{Q}, \omega) = exp(-\hbar\omega/2k_BT)S^{cl}(\mathbf{Q}, \omega) \tag{19}$$

and analogously for incoherent scattering:

$$S_s(\mathbf{Q}, \omega) = exp(-\hbar\omega/2k_BT)S_s^{cl}(\mathbf{Q}, \omega) \tag{20}$$

Since in this article, we will essentially deal only with classical scattering functions, the superscript "cl" for classical functions will be omitted.
The following special cases of Van Hove's correlation functions are of particular interest. At $t = 0$, we have

$$G_s(\mathbf{r}, t = 0) = \delta(\mathbf{r}) \quad and \quad G(\mathbf{r}, t = 0) = \delta(\mathbf{r}) + g(\mathbf{r}) \ , \tag{21}$$

where $g(\mathbf{r})$ is the instantaneous pair correlation function accessible through diffraction experiments. From this one gets

$$S(\mathbf{Q}) = \int_{-\infty}^{+\infty} S(\mathbf{Q},\omega)\mathrm{d}\omega = 1 + \int_{-\infty}^{+\infty} g(\mathbf{r})\mathrm{e}^{\mathrm{i}\mathbf{Q}\mathbf{r}}\mathrm{d}\mathbf{r} \ = I(\mathbf{Q}, t=0) \qquad (22)$$

Furthermore, we note that at $\mathbf{r} \ = 0$, $G_\mathrm{s}(\mathbf{r},t)$ is the probability that a certain nucleus which was at $\mathbf{r} = 0$ for $t = 0$, is still (or again) at $\mathbf{r} = 0$ for a time t.

2.2 The Elastic Incoherent Structure Factor

Another important special case concerns the behaviour of the correlation functions at very long times. For an atom diffusing in a space which is very large as compared to the interatomic distances, the self-correlation function $G_\mathrm{s}(\mathbf{r},t)$ vanishes, if t goes to infinity, whereas, for an atom *bound to a finite volume* (e.g. as part of a rotating molecule fixed in a crystal), $G_\mathrm{s}(\mathbf{r},t)$ approaches a finite value $G_\mathrm{s}(\mathbf{r},\infty)$ for $\mathbf{r}$ varying in the interior of this volume. In fact, very generally, the self-correlation function can be split into its asymptotic value in the long-time limit and a time-dependent term $G'_\mathrm{s}(\mathbf{r},t)$, according to

$$G_\mathrm{s}(\mathbf{r},t) = G_\mathrm{s}(\mathbf{r},\infty) + G'_\mathrm{s}(\mathbf{r},t) \qquad (23)$$

The Fourier transform of this expression reads :

$$S_\mathrm{s}(\mathbf{Q},\omega) = (2\pi)^{-1} \int_{-\infty}^{+\infty}\int_{-\infty}^{+\infty} \mathrm{e}^{\mathrm{i}(\mathbf{Q}\mathbf{r}-\omega t)}[G_\mathrm{s}(\mathbf{r},\infty) + G'_\mathrm{s}(\mathbf{r},t)]\mathrm{d}\mathbf{r}\mathrm{d}t \ . \qquad (24)$$

which gives

$$S_\mathrm{s}(\mathbf{Q},\omega) = S^{el}_\mathrm{s}(\mathbf{Q})\delta(\omega) + S^{in}_\mathrm{s}(\mathbf{Q},\omega) \qquad (25)$$

It is seen that the incoherent scattering function is decomposed into a purely elastic line, $S^{el}_\mathrm{s}(\mathbf{Q})\delta(\omega)$, with the integrated intensity $S^{el}_\mathrm{s}(\mathbf{Q})$, and a nonelastic component, $S^{in}_\mathrm{s}(\mathbf{Q},\omega)$. The elastic line is the result of diffraction of the neutron on the "infinite time" *distribution in space of a single nucleus spread over a finite volume by its motion*, as already pointed out by Stiller [7]. Therefore we can derive information about the structure in a very direct way from *incoherent* scattering [8]. This is clearly a rather important result of the Van Hove theory. We now turn to its application which will be further discussed later, in the context of practical examples in the subsequent Sections.

In order to systematically exploit the theoretical fact expressed by eq. (25) in neutron scattering experiments, the concept of the *elastic incoherent structure factor* (EISF) was formulated by Lechner in 1971 (for reviews see [9], [10] and [11]). The EISF concept provides a method, that permits the extraction of structural information on localized single-particle motions by the determination of the elastic fraction of the measured spectral intensity.

The idea is simple : First, by employing sufficiently high energy-resolution, the measured integrals of elastic (I^{el}) and nonelastic (I^{in}) components of the scattering function in eq. (25) - after trivial corrections for the factor $\frac{k}{k_0}$ (see eq. (3)), the sample self-attenuation and the energy-dependent detector efficiency - are determined separately. Then an intensity ratio involving the two integrals can be defined,

$$EISF = I^{el}/(I^{el} + I^{in}) = AS_{\rm s}^{el}(\mathbf{Q})/[A \int_{-\infty}^{+\infty} S_{\rm s}(\mathbf{Q},\omega)\mathrm{d}\omega] \qquad (26)$$

where A is a normalization factor proportional to experiment parameters such as the incident neutron flux, the sample size, the detector efficiency, the duration of the measurement, etc... Obviously, the difficulty of an absolute intensity calibration, is avoided in the determination of the EISF by eq.(26): The normalization factor cancels, the integral of the incoherent scattering function is equal to 1 by definition, and we simply have $EISF = S_{\rm s}^{el}(\mathbf{Q})$. Here, we have used the relations (25) and (26) as a starting point for obtaining a definition of the EISF. The coefficient $S_{\rm s}^{el}(\mathbf{Q})$ in these two equations is the EISF in its most general form, since it includes *all the motions* of the scattering atom.

However, the determination of this "global" EISF is generally not the immediate aim of an experiment, for the following reasons. First of all, one is often more interested in specific types of motions, than in all of them. Secondly, an unambigous measurement of a global EISF is not easily achieved in just one single experiment. Every measurement has a well defined energy resolution connected with an effective energy transfer window (see the corresponding discussion in Sec. 2.3). Essentially only the dynamics of the specific motions occurring in this energy range are visible, because much slower motions are hidden within the energy resolution function, whereas much faster motions appear only as a flat background. This can be used to experimentally isolate the effect of a specific motion. It is therefore much more interesting to apply the EISF concept to the elastic component of each specific type of motion, e.g. to molecular rotation, rather than to the combined effect of all atomic motions. The expression to be used for the analysis of such specific motions is formally the same as (26). However, we have to replace the nonelastic integral (I^{in}) by the corresponding quasielastic integral (I^{qe}), and keep in mind that the incoherent scattering function, $S_{\rm s}(\mathbf{Q},\omega)$, must now be replaced by a partial incoherent scattering function, $S_{\rm s}^{qe}(\mathbf{Q},\omega)$, consisting merely of an elastic term (measured integral: I^{el}) and a quasielastic term (measured integral: I^{qe}) which correspond to the specific motion under study. The EISF then reads :

$$EISF = I^{el}/(I^{el} + I^{qe}) = AS_{\rm s}^{el}(\mathbf{Q})/[A \int_{-\infty}^{+\infty} S_{\rm s}^{qe}(\mathbf{Q},\omega)\mathrm{d}\omega] \qquad (27)$$

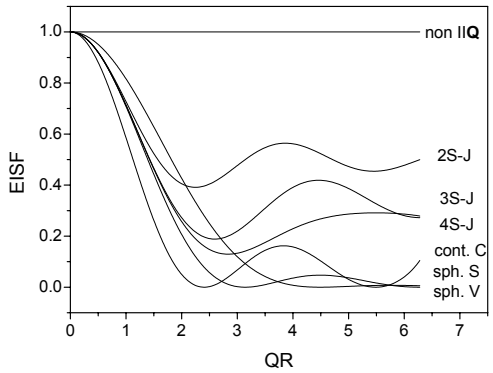

Fig. 1. Elastic incoherent structure factor (EISF) for various models of localized diffusive (e.g. rotational) motion of small side-groups of biological macromolecules, or of small solute molecules or even water molecules in an aqueous solution. The corresponding theoretical expressions are given in Table 1; the abbreviations have the following meaning: *non* $\parallel$ **Q** = no component of motion along the vector **Q**; 2S-J = random jump diffusion between two sites separated by a distance 2R; 3S-J = random jump diffusion between three equidistant sites on a circle of radius R; 4S-J = random jump diffusion between four equidistant sites on a circle of radius R; cont. C = continuous diffusion on a circle with radius R, with the **Q** vector in the plane of the circle; sph. S = continuous diffusion on a spherical surface with radius R ; sph. V = continuous diffusion in the interior of a spherical volume with radius R. Note that two of these models, *non* $\parallel$ **Q** and cont. C, are anisotropic, whereas two, sph. S and sph. V, are intrinsically isotropic. The three jump models are presented in an isotropic form obtained by orientational averaging. The full theoretical expressions for these and other models can be found in [9] and [4].

Here, the effect of faster motions has been subtracted as a flat "inelastic" background and only appears as an attenuating Debye-Waller factor bound to be cancelled, because it is included in the normalization factor A. Note that $S_s^{qe}(\mathbf{Q},\omega)$ by definition has the same normalization as $S_s(\mathbf{Q},\omega)$. The feasibility conditions are that i) the energy resolution is adapted to the time scale of the motion of interest, ii) this motion is sufficiently well separated on the energy-scale from other motions of the same atom, and iii) the assumption of dynamical independence of the different modes from each-other, e.g. rotations and vibrations, represents an acceptable approximation (see eqs.(1) and (2) in Sec. 2.1 of Part II in this Volume). It is this possibility of isolating the EISF of *specific modes of motions*, that has proved of most

practical importance for the application of the technique. This isolation, of course, means separating the elastic from the quasielastic component of the QENS spectrum. Due to an important sum rule concerning the incoherent scattering function, namely the property that its integral is equal to unity, we have

$$EISF(\mathbf{Q}) + QISF(\mathbf{Q}) = 1 \tag{28}$$

where QISF is the quasielastic incoherent structure factor. The latter is the **Q**-dependent spectral weight of the quasielastic component. It obviously contains the same structural information as the EISF, and is sometimes used instead of the latter, for technical reasons (e.g. in case of Bragg contamination of the EISF).

Table 1. EISF expressions corresponding to the curves of Fig. 1 for several models of atomic motion; the meaning of the model names is explained. $[J_0(QR)]$ = Bessel function of the first kind, with integer order; $[j_n(QR)]$ = spherical Bessel function of the first kind, with fractional order; R = radius.

model name	meaning :	EISF
non $\parallel \mathbf{Q}$	no component of motion along the vector **Q**	1.0
2S-J	random jump diffusion between two sites separated by a distance 2R; orientationally averaged function	$\frac{1}{2}[1 + j_0(2QR)]$
3S-J	random jump diffusion between three equidistant sites on a circle of radius R; orientationally averaged function	$\frac{1}{3}[1 + 2j_0(QR\sqrt{3})]$
4S-J	random jump diffusion between four equidistant sites on a circle of radius R; orientationally averaged function	$\frac{1}{4}[1 + j_0(2QR)$ $+2j_0(QR\sqrt{2})]$
cont. C	continuous diffusion on a circle with radius R, with $\mathbf{Q} \parallel$ plane of circle [12]	$[J_0(QR)]^2$
sph. S	continuous diffusion on a spherical surface with radius R [13]	$[j_0(QR)]^2$
sph. V	continuous diffusion in the interior of a spherical volume with radius R [14]	$[3j_1(QR)/QR]^2$

The EISF method represents a strategy for finding the appropriate differential equations and their boundary conditions for the dynamical mech-

anisms of localized atomic motions in condensed matter. In principle, this method can also be applied to pertinent problems concerning biological systems. This is demonstrated by Fig. 1 showing typical EISF curves which are the signatures of specific localized atomic motions and their different geometries in space. The curves have been calculated from the expressions given for various models of motion in Table 1. The models are characterized by the symmetry of the motion, its spatial extension represented by the radius R, and the orientation of the momentum transfer vector **Q** with respect to the atomic displacement vectors. Note that two of these models, "no component of motion along the vector **Q**" (*non* $\parallel$ **Q**) and "continuous diffusion on a circle" (cont. C) [12], are anisotropic, whereas two of them, "continuous diffusion on a spherical surface" (sph. S) [13] and "continuous diffusion in the interior of a spherical volume" (sph. V) [14], are intrinsically isotropic. The three jump model curves shown are presented in a form which is isotropic due to orientational averaging. The full theoretical expressions for these and other models can be found in [9] and [4].

From the shape of the EISF as a function of the dimensionless parameter QR (Q = momentum transfer, R = radius of rotation or radius of the spherical volume of diffusion, respectively), the mechanism of the concerned motion can be recognized. Early and subsequent experiments have been reviewed extensively [9], [15], [10]. In [10], the importance of the dynamic independence approximation for the definition of the EISF of specific motions, the relation between Debye-Waller factor, Lamb-Mößbauer factor and EISF, as well as the observation-time dependence of the latter are discussed in detail. In biology-related studies, the method has been applied for instance to isolate the effects of the motion of small side-groups from the total scattering function of a protein containing membrane [16]. More general discussions of Van Hove's theory and its application can be found in text books; see for instance [2, 4, 17].

2.3 Experimental Energy Resolution

Let us now turn to the problem of experimental resolution. Eqs. (14) and (15) represent a Fourier analysis of the neutron scattering functions $S(\mathbf{Q},\omega)$ and $S_{\mathrm{s}}(\mathbf{Q},\omega)$, respectively, with the Van Hove correlation functions in space and time, $G(\mathbf{r},t)$ and $G_{\mathrm{s}}(\mathbf{r},t)$, as coefficients. We draw the attention to the fact that the scattering functions S and S_{s} defined in Eqs. (4) to (15), as well as the corresponding correlation functions G, G_s, and the intermediate scattering functions I, I_s, cannot be determined experimentally in their pure forms: For instance, the measured scattering functions are broadened due to convolution with the experimental resolution functions $R(\mathbf{Q},\omega)$ in the four-dimensional $(\mathbf{Q},\omega)$ - space. In the case of incoherent scattering, the **Q** - spread of the resolution can often be neglected, when the studied functions are only slowly varying with **Q**. Then it is sufficient to "deconvolute" (see Sec. 5) the measured resolution-broadened "scattering function",

$$[S_s(\mathbf{Q},\omega)]_{meas} = \int_{-\infty}^{+\infty} S_s(\mathbf{Q},\omega')R(\omega-\omega')d\omega' \tag{29}$$

merely from the energy resolution function $R(\omega)$. The latter may have a shape close to a Gaussian or a Lorentzian, with an energy width $\Delta(\hbar\omega)$ defined as the half-width at half maximum (HWHM) [5]. Note that this width is connected, by the uncertainty relation, with the experimental *observation time* Δt_{obs} which is the decay time of the observation function $R^*(t)$ in the Fourier time domain [15], [10], [18]:

$$\Delta(\hbar\omega)\Delta t_{obs} \cong \hbar \tag{30}$$

While the resolution function $R(\omega)$ has the effect of broadening the neutron scattering function along the energy transfer coordinate of the experiment, the observation function $R^*(t)$ is a factor, which increasingly attenuates the Van Hove correlation function, as the Fourier time increases: $R^*(t)$ is the Fourier transform of $R(\omega)$ and is therefore in most practical cases a function essentially decaying with increasing time. The net effect is, that the correlation functions are observed in a Fourier time window, with an upper limit controlled by the decay time-constant of the observation function. The low-time limit of this window has a different origin : For instruments working in (Q,ω)-space, it is mainly a consequence of the (always limited) statistical accuracy of the measurement, because quasielastic intensities typically decrease with increasing energy transfer, and therefore counting statistics become the poorer the larger the energy transfers are as compared to the energy-resolution width.

Let us consider an example, in order to illustrate the implications of experimental resolution in the study of dynamic structure in the framework of the Van Hove formalism (eqs. (7) to (15)): We assume, for simplicity, that the scattering particle carries out a random motion described by a superposition of several components with n different rates, τ_1^{-1}, τ_2^{-1}, ..., τ_n^{-1}. The scattering function will then be a sum of Lorentzians centered at zero energy transfer (see the following Sections). If this quasielastic spectrum is studied with an instrument resolution $\Delta(\hbar\omega)$, the resulting resolution-broadened spectrum will have a width larger than $\Delta(\hbar\omega)$. This "quasielastic peak" will be dominated by contributions from those motions which have rates $\tau_i^{-1} \cong \Delta(\hbar\omega)$. While much slower motions are hidden within the resolution function, much faster motions will produce only a flat "background" which can not be easily distinguished from the usual constant background of the experiment. In order to be able to extract information on all relevant motional components, one needs to carry out several measurements with properly chosen resolutions.

[5] For practical reasons, we prefer here to define the resolution by its HWHM; note, however, that in the literature the resolution width is often represented by its full-width at half maximum (FWHM).

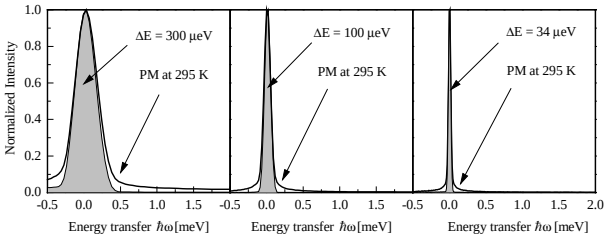

Fig. 2. Purple membrane spectra measured with three different energy resolutions (300 μeV, 100 μeV and 34 μeV (FWHM)) using incident wavelengths $\lambda = 4.54$ Å, 5.1 Å and 6.2 Å, respectively. The shaded spectra represent the resolution function obtained from a vanadium standard sample. In spite of identical dynamics the three PM spectra show strong quasielastic components with rather different apparent linewidths. This is of course due to the different observation times (i.e. different energy resolutions) employed, emphasizing dynamical aspects on different time scales of the system under study. Sample: stacks of purple membrane equilibrated at 98% relative humidity (D_2O), at room temperature. Illuminated sample size: (30×60) mm^2. Measurement times: 3 h ($\Delta E = 300$ μeV), 7 h ($\Delta E = 100$ μeV) and 14.4 h ($\Delta E = 34$ μeV), respectively. Spectra measured by J. Fitter and R. E. Lechner with the multichopper time-of-flight spectrometer NEAT (see Sec. 3.2); Figure from [19].

This procedure may in practice require the application of more than one type of spectrometer. Quasielastic neutron scattering spectra obtained with one single energy resolution only, usually furnish incomplete information. In order to avoid wrong conclusions, it is typically necessary to employ at least three different energy resolutions in the study of a given problem. Figure 2 shows as an example three spectra from a study of purple membrane [19], which demonstrate the qualitative similarity, but quantitative difference of the spectra in such a series of measurements.

Since $\Delta(\hbar\omega)$ is related in a simple way to the instrumental energy spreads of incident and scattered neutrons, the observation time Δt_{obs} is connected with (although not equal to) the coherence time of the incident neutron wave packet.

In spin-echo experiments, where *intermediate* scattering functions are measured (as a function of t), the resolution problem requires a different treatment. Here, instead of the necessity to fold scattering functions with energy resolution functions, the correction for this resolution effect essentially reduces to dividing the measured spectra by the experimental observation function $R^*(t)$.

The principle of experimental observation time, energy and Fourier time windows in quasielastic neutron scattering, and their relevance for the determination of dynamic structure, and especially in problems concerning diffusive atomic and molecular motions in condensed matter, has been discussed extensively in [10] and [18]. For further detailed literature related to the Van Hove concept and quasielastic neutron scattering, we refer to the reviews, monographs and books especially devoted to this topic [4], [20], [10], [21], [22], [9], [23], [17], [11]. A general review of diffusion studies employing quasielastic neutron scattering techniques is given in [24].

3 Instruments for QENS Spectroscopy in $(\mathbf{Q}, \boldsymbol{\omega})$ space

The role of a neutron scattering spectrometer is to monitor neutron intensity as a function of the wavevector $\mathbf{Q}$ (momentum $\hbar\mathbf{Q}$) and the energy $\hbar\omega$ exchanged with the sample. If we except the special case of Neutron Spin-Echo spectrometers, the wavelength, velocity or energy of neutrons, or their distribution as a function of these variables, have to be defined before, and analyzed after scattering in the sample. Several techniques are being used: *Crystal Bragg reflection* (XTL) for wavelength definition as a function of the reflection angle, neutron *time-of-flight* (TOF) selection and measurement using a pulsed incident beam, wavelength-band selection employing a continuous neutron velocity selector. In most of the quasielastic neutron scattering experiments, the scattering function $S(\mathbf{Q}, \omega)$ is directly measured by TOF spectrometry with resolutions from about 1 μeV to a few 1000 μeV, or by *backscattering* (BSC) spectroscopy, with resolutions of the order of $0.1\mu eV$ to $20\mu eV$. This allows to cover, by QENS, a range of diffusion coefficients between 10^{-12} m^2/s and 10^{-8} m^2/s, or, correspondingly, of characteristic times from 10^{-9} s to 10^{-13} s. Last-not-least, *neutron spin echo* (NSE) spectrometers employ neutron polarization, together with polarization analysis to define and determine the phase of neutron spins precessing in magnetic fields. The NSE method permits the direct determination of the intermediate scattering function, $I(\mathbf{Q}, t)$, instead of $S(\mathbf{Q}, \omega)$. This technique extends the Fourier time scale up to 10^{-7} s, corresponding to an energy resolution limit in the neV region, where diffusion coefficients of the order of 10^{-13} m^2/s can be measured. This will be discussed in Sec. 4. The TOF and BSC methods will be explained in the following.

3.1 XTL-TOF Spectrometers

There are different techniques of neutron time-of-flight spectrometry. Basically, XTL-TOF spectrometers[6] [25] use a crystal monochromator to create a

[6] XTL stands for crystal and TOF for time-of-flight

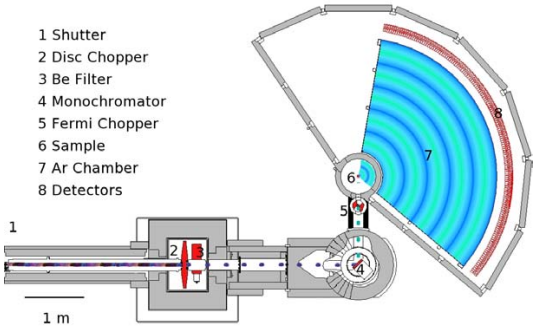

Fig. 3. FOCUS spectrometer at Paul-Scherrer Institut (PSI) [29]; FOCUS is a typical XTL-TOF spectrometer, i.e. a time-of-flight instrument with a Bragg monochromator and a time-of-flight analyzer. While the monochromator selects the incident neutron energy E_0, the energy of the scattered neutrons E is determined by measuring the neutron flight time.

continuous monochromatic beam, i.e. the incident neutron beam is monochromatized by Bragg reflection. For a given Bragg angle Θ and a corresponding reciprocal lattice vector $\mathbf{G}$, the monochromator selects a certain neutron wave number $k_0 = mv_0/\hbar$, following the Bragg equation:

$$|\mathbf{G}| = 2k_0 \sin\Theta \ . \tag{31}$$

The monochromatic beam is then periodically chopped by a disk- or Fermi-chopper, before it hits the sample. The energy distribution of the scattered neutrons is obtained by measuring their time-of-flight from the sample to the detectors which cover a large range of solid angle and consequently of Q-values. A more sophisticated version uses several crystal monochromators (located at slightly different positions and with slightly different orientations on the neutron guide) which reflect several different wavelengths selected. Due to the correlation between the monochromator reflection angle and the wavelength of reflected neutrons (and there velocities), the Fermi-chopper consecutively transmits neutron pulses from these different parts of the incident neutron beam, so that all these neutrons arrive on the detector at the same time. This is the time-focusing principle. The prototype of this spectrometer is IN6 [26, 27, 28] at the ILL. A more recent version of this instrument type is the spectrometer FOCUS at PSI [29] shown by the schematic representation

in Figure 3. This spectrometer uses a monochromator covering a large beam area, which is composed of several tens of crystal pieces with horizontal and vertical focusing (variable radius of curvature). The distance between the guide exit and the monochromator can be varied in order to achieve either a high intensity-low resolution mode or one with lower intensity, but higher resolution. This type of time-of-flight instrument is characterized by five main parameters [30]: the lattice spacing d of the crystals, the monochromator Bragg angle θ_M, the width W of the monochromator, the distances from the guide exit to the monochromator and from the monochromator to the sample, d_{GM} and d_{MS}, respectively. The width of the wavelength distribution obtained by this setup is essentially given by :

$$\Delta\lambda = d\ sin(\theta_M)\ W\ cos(\theta_M) \left| \frac{1}{d_{GM}} - \frac{1}{d_{MS}} \right| \tag{32}$$

Further contributions to the energy resolution, i.e. the energy transfer uncertainty at the detector, are the mosaic spread $\Delta\theta_M$ of the monochromator, the incident beam divergence, and the sample-detector time-of-flight spread due to finite thicknesses of sample and detectors. If these contributions are independent of each-other, they may be added quadratically.
When $d_{GM} \simeq d_{MS}$, the term given by eq (32) vanishes, and the highest possible resolution is achieved, but at the expense of beam intensity. On the other hand, the neutron intensity is maximized, when d_{GM} is chosen as small as possible, the resolution is then lower. Applications of the XTL-TOF technique, using IN6, are described in Secs. 4.4 and 5.2 of Part II in this Volume.

3.2 TOF-TOF Spectrometers

Alternatively, in the case of a TOF-TOF spectrometer, both v_0 (k_0) and v (k) are selected by time-of-flight using (at least) two choppers in front of the sample, with a mutual phase shift which determines v_0. For thermal neutrons, Fermi-choppers are often used, whereas disk-choppers are preferentially employed in the case of cold neutrons. A multi-disk chopper time-of-flight (MTOF) instrument is illustrated schematically in Fig. 4 [31]. The two principal choppers, CH1 and CH2, the sample S and the detectors D are separated by the distances L_{12}, L_{2S}, and L_{SD}, respectively, which have values of the order of several meters. CH1 and CH2 create neutron pulses with widths τ_i and τ_{ii}, and define the incident neutron wavelength λ_0 and its band width. More precisely, the phase difference between CH1 and CH2 allows the latter to select the 'monochromatic' wavelength of the experiment. The scattering processes in the sample then cause neutron wavelength shifts to smaller or larger values of λ . In Fig. 5, a neutron flight-path diagram is shown. It explains the method in more detail and demonstrates the filter action of the various disks of the chopper cascade. While the neutron time-of-flight is measured along the horizontal axis, the vertical axis represents the flight-path between the different elements of the chopper cascade.

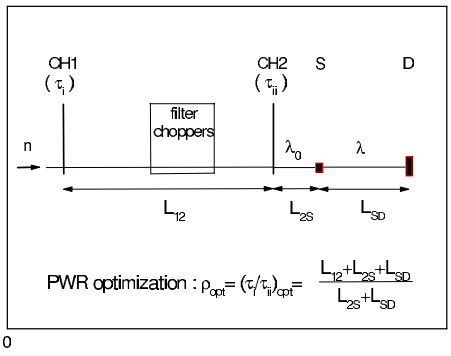

Fig. 4. Schematic sketch of a multi-disk chopper time-of-flight (MTOF) spectrometer : CH1 and CH2 are the two principal choppers defining the monochromatic neutron pulse and its wavelength bandwidth; S = sample, D = detectors; L_{12}, L_{2S}, and L_{SD} are the distances between these elements of the instrument; τ_i and τ_{ii} are the widths of the pulses created by CH1 and CH2, λ_0, λ the incident and scattered neutron wavelenths (after [31]). Inset: the pulse-width ratio (PWR) optimization formula for elastic and quasielastic scattering [32]. Typical instruments of this type are IN5 [33, 34, 35, 36] at ILL in Grenoble, MIBEMOL [37] at LLB in Saclay, both France; NEAT [38, 39, 40, 41] at HMI in Berlin, Germany; and DCS [42] at NIST in Gaithersburg, USA.

The filter choppers, CH_P and CH_R perform pre-monochromatization and pulse-frequency reduction of the beam, respectively, in order to avoid frame-overlap at the monochromator disk CH2 and at the detectors. The spectra shown schematically on the top of the figure, correspond to a study of the rotational motion of OH^- ions [43] with the MTOF spectrometer IN5 at ILL, carried out in 1975 using $4\AA$ neutrons. The diagram also demonstrates the periodicity of the data acquisition procedure, inherent in a pulsed experiment. Each TOF period P_{spec} in principle contains one spectrum. But the duration of the measurement must cover a large number of such periods, the spectra of which (about 10^6 for a measurement time of 3 hours) are added together, in order to obtain sufficient statistical accuracy. The pulse repetition rate P_{spec}^{-1} of the experiment is limited by the necessity of avoiding frame overlap, which means the superposition of the fastest neutrons (scattered with energy gain) within a time-of-flight period and the slowest neutrons (scattered with energy loss) from the previous period. This requires

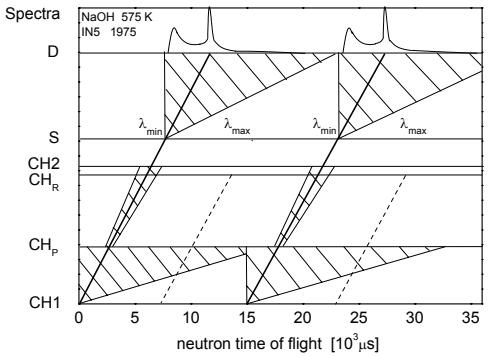

Fig. 5. Neutron flight-path diagram : It demonstrates the filter action of the various disks of the chopper cascade. The vertical axis represents the flight-path between the different elements of the chopper cascade. CH1 defines the initial time-distribution of the neutron pulse; CH_P is the pre-monochromator; CH_R is employed for pulse frequency reduction, in order to avoid frame-overlap at the detectors; finally, CH2 selects the 'monochromatic' wavelength band for the experiment. The time-of-flight (TOF) spectra shown schematically on the top of the figure, correspond to a study of the rotational motion of OH^- ions [43] with the MTOF spectrometer IN5 at ILL, carried out in 1975 using $4\AA$ neutrons. Each spectrum covers one TOF period P_{spec}; see text for more details (from [31]).

$$P_{spec}[\mu s] = 252.78\ C\ \lambda_0[\AA]\ L_{SD}[m] \tag{33}$$

where practical experimental units are indicated. The dimensionless constant C has to be chosen depending on the width of the quasielastic spectrum and the corresponding decay of its intensity on the low-energy side. C is usually in the range of $1.2 \leq C \leq 1.8$.

For a given incident neutron wavelength, the total intensity at the detectors is essentially governed by the factor $(\tau_i \tau_{ii})$, i.e. by the product of the two chopper opening times [32] (see also: [44]). The latter also control the resolution, and thus intensity and resolution are connected through these parameters. The most important and unique feature of this type of instrument is the capability of varying the energy resolution continuously over several orders of magnitude (see Sec. 2.3). We therefore give here explicitly an expression for $\Delta(\hbar\omega)$. The energy resolution width (HWHM) at the detector [32], i.e. the uncertainty in the experimentally determined energy transfer $\hbar\omega$, is given by

$$\Delta(\hbar\omega)[\mu eV] = 647.2(A^2 + B^2 + C^2)^{1/2}/(L_{12}L_{SD}\lambda^3)/2, \tag{34}$$

where

$$A = 252.78\ \Delta L\ \lambda\ L_{12} \tag{35}$$

$$B = \tau_i(L_{2S} + L_{SD}\lambda^3/\lambda_0^3) \tag{36}$$

$$C = \tau_{ii}(L_{12} + L_{2S} + L_{SD}\lambda^3/\lambda_0^3) \tag{37}$$

ΔL is the uncertainty of the length of the neutron flight path, which is mainly due to beam divergence, sample geometry and detector thickness. The constant coefficients in eqs. (34) and (35) are valid, when the quantities L_{12}, L_{2S}, L_{SD}, ΔL are given in [m], λ_0 and λ in [$\AA$], τ_i and τ_{ii} in [μs].

It follows from these expressions, that the energy dependent resolution, for given λ_0, strongly depends on the scattered neutron wavelength λ, whereas the total intensity, as an integral property of the spectrometer, has no such dependence. Furthermore, high resolution is favoured by short pulse widths and by large values of the distances L_{12} and L_{SD}. If these distances are fixed, and if sample geometry, λ_0 and energy transfer have been chosen, then total intensity and resolution-width only depend on the chopper opening times τ_i and τ_{ii}. Best instrument performance regarding intensity and resolution is achieved not only by selecting suitable values of the individual pulse widths, τ_i and τ_{ii}, but also requires the optimization of their ratio (pulse-width ratio (PWR) optimization [32], [38]). The optimization formula for elastic and quasielastic scattering is shown as an inset in 4.
The continuous variation of the energy resolution over three orders of magnitude is achieved by varying the chopper pulse widths τ_i and τ_{ii} (which, e.g., in the case of NEAT is possible by a factor between 1 and 40), and by choosing the incident wavelength (yielding another factor, of up to about 30 for the wavelength range from 4 $\AA$ to 12 $\AA$). Applications of this technique using the MTOF spectrometer NEAT at HMI in Berlin, are described in Secs. 3.4 and 4.3 of Part II, this Volume.

3.3 XTL-XTL Spectrometers

The energy-transfer regime in the μeV range is covered by *back scattering* (BSC) spectrometry [45, 46, 47, 48], which was invented by H. Maier-Leibnitz. BSC-spectrometers are XTL-XTL instruments, i.e. they employ single-crystals as monochromators *and* as analyzers, with Bragg angles close to $\pi/2$ in both cases. For a given incident divergence of the beam, $\Delta\Theta$, the wave number spread produced by reflection from a crystal is given by differentiating Eq. (31)

$$\frac{\Delta k_{\rm div}}{k} = \cot\Theta\,\Delta\Theta\ . \tag{38}$$

For typical Bragg angles and $\Delta k_{\rm div}/k \approx 10^{-2}$ radian one achieves an energy resolution in the percent range. However, for Θ approaching $\pi/2$, $\Delta k_{\rm div}$ from

Eq. (38) goes to zero and we have to include the curvature of $\sin\Theta$ which leads to a second order contribution,

$$\frac{\Delta k_{\rm div}}{k} = \frac{(\Delta\Theta)^2}{8} \quad for \quad \Theta \to \frac{\pi}{2} \; . \tag{39}$$

This situation is called "backscattering" which means that the incident and the Bragg reflected beam are practically antiparallel. The square relation Eq. (39) replaces the linear relation between $\Delta k_{\rm div}$ and $\Delta\Theta$: The intensity is proportional to the incident solid angle $(\Delta\Theta)^2$, and we have $(\Delta\Theta)^2 \propto \Delta k_{\rm div}$ instead of $\Delta\Theta \propto \Delta k_{\rm div}$, which is valid for Bragg angles other than $\pi/2$. This means that under these conditions resolution and intensity are *decoupled in first order*.

Actually, the wavevector spread is larger than $\Delta k_{\rm div}$. Only a finite number of lattice planes contribute to the Bragg line, which causes a finite width of $\mathbf{G}$, the so-called Darwin or *extinction width* [49],

$$\frac{\Delta k_{\rm ex}}{k} = \frac{16\pi N_{\rm c} F_G}{G^2} \; , \tag{40}$$

where F_G is the structure factor for the Bragg reflection at $\mathbf{Q} = \mathbf{G}$, $N_{\rm c}$ is the number of lattice cells per unit volume. As an approximation, both contributions can be added such that

$$\frac{\Delta E_0}{E_0} = 2\left[\frac{(\Delta\Theta)^2}{8} + \frac{16 N_{\rm c} F_G}{G^2}\right] \; . \tag{41}$$

For neutrons from a Ni neutron guide and reflection on an ideal silicon waver, one calculates $\Delta E_0 = (0.24 + 0.08)$ μeV as incident neutron energy spread. For the resolution in energy transfer, $\Delta(\hbar\omega)$, of a modern BSC-spectrometer, such as the backscattering spectrometer IN16 (Fig. 6) at the ILL high-flux reactor [47, 48], one obtains values of $0.09\mu eV$, $0.2\mu eV$, and $0.43\mu eV$ (HWHM), depending on the type of monochromator and analyzer crystals used [48]. So far such values have not been reached by any other kind of crystal spectrometer; they can in principle, however, be achieved also by high-resolution TOF-TOF instruments at future spallation sources [31]. The high energy resolution of IN16 is based on a Bragg angle fixed at 90°; the energy scan is performed by a Doppler drive, moving the monochromator crystal (spherical, perfect Si(111), 450×250 mm^2; label **6** in Fig. 6) with a sinusoidally varying speed $v_{\rm D}$. The resulting energy shift is [50]

$$\frac{\delta E_0}{E_0} = 2\frac{v_{\rm D}}{v_0} \tag{42}$$

which yields an energy window of $\delta E_0 = \pm 14$ μeV for maximum speed values of $v_{\rm D} = \pm 2.5$ m/s and $\lambda_0 = 6.27$ $\mathring{A}$. The various components of the instrument are arranged as follows: A double-deflector array (**1** and **5** in Fig. 6) selects the useful wavelength band from the cold-neutron guide. The first

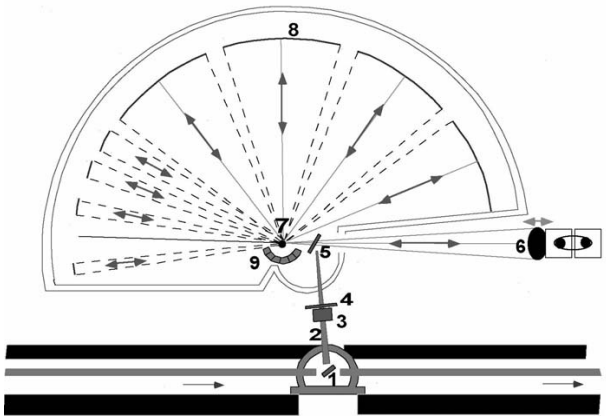

Fig. 6. Backscattering spectrometer IN16 at the ILL high-flux reactor [47, 48], schematic view : **1** = first graphite deflector crystal; **2** = focusing supermirror guide; **3** = Beryllium-Filter; **4** = background chopper; **5** = stationary graphite-crystal deflector chopper; **6** = Doppler monochromator crystal; **7** = sample; **8** = spherically arranged analyzer crystal array; **9** = multi-tube detector array. The Bragg angles at the silicon single crystals (i.e., monochromator and analyzer, before and after scattering of the neutrons by the sample) are close to 90°. Other well-known spectrometers of this type are the backscattering spectrometer at the Jülich FRJ-2 reactor, IN10 [46] and IN13 at ILL in Grenoble, France, and HFBS [51] at NIST in Gaithersburg, USA.

deflector (**1** in Fig. 6), a (broad-band) vertically focusing pyrolythic graphite crystal separates the neutrons to be used from the incident beam and reflects the whole energy-transfer range of about $\pm 14\ \mu eV$, covered by the Doppler motion of the monochromator, into a NiTi supermirror guide (**2** in Fig. 6). The latter focuses these neutrons vertically and horizontally onto the second deflector (**5** in Fig. 6). A Be-filter and a background chopper (**3** and **4**, respectively, in Fig. 6) are located in a gap in the middle of this guide. The second deflector (label **5** in Fig. 6), made of PG(002) crystals with a wide mosaic, is mounted on a chopper wheel with alternating open and reflecting segments. It sends a neutron pulse towards the monochromator (label **6** in Fig. 6). The monochromatic backscattered neutron pulse is transmitted through the open segments to the sample. Obviously the system is designed in such a way, that

the necessary phase relations between Doppler drive, deflector chopper and background chopper are observed. To avoid that the scattered neutrons are directly falling onto the detectors (before they have been filtered by the Si analyzers), the incident beam is periodically interrupted by the background chopper, in phase with the Doppler movement. Only when the beam is closed, the consecutively scattered and analyzed neutrons reach the detectors. This ensures that the useful neutrons are reaching the sample, the analyzers and finally the detectors, while the background that would be caused by neutrons scattered without energy analysis from the sample directly into the detectors, is discriminated. The monochromatic neutrons from the oscillating monochromator crystal, falling onto the sample, being scattered, and finally detected, are individually labeled with the corresponding instantaneous speed of the Doppler drive. The neutrons scattered by the sample are backscattered by spherical shells of Si(111) crystals and thus focussed into a set of ^3He detectors. Each detector corresponds to a certain scattering angle or Q-value. When the energy range is too narrow, the reflected neutron energy can be additionally shifted by heating the monochromator, thus increasing the lattice parameter, and/or using monochromators whose lattice parameter is somewhat smaller or bigger than that of the silicon analyzer [52]. In this way, the range of the spectrometer (and also the resolution) can be adapted to the problems.

Sometimes, backscattering spectrometers are used with the Doppler drive *at rest*, i.e., in the so-called *elastic-window scan* mode of operation (see : [53], [54] and [23] p. 284). In such a measurement one determines the intensity for the spectrometer set at $\omega = 0$, corresponding to the convolution integral $[S_s(\mathbf{Q}, \omega = 0)]_{meas} = (S_s \otimes R)$, where as an example, S_s is the incoherent neutron scattering function and R is the energy resolution function (see eq. (29)). For scattering functions with Gaussian shape in reciprocal space, when they permit a time-independent atomic mean-square displacement to be defined (e.g. for harmonic vibrations), and when the non-elastic scattering contribution to the elastic channel is negligible, the Q-dependence of the scattered intensity at zero energy transfer reads:

$$S_s(\mathbf{Q}, \omega = 0) = C \; exp\,[- < u^2 > Q^2] \tag{43}$$

where C is a normalization factor, the exponential is the Debye-Waller factor, and u is the component of the atomic displacement along the vector $\mathbf{Q}$. This expression may also be employed for any spatially restricted isotropic motion, as long as Q is small enough (Gaussian approximation; see Sec. 3 in Part II of this article, in this Volume). It has even been used for non-Gaussian probability density distributions, for instance in the context of the so-called "dynamical transition" [55],[56],[57], [58],[59] (see Sec. 5.2 in Part II ; see also the article by Lehnert and Weik in this Volume). This is justified, as long as one keeps in mind, that in such cases the quantity $< u^2 >$ becomes a phenomenological parameter with a less precise meaning than in

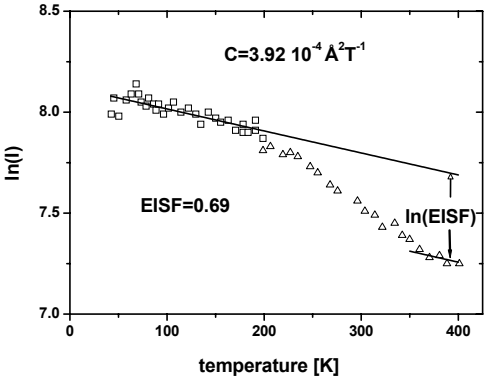

Fig. 7. Example of an apparent observability transition (as opposed to a true dynamical transition, where due to a structural phase transition a new type of motion appears at a transition temperature or in a transition region, in case of a higher order transition) exhibited experimentally by the elastic intensity I of $CsOH \cdot H_2O$ measured as a function of temperature: Logarithmic plot of the elastic-window intensity obtained with IN13 (ILL Grenoble) at $Q = 1.89 \AA^{-1}$. The straight lines show the variation of the Debye-Waller factor in the limits of low T and high T, respectively. The logarithm of the EISF is simply the difference between the values of the two lines at a given temperature [60].

the harmonic-vibration case. This parameter can be used for the qualitative study of the effects due to the variation of external variables, such as the temperature.

Let us now consider a case, where the scattering function has an appreciable quasielastic component, with a temperature-dependent width of the same order of magnitude as the energy resolution of the instrument. For instance, for a Lorentzian-shaped spectrum $S_s(Q,\omega) = (\Gamma/\pi)/(\Gamma^2 + \omega^2)$ (see for instance eqs. (7) or (25) in Part II of this Volume), and assuming a Lorentzian shape for the resolution function as well (approximately valid for the classical BSC spectrometer), with a width (HWHM) $\Delta(\hbar\omega)$, one obtains for the measured window-scan intensity at zero energy transfer,

$$I(Q,\omega=0,T) = \frac{1}{\pi}\frac{1}{(\Gamma(Q,T) + \Delta(\hbar\omega))} \tag{44}$$

We will now, for the purpose of discussion, assume that in our example a single relaxation process (responsible for the Lorentzian line shape) is active

over the whole temperature range considered, and that it shows an Arrhenius type behaviour. Then, for sufficiently small temperatures, the quasielastic line falls entirely into the energy resolution window. Therefore, it does not cause any measurable quasielastic broadening. Then one gets for the window-scan intensity :

$$I(Q, \omega = 0, T) = 1/(\pi \Delta(\hbar\omega)). \tag{45}$$

With increasing temperature, the line width Γ grows, and finally becomes larger than the window $\Delta(\hbar\omega)$; the measured intensity of the window scan then reveals a "stepwise" decrease. Therefore, a simple temperature scan allows to get a qualitative survey of the diffusion or relaxation processes in the sample as a function of temperature.

The intensity "step" represents a (purely methodical) transition from non-observability at low T to observability at high T of the relaxation process. From the shape of this step the relaxation time of the single process can easily be determined. Let us consider this problem for the more complex situation of a localized diffusive process, implying an elastic in addition to a quasielastic Lorentzian component. Here the same experimental method can be applied. If the attenuating effect of (harmonic) vibrational motions is described by a classical Debye-Waller factor, the temperature-dependent window-scan intensity, in logarithmic form, is given by [60]

$$ln(I) = -CTQ^2 + ln(A(Q)/(\pi\Delta(\hbar\omega)) + (1 - A(Q))/[\pi(2\hbar/\tau_{2S} + \Delta(\hbar\omega))] \tag{46}$$

Here CT is the vibrational mean square displacement (with a temperature coefficient C), A(Q) is the EISF, and τ_{2S} is the relaxation time (for a two-site jump model in our example; see Fig. 1 and Table 1). It is interesting to note that the observability transition described by eq. (46) can be used not only to yield the relaxation time τ_{2S}, but also for the determination of the EISF, provided that the mechanism does not change in the T-region of the step. For this purpose, the measured low-temperature straight line of ln(I) vs. T is extrapolated to high T and compared with the measured high-temperature line; the latter is obtained, when due to strongly increased line-broadening, the quasielastic contribution to the intensity becomes negligible. A simple division of the intensities yields the EISF according to the equation [60]:

$$ln[A(Q)/(\pi\Delta(\hbar\omega))] = [ln(I)_{highT}] - [ln(I)_{lowT}^{extrapol}] \tag{47}$$

As an example of such a measurement, Fig. 7 shows the intensity step due to the effect of OH-group reorientations in $CsOH \cdot H_2O$ [60] appearing in the energy resolution window of the BSC spectrometer IN13.
The elastic-window scan method has been employed in numerous biological experiments, in order to determine the temperature dependence of motional amplitudes ("mean-square displacements"), for instance in the context of the "dynamical transition" (see Sec. 5.2 in Part II, this Volume).

3.4 TOF-XTL Spectrometers

Last, but not least, the TOF-XTL technique should be mentioned. This type of hybrid instrument, employs a pulsed polychromatic ("white") incident beam and single-crystals as analyzing filters. It is well adapted to the time-structure of spallation neutron sources. The energies of the incident neutrons are measured with time-of-flight techniques, while the energy of scattered neutrons is fixed by the analyzers. For high energy resolution the crystals are used in backscattering (BSC) or near-BSC geometry ($\theta \simeq \pi/2$), whereas for more moderate resolution $\theta < \pi/2$ is chosen. Since the quality requirements for the crystals depends on these configurations, and for other practical reasons, dedicated instruments have been built for each case. A typical example with analyzer in near-BSC geometry is represented by the inverted geometry instrument IRIS schematically depicted in Fig. 8 [61] at RAL in Chilton. Depending on the type of crystals used, several discrete values of energy resolution in the range from about 1 *to* 55 μeV are achieved. The energy resolution function of such a spectrometer is essentially given by the convolution of four contributions :

$$R(\omega) \simeq f_t(\frac{\Delta t_{mod}}{t}) \otimes f_d(\frac{\Delta d}{d}) \otimes f_\theta(cot(\theta)\Delta\theta) \otimes f_s(\frac{\Delta t_{SD}}{t_{SD}}) \qquad (48)$$

The first function, f_t, arises from the finite pulse width Δt_{mod} produced by the cold moderator of the spallation source or (eventually) by a pulse-shaping chopper; t is the time of flight from the moderator to the detector. f_d is due to the uncertainty of the analyzer crystal's lattice spacing ($\Delta d/d$), and f_θ is the contribution of the Bragg angle uncertainty due to beam divergence and crystal mosaicity, which tends to vanish in perfect BSC geometry. The last function, f_s, is connected with the time-spread Δt_{SD} of the sample-detector flight time t_{SD}, caused by sample and detector thickness. If the four functions are approximated by Gaussian distributions, the elastic resolution $\Delta(\hbar\omega)$ is obtained from the quadratic addition of the individual contributions:

$$\Delta(\hbar\omega) = 2E_0 \left[(\frac{\Delta t_{mod}}{t})^2 + (\frac{\Delta d}{d})^2 + [cot(\theta)\Delta\theta]^2 + (\frac{\Delta t_{SD}}{t_{SD}})^2 \right]^{1/2} \qquad (49)$$

For IRIS, depending on the type of crystals used, several discrete values of energy resolution in the range from about 8 to 15 μeV are achieved. An example of application is described in Sec. 5.1 (see Figs. 13 and 14 of Part II in this Volume).

An example of an inverted-geometry instrument with analyzer scattering configuration significantly deviating from the BSC geometry, is the spectrometer "QENS" at the Intense Pulsed Neutron Source (IPNS) (Argonne, Illinois) [62]. The 22 crystal-analyzer detector-arrays are installed as close as possible to the sample, in order to maximize the analyzed range of solid angle. The crystals are arranged so that they match the "time-focusing-condition" which

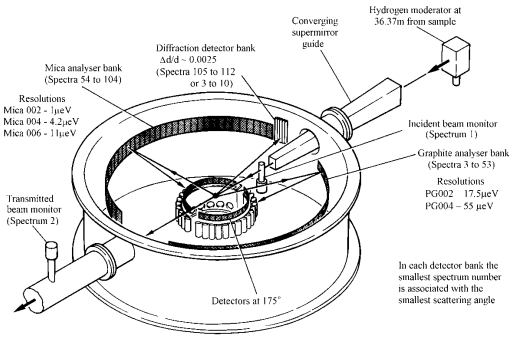

Fig. 8. Design of the high-resolution inverted-geometry backscattering spectrometer IRIS [61] on the ISIS pulsed source. The sample is located in the center of the analyzer vacuum vessel, at a distance of 36.5 m from the cold hydrogen moderator. The incident "white" beam reaches the sample through a converging supermirror guide. Graphite (resolutions $17.5\mu eV$ and $55\mu eV$ and mica (resolutions $1\mu eV$, $4.2\mu eV$ and $11\mu eV$ analyzer banks are arranged laterally on opposite sides; The detectors are mounted around the sample, in a plane slightly below the latter.

minimizes the time uncertainty contribution to the resolution. The elastic energy resolution of the spectrometer is around 80 μeV. An interesting feature of these spectrometers is the possibility to measure - simultaneously with the quasielastic spectra - the diffraction pattern of the sample. This is achieved by scattering from the sample directly into additional detectors, over a very wide wavevector range (up to $\simeq 30\AA^{-1}$ in the case of "QENS"), because of the white beam arriving on the sample.

4 Instruments for QENS Spectroscopy in (Q, t) space

4.1 NSE Spectrometers

Differently from the procedures employed by the QENS techniques discussed in Sec. 3, which are based on energy transfer analysis, it is also possible to study scattered neutron intensities by Fourier time analysis. Before discussing

neutron spin-echo techniques already well-known for this type of analysis, we briefly mention another method recently proposed [63],[64], which has not yet been widely used. It is based on the measurement of the elastically scattered neutron intensity as a function of observation time. If the latter is properly related to the Fourier time, a direct determination of the intermediate scattering function is achieved, without the detour via Fourier transformation. This method has been proposed as an alternative to energy transfer analysis in the use of TOF-TOF techniques capable of continuous tuning of the energy resolution, a feature so far not available on spectrometers employing crystals as monochromators and/or analyzers.

Let us now turn to the NSE method. It was introduced in 1972 by Mezei [65]. For detailed information on this technique, see [66]. NSE measures the sample dynamics in the time domain, via the determination of the intermediate scattering functions (see eqs. (8) and (9)). These functions are measured over a range of several orders of magnitude of Fourier time, up to values as large as $10^{-7}s$. The drastic reduction of intensity necessarily arising, when in measurements with energy-analyzing QENS techniques the energy resolution is increased by reducing the incident and/or scattered neutron energy band widths, is circumvented here. This property of the NSE method is a consequence of the fact, that the energy transfer occurring in the scattering process, $\hbar\omega = E - E_0$, is causing a phase shift of the neutron spin precession angle for each scattered neutron, which is approximately independent of the neutron wavelength. Therefore the energy resolution depends only weakly on those energy widths of E_0 and E, and a rather large incident wavelength bandwidth can be used with little loss in energy resolution. Obviously, an appreciable intensity gain results from this fact. Of course, the latter is not entirely free of charge: it comes, for example, at the expense of the time-resolution on the Fourier time axis (see Sec. 4.3). This can, however, be tolerated, as long as the intermediate scattering functions (relaxation functions) to be measured are slowly varying in time, which is often the case in spin-echo spectroscopy [7].

The phase shift acts for each neutron by its effect on the measured quantity (i.e: the polarisation of the scattered beam). Later in the discussion we will return to the reason, why in these measurements the intermediate scattering function is obtained. In the following, we discuss the basic concept of NSE spectroscopy and very briefly introduce the Neutron Resonance Spin-Echo (NRSE) method .

Spin 1/2 and Larmor precession

A basic property of the neutron, relevant for the NSE technique, is its spin 1/2. The description of the behaviour of spin 1/2 particles can be found in

[7] This argument is similar to the one justifying an appreciable intensity gain in TOF and BSC spectroscopy, due to the integration over large detector solid angle regions, when scattering functions are slowly varying with Q.

standard text books (e.g. [67], [68]); detailed instructions for the use of spin-echo spectroscopy are given in [69, 70, 71, 72]. When a spin 1/2 is submitted to a magnetic field B_z, its component in the direction collinear to the field is quantized. In the fundamental state, two values of S_z are possible $|+\rangle$ (the spin parallel to the field direction) and $|-\rangle$ (antiparallel). Let us now assume that a neutron spin is oriented in a direction having an angle θ with respect to a homogeneous magnetic field. A precessional motion will occur around the magnetic-field direction. The time evolution of the spin can be determined classically by

$$\frac{d\mathbf{S}}{dt} = \gamma \mathbf{S} \times \mathbf{B} \tag{50}$$

This equation describes the precessional motion [73] of $\mathbf{S}$ around $\mathbf{B}$ with a Larmor frequency $\omega_L = |\gamma|B$. Here, $\gamma = -2\pi\ 2916.4\ G^{-1}s^{-1}$ is the gyromagnetic ratio of the neutron. The accumulated precession angle, Φ, of the neutron spin depends linearly on the time t it spends in the magnetic field B and on the strength of this field (we assume decoupling of spin state and neutron position, which is valid for NSE):

$$\Phi = \omega_L t = |\gamma_n|Bt = |\gamma|B\frac{l}{v} \tag{51}$$

where l is the length of the flight path in the field, and v is the neutron velocity. Typically, $5\mathring{A}$ neutrons submitted to a field of 10 Gauss will perform around 37 turns per meter, and when the field is increased to 0.5 Tesla (5000 G) this number can be increased up to 18500.

When the direction of the magnetic field changes, 2 extreme cases can be considered. Let us, for the sake of simplicity, assume that the neutron spin is initially collinear with the field :
1. Slow (or "adiabatic") change of the magnetic field: A change of the field direction, encountered by the neutron on its way along the flight path, is experienced as a rotation of the field in the coordinate frame of the flying neutron. This may be represented by an angular frequency ω_F of rotation, which depends not only on the spatial variation of the field in the laboratory coordinate frame, but also on the neutron velocity. The spin follows adiabatically the change of the field when $\omega_F << \omega_L$: If it was initially collinear with the magnetic field, it will rotate with the latter, i.e., the spin direction is following the field.
2. Sudden (or "non-adiabatic") change of the field: this is the limit opposite to the adiabatic change, i.e., $\omega_F >> \omega_L$; in this case the field variation is so fast that the spin direction can not follow. Such changes are used to initiate the spin precession. This will be explained below.

The Neutron Spin-Echo principle

The general principle of the neutron spin-echo spectrometer is presented in Fig. 9. A neutron of wavelength λ_0' moving in direction Z arrives at t=0 in Z_0,

with its spin in the $|+\rangle$ state with respect to the Z direction. A $\pi/2$ flipper "suddenly" puts the spin state perpendicular to the direction of the field (the description of these flippers is omitted in the context of this book, but the interested reader is referred to ref. [71]). This action initiates a precessional motion in the counter-clockwise sense (the gyromagnetic ratio γ of the neutron is negative).
Let us now assume a beam of polarized neutrons moving perfectly parallel in Z direction (assuming zero beam divergence), with a wavelength distribution $f(\lambda_0^{'})$, the maximum of the distribution being located at λ_0. We now want to calculate, what will be the precession angle distribution at Z_A, if the field path integrals are equal in the two arms. From Z=0 to the sample position Z_S, i.e. in the first arm of the spectrometer, the spin of a neutron of wavelength λ_0 will accumulate a total precession angle of

$$\Phi_1^{\lambda_0} = \frac{\gamma m \lambda_0}{h} \int_0^S B_1 dz = 2\pi N_1^{\lambda_0} \tag{52}$$

where

$$N_1^{\lambda_0} = \frac{\gamma m \lambda_0}{2\pi h} \int_0^S B_1 dz \tag{53}$$

is the number of (positive) spin turns between Z_0 and Z_S. For any neutron with a wavelength $\lambda_0^{'}$ within the incident neutron wavelength distribution, we get:

$$\Phi_1(\lambda_0^{'}) = \frac{\gamma m \lambda_0^{'}}{h} \int_0^S B_1 dz = 2\pi N_1^{\lambda_0} \frac{\lambda_0^{'}}{\lambda_0} \tag{54}$$

The analogous quantities can be calculated for the second arm:
Let us assume that the sample is a purely elastic scatterer and thus the neutron wavelength $\lambda_0^{'}$ is not changed by the scattering process. From Z_S to Z_A the neutron is submitted to a magnetic field in direction opposite to the field before the sample. Then the accumulated precession angle will be

$$\Phi_2^{\lambda_0} = \frac{\gamma m \lambda_0}{h} \int_S^A B_2 dz = -2\pi N_2^{\lambda_0} \tag{55}$$

with

$$N_2^{\lambda_0} = \frac{\gamma m \lambda_0}{2\pi h} \int_S^A B_2 dz \tag{56}$$

which is the number of (negative) spin turns between Z_S and Z_A . For any neutron with a wavelength $\lambda_0^{'}$ within the incident neutron wavelength distribution, we get:

$$\Phi_2(\lambda_0^{'}) = \frac{\gamma m \lambda_0^{'}}{h} \int_S^A B_2 dz = -2\pi N_2^{\lambda_0} \frac{\lambda_0^{'}}{\lambda_0} \tag{57}$$

Finally, we obtain for the total phase angle accumulated by the neutron spin precession of any neutron in the distribution:

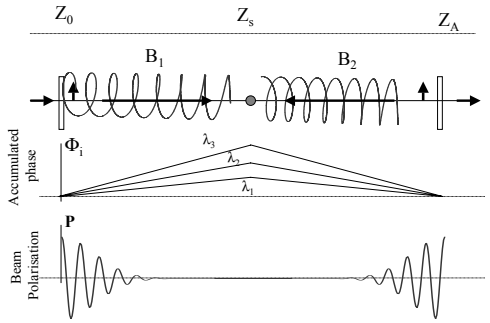

Fig. 9. Principle of the neutron spin-echo spectrometer: A neutron of wavelength $\lambda_0^{'}$ moving in direction Z arrives at t=0 in Z_0, with its spin in the $|+\rangle$ state with respect to the Z direction. Two coils create high magnetic fields of equal strength, but in opposite directions, B_1 and B_2, before and after the sample (upper part). A $\pi/2$ flipper "suddenly" puts the spin state of the arriving neutron perpendicular to the direction of the field. This initiates a precessional motion of the neutron spin in the counter-clockwise sense, while this particle is flying along Z. The spin precession stops after a second $\pi/2$ spin flipper placed after the end of the second coil. The accumulated spin phases Φ_i are proportional to the time, wavelength and distances (central part). The beam polarization $P \approx \langle cos(\Phi_i) \rangle$ is presented in the lower part of the figure. If the sample is a purely elastic scatterer, the neutron wavelength $\lambda_0^{'}$ is not changed by the scattering process. Because of the two magnetic fields with equal strength but opposite signs, in the case of elastic scattering, the total phase angle accumulated by the neutron spin precession during the flight from Z_0 to Z_A, will be $\Phi(\lambda_0^{'}) = 0$. The general case of non-elastic scattering is explained in the text.

$$\Phi(\lambda_0^{'}) = \Phi_1(\lambda_0^{'}) + \Phi_2(\lambda_0^{'}) = 2\pi(N_1^{\lambda_0}\frac{\lambda_0^{'}}{\lambda_0} - N_2^{\lambda_0}\frac{\lambda_0^{'}}{\lambda_0}) = \alpha\lambda_0^{'} \tag{58}$$

where α does not depend on $\lambda_0^{'}$:

$$\alpha = \frac{2\pi}{\lambda_0}(N_1^{\lambda_0} - N_2^{\lambda_0}) \tag{59}$$

It is easy to realize that at the "echo-point", where the field path integrals in the first and in the second arm of the spectrometer are equal, the total phase angle accumulated by the neutron spin precession will be $\Phi(\lambda_0^{'}) = 0$, and this is true for any neutron velocity; i.e., this result is independent of $\lambda_0^{'}$.

Transmission of polarizers and analyzers

Polarizer and analyzer are key elements of the spectrometer. The polarizer is used to prepare a polarized beam (i.e. it selects neutrons with only one of the two quantized neutron spin states). For long-wavelength neutrons ($\lambda > 3\mathring{A}$), as are generally used in NSE experiments (at least for quasielastic measurements), most of the polarizers employ the principle of magnetic reflection or transmission of supermirrors. For shorter wavelengths, Haeussler-like crystals are used. A potentially very interesting technique for spin analysis is the use of a ^3He polarizer and/or analyzer. For the spin-echo technique a ^3He polarizing filter unit would have the very interesting property of being simultaneously usable over a wide angular range and independently of the neutron wavelength. At the time of writing the beam polarization achieved with ^3He is however not yet good enough for spin-echo experiments.
The polarizer transmits only neutrons with one of the spin components. The exact fraction of the neutron beam transmitted is not relevant for the principle of the technique, but it should be maximized for the purpose of obtaining good statistical accuracy of the measurements. The number of incident neutrons is usually monitored just before the sample position. For our present purpose, the interesting problems will be
1- to compute the probability of transmission through the analyzer for a neutron whose spin angle with the static field B_A inside the analyzer is given by θ.
2- to determine the beam polarization of a neutron population whose spin angles are given by the normalized distribution $F(\theta)$.
These problems require a quantum-mechanical calculation. The spin-state wave function for the neutron spin precessing in the field B_A is

$$|\Psi\rangle = e^{-i\tilde{\Phi}}\, cos\frac{\theta}{2}\, |+\rangle + e^{i\tilde{\Phi}}\, sin\frac{\theta}{2}\, |-\rangle \tag{60}$$

where $\tilde{\Phi}$ and θ are the spherical coordinates defining the orientation of the spin with respect to the analyzer field. Each neutron spin will have the probabilities $p_{|+\rangle} = cos^2\frac{\theta}{2}$ and $p_{|-\rangle} = sin^2\frac{\theta}{2}$, to be either in the $|+\rangle$ or in the $|-\rangle$ state, respectively.
The solution of problem 1 is that only $|+\rangle$ neutrons will be transmitted, the probability of transmission being given by $p_{|+\rangle} = cos^2\frac{\theta}{2}$. Thus for a neutron flux N incident on an idealized analyzer (i.e. with no absorption losses), with the normalized spin-precession phase-angle distribution $F(\theta)$, the flux of neutrons transmitted by the analyzer will be

$$N^{|+\rangle} = \int F(\theta) cos^2(\frac{\theta}{2}) d\theta \tag{61}$$

Using a well-known trigonometric relation for the square of the cosine, we can compute the transmission of the analyzer:

$$T = \frac{N^{|+\rangle}}{N} = \frac{\int F(\theta)(1 + cos(\theta))d\theta}{2\int F(\theta)d\theta} = \frac{1}{2}(1 + \langle cos(\theta)\rangle) \tag{62}$$

It is straightforward to show that $\langle cos(\theta)\rangle$ corresponds to the polarisation of the transmitted beam,

$$P = \frac{p_{|+\rangle} - p_{|-\rangle}}{p_{|+\rangle} + p_{|-\rangle}}, \tag{63}$$

which is equivalent to:

$$P = \frac{\int F(\theta)(cos^2(\frac{\theta}{2}) - sin^2(\frac{\theta}{2}))d\theta}{\int F(\theta)d\theta} = \langle cos(\theta)\rangle \tag{64}$$

Getting a spin echo, as a measure of the polarisation

We now return to equation (58), because we want to compute the polarization of the scattered beam. We will treat the problem for two different cases:
1- the wavelength of neutrons is not changed by the scattering process
2- for a quasielastic distribution of energy exchange between the sample and the neutron beam.
First, assuming a *purely elastic scatterer*, $\Phi(\lambda_0^{'})$ does not depend on the sample, but simply on the incident wavelength distribution $f(\lambda_0^{'})$, which is assumed to be Gaussian. The final beam polarization can then be computed,

$$P = \int_0^\infty f(\lambda_0^{'})cos(\alpha\lambda_0^{'})d\lambda_0^{'} \tag{65}$$

with

$$f(\lambda_0^{'}) = \frac{1}{\sqrt{2\pi\sigma^2}}e^{-\frac{(\lambda_0^{'}-\lambda_0)^2}{2\sigma^2}} \tag{66}$$

where α was defined by eq. (59), and σ is the standard deviation of the wavelength distribution. The above integral has a simple analytical solution, if the integration is performed from $-\infty$ to $+\infty$, which is possible, because the assumed (in good approximation) Gaussian shape of the distribution to be integrated is practically zero for negative (unphysical) values of the wavelength. The integral yields for the beam polarization

$$P = cos(\alpha\lambda_0)e^{-\frac{\alpha^2\sigma^2}{2}} \tag{67}$$

The variation of the beam polarization in the neighbourhood of the echo point is shown in Fig. 10. It presents a full echo scan around the spin-echo maximum condition, $\int B_1 dl = \int B_2 dl$. In such a scan, the field path integral in the secondary spectrometer (coil 2) is varied by changing the current $\mathbf{i}$ of a small additional solenoid coil. This variation can be computed. Writing for the field path integral of the solenoid,

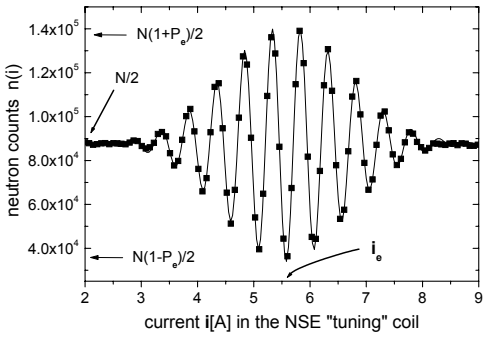

Fig. 10. Full echo (asymmetric current scan) measured (full squares) with the spectrometer MUSES [74] at the point Z_A, (see Fig. 9). The continuous line is the fit of expression (69) to the measured data points. P_e and i_e, respectively, are the scattered beam polarization and the current of the NSE tuning coil, at the echo point (where $\int B_1 dl = \int B_2 dl$). N is the number of polarized neutrons per integrated monitor count unit, scattered by the sample towards the analyzer (see text). The maximum and minimum numbers of neutrons that are transmitted by the analyzer, when the current $\mathbf{i}$ is varied, $N(1+P_e)/2$ and $N(1-P_e)/2$, are also indicated. N/2 is the number of neutron counts, when - outside of the spin-echo region - the beam is completely depolarized.

$$\int Bdl = \mu_0 \tilde{N} \mathbf{i} \tag{68}$$

where $\tilde{N}$ is the number of turns of the solenoid wire per unit of length, we get the function (continuous line) plotted together with the measured data points of the full echo scan in Fig. 10:

$$n(\mathbf{i}) = \frac{N}{2}(1 + P_e * cos(\tilde{\alpha}(\mathbf{i} - \mathbf{i}_e)\lambda_0)e^{-\frac{(\tilde{\alpha}(\mathbf{i}-\mathbf{i}_e)\sigma)^2}{2}} \tag{69}$$

with

$$\tilde{\alpha} = \frac{\gamma 10^4 \tilde{N} l m \mu_0}{h} \tag{70}$$

where l = coil length, m = neutron mass, h = Planck's constant, μ_0 = permeability in free space. P_e and $\mathbf{i}_e$, respectively, are the scattered neutron beam polarization and the current of the NSE tuning coil, at the echo point (where $\int B_1 dl = \int B_2 dl$). N = number of polarized neutrons per integrated monitor count unit, scattered by the sample towards the analyzer. The maximum and minimum numbers of neutrons that are transmitted by the analyzer, when

the current **i** is varied, $N(1+P_e)/2$ and $N(1-P_e)/2$, are indicated by horizontal arrows. N/2 is the number of neutron counts, when - outside of the spin-echo region - the beam is completely depolarized.

Measuring quasielastic neutron scattering

We now assume the scattering process to be quasielastic. The energy exchanged between the neutron and the sample during the scattering process is :

$$\hbar\omega = \frac{\hbar^2 k^2}{2m} - \frac{\hbar^2 k_0^2}{2m} \tag{71}$$

This will induce a change $\delta\lambda$ of the neutron wavelength, so that for incident neutrons with wavelength $\lambda_0^{'}$ the scattered neutron wavelength is $\lambda = \lambda_0^{'} + \delta\lambda$. The polarization of the scattered beam can be expressed as follows,

$$\langle P \rangle = \int_0^{+\infty} I(\lambda_0^{'}) \int_{-\lambda_0^{'}}^{+\infty} p(\lambda_0^{'}, \delta\lambda) cos(\Phi(\lambda_0^{'}, \delta\lambda)) d(\delta\lambda) d\lambda_0^{'} \tag{72}$$

Here, $p(\lambda_0^{'}, \delta\lambda)$ is the probability that a neutron scattering process with incident wavelength $\lambda_0^{'}$ and with a change in neutron wavelength $\delta\lambda$ occurs; note that the maximum possible negative value of $\delta\lambda$ is equal to $\lambda_0^{'}$. The function $p(\lambda_0^{'}, \delta\lambda)$, when transformed from the $\delta\lambda$-transfer to the energy-transfer axis, turns into nothing else but the scattering function $S(\mathbf{Q}, \omega)$. $\Phi(\lambda_0^{'}, \delta\lambda)$ is the total precession angle. Note also, that writing expression (72) we have assumed a perfect spectrometer : the incident beam is perfectly polarised, all the neutrons are transmitted through the spectrometer (whatever the wavelength) and with no beam depolarisation. We will come back to this assumption, when discussing the different spectral windows and resolutions of quasielastic spectrometers. It is important to realize that the total precession angle $\Phi(\lambda_0^{'}, \delta\lambda)$ represents the energy transfer $\hbar\omega$ which corresponds to the change $\delta\lambda$ in neutron wavelength, caused by the scattering process :

$$\Phi(\lambda_0^{'}, \delta\lambda) = 2\pi(N_1^{\lambda_0} \frac{\lambda_0^{'}}{\lambda_0} - N_2^{\lambda_0} \frac{\lambda_0^{'} + \delta\lambda}{\lambda_0}) = \alpha\lambda_0^{'} - 2\pi N_2^{\lambda_0} \frac{\delta\lambda}{\lambda_0} \tag{73}$$

At the echo point (for QENS experiments, the field path integrals are identical in the first and the second arm) $\alpha = 0$ and hence

$$\Phi(\lambda_0^{'}, \delta\lambda) = \frac{\gamma m}{h} \int_0^S B_1 dz \delta\lambda \tag{74}$$

For quasielastic scattering, it is assumed that the energy gained or lost by the neutrons remains much smaller than the initial energy of the neutron, i.e. $\frac{\delta\lambda}{\lambda_0^{'}} \ll 1$, hence

$$\delta\lambda \approx -\frac{m(\lambda_0^{'})^3\omega}{2\pi h} \tag{75}$$

and thus,

$$\Phi(\lambda_0^{'},\delta\lambda) = -\frac{\gamma m^2}{2\pi h^2}\int_0^S B_1 dz(\lambda_0^{'})^3\omega \tag{76}$$

Finally, the scattered beam polarization can be written

$$\langle P\rangle \approx \int_0^{+\infty} I(\lambda_0^{'})\int_{-\infty}^{+\infty} S(\mathbf{Q},\omega)cos(\omega\tau_{NSE})d\omega d\lambda_0^{'} \tag{77}$$

with

$$\tau_{NSE} = \frac{m^2\gamma\int Bdz}{2\pi h^2}(\lambda_0^{'})^3 \tag{78}$$

Note that the second integral in eq. (77) is the real part of the Fourier-transform of the dynamic structure factor $S(\mathbf{Q},\omega)$. The spin-echo time τ_{NSE} approximates the Fourier time t, and it is important to note that it is proportional to the third power of the wavelength (see also Sec. 4.3). Thus, it is now evident that

$$\langle P\rangle \approx I(Q,t) \approx \int_{-\infty}^{+\infty} S(\mathbf{Q},\omega)cos(\omega\tau_{NSE})d\omega \tag{79}$$

The $\approx$ symbol stands for the fact that $S(\mathbf{Q},\omega)$ is only approximately a symmetric function in ω, and that the integration over the wavelength distribution $I(\lambda_0^{'})$ in eq. (77) has a certain smearing or broadening effect on $I(Q,t)$.

The reason, why NSE spectroscopy measures sample dynamics in the time domain, is that the analyzer transforms a quantity proportional to the time, $\Phi(\lambda_0^{'})$, into a cosine: $cos(\Phi(\lambda_0^{'}))$; the summation over all the scattered intensity ($\simeq S(\mathbf{Q},\omega)$) weighted by this cosine function, Fourier-transforms the dynamic structure factor. One should nevertheless keep in mind, that only the real part of the FT is measured, and thus $\langle P\rangle \simeq I(Q,t)$ only, if $\simeq S(\mathbf{Q},\omega)$ is an (almost) even function. This is however usually the case for NSE experiments, because they probe the very low-frequency part of the dynamic structure factor, where the spectral asymmetry due to the detailed balance factor can be neglected and $S(\mathbf{Q},\omega)$ is to a good approximation an even function, as long as the temperature is not too low. For an application of this technique, see Sec. 3.2 in Part II of this Volume.

4.2 Neutron Resonance Spin-echo Spectrometry

In resonance spin-echo spectrometry[75] [76], the two high magnetic-field precession coils are substituted by four radio-frequency coils, two in the first arm and two in the second (see Fig. 11). The field geometry in the coils is as follows : a static high field $\mathbf{B}_0$, e.g. oriented vertically, and perpendicular to it a radio-frequency field $\mathbf{B}_1(t)$ rotating in the horizontal plane.

$$\mathbf{B}(t) = \mathbf{B}_0 + \mathbf{B}_1(t) \tag{80}$$

The resonance condition is reached when the frequency of the Larmor precession induced by the static field, $\omega_0 = -\gamma_n B_0$, is equal to the frequency of the rotating field ω_f : then - from the point of view of the neutron spin in the coordinate frame of the rotating field, the magnetic field $\mathbf{B}_0$ vanishes. Under this condition, the motion of the neutron spin in the rotating frame associated with $\mathbf{B}_1(t)$, can be simply reduced to a Larmor precession with a frequency $\omega_1 = -\gamma B_1$. The field $\mathbf{B}_1$ is chosen so that a neutron arriving in a coil with a spin oriented in the scattering plane, will leave it in the same plane, after having performed a precession of π around $\mathbf{B}_1(t)$:

$$\pi = \gamma B_1 \frac{d}{v} \tag{81}$$

where d is the coil thickness and v the neutron velocity. One now has to compute the spin orientation along the neutron path through the spectrometer, in the scattering plane. Suppose, the spins are polarized in the direction $\mathbf{y}$. Let us denote the angle between the spin orientation and $\mathbf{y}$ by ϕ, and the four coils by A,B,C and D; t_A, $t_{A'}$ are the times at which a neutron enters and leaves the coil A, and so on. The angle after the first coil can be written as :

$$\phi_{A'} = \omega_f \frac{d}{v} + 2\omega_f t_A - \phi_A \tag{82}$$

Only within these coils the neutron spins are submitted to a magnetic field and consequently the remaining neutron path has to be shielded from any magnetic contamination (earth magnetic field ...). After computation of the neutron spin phase along the neutron path, and assuming a perfect spectrometer, one can obtain the echo condition (i.e., the condition for which all the spins are polarized in the same direction as before entering the spectrometer):

$$\frac{l_{AB} + d}{v} - \frac{l_{CD} + d}{v'} = 0 \tag{83}$$

with l_{AB} and l_{CD} being the distances between the coil centers in the first and in the second arm, respectively, which for an elastic or quasielastic process simply reduces to $l_{AB} = l_{CD}$. The measured quantity is the polarization of the scattered beam in the $\mathbf{y}$ direction (or $\mathbf{z}$ after an adiabatic $\pi/2$ turn). If ϕ is the angle ($\mathbf{y}$,S_i) between the neutron spin orientation and $\mathbf{y}$ after the fourth coil, the contribution of each spin to the total polarization is given by

$$P_z(\lambda_0^{'}, \delta\lambda) \approx \cos(2\omega_f \frac{l+d}{h} m\delta\lambda) \tag{84}$$

Similar to NSE, after summation over all neutron contributions one obtains

$$\langle P \rangle = \int_0^{+\infty} I(\lambda_0^{'}) \int_{-\lambda_0^{'}}^{+\infty} p(\lambda_0^{'}, \delta\lambda) cos(2\omega_f \frac{l+d}{h} m\delta\lambda) d(\delta\lambda) d\lambda_0^{'} \tag{85}$$

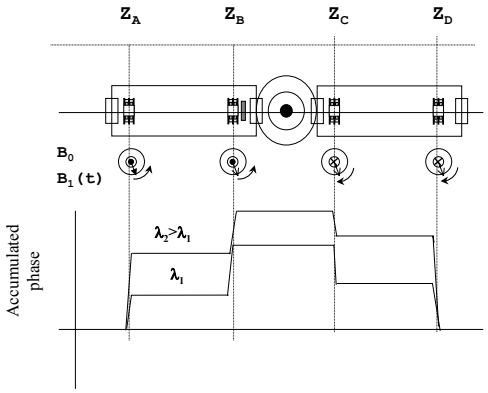

Fig. 11. Schematic description of the NRSE principle: Four radio-frequency coils, well-shielded against magnetic contaminations, such as the earth's magnetic field, are placed as two pairs in the two arms of the spectrometer at the positions Z_A, Z_B, Z_C, and Z_D, respectively. A static high field B_0, e.g. oriented vertically, and perpendicular to it, a radio-frequency field $B_1(t)$ rotating in the horizontal plane, are established. In the lower part of the figure the accumulated phase angles of the neutron spin precession are indicated schematically for the cases of elastic scattering for two different wavelengths, respectively.

So, within a quasielastic process, we have :

$$\langle P\rangle \approx \int_0^{+\infty} I(\lambda_0^{'}) \int_{-\infty}^{+\infty} S(\mathbf{Q},\omega) cos(\omega\tau_{NRSE}) d\omega d\lambda_0^{'} \tag{86}$$

with

$$\tau_{NRSE} = 2\omega_f \frac{l+d}{2\pi} \frac{m^2}{h^2} (\lambda_0^{'})^3 \tag{87}$$

where τ_{NRSE} is the spin-echo time of this method. Again, the spin-echo time is proportional to the third power of the wavelength, and - analogous to eq. (79) -

$$\langle P\rangle \approx I(Q,t) \approx \int_{-\infty}^{+\infty} S(\mathbf{Q},\omega) cos(\omega\tau_{NRSE}) d\omega \tag{88}$$

The consequence of this, and of the use of large incident wavelength bandwidths on the time-resolution will be considered in the next Section.

4.3 Observation Function, Effect of Wavelength Distribution on Spin-Echo Time; Miscellaneous

In the spin-echo case, the experimental observation function $R^*(t)$ (compare Sec. 2.3) is characterized by the time-dependent decay of the polarization, due to spectrometer imperfections and neutron population distributions (field inhomogeneities, flipper and polarizer/analyzer efficiencies, spectrometer transmission, wavelength distribution, beam divergence ...). In principle, just as in the case of $(\mathbf{Q}, \omega)$-spectrometers, the decay of the observation function limits the time range, where intermediate scattering functions can be determined. The limit is characterized by the observation time, $\Delta\tau_{obs}$, i.e. the decay-time of the observation function, which is the inverse of the virtual resolution width (HWHM) the spin-echo spectrometer would have after transformation to the energy axis. Here, there is however a second, independent upper limit, τ_m , of the spin-echo spectrometer's time window, determined by the limit of the ability of the coils to produce high magnetic fields. To compare with other spectrometers and to evaluate the experimental instrument resolution indicating the maximum time up to which a dynamical phenomenon can be measured, one has to compare the value of the observation time, $\Delta\tau_{obs}$, to τ_m. If $\Delta\tau_{obs}$ is smaller than τ_m, good statistical accuracy of intermediate scattering functions measured at large times (i.e. close to τ_m) will be difficult to obtain. For the energy-resolution correction, the value of the observation function has to be measured for each spin-echo time and for each wavevector transfer Q, in general [8], employing a specimen which is a purely elastic scatterer, with a structure factor as close as possible to that of the sample.

We have shown above, that the spin-echo time is given by $\tau = \eta(\lambda_0^{'})^3$ where the coefficients η applying for the two different techniques, are defined by formulae (78) and (87) for NSE and NRSE, respectively. Here, $\lambda_0^{'}$ is the wavelength of the incident neutrons. One of the key points to achieve high resolution in neutron spin-echo spectroscopy is, to first order, the decoupling of intensity and resolution. This allows the use of broad incident wavelength distributions at little cost in energy resolution. The broad wavelength distribution, together with the very strong $\lambda_0^{'}$ dependence of the spin-echo time, are however not without consequence: Since an average over the wavelength distribution has to be taken (see eqs. (77) and (86)), this amounts to an integration over a corresponding spin-echo time spread. The mean value of the spin-echo time and the time integration window are easily obtained. First, a simple computation of the mean spin-echo time,

$$\langle\tau\rangle = \int \tau(\lambda_0^{'}) f(\lambda_0^{'}) d\lambda_0^{'} \tag{89}$$

shows that this mean value is slightly different from the time corresponding to the maximum wavelength of the distribution. For a velocity selector with

[8] in the case of NRSE, when S(Q) is a slowly varying function in the Q-range of the experiment, it is often sufficient to do this for only one value of Q

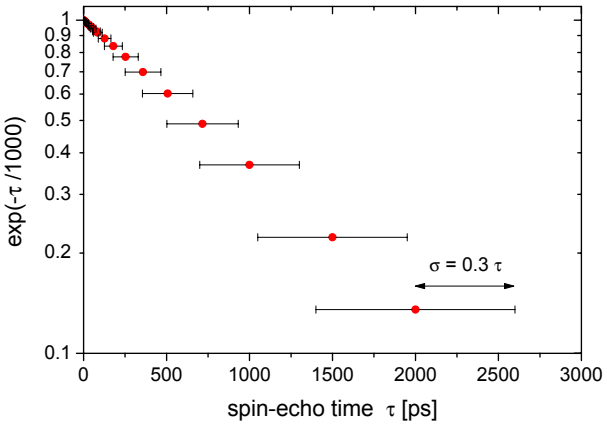

Fig. 12. Logarithmical plot of an exponentially decaying intermediate scattering function, $I(\mathbf{Q},t)$, on a linear time-scale, showing typical spin-echo time integration windows of a spin-echo spectrometer with a velocity selector selecting a wavelength band with $\Delta\lambda_0/\lambda_0 \simeq 0.15$ (FWHM). The horizontal bars represent the standard deviation σ of the spin-echo time τ

$\Delta\lambda_0/\lambda_0 \simeq 0.15$ (FWHM) one obtains,

$$\langle\tau\rangle \simeq 1.02\ \alpha\lambda_0^3 \tag{90}$$

But, more important is the width of the spin-echo time distribution σ_τ. It can be estimated by the computation of the standard deviation,

$$\sigma_\tau = \sqrt{\langle\tau^2\rangle - \langle\tau\rangle^2} \tag{91}$$

This gives $\sigma_\tau \simeq 0.31\tau_0$, where for a given magnetic field, τ_0 is the spin-echo time corresponding to the wavelength λ_0. Figure 12 shows a logarithmical plot of an exponentially decaying intermediate scattering function, $I(\mathbf{Q},t)$, on a linear time-scale. For different spin-echo times the "time integration windows" ($\pm\sigma_\tau$) are indicated by horizontal bars.

NSE spectroscopy is often used for the measurement of slowly decaying relaxation functions. In such cases, the consequence of such broad time integration windows is sometimes of little importance and usually neglected.

5 Miscellaneous Technical Points: MSC, Calibration, Contrast

Let us finally mention a few technical points concerning the analysis of data originating from QENS experiments. At first, we consider those aiming at the direct determination of Van Hove's scattering functions in (momentum, energy)-space. An important problem in the evaluation of quasielastic neutron scattering spectra is the accurate consideration of the experimental resolution. Although straightforward, this is complex, if the spectrum is a sum of several quasielastic components, eventually superimposed by a purely elastic line, either due to the fact that the diffusive motion is localized, or caused by parasitic incoherent scattering from the host material in which the particles perform a diffusive motion. The measured spectra are convolutions of the scattering function with the resolution function. Since a direct deconvolution generally encounters practical difficulties, in a typical analysis the data are usually not directly corrected for resolution, but an inverse procedure is employed. It consists in folding the theoretical model with the measured resolution function and comparing the result to the measured spectra via non-linear least-squares fitting calculations. This method, which amounts to an indirect deconvolution, is well-known, and standard software packages are available in the Neutron Scattering Centers.

Another problem is multiple scattering (MSC). In principle, a neutron reaching the detector, may have been scattered in the sample once , twice, or even several times. For a given nominal scattering angle φ or *nominal* Q value ($Q \cong (4\pi/\lambda)\sin(\varphi/2)$) the weighted double-, triple-, ... scattering spectra are then superimposed on the single-scattering data. The MSC components should be minimized by using sufficiently thin samples. It is usually assumed that a reasonable sample thickness (a compromise between maximizing single-scattering of neutrons and minimizing the contribution of multiple to total scattering) should correspond to a transmission of $T \simeq 0.9$ (roughly 10% of the incident beam is scattered once and about 1% more than once). This leads for example to about 0.2 mm thickness for $\lambda = 5\AA$ in the case of light water and to about 2 mm for deuterated water. Nevertheless, each case should be carefully studied especially with respect to sample absorption and geometry. A numerical correction is often necessary. Analytical methods [77] directly applied to the theoretical models, and model- independent Monte-Carlo techniques (see for instance [78], [79]) are employed for this purpose. For the multiple scattering correction of NSE experiments, the same principles as already described apply, except that this has to be applied in the time domain, where instead of the deconvolution a simple division by the observation function has to be performed.

The third problem is *calibration*, which means the absolute determination of the scattered intensity, instead of quoting "arbitrary units". Calibration is performed, for instance, by comparing the scattered intensity of a sample to

that of a vanadium scatterer which has the same scattering geometry as the sample itself, and whose incoherent scattering cross-section is well-known (provided that there is no hydrogen contamination). In NSE experiments, usually a relative intensity normalization of the measured intermediate scattering function I(Q,t) is performed. For each spin-echo time, the measured polarization is divided by the polarization measured at $\tau = 0$ (i.e., determined without a magnetic field in the coils). Theoretically, $I(Q, \tau = 0)$ should be equal to $S(Q) = \int_{-\infty}^{\infty} S(Q, \omega) d\omega$, but due to the fact that the spectrometer transmits only a wavelength band with a limited width, the integral over the scattering function remains incomplete. If a significant amount of the scattered intensity is outside of the spectrometer window, the normalization will therefore not be absolute. For an absolute calibration the required structure factor $S(Q)$ of the sample must be determined independently, for practical reasons on a different instrument which does not have such a limited bandwidth transmission.

For many elements coherent and incoherent scattering coexists, and it is difficult to *separate the contributions* $S(\mathbf{Q}, \omega)$ and $S_{\mathrm{s}}(\mathbf{Q}, \omega)$. Spin-incoherent scattering causes a fraction of $(2/3)[\sigma_{\mathrm{inc}}/(\sigma_{\mathrm{inc}} + \sigma_{\mathrm{coh}})]$ of the neutrons to flip their spin in a polarized neutron beam, whereas coherent and isotope incoherent scattering occurs without spin flip. The high intensity of polarized beams available at the reactor of the ILL in Grenoble allows to apply this property for a direct separation of the coherent and spin-incoherent contributions, even in the study of quasielastic scattering, by orienting spin polarizer and analyzer parallel and anti-parallel,respectively ([80]; see also [81]). In NSE experiments, the spin incoherent contribution to the signal can however also induce a significant reduction of the polarization due to its spin-flip component which introduces a negative term (see eq. (63)). This adds additional problems of normalization and interpretation, which we will not discuss in the framework of this article.

In biological problems, the interpretation of the results from measurements in (Q, ω)-space is comparatively straightforward, since due to the preponderance of hydrogen atoms in biological matter one can make use of the dominant incoherent scattering of the proton.
The coherent scattering spectrum arises from scattering length density fluctuations in space and time. In the presence of macromolecules in a solution, scattering length fluctuations are characterized by the size of the molecules; their effect dominates the small Q regime of the spectrum. At low concentration (when the interactions between neighbouring molecules are negligible) the molecular form factor can be directly determined by experiment. When the concentration increases, macromolecular interaction leads to significant pair-correlations and (via the structure factor) becomes important in the scattered intensity. A relevant factor is the scattering length density contrast between, for example, the solvent and the solute molecules. The

coherent scattering lengths of hydrogen and deuterium are very different: $b_c^H = -3.741\ Fermi$ and $b_c^D = 6.674\ Fermi$ [9]. The deuteration of a solute macromolecule (or of the solvent) allows to strongly increase the coherent part of the spectrum. Note, that this is another important means of separating coherent and incoherent scattering components. In NSE experiments, where spin-flip causes a large background, the possibility of using deuterated samples can be decisive for the feasibility of the measurements.

More information on modern QENS spectrometers can be found in the Instrumentation Brochures and on the internet home pages of the Neutron Scattering Centers (ILL in Grenoble, France; LLB in Saclay, France; BENSC at HMI in Berlin, Germany; ISIS at RAL in Chilton, UK; NIST in Gaithersburg, USA; FZ Jülich, Germany; FRM-II München, Germany; IPNS at Argonne, USA; PSI Villigen, Switzerland).

6 Summary

We have given an overview of theory and experimental techniques of quasielastic and low-energy inelastic neutron scattering. Apart from the basics of scattering functions and correlation functions, elastic and quasielastic incoherent structure factors have been treated, and the importance of energy resolution and observation time and their variation have been emphasized. A number of selected instruments have been described, which are representative for different ranges of momentum transfer $\mathbf{Q}$, energy transfer $\hbar\omega$ and energy resolution $\Delta\hbar\omega$, or Fourier time t and observation time Δt_{obs}. While, in principle, all types of instrument can cover the same or similar Q-ranges depending on the incident neutron wavelength, this is not so for $\hbar\omega$, $\Delta\hbar\omega$, t and Δt_{obs}. Moderate, high and very high energy resolution are provided by time-of-flight, backscattering and spin-echo techniques, respectively. There is however appreciable overlap between the resolution ranges of different instruments, and this is beneficial, since results from different instruments must often be combined. Furthermore, it is also important to realize, that - because molecular motions occur on time-scales extending over many orders of magnitude - the access to every possible resolution is required, i.e., there is no "bad resolution". As a consequence, the application of *observation-time dependent* quasielastic neutron scattering, in order to investigate dynamic effects due to diffusive atomic and molecular motions has been rapidly expanding and has a very promising future. The high intensities available at modern neutron scattering instruments and especially in the near future at the high-power spallation neutron sources now under construction, will allow the systematic experimental study of such motions on time scales extending over six orders of magnitude at least, and as a function of external parameters.

[9] $1\ Fermi = 10^{-13}\ cm$

Regarding the problem, which instrument to choose for a given task, or which spectrometer to start with, it is clear that the relevant temporal and spatial scales are the first criteria to be considered. There are also some general remarks to be made: Once the scale question has been settled, one must decide, whether it is better to employ a $(\mathbf{Q}, \omega)$- or a $(\mathbf{Q}, t)$-instrument. Spectrometers working in $(\mathbf{Q}, \omega)$-space are more efficient for the study of small quasielastic or inelastic effects in the presence of large elastic components. The reason is, that under conditions of sufficient energy resolution, elastic and non-elastic phenomena are experimentally well separated, whereas in the case of $(\mathbf{Q}, t)$-techniques the elastic term of the scattering function leads to a time-independent (possibly large) "elastic" background underneath the time-dependent relaxation function to be studied. Without this problem, i.e., when the elastic component is small or absent, $(\mathbf{Q}, t)$-instruments are very well suited, especially if rather long Fourier times are required. Furthermore, it is known that the latter techniques are generally more suitable for coherent than for spin-incoherent scattering, because the spin-flip scattering component reduces the useful intensity and can appreciably deteriorate the signal-to-noise ratio. The detailed performance (spectral and reciprocal-space regions, i.e. time and energy domains, momentum-transfer ranges, measurement efficiency) of the different QENS techniques, TOF, BSC, NSE, NRSE, in various experimental situations, is best appreciated by comparing different experimental results (for a few examples, see Part II in this Volume). The question, how to make best use of the complementarity of the different techniques, in order to obtain a maximum of information, must be addressed systematically on the basis of such a comparison before any experimental study.

References

1. L. Van Hove, Phys. Rev. **95**, 249 (1954)
2. S. W. Lovesey, *Theory of Neutron Scattering from Condensed Matter*, Clarendon Press, Oxford 1984
3. G. L. Squires, *Introduction to the Theory of Thermal Neutron Scattering*, University Press, Cambridge 1978
4. M. Bée, *Quasielastic Neutron Scattering: Principles and Applications in Solid State Chemistry, Biology and Materials Science*, (Adam Hilger, Bristol, 1988)
5. L. Koester, H. Rauch, E. Seymann, Atomic Data and Nuclear Data Tables **49**, 65 (1991)
6. V. F. Sears, Physics Reports **82**, 1 (1982)
7. H. Stiller, in *Inelastic Scattering of Neutrons*, Vol.2 (IAEA Vienna, 1965)p. 179
8. K. Sköld, J. Chem. Phys. **49**, 2443 (1968)
9. A. J. Leadbetter and R. E. Lechner, in *The Plastically Crystalline State*, ed. J. N. Sherwood, (J. Wiley and Sons, New York, 1979)pp. 285-320

10. R. E. Lechner, in: *Quasielastic Neutron Scattering*, J. Colmenero, A. Alegría and F. J. Bermejo (Eds.), Proceedings of the Quasielastic Neutron Scattering Workshop QENS'93, San Sebastián, Spain 1993 (World Scientific, Singapore 1994)pp. 62-92
11. M. Bée, Chemical Physics **292**, 121 (2003)
12. A. J. Dianoux, F. Volino and H. Hervet, Mol. Phys. **30**, 1181-1194 (1975)
13. V. F. Sears, Can. J. Phys. **45**, 237 (1967)
14. F. Volino. A. J. Dianoux, Mol. Phys. **41**, 271 (1980)
15. R. E. Lechner, in: *Mass Transport in Solids* , F. Benière and C. R. A. Catlow (Eds.), NATO ASI (1981: Lannion, France) Series B: Physics, Vol. 97, (Plenum Publ. Corp. New York, 1983)pp. 169-226
16. J. Fitter, R. E. Lechner, G. Büldt, N. A. Dencher, Proc. Natl. Acad. Sci. USA **93**, 7600-7605 (1996).
17. T. Springer, *Quasielastic Neutron Scattering for the Investigation of Diffusive Motions in Solids Liquids*, Springer Tracts in Modern Physics Vol. 64, Springer-Verlag, Berlin (1972)
18. R. E. Lechner, Physica B **301**, 83-93 (2001)
19. B. Rufflé, J. Ollivier, S. Longeville, R.E. Lechner, Nucl. Instr. and Methods A **449**, 322 (2000)
20. D.L. Price, K. Sköld, (eds.), *Neutron Scattering*, Chapters 8-11 in: Methods of Experimental Physics, Vol. 23, part B, Academic Press London (1987)
21. R. E. Lechner, C. Riekel, in: *Neutron Scattering and Muon Spin Rotation*, Springer Tracts in Modern Physics Vol. 101, Springer-Verlag, Berlin (1983) pp. 1-84.
22. D. Richter, in: *Neutron Scattering and Muon Spin Rotation*, Springer Tracts in Modern Physics Vol. **101**, Springer-Verlag, Berlin (1983) pp. 85-222.
23. S. W. Lovesey, T. Springer (eds.), *Dynamics of Solids and Liquids by Neutron Scattering*, Topics in Current Physics Vol. 3, Springer-Verlag, Berlin (1977)
24. T. Springer and R. E. Lechner, *Diffusion Studies of Solids by Quasielastic Neutron Scattering*, Chapter 3 in : *Diffusion in Condensed Matter*, Eds. P.Heitjans and J. Kärger, Springerverlag, Berlin, Heidelberg (2005) pp. 93-164.
25. C. G. Windsor, *Pulsed Neutron Scattering*, Taylor & Francis, London (1981)
26. R. Scherm, C. Carlile, A. J. Dianoux, J. Suck, J. White, ILL Internal Report 76S235 (1976)
27. Y. Blanc, ILL Internal Report 83BL21G (1983)
28. see home page, http://www.ill.fr/YellowBook/IN6/
29. J. Mesot, S. Janssen, L. Holitzner and R. Hempelmann, J. Neutron Research **3**, 293-310 (1996)
30. H. Mutka, Nucl. Instr. and Methods in Phys. Res. A, **338**, 144-150 (1994)
31. R. E. Lechner, in *Proceedings of ICANS-XV Conference, Tsukuba, 2000*, eds. J. Suzuki and S. Itoh (JAERI, Tokai-mura, Japan, 2001)pp. 357-376
32. R. E. Lechner, in *Neutron Scattering in the 'Nineties* (IAEA Vienna, 1985)pp. 401-407
33. R. Scherm, Jl-295-NP, Internal Report, KFA Jlich (1965).
34. F. Douchin, R. E. Lechner and Y. Blanc, Internal Technical Report, ITR **26**/73, ILL Grenoble (1973).
35. J. Ollivier, H. Casalta, H. Schober, J. C. Cook, P. Malbert, M. Locatelli, C. Gomez, S. Jenkins, I. J. Sutton, M. Thomas, Appl. Phys. A **74** [Suppl.], S305-S307 (2002).

36. J. Ollivier, M. Plazanet, H. Schober, J. C. Cook, Physica B **350**, 173-177 (2004).
37. S. Hautecler, E. Legrand, L. Vansteelandt, P. d'Hooghe, G. Rooms, A. Seeger, W. Schalt and G. Gobert, in: *Neutron Scattering in the 'Nineties* (IAEA Vienna, 1985) p. 211.
38. R. E. Lechner, in *Proceedings of ICANS-XI*, KEK Report 90-25, eds. M. Misawa, M.Furusaka, H. Ikeda, N. Watanabe (Natl. Lab. for High-Energy Physics, Tsukuba, March 1991)pp. 717-732.
39. R. E. Lechner, Physica B **180 & 181**, 973 (1992).
40. R. E. Lechner, Neutron News **7**(4), 9 (1996).
41. R. E. Lechner, R. Melzer, J. Fitter, Physica B **226**, 86 (1996).
42. J. R. D. Copley, Nucl. Instr. and Methods A **291**, 519-532 (1990).
43. J. G. Smit, H. Dachs and R. E. Lechner, Solid State Commun. **29**, 219-223 (1979).
44. R. E. Lechner, Appl. Phys. A **74**[Suppl.], S151 (2002)
45. B. Alefeld, M. Birr, A. Heidemann, Naturwissenschaften **56**, 410 (1969)
46. B. Alefeld, T. Springer, A. Heidemann, Nucl. Sci. Eng. **110**, 84 (1992)
47. B. Frick, A. Magerl, Y. Blanc, R. Rebesco, Physica B **234-236**, 1177 (1997)
48. B. Frick, Neutron News **13**, 15 (2002)
49. H. Rauch, in: Topics in Mod. Physics (H. Dachs, ed.), Vol. 6 *Neutron Diffraction*, Springer-Verlag Berlin (1978)
50. C. G. Shull, N. S. Ginrich, J. Appl. Phys. **35**, 678 (1964)
51. P. M. Gehring, D. A. Neumann, Physica B **241-243**, 64-70 (1998).
52. A. J. Dianoux, Physica B **182**, 389 (1992)
53. A. Kollmar and B. Alefeld, in: ed. R. M. Moon, *Proceedings of the Conference on Neutron Scattering*, Gatlinburg, Tenn. USA 1976 (National Techn. Information Service, U.S. Dept. Of Comm., Springfield, 1976)pp. 330-336.
54. M. Prager, W. Press, B. Alefeld and A. Hüller, J. Chem. Phys. **67**, 5126 (1977)
55. G. P. Singh, F. Parak, S. Hunklinger, K. Dransfeld, Phys. Rev. Letters **47**, 685-688 (1981).
56. F. Parak, E. W. Knapp, D. Kucheida, J. Mol. Biol. **161**, 177-194 (1982)
57. F. Parak, in: *Biomembranes, Methods in Enzymology, Volume 127*, ed. L. Packer (Academic Press, Inc. London, 1986) pp. 197-206.
58. W. Doster, S. Cusack, W. Petry, Nature **337**, 754-758 (1989).
59. W. Doster, S. Cusack, W. Petry, Phys. Rev. Lett. **65**, 1080-1083 (1990).
60. R. E. Lechner, H.-J. Bleif, H. Dachs, R. Marx and M. Stahn, Solid State Ionics **46**, 25 (1991)
61. C. J. Carlile and M. A. Adams, Physica B **182**, 431-440 (1992)
62. R. W. Connaster Jr., H. Belch, L. Jirik, D. J. Leach, F. R. Trouw, J.-M. Zanotti, Y. Ren, R. K. Crawford, J. M. Carpenter, D. L. Price, C.-K. Loong, J. P. Hodges, K. W. Herwig, in *Proceedings of ICANS-XVI Conference, Düsseldorf-Neuss, 2003*, eds. G. Mank and H. Conrad (FZ Jülich, Germany, 2003)pp. 279-288
63. W. Doster, M. Diehl, W. Petry, M. Ferrand, Physica B **301**, 65 (2001)
64. W. Doster, M. Diehl, R. Gebhardt, R. E. Lechner, J. Pieper, Chem. Phys. **292**, 487-494 (2003)
65. F. Mezei, Z. Physik **255**, 146-160 (1972)
66. F. Mezei, ed., *Neutron Spin Echo*, Lecture Notes in Physics **128**, Springer Berlin (1980)

67. C. Cohen-Tannoudji, B. Diu and F. Laloë, *Mécanique Quantique I*, Hermann ed. Paris (1977).
68. R. P. Feynman, *The Feynman lectures on Physics*, Quantum Mechanics, Addison-Wesley (1965).
69. J. B. Hayter, Z. Physik B **31**, 117-125 (1978).
70. J. B. Hayter, J. Penfold, Z. Physik B **35**, 199-205 (1979).
71. O. Schärpf, in: *Neutron Spin Echo*, Lecture Notes in Physics **128**, F. Mezei Ed., (Springer Verlag 1980),pp. 27-52.
72. J. B. Hayter, in: *Neutron Spin Echo*, Lecture Notes in Physics **128**, F. Mezei Ed., (Springer Verlag 1980),pp. 53-65.
73. F. Mezei, in: *Coherence and Imaging Processes in Physics*, M. Schlenker, M. Fink, J. P. Goedgebuer, C. Malgrange, J. C. Vienot and R. H. Wade, Eds., Vol. **112**, (Springer-Verlag, Les Houches, 1979)pp. 282-295.
74. S. Longeville, W. Doster, M. Diehl, R. Gähler, W. Petry, in: *Neutron Spin-Echo Spectroscopy*, Lecture Notes in Physics, Vol. **601**, eds. F. Mezei, C. Pappas, T. Gutberlet (Springer-Verlag, Berlin, 2003), pp. 325-335.
75. R. Gähler and R. Golub, Z. Physik B - Condensed Matter **65**, (1987) 269-273.
76. R. Golub and R. Gähler, Physics Lett. A, **123**, (1987) 43-48.
77. V. F. Sears, Adv. Physics **24**, 1 (1975)
78. R. E. Lechner, G. Badurek, A. J. Dianoux, H. Hervet and F. Volino, J. Chem. Phys. **73**, 934 (1980)
79. M. Russina, F. Mezei, R. E. Lechner, S. Longeville and B. Urban, Phys. Rev. Letters **84**, 3630 (2000)
80. C. Lamers, O. Schärpf, W. Schweika, J. Batoulis, K. Sommer, D. Richter, Physica B **180&181**, 515 (1992)
81. J. C. Cook, D. Richter, O. Schärpf, M. J. Benham, D. K. Ross, R. Hempelmann, I. S. Anderson, S. K. Sinha, J. Phys. Condensed Matter **2**, 79 (1990)

Available online at www.sciencedirect.com
SCIENCE DIRECT®
Chemical Physics 292 (2003) 413–424
Chemical Physics
www.elsevier.com/locate/chemphys

Myoglobin in crowded solutions: structure and diffusion

S. Longeville[a,*], W. Doster[b], G. Kali[c]

[a] Laboratoire Léon Brillouin, CEA-CNRS, DSM-DRECAM, CEA Saclay, 91191 Gif-sur-Yvette, France
[b] Technische Universität München, Physik department e13, James Franck Strasse 1, D-85747 Garching, Germany
[c] Institut Laue-Langevin, 6 rue J. Horowitz, BP 156, F-38042 Grenoble Cedex, France

Received 20 December 2002; in final form 23 May 2003

Abstract

We present a neutron scattering study of the structure and diffusion of myoglobin solutions at high concentration. The protein–protein structure factor was determined by small angle neutron scattering (SANS) measurements using mean spherical analysis (MSA), and the intermediate scattering function was measured by neutron spin-scho spectroscopy. We observe the cross-over between self-diffusion at high Q and collective diffusion below the structure factor maximum. The self-diffusion coefficient decreases exponentially with concentration. The collective diffusion coefficient is shown to increase at low Q due to direct interactions.

Keywords: Myoglobin; Diffusion; Crowded solutions; Small angle neutron scattering; Neutron spin-echo

1. Introduction

Mainly due to the high concentration of proteins, the interior of biological cells is crowded with macromolecules whose volume fraction range up to 0.3. Under these conditions protein–protein interactions play a central role. In vivo, transient clusters of enzymes are formed depending on physiological requirements. A particular aspect concerns the transport of small molecules like oxygen by protein diffusion. The exchange of oxygen in the lung and in muscle cells is facilitated by macromolecular diffusion [1]. Red blood cells (RBC) are tightly packed with oxygen carrier hemoglobin. In the lungs hemoglobin binds O_2 and releases it in muscle cells, this hetero-association/dissociation must be done near the RBC membrane because of the very low solubility of oxygen. Consequently, the transport of oxygen depends on a delicate balance between two opposing factors: High protein concentrations, which will enhance the quantity of stored oxygen in the RBC, and crowding, which will depress the speed of oxygen binding (due to diffusion limited kinetics) because of strong protein interactions. In fact, an optimum concentration for the oxygen flux is observed [1]. Similarly, myoglobin is present at high concentration in muscle cells. It stores oxygen near the cell surface and is supposed to facilitate oxygen

* Corresponding author. Tel.: +33-(0)-1-69-08-75-30; fax: +33-(0)-1-69-08-82-61.
E-mail address: slongville@cea.fr (S. Longeville).

0301-0104/03/$ - see front matter © 2003 Elsevier Science B.V. All rights reserved.
doi:10.1016/S0301-0104(03)00292-1

transport to mitochondria by simple diffusion. One central goal of our project is to clarify the question, whether the mobility of different components in a living cell can be understood based on their intermolecular interactions. To this end we study the diffusion of myoglobin and hemoglobin molecules at high concentration. As a first step, we perform a structural analysis of the solution, based on SANS data (small angle neutron scattering) and the molecular form factor measured on dilute myoglobin solutions. As a result we obtain an estimate of the intermolecular structure factor, which is relevant to diffusion. In the second step we measure the time dependence of protein diffusion on the scale of the intermolecular distance using neutron spin-echo spectroscopy. Such a study provides insight into mechanistic aspects: How much is the diffusion coefficient depressed with concentration? How does the diffusion coefficient behave in the vicinity of the intermolecular structure factor maximum, where the interaction is most pronounced? Can we discriminate between short-time and long-time diffusion coefficient? How is hydrodynamic interaction between proteins affecting diffusion? Similar questions however on a different length scale were studied using dynamic light scattering (Photon Correlation Spectroscopy) first by Doherty and Benedek [2] on BSA, and later by Weissman et al. [3] and Weissmann and Marque [4]. Light scattering records the concentration fluctuations of over typical distances of few 1000 Å and requires optically transparent samples.

The paper is organised as follows: In Sections 2 and 3 we introduce the theoretical background generally used for structure and dynamics analysis by neutron scattering. Section 4 is devoted to experimental details and Sections 5 and 6 to the experimental results and analysis. Section 7 is devoted to discussion and conclusions are given in Section 8.

2. Theoretical background for SANS data analysis

The neutron intensity scattered by a solution of monodisperse spherical macromolecules is given by

$$I(Q) = (A * F(Q) * S(Q) + B) \otimes R(Q), \quad (1)$$

where A is an amplitude factor, B is a "background", $F(Q)$ is the normalised molecular form factor and $S(Q)$ the structure factor of the macromolecules. $R(Q)$ denotes the resolution function of the diffractometer and $\otimes$ refers to the convolution product.

2.1. The amplitude factor A

For a solution of spherical macromolecules, A depends on the volume fraction Φ, the specific volume v_0 of the macromolecules ($\Phi = v_0 C[\mathrm{mM}] \cdot N_a$), and the difference in the coherent scattering length densities between protein and solvent $(\Delta\rho)^2$ in cm^{-2} (see for example [5]), with N_a is the Avogadro number

$$A = \Phi v_0 (\Delta\rho)^2. \quad (2)$$

The experiments are performed on D-exchanged myoglobin in D_2O solutions, in order to maximise the contrast between the molecules and the solvent. The scattering length density for D_2O is obtained from

$$\bar{\rho}_s = \frac{d(T)}{M} N_a (2b^c_D + b^c_O), \quad (3)$$

where b^c_O is the coherent scattering length of oxygen, b^c_D of deuterium. Following Ref. [6] the density of D_2O at $T = 37$ °C amounts to $\simeq$1.099 g cm^{-3}. It then follows for D_2O

$$\bar{\rho}_s = 6.327 \times 10^{10}\ \mathrm{cm}^{-2}.$$

The coherent scattering length density for protein molecules can be defined as

$$\bar{\rho}_p = \frac{\sum_i b^c_i}{v_p}$$

for fully protonated myoglobin one obtains

$$\bar{\rho}_p = 1.852 \times 10^{10}\ \mathrm{cm}^{-2}.$$

However in reality only a fraction of the labile protons exchanges with the deuterons of the solvent. Assuming that N_H denotes the total number of hydrogen atoms and f is the fraction of exchanged protons of the protein (fN_H deuterium on the protein, assumed to be homogeneously distributed) one finally can write

$$(\bar{\Delta}\rho)^2 = \left(\frac{\sum_{i\neq H} b_i^c + fN_H b_D^c + (1-f)N_H b_H^c}{\bar{v}_p} - \rho_s\right)^2. \quad (4)$$

2.2. The background contribution B

The background contribution includes the incoherent scattering from both the solvent and the protein molecules, as well as the low angle contribution of the coherent scattering of D_2O. The latter is supposed to be constant within the accessible Q-range of the experiment. It is thus possible to extrapolate the solvent contribution of the solvent to infinite dilution. The incoherent scattering arises from the hydrogens, the deuterium and the nitrogen atoms of the protein molecules. This contribution can be written as

$$B = (1-\Phi)I^S(0) + \rho\left(n_N b_N^{i^2} + fNb_D^{i^2} + (1-f)Nb_H^{i^2}\right), \quad (5)$$

where n_N denotes the number of nitrogen atoms per molecule, b^i refer to incoherent scattering lengths. We assume that the exchanged proton atoms have been removed from the solvent by successive dialysis. $I^S(0)$ includes incoherent and coherent contributions from the solvent.

2.3. Molecular form factor of myoglobin in solution

The normalised coherent molecular form factor can be written as

$$F(Q) = \frac{1}{\sum_{i,j} b_i^c b_j^c}\left\langle \sum_{i,j} b_i^c b_j^c e^{-i\mathbf{Q}\cdot\mathbf{r}_{ij}} \right\rangle \quad (6)$$

the bracket corresponds to the average over all equiprobable molecular orientations, b_i to coherent scattering lengths. Finally we get

$$F(Q) = \frac{1}{\sum_{i,j} b_i^c b_j^c}\sum_{i,j} b_i^c b_j^c \frac{\sin(Q\cdot r_{ij})}{Q\cdot r_{ij}}. \quad (7)$$

Assuming a spherical shape for myoglobin, then the form factor is given by the classical equation [7]

$$F(Q) = \left[\frac{3}{(Q\cdot R)^3}(\sin(Q\cdot R) - Q\cdot R\cos(Q\cdot R))\right]^2. \quad (8)$$

The radius R corresponds to the exact radius of the sphere and is related to the radius of gyration by the formula $R_g^2 = 3/5R^2$. The radius of gyration is generally extracted from the measurements by the expansion of the form factor in the Guinier regime ($QR \ll 1$)

$$F(Q) \sim e^{-\frac{1}{3}Q^2 * R_g^2}. \quad (9)$$

2.4. The structure factor of concentrated protein solutions

The determination of the protein structure factor is performed via computation of the Ornstein–Zernike equations (OZE) relating the pair correlation function $h(r) = g(r) - 1$ to the direct correlation function $c(r)$

$$h(r) = c(r) + \frac{6}{\pi}\eta\int c(\mathbf{r}')\cdot\mathbf{h}(|\mathbf{r}-\mathbf{r}'|)\,\mathbf{d}^3\mathbf{r}. \quad (10)$$

In the reciprocal space the OZE can be written as

$$S(Q) = 1 + \hat{h}(Q) = \frac{1}{1-\hat{c}(Q)}, \quad (11)$$

where

$$\hat{c}(Q) = \rho\int_V c(r)e^{-i\mathbf{Q}\cdot\mathbf{r}}\mathbf{d}^3\mathbf{r}, \quad (12)$$

where $\rho = C[\mathrm{mM}]\cdot N_a = \Phi/(4/3\pi\cdot R^3)$ is the number of molecules per unit volume due to the isotropy of the system

$$\hat{c}(Q) = \frac{24\Phi}{\sigma^3}\int_0^\infty c(r)\frac{\sin(Q\cdot r)}{Q}\cdot r\,\mathrm{d}r. \quad (13)$$

To solve the OZE equations one needs a closure relation. Different approximations have been developed in the preceding decades such as mean spherical approximation (MSA) or hypernetted chain approximation (HNC). For the first case (MSA) there is a direct and very simple relation between $c(r)$ and the pair-potential function $V_{ij}(r)$:

$$c(r) = -\beta V_{ij}(r) \quad \text{for } r > \sigma_0 \quad (14)$$

and

$$g(r) = 0 \quad \text{for } r < \sigma_0. \quad (15)$$

Although at least three types of charged species are present in solution, the macromolecule and the

positive and negative ions in the buffer, we treat the solution as a one-component system. This is reasonable because the relative scattering intensity of the solvent ions is negligible. The macromolecule is considered as surrounded by a dielectric continuum and the effect of the charges on the structure are taken into account via their modification of the inter-protein potential. They screen the electrostatic potential, this is the one component model (OCM) with Debye–Hückel approximation (DHA) (i.e: the Derjaguin–Landau–Vervey–Overbeek: DLVO potential – in its simplest form: Hard sphere with Yukawa tail) as defined by:

$$\beta V_{ij}(r) = +\infty \quad \text{for } r < \sigma_0, \tag{16}$$

$$\beta V_{ij}(r) = V_{ij}(\sigma_0)\sigma_0 \frac{e^{-\kappa(r-\sigma_0)}}{r} \quad \text{for } r > \sigma_0, \tag{17}$$

$$V_{ij}(\sigma_0) = \frac{Z_p^2 L_B}{(1+\kappa\sigma_0/2)^2}\frac{1}{\sigma_0}, \tag{18}$$

where $L_B = e^2/(4\pi\epsilon_0\epsilon kT)$ is the Bjerrum length (the minimum distance which can be supported between two charges in a solvent) $L_B \sim 7.5$ Å in H_2O at 25 °C and $L_B \sim 7.25$ Å in D_2O at 37 °C. ϵ is the relative dielectric constant $\varepsilon = 74.32$ in D_2O at 37 °C. σ_0 is the protein diameter. Z_p is the charge of the protein in unity of electron charge e. $\kappa = (4\pi L_B \Sigma_{i=1}\rho_i Z_i^2)^{1/2}$ is the inverse Debye screen length *due to small ions*. κ^{-1} has the dimension of a distance. For aqueous solution with added monovalent salt (NaCl)

$$\kappa^{-1}(\text{Å}) = L_D = \frac{8.13}{\sqrt{L_B(\text{Å})I(\text{mol } l^{-1})}}, \tag{19}$$

where I is the ionic strength of the solution

$$I = \frac{1}{2}\sum_i C_i(\text{mol } l^{-1})Z_i^2. \tag{20}$$

2.5. Algorithm for $S(Q)$ data fitting

2.5.1. The analytical solution by Hayter and Penfold [8]

They computed analytically the solution of Eq. (10) with approximations (16)–(18).

For $r < \sigma_0$

$$c(x) = A + Bx + \frac{1}{2}\eta A x^3 + \frac{C\sinh(kx)}{x} + \frac{F(\cosh(kx)-1)}{x} \tag{21}$$

with $x = r\sigma_0$

for $r > \sigma_0$

$$c(x) = -\gamma\exp(-kx)/x. \tag{22}$$

This expression is given in reduced units but is quite similar to (17) and (18). Details on parameter A, B, C, F and γ are given in [8].

2.5.2. The correction method of [9]

The DLVO potential does not account for any dependence on the concentration, and this approximation is strictly valid only for $\Phi \to 0$. However, the ionic strength of the solution will increase with concentration of the macromolecules. In a paper by Belloni [9] a rescaling method is introduced which can directly be incorporated in the preceeding MSA algorithm of Hayter and Penfold [8]. In this generalised one component model (GOCM) the interaction potential for $r > \sigma_0$ remains of the Yukawa type with $\kappa = 1/L_D$ and L_D is the Debye length due to small ions. Only the prefactor, hence the contact potential is rescaled (Fig. 1).

$$\beta V_{ij}(r) = V_{ij}(\sigma_0)\sigma_0 \frac{e^{-\kappa(r-\sigma_0)}}{r} \quad \text{for } r > \sigma_0 \tag{23}$$

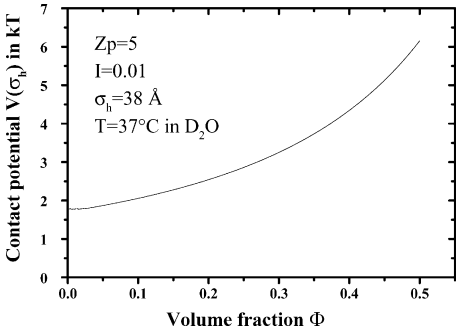

Fig. 1. Volume fraction dependence of the contact potential $V(\sigma_0)$ using the rescaling method of [9].

with

$$V_{ij}(\sigma_0) = Z_p^2 L_B X^2 \frac{e^{-\kappa\sigma_0}}{\sigma_0} \quad (24)$$

The parameter X^2 depends on the screening parameter κ and volume fraction Φ; it is calculated as follows

$$X = ch(\kappa\sigma_0/2) + U(\kappa\sigma_0/2ch(\kappa\sigma_0/2) - sh(\kappa\sigma_0/2)), \quad (25)$$

where

$$U = \frac{\mu}{(\kappa\sigma_0/2)^3} - \frac{\gamma}{\kappa\sigma_0/2} \quad (26)$$

and

$$\gamma = \frac{\Gamma\sigma_0/2 + \mu}{1 + \Gamma\sigma_0/2 + \mu}, \quad (27)$$

where Γ is found by solving numerically the MSA equation

$$\Gamma^2 = \kappa^2 + \frac{q_0^2}{(1 + \Gamma\sigma_0/2 + \mu)^2}, \quad (28)$$

where $\mu = 3\Phi/(1 - \Phi)$ and

$$q_0^2 = \frac{24Z^2e^2\Phi}{4\pi\varepsilon_0\varepsilon_r\sigma_0 kT}. \quad (29)$$

3. Theoretical background for NSE data analysis

Neutron spin-echo spectroscopy [10,11] measures the polarisation $P(Q,\tau)$ of the neutron beam scattered by a sample as a function of the wave vector Q and the Fourier time τ. To a first approximation, $P(Q,\tau)$ is equal to the intermediate scattering function of the system $I(Q,t) = S(Q,t)/S(Q)$. If the scattering process is coherent (favourable for NSE measurements) we obtain for a solution of macromolecules

$$S(Q,t) = \frac{1}{\rho}\sum_{i,j}|F(Q)|^2\langle\exp(-iQ\cdot[r_i(0) - r_j(t)])\rangle, \quad (30)$$

where ρ is the number density of protein per unit volume, $F(Q)$ the molecular form factor (non-normalised), $r_i(0)$ the position of protein i at time $t = 0$ and $r_j(t)$ of protein j at time t. From the intermediate scattering function one can define a generalised diffusion coefficient which is wave vector and time dependent

$$D(Q,t) = -\frac{1}{Q^2}\frac{\partial}{\partial t}\ln(I(Q,t)). \quad (31)$$

For such measurements $D(Q,t)$ is a collective diffusion coefficient, it is related to the decay of the pair correlation function.

4. Sample preparation and neutron scattering experiments

4.1. Sample preparation

Salt-free solutions were prepared from (horse heart) myoglobin (Sigma). A given amount of D-exchanged dry protein (g) per volume of solvent was dissolved in D_2O. The concentrations were then calculated using a specific volume of 0.74 cm^3 g^{-1} [12]. No salt was added.

4.2. SANS experiments

SANS measurements were made at the diffractometer PACE located on the cold source guide G1 of the Orphée reactor of the Laboratoire Léon Brillouin (CEA Saclay). The incident wavelength was set to $\lambda = 6.07$ Å with a wavelength spread of $\Delta\lambda/\lambda = 0.1$. In order to cover the full wave vector range corresponding to the relevant structure factor we used two configurations corresponding to two sample-detector distances $L_{SD}^1 = 0.768$ m and $L_{SD}^2 = 4.618$ m. The respective wave vector range were $Q = 0.04$–0.4 Å^{-1} and $Q = 0.0067$–0.071 Å^{-1}. The samples were 1 mm thick which correspond to transmission ~0.8. Six different solutions ranging from 6 mM up to 30 mM were studied at the physiological temperature $T = 37$ °C. The molecular form factor was measured on two solutions 0.25 and 0.5 mM. Since the differences in shape were limited to uncertainties of the measurements, we assume the forward scattering intensity as arising from $F(Q)$.

The spectra were corrected for background, empty cell and absorption by the standard procedure following [13], no solvent subtraction was performed prior to data analysis.

4.3. NSE experiments

Three neutron spin-echo spectrometers G_1bis and MESS of the LLB and IN15 of the ILL were used for measurements of the intermediate scattering function (ISF). We studied different solutions with myoglobin concentrations ranging from 5.2 to 35 mM. This corresponds to a volume fraction of $\Phi \sim 0.07$ up to $\Phi \sim 0.44$.

G_1bis is a, high flux, medium wave vector, mixed resonance-conventional spin-echo spectrometer [14,15]. We used incident wavelength of $\lambda = 10$ Å, with a Full Width Half-Maximum (FWHM) of the distribution of $\delta\lambda/\lambda = 0.13$. Measurements were performed without other collimations than the resonance coils windows corresponding approximately to $\gamma \sim 1.2°$. It was used in the wave vector range $Q \sim 0.05$–0.25 Å^{-1}. The Fourier time range was $\tau \sim 30$ ps–22 ns. MESS is a SANS NSE spectrometer, with a the distance sample to detector of $L_{SD} \sim 6$ m. The beam collimation is $\gamma \sim 0.5°$, which allows measurements down to $2\theta \sim 1°$. The maximum wavelength distribution was set to $\lambda \sim 6$ Å, with a full width half maximum $\delta\lambda/\lambda = 0.18$. The minimum wave vector of the measurement was $Q = 0.025$ Å^{-1}. IN15 is a long wavelength SANS NSE spectrometer located on the High Flux reactor of the Institut Laue Langevin. It takes advantage of the λ^3 dependence of the spin-echo time to reach very high times. Two wavelengths were used for the experiments, $\lambda \sim 9$ Å and $\lambda \sim 15$ Å to cover the full range of relevant wave vector to be compared with the other spectrometers. The maximum Fourier time was $\tau \sim 200$ ns. The full width half maximum of the incident wavelength distribution was set to $\delta\lambda/\lambda = 0.15$. The minimum wave vector of the measurement was $Q = 0.022$ Å^{-1}.

For all spin-echo experiments we used 30×40 mm^2 quartz cell of 1 mm thickness oriented perpendicular to the incident beam.

5. SANS results

The corrected spectra are shown on Fig. 2 in absolute intensities (cm^{-1}) for myoglobin concentrations ranging from 6 to 30 mM. We used a scaling factor to adjust the intensity of the small Q configuration to the high Q one, but the discrepancy remains smaller than 8%. The molecular form factor was measured in two dilute solutions of 0.25 and 0.5 mM. This corresponds, respectively, to volume fractions $\Phi \sim 3.1 \times 10^{-3}$ and $\Phi \sim 6.2 \times 10^{-3}$. The radius of gyration extracted from the Guinier regime was $R_g \sim 15.9$ Å, compatible with the value previously reported in the literature [16,17]. The measured myoglobin form factor is compared with the intra-molecular form factor refined from the crystallographic structure and compared to the form factor of a sphere (convoluted by instrumental resolution). The results of the refinements are shown on the Fig. 3 for myoglobin, the extracted radius of the protein is $R = 20.6$ Å. The results measured by SANS and deduced from X-ray scattering are comparable with a good degree of accuracy.

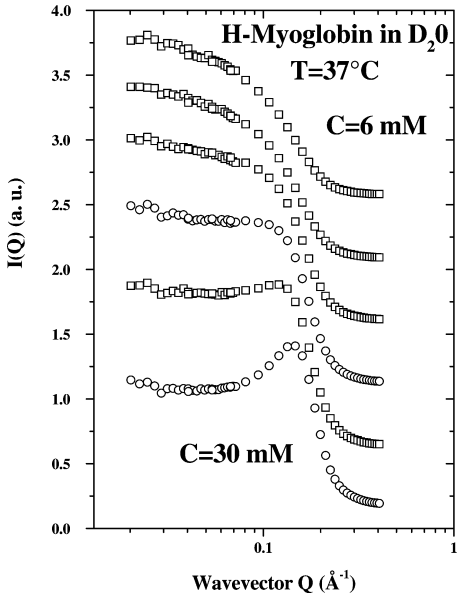

Fig. 2. Neutron scattering intensity $I(Q)$ measured from concentration myoglobin solutions at different concentrations: 6 mM (94 mg ml^{-1}), 10 mM (169 mg ml^{-1}), 15 mM (254 mg ml^{-1}), 20 mM (338 mg ml^{-1}), 25 mM (423 mg ml^{-1}) and 30 mM (508 mg ml^{-1}).

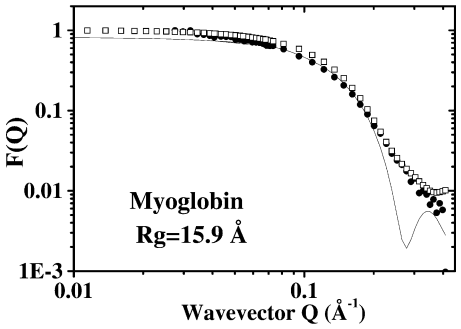

Fig. 3. Normalised form factor of myoglobin calculated from the PDB structure (open squares), measured experimentally on Mb solution of 0.25 mM (full circles) and compared to the form factor of a sphere convoluted by experimental resolution (full line), Eq. (8).

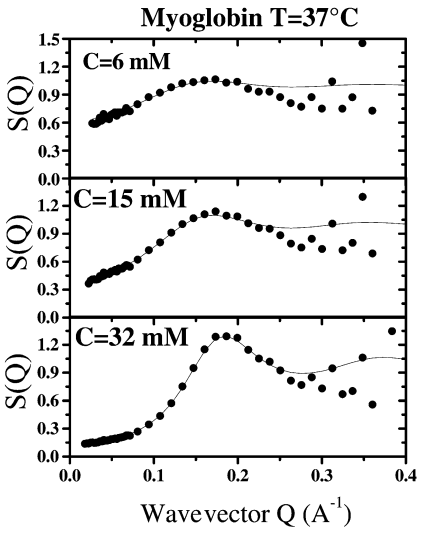

Fig. 4. Structure factor $S(Q)$ of myoglobin solutions ranging from 6 to 30 mM. The points are deduced from experiments and continuous lines the refinements using RMSA.

The refinements of the spectra were performed using the RMSA algorithm with the experimental molecular form factor of myoglobin. A contribution was added in order to account for an additional intensity at low wave vectors probably arising from small amount of aggregation. At high concentrations a maximum in $S(Q)$ emerges, due to intermolecular repulsive interactions. The results of the refinements are shown in Fig. 4, the points are the values of $S(Q)$ deduced from the SANS measurements and the continuous lines were deduced from the analytical formulae. Two parameters are relevant for the structure factor refinements, the radius of the protein and the absolute protein charge $|Z_p|$. The two other parameters are the amplitude factor and background intensity. They depend on the protein volume, on the protein concentration and the number of exchanged protein labile protons.

5.1. The amplitude factor A: Can we use it to compute the number of exchanged protons?

The amplitude factor A was refined using formulae (2) and (4), v_0 and Φ were computed from the protein diameter $\sigma_0 = 2R$ and concentration at each step of the refinement. We finally get $f \simeq 0.05 \pm 0.01$ for concentration ranges 6–30 mM. This corresponds approximately to 20% of labil protons which has been exchanged. However due to the necessity to introduce a factor for the superposition of the two configuration spectra, this value could be affected by significant systematic errors.

5.2. The background contribution B: Is it sensitive to the number of exchanged protons?

The background intensity was refined as a function of the concentration. The fraction of exchanged protons is found to be negligible. However, the maximum difference between fully exchanged and nonexchanged protein solution (only 257 protons can theoretically be exchanged) corresponds to $f = 0.21$ which induces a intensity difference of the order of 0.01 cm^{-1}. To measure with such a precision would require a very high statistics, and moreover at high D_2O fraction such an intensity difference can easily arise from the isotopic impurity of heavy water. It is thus very

difficult to extract any fraction of exchanged protons from the incoherent scattering intensity.

6. The neutron spin-echo results

The results obtained by neutron spin-echo spectroscopy are shown in Fig. 6 (G_1bis) [18] and Fig. 7 (IN15) for solute concentration of 14.7 and 30 mM. These values correspond to volume fraction of $\Phi \sim 0.2$ and $\Phi \sim 0.4$. For the range of wave vectors and concentration under investigation we could not detect in the time dependence of the intermediate scattering function any departure from the single exponential behaviour: The curves were refined using a stretched exponential function and the results concerning the stretching parameter indicate $\beta \simeq 1$. This needs to be verified for cases where the full decay of the intermediate scattering function is not observed. We corrected for λ^3 dependence of the spin-echo time by directly introducing the $D(Q) \cdot Q^2$ in $I(Q,t)$ as was previously described [18]. Such a definition should include all pair contribution but as was mentioned above we assumed that the coherent scattering length density between protein and solution are strong enough to neglect any contribution other than the protein–protein one (especially incoherent scattering). The results of the refinements are shown of Fig. 8, $D(Q)$ was obtained with the 3 different spectrometers for different concentrations. For each protein volume fraction Φ the wave vector dependence of the apparent diffusion coefficient $D(Q)$ is always the same. $D(Q)$ tends to a plateau value D^{ϕ} at high wave vectors and increases at low wave vectors. D^{ϕ} is strongly volume fraction dependent as can be seen in Fig. 8 and was shown in more details on Fig. 5 of [18]. Due to the limited wave vector range of measurements ($Q > 0.025$ Å^{-1}) we were not able to verify that $D(Q)$ tend to a constant value at low wave vectors.

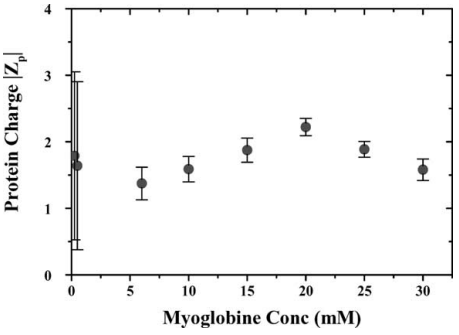

Fig. 5. Effective protein charge $|Z_p|$ obtained from RMSA analysis of myoglobin solutions with concentrations ranging from 6 to 30 mM.

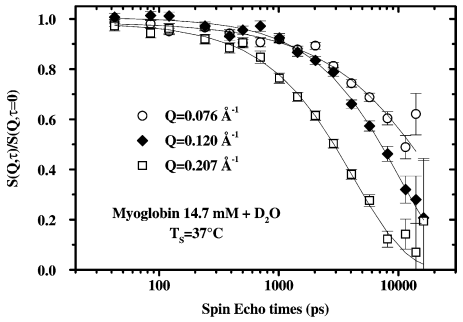

Fig. 6. Intermediate scattering function measured on the spin-echo spectrometer G_1bis for myoglobin solutions of 14.7 mM and three different wave vectors around the structure factor maximum.

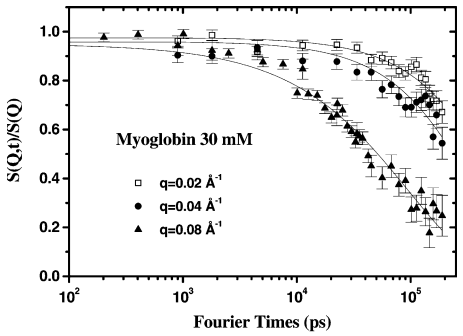

Fig. 7. Intermediate scattering function measured on the spin-echo spectrometer IN15 for myoglobin solutions of 30 mM and three different wave vectors.

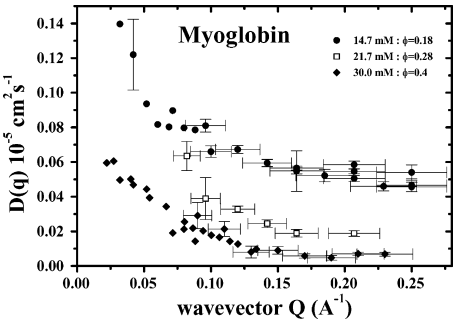

Fig. 8. Wave vector dependence of the apparent diffusion coefficient $D(Q)$ for three different myoglobin concentrations. One can observe a plateau at high Q, which is related to the self-diffusion coefficient $D(Q) \simeq D_s^{\phi}$, and the increase at low wave vector is due to the direct electrostatic interaction (see text).

7. Discussion

7.1. D^{ϕ}: the self-diffusion coefficient

According to the Figs. 4 and 8 the plateau in $D(Q)$ is observed in the regime of wave vectors corresponding approximately to $S(Q) \simeq 1$. In this regime the moment rule pointed out by de Gennes [19] for coherent neutron scattering in simple liquids is de-facto respected. The incoherent approximation of coherent neutron scattering postulated by Vineyard [20] is valid. In other terms, since $QR \gg 1$, a small modification of $\Delta r = r_i(0) - r_j(t)$ (i and j refer to proteins) induces a strong phase shift in the exponential term and thus the average over the nearest neighbours reduces the $i, j \neq i$ term in the scattering function to 0. This was also pointed out for light scattering experiments [21] on colloids. Thus for a solution of protein in D_2O, the intermediate scattering function measured by coherent neutron scattering reduces to

$$I^{c}(QR \gg 1, t) \simeq \langle \exp(-iQ \cdot [r_i(0) - r_i(t)]) \rangle. \quad (32)$$

Hence, within a good approximation, D^{ϕ} is equivalent to the self-diffusion coefficient $D^{\phi} \simeq D_s$ which is generally deduced from neutron scattering measurements as the $Q = 0$ limit of incoherent scattering.

$$D^{\phi} = D^{c}_{QR \gg 1}(Q) \simeq D_s = \lim_{Q \to 0} D^{s}(Q). \quad (33)$$

We have reported previously the volume fraction dependence of D^{ϕ} [18]. It is consistent with the results obtained with macroscopic tracer diffusion techniques by previous authors [22] on myoglobin, but the concentration range of measurements was extended.

7.2. $D(Q)$: the apparent diffusion coefficient

As mentioned above $D(Q)$ measures the *collective* diffusion of the protein in solutions over distances $d \simeq 2\pi/Q$. Structural (direct interaction due to inter-particle potential) and hydrodynamic interactions (effect of the motions of a particle on others via solvent) are generally separated [23–25] using

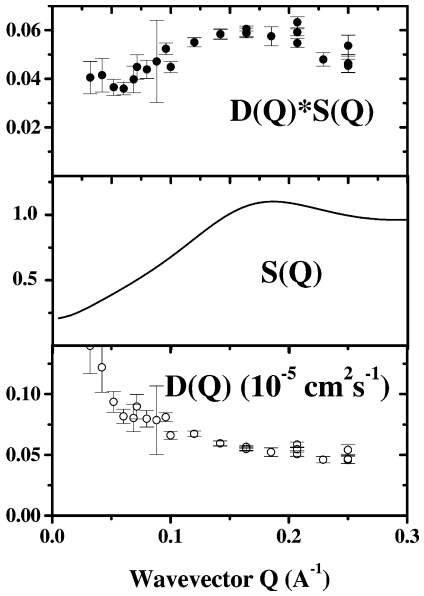

Fig. 9. Apparent diffusion coefficient $D(Q)$ deduced from NSE measurements (bottom), structure factor deduced from RMSA analysis (middle) and $S(Q) \cdot D(Q)$ for myoglobin solutions of 14.7 mM ($\Phi \sim 0.2$).

$$D(Q) = D_\infty \frac{H(Q)}{S(Q)}, \tag{34}$$

where D_∞ is the infinite dilution diffusion coefficient given by Stokes–Einstein relation: $D_\infty = kT/6\pi\eta R$ for a spherical particle. $H(Q)$ denotes the hydrodynamic factor. $H(Q) = 1$ if there is no hydrodynamic effects. We used the structure factor determined by the RMSA refinements and the measured $D(Q)$ to compute the product $D(Q)\cdot S(Q)$. It is presented on Figs. 9 and 10 for two different concentrations corresponding, respectively, to volume fractions $\Phi \simeq 0.2$ and $\Phi \simeq 0.4$. The top of Fig. 9 shows that the hydrodynamic factor is wave vector dependent for $\phi \sim 0.2$. It seems to oscillate in phase with the structure factor. For a given wave vector $H(Q)$ is very strongly protein volume fraction dependent. For a 30 mM solution of myoglobin (Fig. 10) the product $S(Q)\cdot D(Q)$ also seems to oscillate in phase with the structure factor although the results are very noisy. The magnitude of the error bar results from the incomplete decay measurement of the intermediate scattering function in the experimental time window. $I(Q,t)$ can not be measured down to $I(Q,t) \simeq 0$ for high concentration myoglobin solutions for small wave vectors on IN15 spectrometer, and over the full wave vector range for G_1bis.

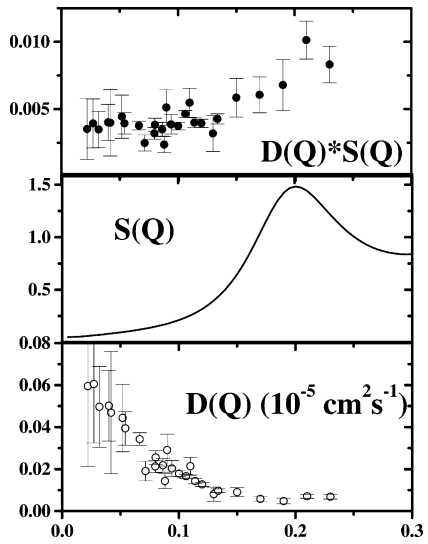

Fig. 10. Apparent diffusion coefficient $D(Q)$ deduced from NSE measurements (bottom), structure factor deduced from RMSA analysis (middle) and $S(Q)\cdot D(Q)$ for myoglobin solutions of 30 mM ($\Phi \sim 0.4$).

7.3. D^c: the collective diffusion coefficient

The apparent diffusion $D(Q)$ measured on protein solutions by DLS does not show any significant wave vector dependence [26]. This quantity has been interpreted as the concentration fluctuation relaxation, and is often related to the transport diffusion coefficient *when a protein concentration gradient is observed*. The characteristic distances probed by DLS (few 1000 Å are much larger than the one measured by NSE in this experiment (50 Å to few 100 Å) so due to the limited wave vector range of the measurements ($Q > 0.025$ Å^{-1}) we were not able to observe any plateau in $D(Q)$ at small wave vectors. One should nevertheless notice from the Fig. 9 that the lowest wave vector limit in $D(Q)$ seems to be less concentration dependent than the self-diffusion coefficient which agrees with previous observations based on different techniques [27].

8. Conclusion

We have performed static and dynamic neutron scattering measurements on myoglobin solutions to study the structure and diffusion processes as a function of the concentration. The structure seems correctly described by the RMSA refinements using a Yukawa type screened electrostatic potential, although the pD of the solution is near the isoelectric point of the protein (hence it carries a small charge), and no buffer was added to the solution to increase the protein charge. The radius of the protein deduced from RMSA analysis ($R \simeq 16$ Å) corresponds approximately to the value which can be deduced from SANS measurements ($R \simeq 17.3$ Å) [16]. The small discrepancy probably arises from the nonspherical shape of myoglobin and the repartition of

exchanged protons atoms near the protein surface. It is interesting to note that the myoglobin concentration deduced from the analysis is slightly lower than the one measured by other methods on our sample. Such an observation was previously reported by Krueger on hemoglobin in blood cells [28] and in solution [29]. It was interpreted by the authors as resulting from oligomer formation. In our case small aggregation can be observed in the very small wave vector range of SANS measurement, but the total amount of protein involved in such phenomena is certainly small since no stretching is observed in the intermediate scattering function measured by NSE. The protein charge $|Z_p| \simeq 2$ and is not concentration dependent. The question whether the structure of water (or solvent in general) can be neglected still remains an open question in particular with respect to the possible structure induced by counter ions clouds around the protein. Indirectly the structure of water is important due to its effect on the dielectric constant. We neglect both effects, and suppose that on this lengths scales the medium can be considered homogeneous. It was suggested that the DLVO potential is not valid for biological objects [30] but in our special case due to the very small charge carried by the protein and the small salt content this objection is probably not relevant. The self-diffusion coefficient, of an almost spherical protein with radius R, can be measured for $QR \gg 1$ by coherent neutron scattering. The effect of hydrodynamic interaction is observed whatever the length scale which has been studied in this experiment. These indirect interactions are responsible for the slowing down of the self-diffusion coefficient D_s, since the structure factor in the wave-vector range were it can be measured is $S(Q) \simeq 1$. The hydrodynamic factor $H(Q)$ is wave vector dependent and seems to oscillate in phase with the structure factor, as measured for the concentration up to $\Phi \simeq 0.4$. For wave vectors below a certain value, collective behaviour due to interactions start to dominate with a speed up of the diffusion. In this Q range we probe the Fourier components of concentration fluctuations $\delta\Phi_q$ of wavelength bigger than the mean intermolecular distances. These decay faster due to collective behaviour. The collective diffusion coefficient is generally assumed to be

$$D_c = \frac{1}{f}\frac{\partial \pi}{\partial C}, \tag{35}$$

where f is the solvent friction coefficient and $\partial\pi/\partial C$ the reciprocal osmotic compressibility. The later term acts as a force which tends to relax the concentration fluctuations. Nevertheless due to limited wave vector range of the experiment we were not able to measure the collective diffusion observed by QLS.

Acknowledgements

We would like to thank D. Lairez and A. Brulet from LLB, for respective help in conducting SANS measurements on PACE and spin-echo measurements on MESS.

References

[1] J.B. Wittenberg, J. Biol. Chem. 241 (1966) 104.
[2] P. Doherty, G.B. Benedek, J. Chem. Phys. 61 (1975) 5426.
[3] M.B. Weissman, R.C. Pan, B.R. Ware, J. Chem. Phys. 70 (1979) 2897.
[4] M.B. Weissman, J. Marque, J. Chem. Phys. 73 (1980) 3999.
[5] B. Jacrot, Rep. Prog. Phys. 39 (1976) 911.
[6] R.J. Millero, R. Dexter, E. Hoff, J. Chem. Eng. Data 16 (1971) 86.
[7] J.S. Higgins, H.C. Benoît, in: Gen. Ed. S.W. Lovesey, E.W.J. Mitchell (Eds.), Polymer and Neutron Scattering, Oxford Series on Neutron Scattering in Condensed Matter, vol. 8.
[8] J.B. Hayter, J. Penfold, Mol. Phys. 42 (1981) 109.
[9] L. Belloni, J. Chem. Phys. 85 (1986) 519.
[10] F. Mezei, Z. Physik B 255 (1980) 146.
[11] F. Meizei (Ed.), Neutron Spin-Echo, Lecture Notes in Physics, Springer, Berlin, 1980.
[12] J. Behlke, I. Wandt, Acta Biol. Med. Germ. 31 (1973) 383.
[13] J.P. Cotton, in: P. Lindner, T. Zemb (Eds.), Neutron, X-Ray and Light Scattering, Elsevier, Amsterdam, 1991, p. 3.
[14] R. Gähler, R. Golub, Z. Physik B – Condens. Matter 65 (1987) 269.
[15] R. Golub, R. Gähler, Phys. Lett. A 123 (1987) 43.
[16] K. Ibel, H.B. Stuhrmann, J. Mol. Biol. 93 (1975) 255.
[17] C. Loupiac, M. Bonetti, S. Pin, P. Calmettes, Eur. J. Biochem. 269 (2002) 4731.
[18] S. Longeville, W. Doster, M. Diehl, R. Gähler, W. Petry, in: F. Mezei, C. Pappas, T. Gutberlet (Eds.), Neutron Spin

Echo Spectroscopy, Basic Trends and Applications, Lecture Notes in Physics, vol. 601, Springer, Berlin, 2002.
[19] P.G. de Gennes, Physica 25 (1959) 825.
[20] G.H. Vineyard, Phys. Rev. 110 (1958) 999.
[21] P.N. Segré, O.P. Behrend, P.N. Pusey, Phys. Rev. E 52 (1995) 5070.
[22] V. Riveros-Moreno, J.B. Wittenberg, J. Biol. Chem. 247 (1972) 895.
[23] B.J. Ackerson, J. Chem. Phys. 64 (1976) 242.
[24] P.N. Pusey, J. Phys. A: Math. Gen. 8 (1975) 1433.
[25] P.N. Pusey, in: J.P. Hansen, D. Levesque, J. Zinn-Justin (Eds.), Liquids, Freezing and the Glass Transition, Elsevier, Amsterdam, 1991 (Chapter 10).
[26] Y.S. Oh, C.H. Johnson, J. Chem. Phys. 74 (1981) 2717.
[27] R.S. Hall, C.H. Johnson, J. Chem. Phys. 72 (1980) 4251.
[28] S. Krueger, R. Nossal, Biophys. J. 53 (1988) 97.
[29] S. Krueger, S.H. Chen, J. Hofrichter, R. Nossal, Biophys. J. 58 (1990) 745.
[30] M. Bostrom, D.R.M. Williams, B.W. Ninham, Phys. Rev. Lett. 87 (2001) 168103.